Studying dark matter haloes with weak lensing

Velander, M.B.M.

Studying Dark Matter Haloes with Weak Lensing

Studying Dark Matter Haloes with Weak Lensing

PROEFSCHRIFT

ter verkrijging van
de graad van Doctor aan de Universiteit Leiden,
op gezag van de Rector Magnificus prof. mr. P. F. van der Heijden,
volgens besluit van het College voor Promoties
te verdedigen op woensdag 20 juni 2012
klokke 11.15 uur

door

Malin Barbro Margareta Velander

geboren te Lund, Zweden
in 1983

Promotiecommissie

Promotor:	Prof. dr. K. H. Kuijken
Overige leden:	Prof. dr. M. Franx
	Prof. dr. A. Taylor (Edinburgh University, UK)
	Dr. H. Hoekstra
	Dr. J. Brinchmann

For my husband
and our little one

Cover: *Chinese Kite Cluster* by Gabrian J. van Houdt

Table of Contents

Introduction 1

The vast unknown that is our Universe has always fascinated mankind. Though science is progressing fast and efficiently, still a large number of riddles remain unsolved. Every decade brings with it new discoveries, but more often than not a breakthrough gives rise to yet more questions. Amongst the main advancements of the past quarter-century is the uncovering of dark matter and dark energy as the principal ingredients of our standard model of cosmology. With this model our understanding of the mechanisms behind the origin and the evolution of our Universe has progressed immensely, but to advance further we have do answer this: what is dark matter and dark energy? To help bring clarity to the nature of these phenomena we study the distribution of matter within galaxies, within galaxy clusters, and throughout our Universe. A relatively recent technique, developed in the last couple of decades, has the ability to map matter regardless of whether it is visible or dark and without it having to be confined to large overdensities such as galaxy clusters. This technique is known as *weak gravitational lensing* and it is a highly powerful probe of cosmology.

With this Thesis I aim to increase our knowledge of the distribution of matter in galaxies and galaxy clusters both by further developing the theoretical framework for weak lensing, and by using large optical surveys to observe the weak lensing signal directly. I therefore start with a brief introduction to cosmology and to gravitational lensing, with an emphasis on weak lensing and the current status of lensing distortion software.

1.1 Cosmology

1.1.1 The concordance model of cosmology

Cosmologists study the Universe as a whole and are striving to understand how it was formed and how it has arrived at the point where we are now. How did the initially nearly smooth and homogeneous matter distribution evolve to form the stars, galaxies and galaxy clusters that surround us today? To describe this process we use a template which we know to be a fairly accurate description of reality. The one currently favoured by cosmologists is known as ΛCDM, where Λ represents *dark energy* and CDM stands for *cold dark matter*. This model attempts to simultaneously explain the growth of matter structure

observed throughout the Universe, the temperature structure observed in the cosmic microwave background (CMB), and the accelerated expansion of the Universe indicated by e.g. supernova studies. In the process ΛCDM quantifies the size of the mass-energy density constituents. Surprisingly, the known components of the Standard Model of Particle Physics, such as electrons, protons and neutrons, compose only a minor part — about 5% — while the majority of the matter constituents appears to be something new: dark matter. Even more surprising is that the majority of the energy density appears to be composed of the mysterious dark energy which makes up some 70% of the total. Dark matter is necessary for structure formation as it adds gravity which holds large structures such as galaxies or clusters of galaxies together. Though we have not yet determined exactly what dark matter is, there are some indications of what it could possibly be. Traditionally there are three categories of dark matter: *cold*, *warm* and *hot*. These labels refer to how fast the particles were able to move at the very beginning of the Universe. Cold dark matter became non-relativistic early on, while hot dark matter stayed relativistic until shortly before the epoch known as recombination during which atoms formed. Since we know the temperature of the Universe at that time, this also sets limits on the masses of such particles, with hot dark matter being much lighter than cold dark matter. The most commonly known candidate for a hot dark matter particle is the neutrino. Neutrinos are very light and conform to the constraint that dark matter has to be only *weakly interacting*, making them hard to detect. A model dominated by hot dark matter is inconsistent with hierarchical galaxy formation though, so this alternative has effectively been ruled out via observations. Warm dark matter is then more feasible, and behaves similarly to cold dark matter on large scales though there may be differences on small scales. The most commonly considered candidate warm dark matter particle is the sterile neutrino which is more massive than its hot dark matter counterpart. However, since these sterile neutrinos are not well motivated in particle physics, the current standard model of cosmology prefers cold dark matter. There is now a plethora of candidates for what cold dark matter could be since there is no real upper limit to the mass allowed. Thus these candidates range from the hypothetical *weakly interacting particles* (WIMPs), which may be massive neutrinos or so-called axions, to *massive compact halo objects* (MACHOs) which could refer to dwarf planets or black holes. Observations have, however, ruled out MACHOs as the sole explanation for dark matter (see e.g. Section 1.2.2) and so it is generally concluded that dark matter must be a new type of cold particle, yet to be discovered. The nature of dark energy requires some further introduction and is therefore discussed later in this Section.

ΛCDM has gained great support due to its ability to successfully reproduce a universe much like ours. Of the triumphs of the model, the results from the Cosmic Background Explorer (COBE; Mather, 1982; Gulkis et al., 1990; Mather et al., 1990) and its successor the Wilkinson Microwave Anisotropy Probe (WMAP; Bennett et al., 2003; Spergel et al., 2003; Jarosik et al., 2011) stand out. The two space missions have together accumulated 15 years' worth of CMB data, producing exceedingly accurate measurements of the echoes of the Big Bang via the CMB angular power spectrum, shown in Figure 1.1. The best-fit model, assuming ΛCDM, is also shown in the Figure, clearly demonstrating that ΛCDM describes current cosmological observations well. This is just one example of ways to constrain cosmology though. Another very powerful probe is

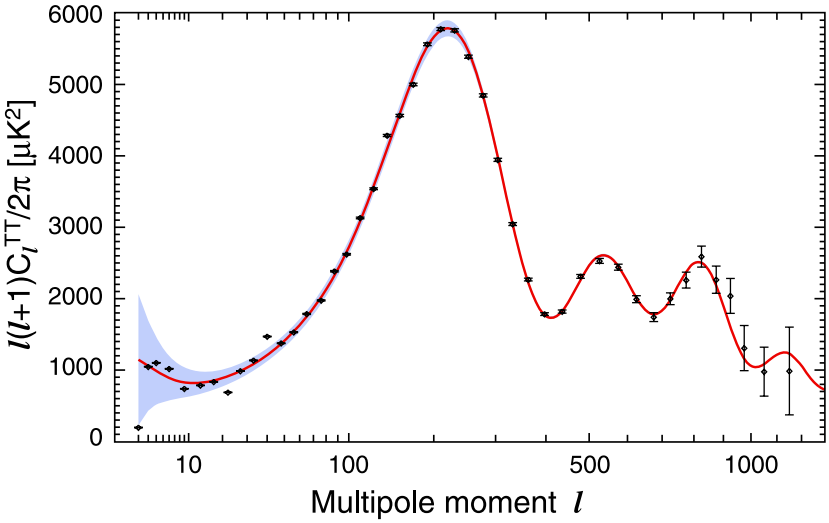

Figure 1.1 The CMB angular power spectrum from the 7-year WMAP data release. The red curve represents the best-fit ΛCDM model and the grey band shows the cosmic variance expected for that model. The first, second and third acoustic peaks are highly constrained. Figure originally published in Larson et al. (2011).

weak lensing which will be introduced later, and yet more probes are discussed in Section 1.1.3.

Selected best-fit parameters from the WMAP 7-year data release are quoted in Table 1.1 and this is also the cosmology assumed throughout this Thesis unless explicitly stated otherwise. These are the aspects of ΛCDM that are relevant to weak gravitational lensing, which is the focus of this work. Conversely, weak gravitational lensing can be used to constrain most of these parameters. To elaborate on the meaning of the parameters in Table 1.1, further background is needed.

Our Universe is expanding which means that objects that are not gravitationally bound together will move away from each other. Therefore we see galaxies and galaxy clusters receding from us in all directions and the further away from us an object is, the faster it moves away from us. The *Hubble constant* H_0 relates this recessional speed to the distance from us via Hubble's Law:

$$v = H_0 D \tag{1.1}$$

The exact value of the Hubble constant is important for interpreting all cosmological results since it affects distances and thus volumes and densities. In most applications, the dimensionless version of the Hubble parameter, h, is used, and it is defined as

$$H_0 \equiv 100\ h\ \mathrm{km\,s^{-1}\,Mpc^{-1}} \tag{1.2}$$

so for the value of H_0 given in Table 1.1 we have $h \simeq 0.70$. Furthermore, objects that are moving away from us will have an electromagnetic spectrum which is shifted towards the redder end due to a stretching of light waves (known as the Doppler effect), and thus we can determine the distance to a distant object via

Table 1.1 Cosmological parameters from the WMAP 7-year data release (Jarosik et al., 2011). These parameters are the result of combining WMAP data with priors from baryonic acoustic oscillations based on the Sloan Digital Sky Survey Data Release 7 (Percival et al., 2010) and from the present-day Hubble constant value determined using 240 Cepheid variables and as many supernovae type Ia (Riess et al., 2009).

Parameter	WMAP7+BAO+H_0 value	Comment
H_0	$70.4^{+1.3}_{-1.4}$ km s^{-1} Mpc^{-1}	The Hubble constant
Ω_b	0.0456 ± 0.0016	Baryon density
Ω_{dm}	0.227 ± 0.014	Dark matter density
Ω_Λ	$0.728^{+0.015}_{-0.016}$	Dark energy density
σ_8	0.809 ± 0.024	Fluctuation amplitude at $8h^{-1}$ Mpc
w	-0.980 ± 0.053	Equation of state

its *redshift* z:

$$1 + z = \frac{\lambda_{\rm obs}}{\lambda_{\rm emit}} \tag{1.3}$$

where $\lambda_{\rm obs}$ and $\lambda_{\rm emit}$ are the observed and emitted wavelengths respectively. Cosmologists often use redshift as a measure of distance to objects, and also — somewhat confusingly — as a measure of time.

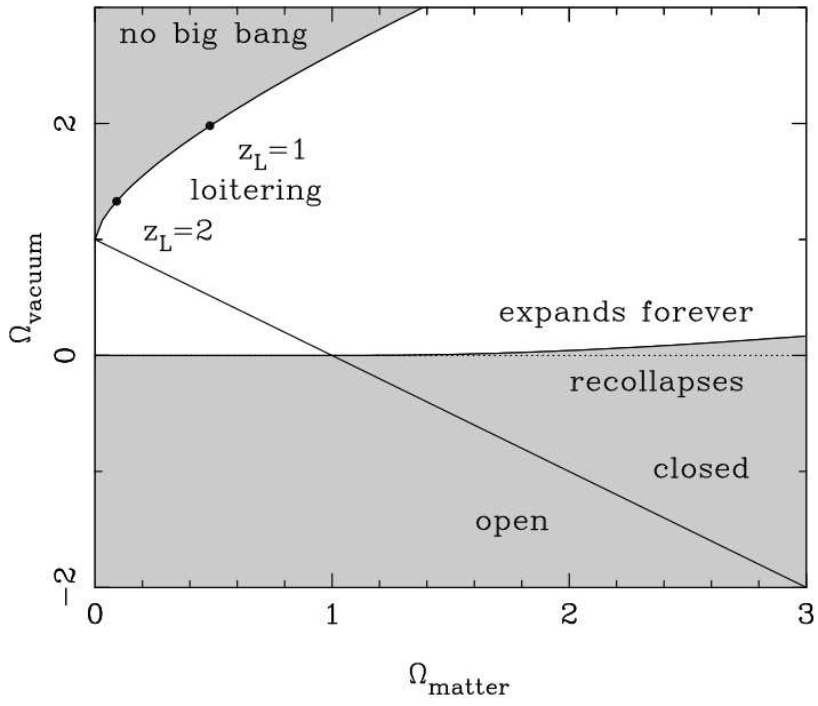

Figure 1.2 Influence of the two main energy density parameters on the overall behaviour of the Universe. Here, $\Omega_{\rm matter}$ and $\Omega_{\rm vacuum}$ are identical to the Ω_m and Ω_Λ parameters mentioned in the text. Figure originally published in Peacock (1999).

We can define a *critical density* $\rho_{\rm crit}$ at time t for which the local Universe is *flat*, i.e. where the angles of a triangle add up to 180°, as

$$\rho_{\rm crit}(t) = \frac{3H^2(t)}{8\pi G} \tag{1.4}$$

Note here that the H parameter is time-dependent; this is the *Hubble parameter* which defines the relative expansion rate at that point in time, and $H_0 \equiv H(t_0)$. G is the gravitational constant. Using this we can then derive a *density parameter* Ω_X which represents the ratio of the actual density to the critical density:

$$\Omega_X = \frac{\rho_X}{\rho_{\rm crit}} = \frac{8\pi G\rho}{3H^2(t)} \tag{1.5}$$

where the subscript X can represent any mass-energy density constituent. Ω_b, Ω_{dm} and Ω_Λ are then the density of baryons, dark matter and dark energy compared to the critical density, and these constants evolve with time and therefore with redshift. Adding the two first parameters together we get the total matter density $\Omega_m = \Omega_b + \Omega_{dm}$. The influence of these parameters on the global behaviour of the Universe is illustrated in Figure 1.2. The solid straight line for which $\Omega_{\rm tot} = \Omega_m + \Omega_\Lambda = 1$ represents a flat universe. For $\Omega_{\rm tot} > 1$ the model is spatially *closed* which means that it has a finite volume and positive curvature everywhere, i.e. the angles of a triangle add up to more than 180° like on the surface of a sphere. Conversely, for $\Omega_{\rm tot} < 1$ the Universe is spatially *open*, has infinite volume and negative curvature everywhere. This type of universe is usually illustrated by a saddle-like shape. Figure 1.2 also shows that a negative Ω_Λ causes the Universe to eventually recollapse while it will continue to expand forever for a positive parameter (in most cases). There is also the possibility of a 'loitering' model with a maximum redshift and infinite age, and for high values of Ω_Λ there is no Big Bang. The current parameter estimates thus support a flat universe which will be expanding forever. We can write the Hubble parameter in terms of density parameters and redshifts:

$$H^2(a) = H_0^2\left[\Omega_\Lambda + \Omega_m a^{-3} + \Omega_r a^{-4} - (\Omega_{\rm tot} - 1)a^{-2}\right] \tag{1.6}$$

where $a = 1/(1+z)$ is a scale factor, Ω_r is the density of radiation energy and $\Omega_{\rm tot}$ is equal to 1 for a spatially flat Universe. All density parameters are defined at the present time, t_0.

The next parameter in Table 1.1, σ_8, is a crucial parameter for cosmology. Formally it is the fluctuation amplitude within a sphere of radius $8\,h^{-1}$ Mpc and functions as a normalisation for the linear matter power spectrum. The value of this parameter influences the growth of structure in the Universe. If it is too low, the fluctuations in the early Universe were too small to feasibly allow for the formation of the stars and galaxies we see today. Finally, the parameter $w \equiv p/\rho c^2$, where p is pressure, defines the equation of state of a postulated contribution to the overall energy density from an unknown quantity. For $w \simeq -1$ this quantity causes an accelerated expansion and the Universe is thus expanding at an ever-increasing rate due to some unknown energy contribution, commonly referred to as dark energy. The presence of this dark energy has been corroborated via several observational indicators of an accelerated expansion (see Section 1.1.3). Just as for dark matter, we have yet to confirm the exact nature of dark energy, though candidates may be categorised as either a constant homogeneous energy

density or *scalar fields* which may vary through space-time. The scalar fields alternative is discussed further in the next Section, but the concordance model ΛCDM assumes a constant energy density which is represented by the cosmological constant Λ. The use of this particular constant is a nod to Einstein and his attempt to balance his field equations to obtain a static universe. Though Einstein's exact solution has since been proven unstable, the recycling of his constant to represent an accelerating universe signifies the similarities between his constant and the behaviour of modern dark energy.

1.1.2 Alternative models

Although ΛCDM is generally accepted as the most successful model for describing our Universe given current observations, there are alternative descriptions. One of the main criticisms of ΛCDM is the need for unknown 'dark' quantities and this has been the motivation for the development of alternatives. ΛCDM assumes in general that the laws of physics hold true throughout the Universe. A family of alternative models reason that this assumption may be false and that laws of gravity require modifying at large distances. Amongst the most well-known are *Modified Newtonian Dynamics* (MOND; Milgrom, 1983) and *Tensor-Vector-Scalar gravity* (TeVeS; Bekenstein, 2004).

MOND was initially introduced as a way to model the flat rotation curves of galaxies without the need for dark matter. The puzzle of galaxy rotation curves was first noted by Rubin & Ford (1970). Studying the Andromeda galaxy, they found that the velocities of stars in the disk stayed constant rather than decreased with distance as would be expected from classical mechanics. The stars in the outer regions of the disk were thus moving much faster around the centre of the galaxy than should be possible. Freeman (1970) noted a similar behaviour in their sample of disk galaxies, tentatively suggesting that there is undetected matter beyond the optical extent of NGC 300. Rubin et al. (1980) then used a larger galaxy sample to conclude, inspired by a remarkable prediction by Zwicky (1933), that there must be a significant amount of unseen mass beyond the limit of the optical observations. The work of Vera Rubin and colleagues on galaxy rotation curves thus constitutes the first real evidence for dark matter — or an indication that classical mechanics is an inaccurate description on galaxy scales. As the name implies, MOND modifies Newtonian dynamics by allowing for some critical acceleration a_0 below which the classical Newtonian force-acceleration relation, $F \propto a$, breaks down. The acceleration close to massive structures thus obeys general relativity, but at large enough distances force is related to acceleration via $F \propto a^2/a_0$. This theory has been highly successful in modelling the rotation curves of galaxies, particularly for galaxies with low surface brightness which represent an extreme where ΛCDM is currently not as powerful. However, on a galaxy cluster scale MOND still requires more mass than what is observed in baryonic form, with massive neutrinos being suggested as a possibility (Sanders, 2007). Furthermore, because MOND is non-relativistic it cannot reproduce gravitational lensing, or indeed cosmology as a whole and is unable to model the CMB power spectrum. TeVeS was then developed as a relativistic generalisation of MOND and successfully models phenomena that MOND does not. It can reproduce the first and second acoustic peaks in the observed CMB power spectrum shown in Figure 1.1, though this necessitates the inclusion of massive neutrinos (McGaugh, 2004;

Skordis et al., 2006). For the tertiary and higher peaks, the amplitude is too low even with added neutrinos because a baryon-only model necessarily predicts that the peak amplitudes should be monotonically decreasing. As for MOND, TeVeS is also relatively successful in modelling spherically symmetric clusters, although again massive neutrinos are required for an essential dark halo and the neutrino mass necessary is unrealistically large (Takahashi & Chiba, 2007). Merging clusters, a few cases of which are discussed in Section 1.3.4, also pose a problem.

MOND and TeVeS have primarily been developed as an alternative to dark matter rather than attempting to replace the full ΛCDM description which includes considerations of the accelerated expansion of the Universe. Though there has been some work on the acceleration implied in TeVeS (Zhao, 2007; Hao & Akhoury, 2009), further exploration is needed in this area. Other models have been suggested as an alternative to the cosmological constant Λ as mechanisms for accelerating the expansion of the Universe. Amongst the first alternative explanations to be suggested is *quintessence* — a fifth fundamental force which is repulsive. Evolved from string theory, another intriguing model is that of the brane cosmology. *Brane* here is short for membrane, and in this cosmology space-time as we know it is confined to a brane embedded in a higher-dimensional space known as the *bulk*. The fundamental forces of nature are localised to the brane while gravitational force is not, which means that our brane can interact gravitationally with the bulk and with other branes. In one version of brane theory, the Big Bang is the result of a collision between two parallel branes (Khoury et al., 2001). The flavour that has gained most support are the Randall-Sundrum models which assume a five-dimensional space in total, i.e. only one extra dimension for the bulk (Randall & Sundrum, 1999a,b,c). The fifth dimension is finite and there are two branes in the model, although in one version one of the two branes is placed infinitely far away, effectively leaving a sole brane in the model. The energies of the two branes cause a severe warping of spacetime along the fifth dimension. An effective cosmological constant is the automatic result of this model (Cline et al., 1999).

Developing alternative methods to describe our Universe is ultimately beneficial to science because they do further our insight into physical mechanisms, though a completely satisfactory version has yet to emerge. ΛCDM is currently the model that is most successful at recovering what we see in observations on a large range of scales and for many different types of structure. It has to be kept in mind, however, that it is just a model and that it, too, has applications which are not completely understood. Emphasis should also be put on the fact that dark matter and dark energy are just descriptors for gravitational and accelerating fields which help us visualise these fields. Whether the forces involved are due to actual dark particles or due to as yet unknown physics, the effect is the same. And there is a lot of work to be done still before we can claim to fully understand the Universe we live in. The probes of cosmology described below are therefore vital for furthering that understanding.

1.1.3 Cosmology probes

There are several ways to test and constrain our cosmology models and often each such probe is more sensitive to some parameters than others. Combining several datasets will therefore result in much tighter constraints on cosmology

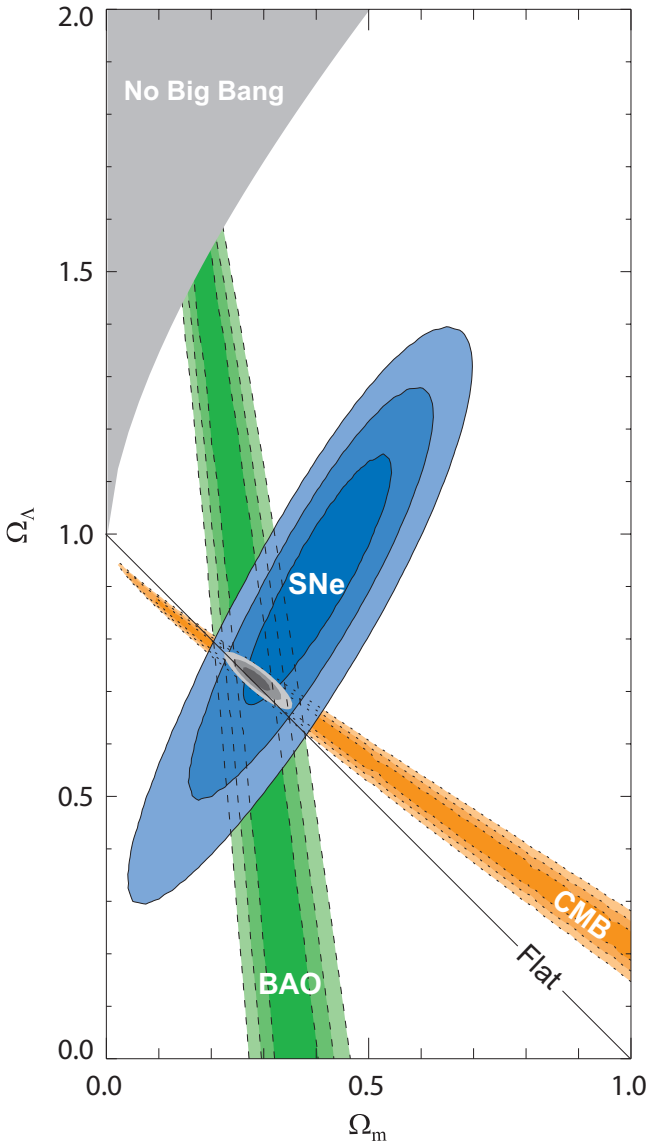

Figure 1.3 Combining several independent datasets to constrain cosmology (c.f. Figure 1.2). The datasets shown in this figure are the results from the cosmic microwave background (CMB; Dunkley et al., 2009), baryon acoustic oscillations (BAO; Eisenstein et al., 2005) and supernovae (SNe; Kowalski et al., 2008). Though each dataset is degenerate in some sense, combining them all gives tight constraints on Ω_m and Ω_Λ (contours at intersection). Figure originally published in Kowalski et al. (2008).

than each on its own.

The CMB power spectrum is sensitive in shape, peak location and relative peak heights to the underlying cosmology (see Figure 1.1, and e.g. Hu & White, 1996; Peacock, 1999). The location of the first acoustic peak is related to the

curvature of the Universe; we now know that the Universe is essentially flat. Furthermore, the location of each peak relative to the previous one is an indicator of the nature of the primordial density perturbations. The peak locations measured by WMAP provide strong support for dark energy. Regarding amplitudes, the amplitude of the first peak compared to the second one (or odd peaks versus even ones) holds information on the baryon density. The more baryons present, the more relatively suppressed the second peak is. Finally, by determining the height of the third peak we determine the ratio of dark matter density to radiation density, and since we know the radiation density from other measurements it gives us the dark matter density in the Universe. However, different parameters may affect the power spectrum in a similar way, which means that we cannot tell whether the shift in one direction is due to the variation of one parameter or another. This is what is known as a *parameter degeneracy*. As an example, the Ω_m and H_0 parameters are degenerate which is why the spread in allowed values for Ω_m is so large (see Figure 1.3). To break such a degeneracy, independent measurements of H_0 are needed and these measurements may be provided by e.g. studies of supernovae (SNe).

Historically, SNe provided one of the first indications of an accelerated expansion (Riess et al., 1998; Perlmutter et al., 1999). SNe is a collective name for all types of stars exploding during, or at the end of, their life cycle. There are several mechanisms that can cause such an explosion, but for cosmological applications one mechanism is of particular interest: that which leads to a Type Ia SN. This species inevitably results in a characteristic light curve, i.e. how the luminosity resulting from the explosion decays with time is identical for all SNe of a given brightness. By precisely measuring such a light curve and comparing it to the observed brightness, the distance to the SN can be accurately inferred. The redshift of the SN host galaxy is then used to constrain the relationship between distance and redshift which in turn constrains Ω_m and Ω_Λ, breaking the degeneracy in the CMB power spectrum as described above (again, see Figure 1.3).

Another probe which allows the breaking of the above degeneracy is the study of large-scale structure (LSS). The way galaxies are distributed throughout the observable Universe is a measure of how matter is distributed and how it clusters, something which is sensitive to Ω_m. Galaxies have therefore been mapped in redshift space through spectroscopic surveys such as the Two-Degree-Field Galaxy Redshift Survey (2dFGRS; see e.g. Cole et al., 2005, for results from the final data set) and the Sloan Digital Sky Survey (SDSS; see e.g. Tegmark et al., 2004). However, because we do not know exactly how the locations of galaxies correspond to the location of the underlying dark matter, interpreting the results in terms of Ω_m is difficult. It requires a description of how well galaxies trace the total mass distribution, and this description is quantified via the *galaxy bias*. The choice of bias constitutes an uncertainty in LSS measurements and needs to be further investigated. In general though, we see a pattern of clustered matter and filaments connecting the clusters, and between the filaments we see voids where there is no matter. This pattern is commonly known as the *Cosmic Web* and the voids are a signature of sound waves created by cosmological matter perturbations in the early Universe, identified as baryon acoustic oscillations (BAO). The imprint of BAO on the matter power spectrum provides a characteristic length scale, and measuring it constrains the distance-redshift relation giving a measure of Ω_m (e.g. Eisenstein et al., 2005,

as in Figure 1.3).

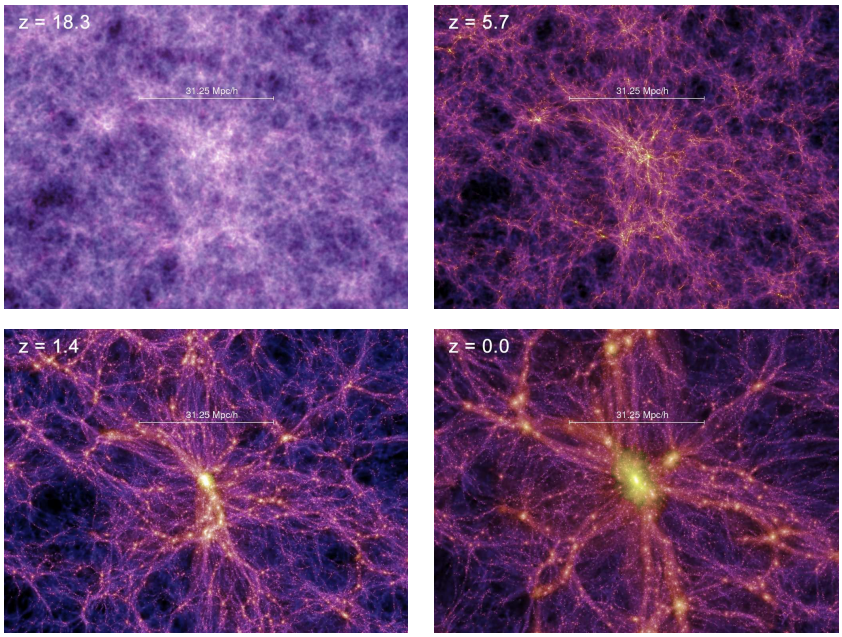

Figure 1.4 Millennium simulation slices at progressively lower redshifts as printed on each panel. The scale of all slices is the same. Images originally published in conjunction with Springel et al. (2005).

A different approach to studying cosmology is to create a new cosmos using the physical laws and properties we are aware of so far. This can be done using so-called *N-body simulations* which take (dark) matter particles, place them according to some initial conditions and let them interact over the life-span of the Universe. Comparing these simulations at different points in redshift to real observations at the same redshifts tells us how well we have understood the underlying physical processes. Currently, the most widely known and used N-body simulation is that of the Millennium Simulation (Springel et al., 2005). Shown in Figure 1.4 are four slices from this dark matter only simulation at different redshifts which illustrate the growth of structure from a nearly homogeneous matter distribution at $z = 18.3$ to a galaxy cluster at $z = 0.0$. One application of N-body simulations is, for instance, that the density profile of a simulated cluster may be modelled and then compared to an equivalent observed cluster studied using gravitational lensing, a technique with the power to map the full mass distribution, to see how well the profiles agree. Studying clusters at different redshifts allows us to investigate the evolution of structure as well. A significant limitation of most N-body simulations is, however, that they use only dark matter particles and disregard the influence of baryons. The reason for this is partly that baryons are expected to follow the general distribution of dark matter and partly that the processes involved are less well understood. The comparison with lensing observations, which are sensitive to all mass, may therefore be somewhat restricted but may also inform us of how the inclusion of baryons affects the dark matter only Universe. This is far from the sole appli-

cation of gravitational lensing in the context of cosmology, and so the technique will be more extensively discussed in the next Section.

1.2 Gravitational lensing overview

Gravitational lensing is the collective name given to a set of methods, all of which have a common goal: to probe gravitational fields irrespective of whether their source is visible or not. In some cases gravitational lensing is the only way to detect what cannot be seen directly through telescopes. As such, the methods are beneficial to the study of the dark components of our Universe discussed in Section 1.1, as well as to the search for extrasolar planets otherwise drowned in the flux of their surroundings.

In essence, gravitational lensing methods exploit the bending of light rays caused by gravitational potentials. As the light travelling from background sources gets *lensed* by foreground structures, the source appears displaced, magnified and distorted. Since this is a purely geometrical effect and since it depends only on the total amount of matter in the intervening structure, no assumptions on the physical state of the lens need be made. This makes gravitational lensing exceedingly powerful.

1.2.1 Fundamentals of lensing

Before elaborating on the different applications of gravitational lensing, the fundamental ideas have to be understood. Here I give a brief introduction to the different concepts involved; for a more in-depth review I refer the reader to Bartelmann & Schneider (2001). The general geometry of gravitational lensing is illustrated in Figure 1.5, and this simple image turns out to represent reality well. The light from a background *source* is deflected by a foreground structure which acts as a *lens*. A customary simplification of this theory is that of the *thin lens approximation*: the light ray is instantaneously deflected at the lens plane. Though this is not strictly correct, it is a valid assumption if the spread of the lensing mass along the line-of-sight is much smaller than the angular diameter distances involved, something which is true in most lensing systems (though for the cosmic mass distribution a more general description is necessary; see Section 1.3.2). As is clear from Figure 1.5, the source image appears displaced with respect to its true position as a result of gravitational lensing. Unfortunately it is difficult to take advantage of this effect observationally since the intrinsic position is not known. However, deflection angle $\hat{\boldsymbol{\alpha}}$ is related to the impact parameter $\boldsymbol{\xi}$ via

$$\hat{\boldsymbol{\alpha}} = \frac{4GM}{c^2\boldsymbol{\xi}} \tag{1.7}$$

where G is the gravitational constant, M is the mass of the lens and c is the speed of light. Thus the amount of deflection is determined not only by the lens mass but also by the impact parameter and this results in a distortion. In extreme geometrical setups where the source is perfectly aligned to lie right behind the lens, the image will be circular. This is known as an *Einstein Ring*, the radius of which is known as the *Einstein radius* θ_E which is directly related

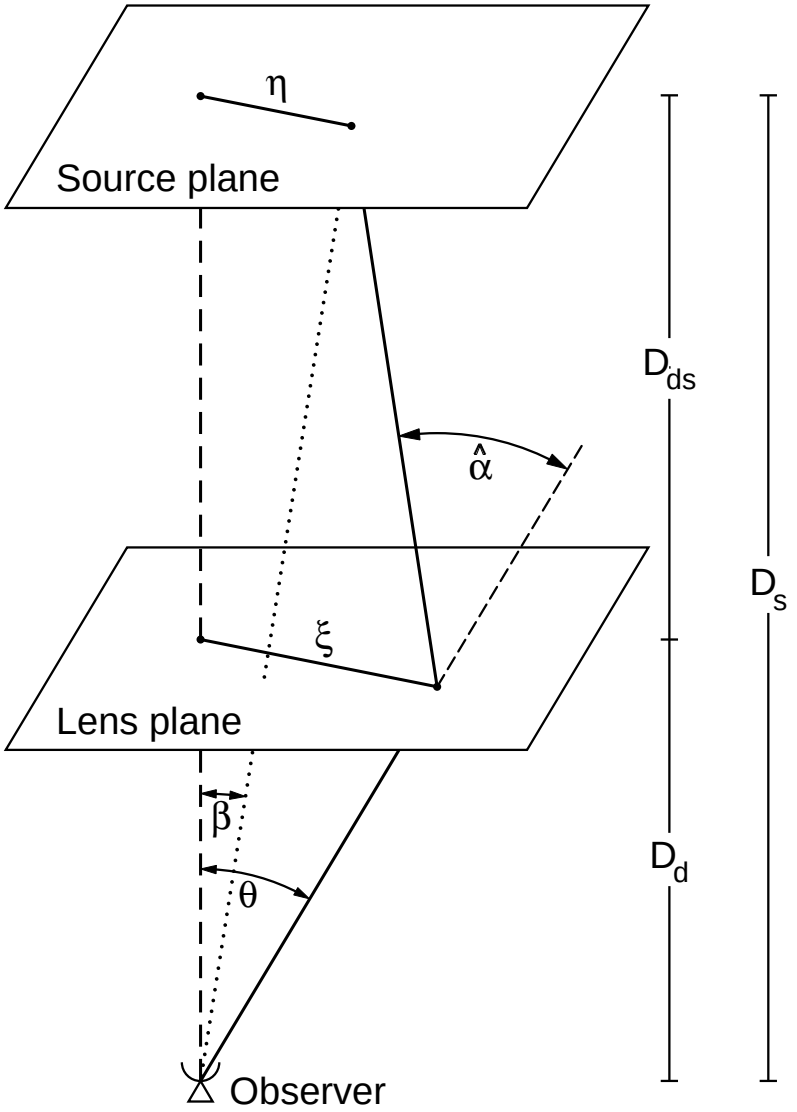

Figure 1.5 Schematic of a typical gravitational lens system. A light ray travelling from a source at position η is deflected by a lens in the lens plane. If there was no lens the source would have been observed at angle β. In the presence of a lens, however, the deflection angle is $\hat{\boldsymbol{\alpha}}$ with the impact parameter $\boldsymbol{\xi}$ which results in the source being observed at angle θ instead. D_s, D_d (D_l in the text) and D_{ds} (D_{ls}) are the angular diameter distances to the source, to the lens and between the lens and the source respectively. Figure originally published in Bartelmann & Schneider (2001).

to the mass of the lens; for a point mass it is given by

$$\theta_E = \frac{D_{ls}}{D_l D_s} \frac{4GM}{c^2} \tag{1.8}$$

We can now define the *lensing equation*:

$$\boldsymbol{\beta} = \boldsymbol{\theta} - \boldsymbol{\alpha}(\boldsymbol{\theta}) \tag{1.9}$$

This basic equation relates the observed position angle $\boldsymbol{\theta} = \boldsymbol{\xi}/D_l$ to the true position $\boldsymbol{\beta}$ and the reduced deflection angle $\boldsymbol{\alpha} = \hat{\boldsymbol{\alpha}} D_{ls}/D_s$. Furthermore, the thin lens approximation allows us to assume that the lensing mass lies on a 2D lens plane and we can therefore define the 2D surface mass density $\Sigma(\boldsymbol{\xi})$ of the lens

$$\Sigma(\boldsymbol{\xi}) = \int \rho(\boldsymbol{\xi}, z)\, \mathrm{d}z \tag{1.10}$$

where ρ is the 3D mass density and z is the third dimension. Now, the lensing equation (Equation 1.9) can have more than one solution resulting in multiple images on the sky; if this happens the lens is said to be *strong*. This condition may be quantified using a dimension-less surface mass density, or *convergence*, κ:

$$\kappa(\boldsymbol{\theta}) = \frac{\Sigma(\boldsymbol{\xi})}{\Sigma_{\mathrm{crit}}} \tag{1.11}$$

where Σ_{crit} is the *critical surface mass density* which is defined as

$$\Sigma_{\mathrm{crit}} = \frac{c^2}{4\pi G} \frac{D_s}{D_l D_{ls}} \tag{1.12}$$

If the surface mass density is greater than this critical limit, i.e. if $\kappa \geq 1$, then multiple images are produced and we enter the strong lensing regime. The convergence may also be integrated over to define the *lensing potential* ψ of the system:

$$\psi(\boldsymbol{\theta}) = \frac{1}{\pi} \int_{\mathbb{R}^2} \kappa(\boldsymbol{\theta}') \ln |\boldsymbol{\theta} - \boldsymbol{\theta}'|\, \mathrm{d}^2\theta' \tag{1.13}$$

which can be related to the reduced deflection angle via $\boldsymbol{\alpha} = \nabla\psi$; the deflection angle is thus the gradient of the deflection potential. It also satisfies Poission's equation $\nabla^2\psi(\boldsymbol{\theta}) = 2\kappa(\boldsymbol{\theta})$.

Having introduced the basic concepts in gravitational lensing theory, I now move on to observational applications. Though the main emphasis of this Thesis is *weak lensing* it is instructive to briefly touch upon the related topics of *microlensing* and *strong lensing* as well.

1.2.2 Microlensing

In the beginning of last century, Einstein's theory of General Relativity (GR) was still new and required observational evidence for credibility. Gravitational microlensing provided such early evidence when Eddington set out on an expedition to confirm Einstein's prediction that a star passing close to the Sun would appear displaced due to its gravitational field. The exact displacement predicted by GR was 1.75 arcsec for a star at the solar limb, whereas Newtonian gravity predicted a mere 0.87 arcsec (i.e. half that of GR). To discriminate between the two theories, Eddington took advantage of the full solar eclipse on May 29, 1919. The displacement found by him and his collaborators was 1.61 ± 0.30 arcsec which clearly favours General Relativity (Dyson et al., 1920) and shows the power of the gravitational lensing technique.

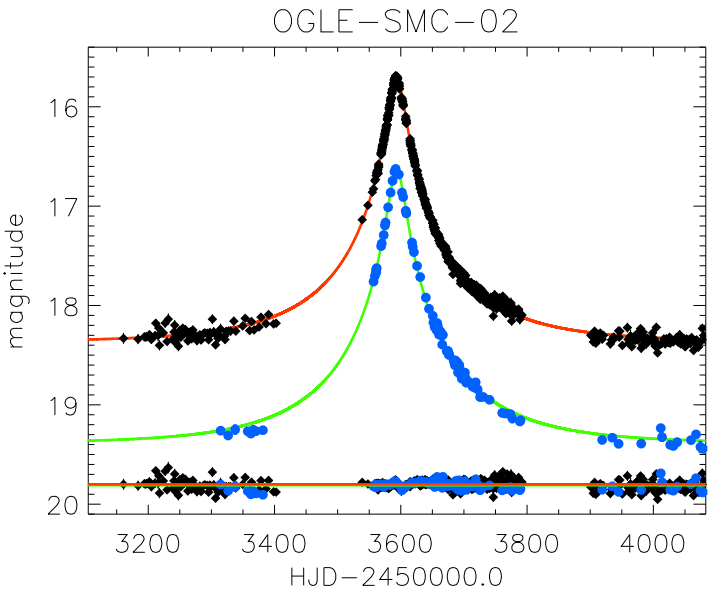

Figure 1.6 Example lightcurve caused by a microlensing event. The top two datasets are the same event observed in different filters, with the best-fit microlensing model shown as well. The bottom graph shows the residuals of the model fit. Figure originally published in Wyrzykowski et al. (2011).

Microlensing is a transient effect, caused by a foreground object often located in our own Milky Way galaxy passing in front of a bright background source. As the alignment between the source, the lens and the observer changes, the apparent brightness of the source is boosted and then diminished, causing the characteristic shape of the light curve shown in Figure 1.6. Since the event is transient, a potential source has to be monitored for some time to observe an event, but unfortunately such an event cannot be predicted. The probability of microlensing being observed is thus very low and therefore large dedicated surveys regularly scanning millions of stars are crucial for detection. Generally these surveys are trained towards areas with a high density of background stars, such as the centre of the Galaxy or another nearby galaxy like the Large Magellanic Cloud (LMC) or Andromeda. The microlensing *optical depth* is a measure of the probability of a source undergoing a microlensing event at a given time; the optical depth towards the centre of our Galaxy is $\tau = 2.43 \times 10^{-6}$ (Alcock et al., 2000b) while the equivalent measure towards the LMC is $\tau = 3.6 \times 10^{-8}$ (Tisserand et al., 2007). However, choosing a suitable backdrop is more dependent on which type of population is to be observed. If we are interested in objects in the halo of our Galaxy for instance, the galactic bulge is unavailable to us and an external galaxy is necessary.

Currently there are two major applications of microlensing: the search for MACHOs and other dark transient objects, and the search for extrasolar planets. A MACHO passing in front of a star would produce a light curve such as the one shown in Figure 1.6 but the lensing object itself would not be seen.

Therefore other potential causes of a change in brightness, such as the intrinsic variability of the source star, have to be ruled out before a successful detection can be claimed. Two collaborations that have been working to identify candidates in the Milky Way halo are the MACHO and EROS collaborations. MACHO's results contradict the hypothesis that our halo consists of MACHOs, effectively ruling out the theory that dark matter is composed of such massive objects (Alcock et al., 2000a). EROS provided agreement with these findings; they found that the maximum fraction of the halo mass that could consist of MACHOs is 8% (Tisserand et al., 2007). They also ruled out MACHOs in the mass range $0.6 \times 10^{-7}\ M_\odot < M < 15\ M_\odot$ as the primary occupants of the halo.

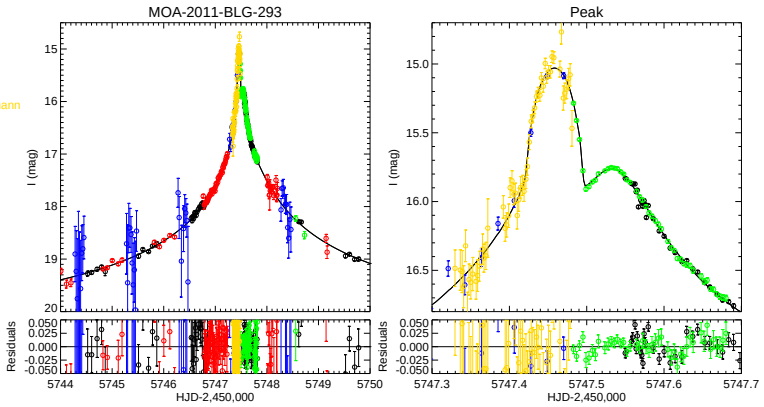

Figure 1.7 Example lightcurve caused by the star-and-planet system MOA-2011-BLG-293. The top two panels show the full light curve (left) and an enlarged view of the peak (right), with the best-fit microlensing model also shown in each case. The bottom panels show the residuals of each model fit. Figure originally published in Yee et al. (2012).

If the lens consists of more than one object, such as a binary star or a star and a planet, the light curve displays several peaks as illustrated in Figure 1.7. This is a direct way of finding extrasolar planets and determining their properties. From the observed light curve alone, the mass distribution in the lens may be deduced and thus the mass of the planet(s) can be determined. To date, 15 extrasolar planetary systems, with planets ranging in mass from 0.01 M_J to 3.7 M_J and separations of 0.66 AU to 5.1 AU, have been discovered using this technique (Yee et al., 2012; Bennett et al., 2012). This number is relatively low compared to the rival radial velocity detection method, but the list is rapidly growing as surveys collect more data. Such surveys include the Optical Gravitational Lensing Experiment (OGLE: Udalski et al., 1992; Udalski, 2003) and Microlensing Observations in Astrophysics (MOA: Bond et al., 2001; Sumi et al., 2003). An interesting discovery to come out of MOA is that of a population of planetary-mass objects that are seemingly not gravitationally bound to host stars (Sumi et al., 2011). Such a population could be explained via various scattering scenarios, but the number of candidate planets found indicates that the size of the population is almost twice that of main-sequence stars. This is larger than would be expected from scattering. However, the planets are only defined as isolated because no corresponding star was detected during the mi-

crolensing event. Sumi et al. (2011) offered the explanation that the planets may simply be bound in a very large orbit which gives a lower bound on their separation of $7 - 45$ AU. None the less, this discovery could have an impact on planet formation theories if the planetary objects are indeed orphaned (Bowler et al., 2011). The power of microlensing thus lies with its ability to detect dark compact objects in our own Galaxy and those nearby, thereby challenging theories of both dark matter and thus cosmology, and of planet and star formation. For applications of the related theories of strong and weak lensing, however, we have to move to a much grander scale.

1.2.3 Strong lensing

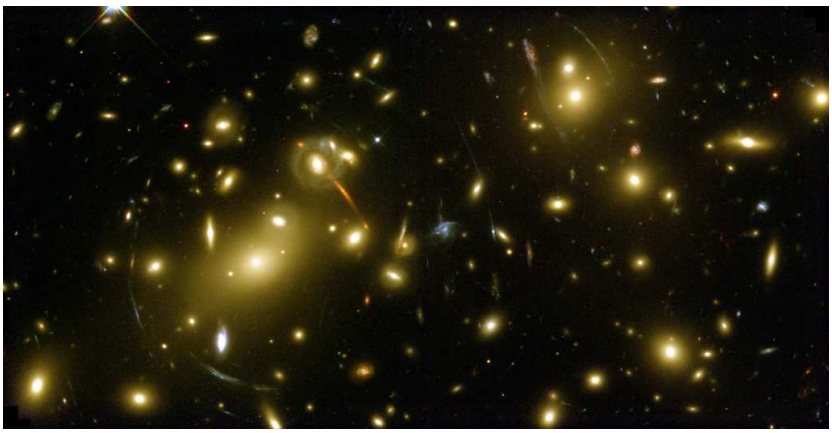

Figure 1.8 Example of strong lensing: the massive galaxy cluster Abell 2218 imaged by the Hubble Space Telescope in 1999. Image credit: NASA/ESA, A. Fruchter and the ERO Team (STScI, ST-ECF).

Distant clusters of galaxies display remarkable arc-like images such as those manifested in the stunning Abell 2218 (Figure 1.8). These source images are clear examples of strong gravitational lensing and typically appear in massive structures such as galaxy clusters or close to individual galaxies. As mentioned in the introductory Section 1.2.1, a condition for strong lensing is that the surface density is greater than the critical limit $\Sigma_{\rm crit}$, i.e. that $\kappa \geq 1$. Alternatively, for a source which is much smaller than the angular scale on which lens properties change, the mapping between source and lens plane can be linearised using a Jacobian matrix $\mathbf{A}(\boldsymbol{\theta})$:

$$f(\boldsymbol{\theta}) = f^s \left[\boldsymbol{\beta}_0 + \mathbf{A}(\boldsymbol{\theta}_0) \cdot (\boldsymbol{\theta} - \boldsymbol{\theta}_0)\right] \tag{1.14}$$

where f is the observed surface brightness distribution in the lens plane, f^s is the corresponding brightness distribution in the source plane, $\boldsymbol{\theta}_0$ is a point within the image corresponding to the point $\boldsymbol{\beta}_0$ within the source and

$$A_{ij}(\boldsymbol{\theta}) \equiv \frac{\partial \beta_i}{\partial \theta_j} = \delta_{ij} - \partial_i \partial_j \psi(\theta) \tag{1.15}$$

where we use the shorthand $\partial_i \equiv \partial / \partial \theta_i$. The *magnification* μ is the ratio of the observed flux from the image to that from the unlensed source, and this is

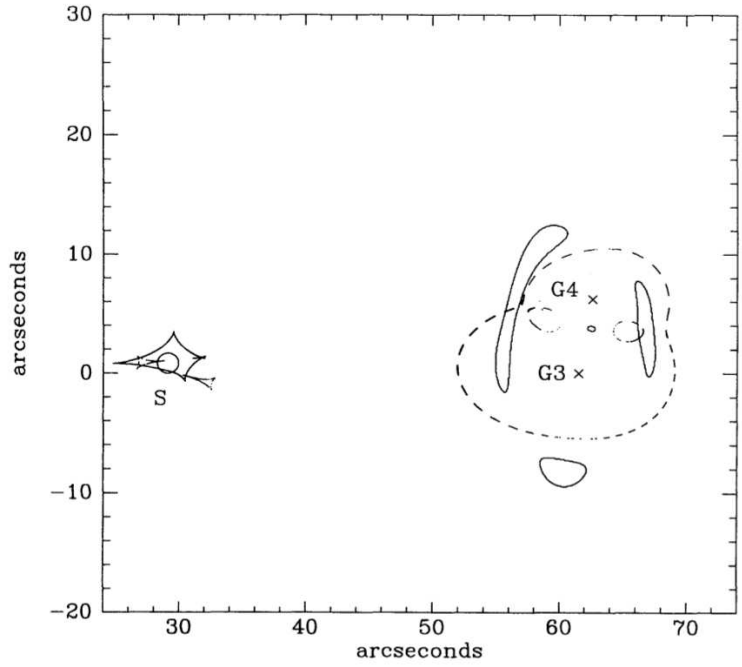

Figure 1.9 Strong lensing reconstruction of (part of) Abell 2218, with the cluster centre located at the origin. The crosses mark the two galaxies responsible for the majority of the lensing effect, and the arcs being modelled are also shown. The circle labelled S represents the size and location of the source. Dashed lines represent critical lines in the lens plane, while the curves close to the source represent the corresponding caustics. Figure originally published in Saraniti et al. (1996).

simply given by

$$\mu = \frac{1}{\det \mathbf{A}} \tag{1.16}$$

A more rigorous definition of strong lensing is then a system for which $\det \mathbf{A} = 0$, and in which multiple images are produced. A strong lens will have a locus in the image plane for which this condition holds true, and this locus is known as a *critical curve*. This curve can be visualised as a smooth loop. When the critical curve is mapped back to the source plane it is instead known as a *caustic* which will, contrary to its corresponding critical curve, generally display cusps. Along a critical curve, the magnification formally diverges and sources near these are highly magnified and distorted, resulting in the long arcs visible in Figure 1.8. The number of images associated with a particular source also depends on its vicinity to a critical curve, providing additional constraints. These effects are illustrated in Figure 1.9 which shows the reconstruction of a sub-cluster within Abell 2218, as modelled by Saraniti et al. (1996).

The main advantages of studying galaxy cluster lenses were recognised very early on by the bold visionary Zwicky who anticipated that we would be able to use clusters to trace the unseen mass (Zwicky, 1937), also predicted by himself (Zwicky, 1933). He further envisioned that given good enough imaging we

could study the distant sources behind clusters. Both these predictions have proved accurate, even though strong lensing was not observed until much later (e.g. the double quasar Q0957+561 and giant arcs; Walsh et al., 1979; Lynds & Petrosian, 1986; Soucail et al., 1987). Observers can use the arcs and multiple images in clusters or around single galaxies to model the critical curves and thus constrain the mass distribution within the lens. Lensing therefore offers a unique way to probe substructure. Clusters consist of several galaxies that are interacting now, or has done at some point in the past. Through these interactions and via their traversing through the cluster core, the extended dark matter haloes surrounding member galaxies are expected to be tidally stripped. This view is corroborated by evidence that cluster galaxies undergo strong morphological evolution including quenched star formation (e.g. Jones et al., 2000; Kodama & Bower, 2001; Treu et al., 2003). By accurately modelling the distribution of mass in the inner regions of clusters using individual cluster members, direct evidence of such stripping can be gathered, providing support for the theory of hierarchical merging as the main process in cluster assembly. The accuracy of such analyses is further improved by including weak lensing signals (see Section 1.3) since strongly lensed arcs are rare (e.g. Natarajan et al., 2007, 2009). Strong lensing has also been used to tentatively detect substructure in galaxy-size lenses consistent with predictions from ΛCDM (Vegetti et al., 2010).

As already mentioned, another use for these massive lenses is to employ them as Nature's own telescopes. Due to the great magnification effects involved we are privy to objects that would otherwise be too far away or too faint for us to see. These background objects do most likely not suffer from any prominent selection bias other than that related to the distances involved in the geometrical setup, although intrinsically brighter sources will produce brighter arcs for a given geometry. Though rare, magnifications of up to 4 magnitudes have been measured (Seitz et al., 1998) and increases in brightness of more than 1.5 magnitudes are relatively common (e.g. Richard et al., 2011). The magnification is wavelength independent, so the background sources can be fully studied for morphology and physical properties that would otherwise not be resolved. This yields insight into a very high redshift regime which we could not study in such detail directly. The *cosmic telescope* as a tool to detect high-redshift galaxies has since its first use heralded the discoveries of the most distant galaxies of their time (e.g. Franx et al., 1997; Ellis et al., 2001; Hu et al., 2002; Kneib et al., 2004). Some studies have claimed detections of candidate galaxies at redshifts as high as $z = 10.2$ using this technique (Stark et al., 2007), clearly on par with the highest-redshift galaxy candidate ever discovered ($z = 10.3$; Bouwens et al., 2011). Detecting and analysing such early galaxies is essential for our understanding of the era when the first stars and galaxies were assembled and objects such as quasars formed. It also provides vital clues to the process that led to the cosmic reionization, a crucial phase during the evolution of the early Universe.

Finally, strong lensing clusters have the power to constrain cosmology directly since the effect is dependent on angular diameter distances. These distances in turn are defined by the geometry of the Universe and in particular on the parameters Ω_m and w. For clusters with several arc sets due to sources at known but different redshifts, the Einstein radii may be compared. The ratio of the radii then holds information on the fundamental geometry of the Universe

(e.g. Link & Pierce, 1998; Golse et al., 2002; Soucail et al., 2004; Jullo et al., 2010). Encoded in arc properties is also the value of the Hubble parameter H_0. It can be constrained independently of cosmology by measuring the time delay between arcs originating from the same time-varying source (e.g. Blandford & Narayan, 1986; Saha et al., 2006; Oguri, 2007; Paraficz & Hjorth, 2010; Riehm et al., 2011). The number of giant arcs observed is also tied to the background cosmology, and in particular to the σ_8 parameter. Bartelmann et al. (1998) showed that the observed arc statistics differs from that predicted by ΛCDM, and this discrepancy has yet to be fully resolved. It may be explained by observational effects such as a poorly understood source population or substructure (Horesh et al., 2005), or physical effects due to baryons like cooling and star formation (Meneghetti et al., 2010). Furthermore, the observed giant-arc statistics may be an interesting indicator of primordial non-Gaussianity (D'Aloisio & Natarajan, 2011). Whatever the origin of the excess, it is clear that strong lensing has a lot to offer when it comes to confirming our understanding of cosmology. The applications of this effect are naturally focussed on large structures and although we have given only a brief overview here, clusters are very powerful probes of the geometry of the Universe (see Kneib & Natarajan, 2011, for a recent review). To take full advantage of these cosmological behemoths, however, we have to break away from the restrictions of strong lensing. Arcs are rare and contingent on serendipitous alignments and high-density regions. Combining the strengths of this technique with weak lensing, which is ubiquitous, will allow us to study clusters in ever more detail.

1.3 Weak lensing

Weak gravitational lensing is a relatively new study, with the first detection recorded by Tyson et al. (1990). Given sufficient depth and area, and good enough image quality, this statistical alignment of galaxies can be observed anywhere on the sky. The power of this technique to explore the unseen matter in clusters, in galaxies and even in the Cosmic Web is hence unrivalled. We will therefore review the fundamentals of this method in a bit more detail than its sister practices above, though for a thorough treatment we refer the reader to Bartelmann & Schneider (2001) and Schneider (2005).

1.3.1 Convergence, shear and flexion

As described in Section 1.2.1, a distinguishing limit between strong and weak lensing is the critical surface density $\Sigma_{\rm crit}$ and the related convergence κ. Starting from Equation 1.15 we can write the mapping between source and lens plane as

$$\beta_i \simeq A_{ij}\theta_j \tag{1.17}$$

This holds true for small source galaxies where the convergence is constant across the source image. Rewriting Equation 1.15 we can also get an alternative description of the distortion matrix $\mathbf{A}$:

$$\mathbf{A} = \begin{pmatrix} 1-\kappa-\gamma_1 & -\gamma_2 \\ -\gamma_2 & 1-\kappa+\gamma_1 \end{pmatrix} \tag{1.18}$$

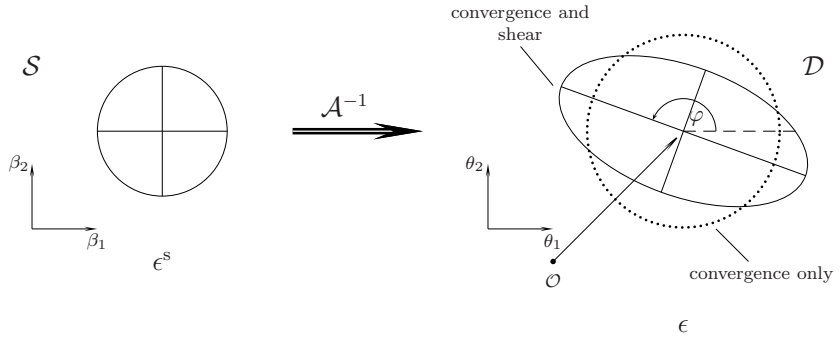

Figure 1.10 Effect of shear and convergence. On the left is the original circular source, while the lensed image is on the right. Convergence only results in an enlargement of the source image while the shear causes a stretch entailing a difference in axis ratio. The orientation of the resulting ellipse depends on the relative amplitudes of γ_1 and γ_2 as illustrated in Figure 1.11. This figure was originally published in Schneider (2005).

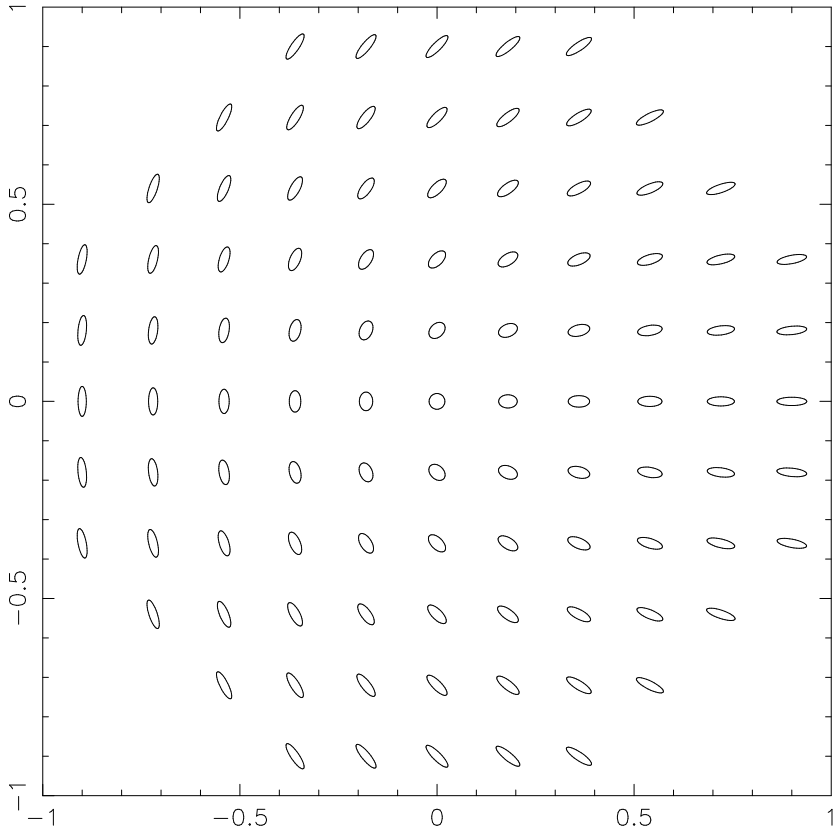

Figure 1.11 Orientation of the ellipse resulting from the relative amplitudes of γ_1 (on the x-axis) and γ_2 (on the y-axis) applied to a circular source. Figure originally published in Schneider (2005).

where γ_1 and γ_2 are the two components of the *shear* induced by the lensing potential: $\gamma = \gamma_1 + i\gamma_2$. These shear components are related to the lensing potential ψ via

$$\gamma_1 = \frac{1}{2}(\psi_{11} - \psi_{22}) \tag{1.19}$$

$$\gamma_2 = \psi_{12} \tag{1.20}$$

where e.g. $\psi_{11} = \partial_1^2\psi$ is the second derivative of the lensing potential. Defining the complex gradient operator

$$\partial = \partial_1 + i\partial_2 \tag{1.21}$$

using the same shorthand as before we can also relate the shear to convergence in a way which compactly shows that shear is the second-order gradient of the lensing potential:

$$\gamma = \partial\partial\psi \tag{1.22}$$

The effect of shear on a source image is to stretch it in one direction as illustrated in Figure 1.10 with the direction dependent on the relative amplitudes of the γ_1 and γ_2 distortions. As is clear from Figure 1.11, the transformation $\gamma \rightarrow -\gamma$ results in a 90° rotation and pure γ_2 is at 45° to pure γ_1. Generally we also assign a property known as *spin* to weak lensing distortions. A distortion type with spin s is invariant under a rotation of $\phi = 360°/s = 2\pi/s$ radians. Since an ellipse rotated by 180° looks the same, shear is a *spin-2 quantity*. The lensing displacement field α is a spin-1 quantity which is also the gradient of the spin-0 lensing potential:

$$\alpha = \alpha_1 + i\alpha_2 = \partial\psi \tag{1.23}$$

We can now interpret ∂ as a *spin-raising operator*; applying it once to the lensing potential results in a spin-1 quantity, while applying it twice results in spin-2. Similarly the complex conjugate ∂^* is a *spin-lowering operator*. For instance, the convergence is related to the lensing displacement field and lensing potential via

$$\kappa = \frac{1}{2}\partial^*\alpha = \frac{1}{2}\partial^*\partial\psi \tag{1.24}$$

and is thus a spin-0 quantity.

Equation 1.17 is an approximation that is sufficiently accurate when shear is constant across a source image. If this is is not the case, however, the equation has to be extended to higher orders to encapsulate the variations in shear:

$$\beta_i \simeq A_{ij}\theta_j + \frac{1}{2}D_{ijk}\theta_j\theta_k \tag{1.25}$$

where

$$D_{ijk} = \partial_k A_{ij} \tag{1.26}$$

is a third-order distortion tensor. The lensed surface brightness of a source may now be written

$$f(\boldsymbol{\theta}) \simeq \left\{1 + \left[(A - I)_{ij}\theta_j + \frac{1}{2}D_{ijk}\theta_j\theta_k\right]\partial_i\right\} f^s(\boldsymbol{\theta}) \tag{1.27}$$

where I is the identity matrix. The tensor D captures the distortions responsible for the arc-like shape of weakly lensed images, reminiscent of the giant arcs in

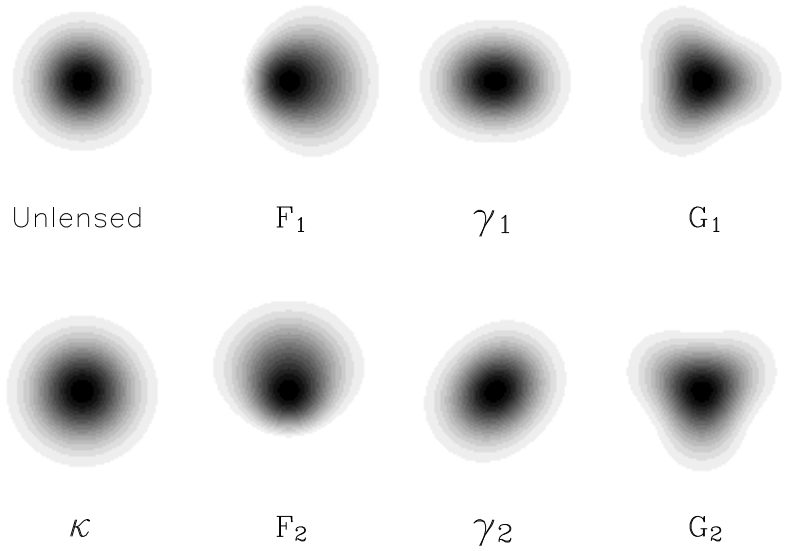

Figure 1.12 Illustration of convergence, shear and flexion distortions as applied to a circular source with a Gaussian density profile. The spin values, as described in the main text, increase from 0 for convergence to 3 for G flexion. Figure originally published in Bacon et al. (2006).

strong lensing (though the giant arcs are usually the result of several distorted images merging, unlike in weak lensing). This tensor can be succinctly expressed in terms of two new quantities, known as *flexion*:

$$D_{ijk} = \mathcal{F}_{ijk} + \mathcal{G}_{ijk} \tag{1.28}$$

where $\mathcal{F}$ is the first flexion, or *F flexion*, and $\mathcal{G}$ is the second flexion, or *G flexion*. The F flexion was first discovered and investigated a decade ago by Goldberg & Natarajan (2002) with a tentative detection in Goldberg & Bacon (2005). Bacon et al. (2006) then developed the notation further and included the G flexion as well. The flexions are the third-order derivatives of the lensing potential and the gradients of convergence and shear:

$$\mathcal{F} = \frac{1}{2}\partial\partial^*\partial\psi = \partial^*\gamma = \partial\kappa \tag{1.29}$$

$$\mathcal{G} = \frac{1}{2}\partial\partial\partial\psi = \partial\gamma \tag{1.30}$$

which, following the above discussion, means that F flexion is a spin-1 quantity while G flexion has spin-3. Convergence, shear and flexion are all illustrated in Figure 1.12.

It should be noted that, unlike convergence and shear, flexion is not dimensionless but has units of inverse length. Furthermore, throughout this Thesis we make the implicit assumption that we are working in the weak lensing regime, i.e. $\kappa \ll 1$. If this condition is broken, our observations would be biased since

what we truly observe are the quantities g, G_1 and G_3 (Schneider & Seitz, 1995; Schneider & Er, 2008):

$$g = \frac{\gamma}{1-\kappa} \tag{1.31}$$

$$G_1 = \partial^* g = \frac{\mathcal{F} + g\mathcal{F}^*}{1-\kappa} \tag{1.32}$$

$$G_3 = \partial g = \frac{\mathcal{G} + g\mathcal{F}}{1-\kappa} \tag{1.33}$$

where g is the *reduced shear* and G_1 and G_3 are the *reduced flexions*. This is a consequence of the *mass-sheet degeneracy*, a well-known potential source of bias in gravitational lensing. The degeneracy arises from the fact that the addition of a sheet of constant surface density in front of the lens will not alter the shear or flexion measurements (Falco et al., 1985). Breaking this degeneracy is possible with magnification measurements in principle, because the magnification reacts differently to a mass sheet. It has also been pointed out that there is some cross-talk between shear and flexion which has to be considered for an unbiased measurement (Viola et al., 2012). Both these effects are significantly reduced in impact in the weak lensing limit. Therefore I do not touch upon it further in this Thesis which is mainly concerned with the lensing signal induced by galaxy-sized halos, but use the approximation that the observed quantities are equivalent to the non-reduced quantities.

1.3.2 Cosmic shear

As light travels through space to reach us it is continuously deflected by the filaments and nodes of the Cosmic Web. Source galaxies are thus sheared and weakly aligned even when there are no large structures in the way. The statistics of these distortions and alignments therefore reflect the statistics of the underlying matter distribution. Though the distortion is minute at less than $\sim 1\%$, this effect was detected at the turn of the millennium (Bacon et al., 2000; Kaiser et al., 2000; Van Waerbeke et al., 2000; Wittman et al., 2000). It is since being measured with ever more refined accuracy using imaging data of ever increasing area, depth and quality, and used to constrain cosmological parameters (e.g. Hoekstra et al., 2002; Brown et al., 2003; Jarvis et al., 2003; Massey et al., 2005; Van Waerbeke et al., 2005; Hoekstra et al., 2006; Semboloni et al., 2006; Benjamin et al., 2007; Schrabback et al., 2007; Fu et al., 2008; Schrabback et al., 2010; Huff et al., 2011). The correlation between shears across the sky as a function of angular scale can be used to derive the lensing power spectrum which is related to the three-dimensional matter power spectrum (e.g. Kaiser, 1992; Bartelmann & Schneider, 2001; Schneider, 2005; Hoekstra & Jain, 2008). Technically, cosmic shear cannot make use of the thin lens approximation used to derive the lensing results quoted so far in this Introduction because the deflection does not take place in a single lens plane. It turns out, however, that under the assumption that the deflection angle is small the end result is a redshift-dependent convergence κ which behaves just like in ordinary lensing (see e.g. Schneider, 2005). We can therefore use ordinary shear measurements to constrain the matter power spectrum, and thus in particular the cosmological parameters Ω_m and σ_8.

Since the measurements do not rely on baryonic tracers there are no assumptions on e.g. galaxy bias necessary and this gives cosmic shear great value. Furthermore, the constraints resulting from cosmic shear intersect the constraints from the CMB in a way that reduces degeneracies adding to the benefits of such analyses. The task of observing this effect is a fairly substantial challenge however, owing to the fact that the distortions are so small. It is impossible to detect a signal on a single galaxy image since the intrinsic ellipticity of the source galaxy is in general much larger than the induced distortion. Assuming that galaxies have random intrinsic ellipticities and that they are randomly oriented on the sky we can discern the lensing signal in a statistical way though. If we average over enough sources we can reduce this *shape noise* and essentially reason that the mean intrinsic shape is circular. Under ideal conditions, any ellipticity observed must then be produced by lensing.

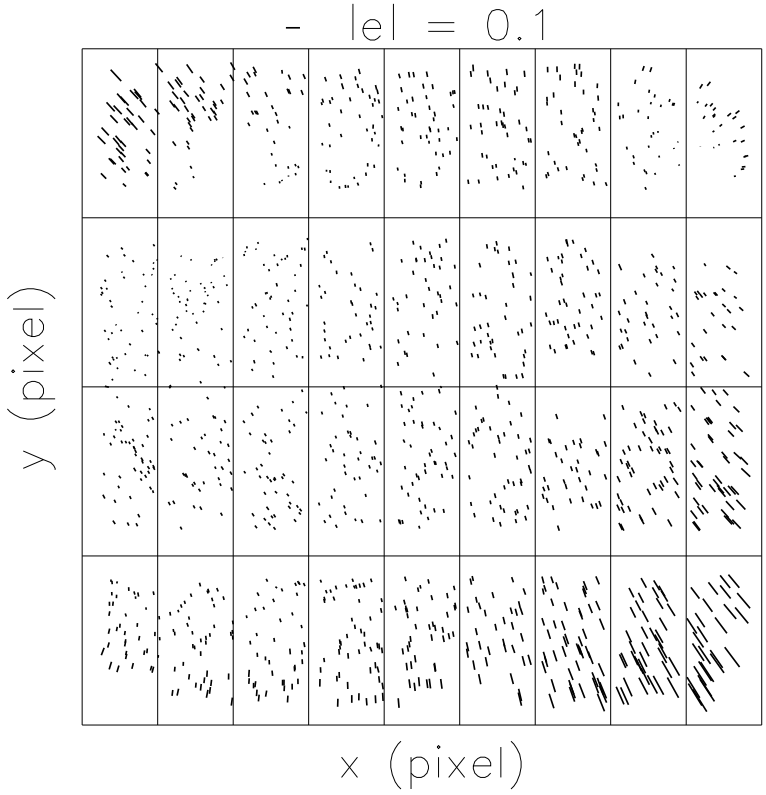

Figure 1.13 Point-spread function (PSF) pattern of a typical field in the Canada-France-Hawaii Telescope Legacy Survey (CFHTLS). Each tick represents the observed magnitude and orientation of a stellar ellipticity. The artificially induced ellipticity is most prominent in the corners in this case. Figure originally published in Fu et al. (2008).

Unfortunately, such ideal conditions are also difficult to attain. A telescope will in general produce a complicated pattern which correlates galaxy ellipticities in a way that imitates a lensing signal. This pattern, illustrated in Figure 1.13, is

usually referred to as the *point-spread function* (PSF), although other distinct processes can be involved as well (such as wind-shake of the telescope). For ground-based surveys the PSF is worsened by turbulence in the atmosphere and these *seeing* conditions tend to blur the galaxy images and dilute their ellipticities. Generally the PSF is corrected for by taking advantage of the fact that stars should be circular. Any ellipticity observed for stars is therefore due to the PSF and this information may be used to model the distortions. Space-based telescopes face other trials, however, such as the gradual degradation of CCD chips due to the constant bombardment of cosmic radiation (resulting in charge-transfer inefficiency or CTI; see e.g. Rhodes et al., 2007, 2010). CTI is the result of so-called charge traps in the silicon surface of a CCD which reveal themselves as artificial trails behind objects on an astronomical image. Again, this can cause a false shear detection if left unaccounted for. Recently though, promising ways to correct for this effect have been suggested either at an image reconstruction level (Massey et al., 2010) or parametrically (as in e.g. Schrabback et al., 2010).

Additional difficulties include the fact that detectors collect photons in square bins (or *pixels*) which places a fundamental lower limit on the size galaxy that can be reliably analysed, and the fact that there is some *intrinsic alignments* of galaxies due to them being affected by tidal fields during formation (e.g. Splinter et al., 1997; Faltenbacher et al., 2002; Lee & Pen, 2008) or lower-redshift tidal fields affecting all higher-redshift sources (Hirata & Seljak, 2004; Heymans et al., 2006b). Another limiting factor is the accuracy of the software used to extract the shear signal from a given image. Great effort has been put into developing reliable software and at the moment there are many alternatives available. To take full advantage of future surveys, however, the accuracy has to be improved even more. An overview of the current shape measurement software state-of-the-art is given in Section 1.3.5, but first I will introduce a different weak lensing application which is more robust against issues such as PSF and CTI: galaxy-galaxy lensing.

1.3.3 Galaxy-galaxy lensing

The source images due to a lens galaxy will be aligned in a circular pattern around the lens, and the distortions of the sources decrease in strength the further from the lens they are. By measuring the average lensing distortion in circular bins of successively increasing size centred on the lens, a function will emerge that encodes the *density profile* of the lens, i.e. it tells us how the mass is distributed within the lens. Since the distortions are weak in general, we again have to average over many lenses and sources in order to decrease the shape noise. This way we can study the density profiles of a galaxy population in a statistical fashion, a technique known as *galaxy-galaxy lensing*. Galaxy-galaxy lensing may also be applied to clusters to complement strong lensing (where available) and to map the matter distribution in these more complicated systems.

The shear components γ_1 and γ_2 and the equivalent flexion components are defined with respect to a Cartesian coordinate system. For galaxy-galaxy lensing studies it is more convenient to define components relative to the lens that the sources are centred on. It is therefore common practice to adopt *tangential* and

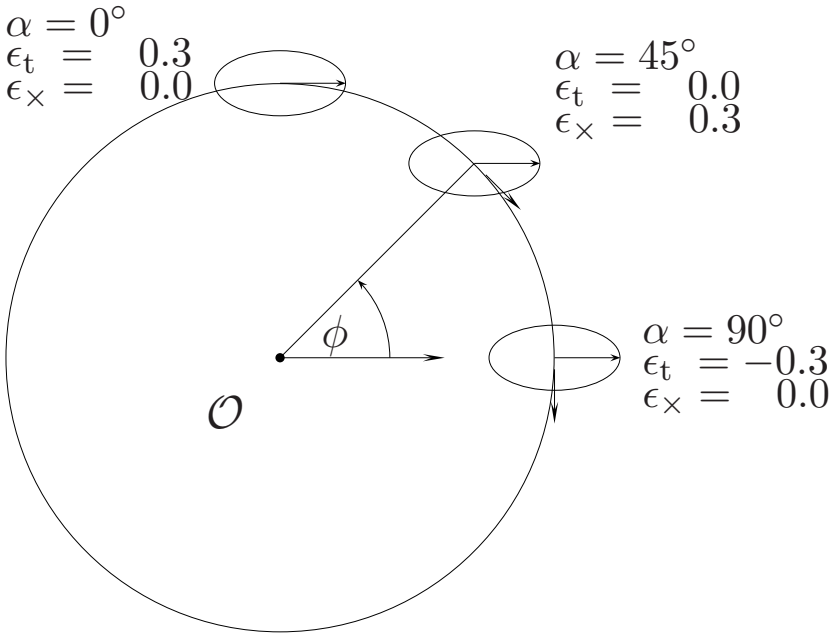

Figure 1.14 Illustration of the tangential and cross components of shear for a circular lens located at the origin $\mathcal{O}$. The background source is located at angle ϕ relative to the horizontal. For a tangentially aligned source, the tangential shear ϵ_t (γ_t in the text) is positive and the cross term $\epsilon_\times$ ($\gamma_\times$) is zero; if ϵ_t is negative instead then the source is radially aligned. A positive or negative cross term with no tangential component signifies a source image angled at 45° relative to the lens. Figure originally published in Schneider (2005).

cross components, γ_t and $\gamma_\times$:

$$\gamma_t = -\Re[\gamma e^{-2i\phi}] = -\cos(2\phi)\gamma_1 - \sin(2\phi)\gamma_2 \quad (1.34)$$
$$\gamma_\times = -\Im[\gamma e^{-2i\phi}] = \sin(2\phi)\gamma_1 - \cos(2\phi)\gamma_2 \quad (1.35)$$

where ϕ is the angle between lens and source image as illustrated in Figure 1.14. Similarly we can define the corresponding components for the flexions:

$$F_t = -\cos(\phi)\mathcal{F}_1 - \sin(\phi)\mathcal{F}_2 \quad (1.36)$$
$$F_\times = \sin(\phi)\mathcal{F}_1 - \cos(\phi)\mathcal{F}_2 \quad (1.37)$$
$$G_t = -\cos(3\phi)\mathcal{G}_1 - \sin(3\phi)\mathcal{G}_2 \quad (1.38)$$
$$G_\times = \sin(3\phi)\mathcal{G}_1 - \cos(3\phi)\mathcal{G}_2 \quad (1.39)$$

where the effect of the spin property is clear in the multiplication factor of the angle ϕ. Averaging as described above, a lensing mass would produce a purely positive tangential signal while a so-called *void* (underdensity) would cause a purely negative signal. The cross terms can never be induced by lensing (for an isolated circular lens) and measurement of such a signal therefore provides a good null test for systematic errors (or *systematics* for short).

Since sources are averaged in circles relative to lens positions, galaxy-galaxy lensing is less sensitive to systematics such as PSF or CTI which tend to induce

correlation between shapes across an entire observed field. There are however other systematics that have to be taken into account. The main concerns include intrinsic alignments of satellite galaxies (see Section 1.3.2) diluting the signal, and neighbouring galaxies at the same redshift having a similar effect simply because they are not lensed. By using redshift information for both lenses and sources these effects can be minimised however, illustrating the importance of accurate redshift measurements for weak lensing analyses. Since weak lensing surveys are generally very large and there are millions of galaxies involved, spectroscopic redshifts are unfeasible. Fortunately, state-of-the-art photometric redshift software is able to produce reliable redshift estimates (see e.g. Hildebrandt et al., 2012, for recent CFHTLS results). Additionally, as suggested by Rowe (2008) and further investigated in Velander et al. (2011) (Chapter 3 in this Thesis), the light from lens galaxies may be bright enough to affect the source shapes measured, particularly in the case of F flexion. This effect can be avoided by not using sources too close to other bright light sources such as the lens. The amplitude of the flexion signal falls off very quickly with distance, however, and we therefore have to go close to the lens in order to detect it. An alternative approach is to model the lens light and remove it from the image before measuring the source shapes (see Section 3.4.3, page 73). Though this seems to work well, we have to be careful not to introduce new artifacts.

Observing the density profiles of galaxies tells us about the total mass of the lenses which provides constraints on various relations between halo mass and the properties of the observed galaxy (see Chapter 4). It is also of interest because N-body simulations predict specific profiles. Confirming or disproving these profiles will provide clues to the underlying physics used when creating the simulation. There are currently two main density profiles being used in weak lensing to determine mass: the *singular isothermal sphere* (SIS) and the *Navarro-Frenk-White profile* (NFW; Navarro, Frenk, & White, 1996). The SIS is a fairly simplistic powerlaw for which the density is inversely proportional to the square of the physical radius r, $\rho(r) \propto r^{-2}$. For such a density profile the shear and flexion profiles are given by

$$|\gamma_t(\theta)| = \frac{\theta_E}{2\theta} \tag{1.40}$$

$$|F_t(\theta)| = \frac{\theta_E}{2\theta^2} \tag{1.41}$$

$$|G_t(\theta)| = \frac{3\theta_E}{2\theta^2} \tag{1.42}$$

where $\theta = \xi/D_l$ is the angular distance from the lens and θ_E is the Einstein radius:

$$\theta_E = 4\pi \left(\frac{\sigma_v}{c}\right)^2 \frac{D_{ls}}{D_s} \tag{1.43}$$

with σ_v the velocity dispersion of the lens. The velocity dispersion of a halo is directly related to its mass via

$$\sigma_v^2 = \frac{GM(r)}{2r} = \frac{1}{2} v_{\rm rot}^2 \tag{1.44}$$

where $M(r)$ is the mass interior to r and $v_{\rm rot}$ is the rotational velocity. This profile thus reproduces the flat rotation curves discussed in Section 1.1.2 since

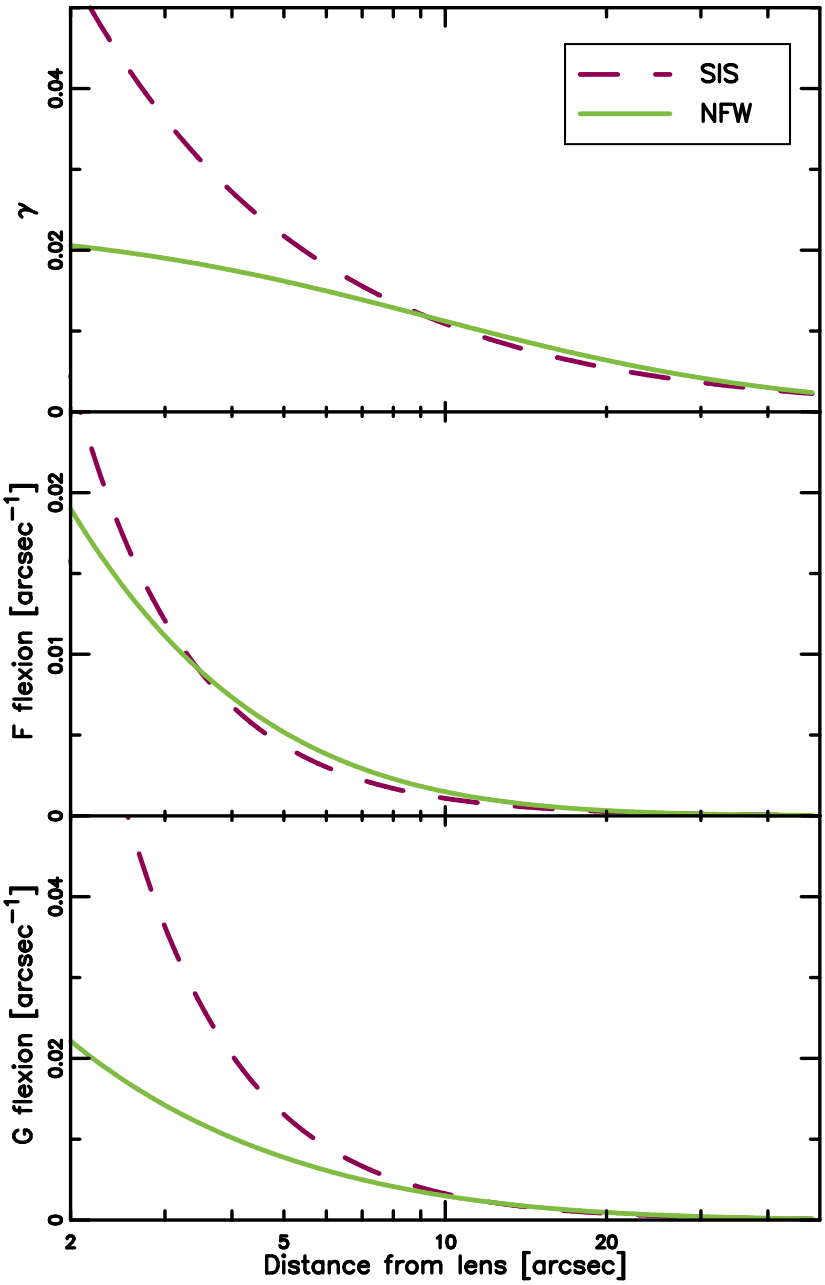

Figure 1.15 Comparison of the singular isothermal sphere (SIS) and Navarro-Frenk-White (NFW) density profiles for shear, F flexion and G flexion (top to bottom). The dashed (solid) line represents the SIS (NFW) profile in each case, and the surface mass density is proportional to the shear.

the rotational velocity is constant, but it is clearly unphysical close to the lens where the density profile approaches infinity.

The NFW profile is motivated by the properties of pure dark matter haloes in

N-body simulations and has a softer inner profile but approaches the behaviour of the SIS on larger scales. The density scales as

$$\rho(x) = \frac{\rho_{\rm crit}(z)\Delta_c}{x(1+x)^2} \tag{1.45}$$

where $x = r/r_s$ is the radius in units of a scaling radius r_s and Δ_c is a dimensionless scaling density. The shear profile for the NFW has been analytically derived by Wright & Brainerd (2000) and the corresponding flexion expressions are given in Bacon et al. (2006). A defining parameter of the NFW halo is also its *concentration* c which is related to its *virial radius* r_{200} within which the total mass is M_{200} (see e.g. Duffy et al., 2008, for a recent relation). The virial radius defines the point where the density of the halo is 200 times the critical density $\rho_{\rm crit}$. M_{200} is frequently used as a measure of the halo mass in weak lensing analyses, and a relation between the NFW halo mass and the SIS Einstein radius is given by e.g. Bacon et al. (2006). A comparison of the SIS and NFW profiles for each of shear, F flexion and G flexion is shown in Figure 1.15 for a halo of mass $M = 1 \times 10^{12}\ h^{-1}\ M_\odot$ at redshift $z_l = 0.35$. The lensing distortions shown are imprinted on sources at redshift $z_s = 0.8$. It is clear that the inner regions are important for distinguishing density profiles and this is an interesting application of flexion since it has the potential to better distinguish between the two profiles. In Chapter 3 we use space-based data to observe galaxy-galaxy flexion and use the measurements to constrain the density profile of an average galaxy.

These profiles are useful for studying isolated galaxies or for characterising the mass distribution on small scales, close to the lens. However, we know that galaxies in general cluster along dark matter filaments and in Cosmic Web nodes. If we do not specifically select galaxies that are isolated, we will see an excess signal on larger scales due to neighbouring galaxies and their haloes adding their signature to the profile. To extract an accurate mass estimate this fact has to be accounted for, and the established approach is to use a *halo model* (e.g. Cooray & Sheth, 2002; Guzik & Seljak, 2002; Mandelbaum et al., 2005; van Uitert et al., 2011). The model becomes more complicated when the lensing signal contribution from satellite galaxies is also included, and when striving to accurately account for the normal baryonic matter in galaxies as well, rather than just the dark matter. In Chapter 4 we briefly review the halo model introduced in van Uitert et al. (2011) and apply it to data from the full Canada-France-Hawaii Telescope Legacy Survey (CFHTLS) with the aim of learning about the connection between dark matter haloes and their corresponding host galaxies. For genuine galaxy clusters however, the approach is slightly different. We discuss this in more detail in Chapter 5, but first I give a qualitative example of the impressive cluster results that can be achieved with weak lensing.

1.3.4 Bullets and train wrecks

The power of combining a weak lensing analysis with other types of mass observations is well illustrated by recent studies of merging galaxy clusters. The merging process causes the matter distribution in such clusters to be highly disturbed, allowing us to study the behaviour of their mass components under such unusual circumstances. This Section will mainly be concerned with two

such clusters which are in stark contrast to each other: the Bullet Cluster (1E 0657-558) at $z = 0.296$ and the Cosmic Train Wreck (Abell 520) at $z = 0.201$.

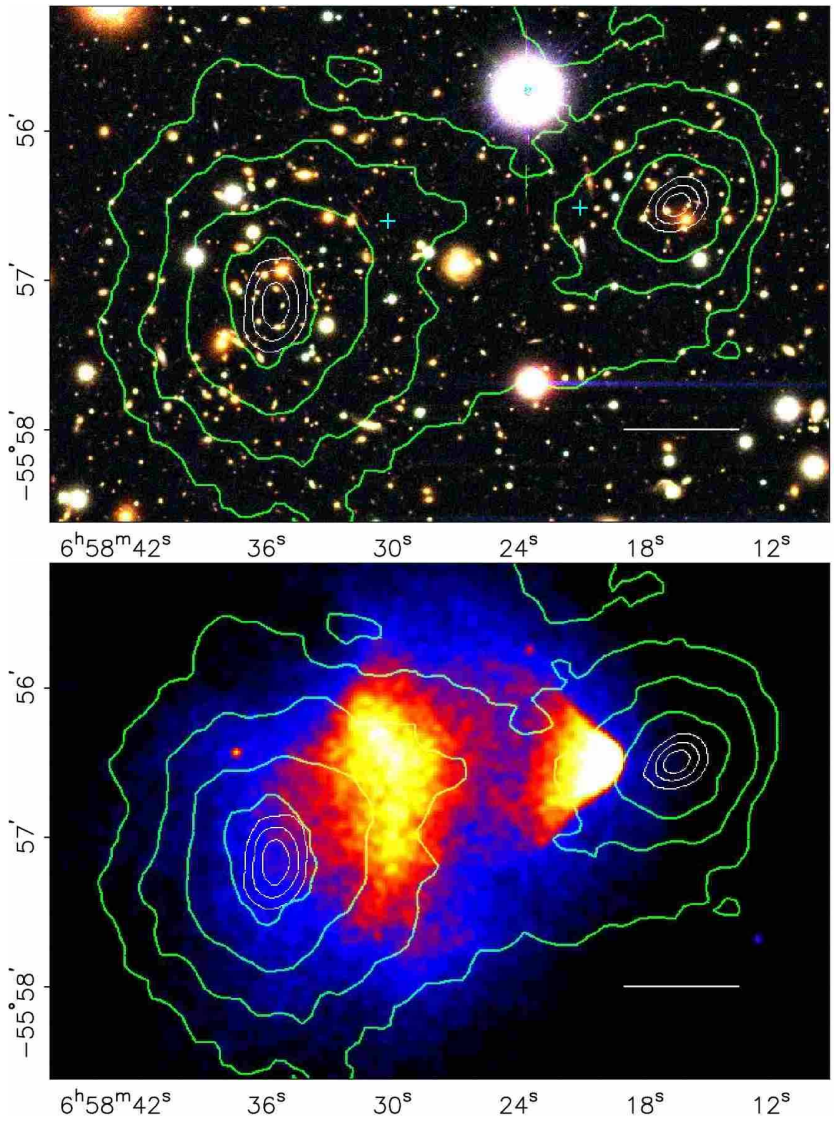

Figure 1.16 Bullet Cluster weak lensing results. The top panel shows the galaxies imaged with the Hubble Space Telescope and the bottom panel shows the plasma imaged with Chandra. Overlaid on both panels are the green contours from the weak lensing analysis, the peaks of which clearly coincide with the two galaxy concentrations rather than with the plasma concentration which contains more baryonic mass. Figures originally published in Clowe et al. (2006).

The Bullet Cluster was made famous by Clowe et al. (2006) when they presented a study where a weak lensing mass reconstruction is compared to the locations of baryons in the cluster. The baryonic components considered in that paper are the galaxies themselves in each of the two merged clusters, and the

plasma displaced from the clusters during the collision. Their results are shown in Figure 1.16 and they are in excellent agreement with what ΛCDM predicts. As the two main clusters pass through each other the galaxies act essentially as collisionless particles and emerge on either side relatively intact. The plasma from each cluster on the other hand is caught in the middle as evidenced by the 'bullet' or shock wave visible in the X-ray imaging (lower panel in Figure 1.16). In the absence of dark matter we would expect the majority of the mass to be contained in the plasma. As is clear from the weak lensing analysis, shown as green contours in Figure 1.16, the mass peaks coincide perfectly with the two galaxy concentrations and there is no evidence of a peak near the bullet. This is consistent with the prediction that dark matter is collisionless and should thus follow the galaxies as the two clusters pass through each other. Since the observations are difficult to explain with models that just modify the gravity strength of ordinary matter, this particular study has become a standard piece of evidence for the existence of dark matter.

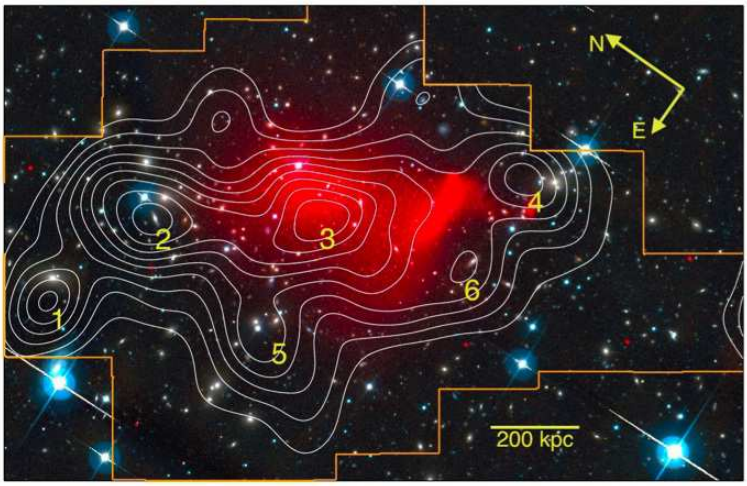

Figure 1.17 Cosmic Train Wreck weak lensing results. The weak lensing mass contours are overlaid a composite image showing both the optical CFHT observations and the Chandra X-ray observations as a diffuse red cloud. Significant weak lensing mass peaks are numbered 1-6 and number 3 coincides with a high plasma concentration in this case, contrary to what is seen in the Bullet Cluster. Figure originally published in Jee et al. (2012).

As a counter-example, the Cosmic Train Wreck which is a merging cluster thought to be at a stage similar to that of the Bullet Cluster has been studied using the same approach (Mahdavi et al., 2007; Jee et al., 2012). The resulting composite image (Figure 1.17) shows six distinct weak lensing mass peaks. Most of these peaks coincide with concentrations of galaxies, with the glaring exception of peak number 3. There are a few faint cluster galaxies in the vicinity of this peak but, more strikingly, that area seems dominated by the high plasma density. This is very puzzling because it seems to indicate that there is

dark matter, *but no associated luminous matter*, left at the centre of the cluster suggesting that the dark matter particles have collided. Comparing the dark matter collisional cross-section estimated from this analysis with the maximum allowed value derived from the Bullet Cluster, it becomes clear that the two analyses are incompatible at a 6σ level. There have been a few suggested explanations for this result, including a Cosmic Web filament centred on peak 3 and pointing straight towards or away from us, but there have to be a fair few fortuitous circumstances for any of these explanations to hold. If all other explanations are ruled out and we are left with collisional dark matter as the only possibility, then the Cosmic Train Wreck constitutes a strong counter-argument to the conclusions drawn from the Bullet Cluster.

These two examples showcase the ability of weak lensing to reveal basic properties of dark matter, thanks to its sensitivity to *all* matter structure in the foreground. It also shows the scientific value in analysing not only well-behaved large structures with settled features but also atypical cases with heavily distorted mass distributions. It is clear that there is a great deal to be learnt via analyses like these.

1.3.5 Shape measurement methods

The challenge of correctly determining the lensing distortions is a significant one. As already discussed, the distortions are small and imprinted on galaxies which are not intrinsically circular. Furthermore, our view of the resulting source images is somewhat muddled by the imaging systems we use to observe them and, in the case of ground-based telescopes, by the atmosphere. Considerable effort has gone into producing a method that can reliably measure shear and flexion, though most of the effort has so far been focused on recovering the shear only. As a result there is a wide variety of shape measurement methods in use today, and I will here give an overview of the most common types.

Moments-based methods

A widespread approach to determining the shape of a galaxy image is to measure the *moments* of its surface brightness distribution. The first (or monopole) moments $\bar{x}$ and $\bar{y}$ correspond to the *centroid* while the second (or quadrupole) moments Q_{ij} encode the ellipticity and higher order (octupole and 16-pole) moments Q_{ijk} and Q_{ijkl} are related to the flexions. By combining these moments, estimators for shear and flexion may be derived in the weak lensing limit (see e.g. Okura et al., 2008):

$$\gamma \simeq \frac{1}{2}\langle\chi\rangle \tag{1.46}$$

$$\mathcal{F} \simeq \left\langle \frac{\zeta}{(9/4) - 3(\mathrm{tr}Q)^2/\xi} \right\rangle \tag{1.47}$$

$$\mathcal{G} \simeq \frac{4}{3}\langle\delta\rangle \tag{1.48}$$

where χ, ξ, ζ and δ are moments combinations:

$$\chi \equiv \frac{Q_{11} - Q_{22} + 2iQ_{12}}{Q_{11} + Q_{22}} \tag{1.49}$$

$$\xi \equiv Q_{1111} + 2Q_{1122} + Q_{2222} \tag{1.50}$$

$$\zeta \equiv \frac{Q_{111} + Q_{122} + i(Q_{112} + Q_{222})}{\xi} \tag{1.51}$$

$$\delta \equiv \frac{Q_{111} - 3Q_{122} + i(Q_{112} - Q_{222})}{\xi} \tag{1.52}$$

In most applications a weight function is applied to the moments in order to limit the effect of noise; these are then known as *weighted moments* and form the basis of the currently most common family of shape measurement methods — the Kaiser-Squires-Broadhurst method (KSB; initially suggested and subsequently developed by Kaiser, Squires, & Broadhurst, 1995; Luppino & Kaiser, 1997; Hoekstra, Franx, Kuijken, & Squires, 1998). A fundamental limitation of KSB is the simplifying assumptions it makes regarding the PSF which are not applicable to more realistic functions (Kaiser, 2000). Even so, the method has been highly successful in practice and the recovered shear still compares well with newer methods. KSB now comes in many flavours, most of them measuring shear only (e.g. Bacon et al., 2000; Erben et al., 2001; Heymans et al., 2005; Schrabback et al., 2007). The extension of KSB to higher orders and thus flexion is known as higher-order lensing image characteristics (HOLICs; Okura et al., 2007, 2008). Additionally, some methods keep to the general philosophy of KSB but vary the weight function (e.g. DEIMOS; Melchior et al., 2011).

Model-fitting methods

The PSF limitation in KSB has inspired the development of alternative methods, and many of them are based on characterising the galaxy brightness distribution through model-fitting. The variation between techniques here is greater than for the moments-based methods simply because there are many different ways to model a galaxy. The general idea is the same though: create a circular or elliptical model galaxy and compare it to an observed source image to determine how much it has been sheared by. The PSF can be accounted for either by convolving the model galaxy with the observed pattern or deconvolving the observed image, though the latter is often discarded due to the difficulty of performing such an operation and its detrimental effect on noise properties.

One way to compare the model galaxy to the source image is to decompose them both into a series of so-called *Shapelets* (Bernstein & Jarvis, 2002; Refregier, 2003; Refregier & Bacon, 2003). The advantage of doing so is to gain analytical expressions for PSF convolution, shear and flexion, making the calculations exact and fast. Shapelets also allow for a more realistic description of the PSF than the one utilised by KSB. This method, however, fundamentally assumes that galaxies are well described by a Gaussian brightness distribution and this limits the reach of the components. Therefore the wings of galaxies are often not well constrained unless very high orders are used, something which is usually difficult because of a lack of pixels. Never the less this approach has proven efficient and accurate and there are several implementations available (Kuijken, 2006; Massey et al., 2007b; Nakajima & Bernstein, 2007; Velander

et al., 2011). This Thesis recounts in part the development of the Velander et al. (2011) version and the use of it to detect flexion in space-based data (see Chapters 2 and 3). A related approach is that of Sérsiclets (Ngan et al., 2009; Andrae et al., 2011) which uses a more realistic basis set derived from the *Sérsic* description of galaxy brightness profiles (Sérsic, 1968). The galaxy can also be modelled as a sum of elliptical Gaussians (Kuijken, 1999; Bridle et al., 2002; Voigt & Bridle, 2010).

In general the above shape measurement pipelines use a least-squares fitting technique, or equivalent, to determine the relevant parameters of the brightness distribution. A different procedure is to use Bayesian statistics, taking the full posterior probability in ellipticity into account. This is exemplified by LENSFIT (Miller et al., 2007; Kitching et al., 2008), a shear measurement software suite which has shown great promise in recent years, both in simulations and on real data. The galaxy images are modelled individually using the sum of two Sérsic profiles to represent the bulge and disk and a full likelihood surface is produced. This likelihood is then used to estimate the shear of the galaxy. However, Bayesian model fitting requires a *prior* (i.e. a best guess) and is therefore sensitive to the exact choice of such a prior. In principle it can be found iteratively using the data at hand, but it is still not clear exactly how strongly a wrong choice would affect the outcome. These worries are relevant for most model-fitting techniques though, since the introduction of additional information is often required due to models being under-constrained by the data. Another fundamental concern is that which also applies to all model-based methods: the model used to imitate a galaxy may not accurately represent the morphology of the true galaxy. To assess the impact of the choices and approximations made in any shear measurement method (be it moments- or model-based), it is vital to use simulated data where we know what the distortion should be.

Simulations to test shape measurement software

Throughout the past decade while the above methods were being developed, lensing simulations designed to test them also evolved. Of particular significance are the shape measurement challenges posed to the weak lensing community as a whole. These blind challenges provide images of simulated sheared galaxies, with the amount of shear unknown to the participants of the challenge. The participants then analyse the images without any preconceptions, thus avoiding *confirmation bias*, and submit an estimate of the shear to the trial organisers. Because the challenge is blind, and because all entrants analyse the same images under the same conditions, the participating methods can be compared and contrasted with each other. So far these trials are limited to shear measurements only, with no flexion applied to the simulated galaxies.

The first such large-scale challenge was the Shear Testing Program (STEP; Heymans et al., 2006a) closely followed by its successor STEP2 (Massey et al., 2007a). The bias of shear measurements was parameterised using a multiplicative bias factor m and an additive factor c:

$$\langle \gamma_i^m \rangle - \gamma_i^t = m_i \gamma_i^t + c_i \tag{1.53}$$

where γ^t is the true (input) shear, γ^m is the measured shear and $i = 1, 2$ represents the component. A negative m thus indicates that the distortion is generally

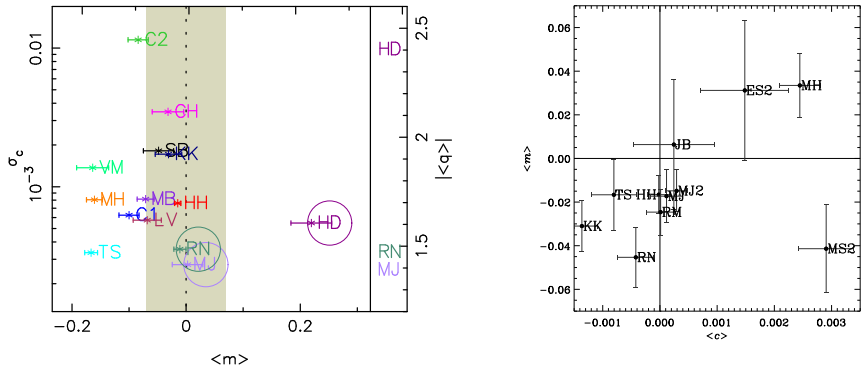

Figure 1.18 Results from STEP (left panel) and STEP2 (right panel) comparing m and c biases for participating methods. Note the difference in scale; the entire figure for STEP2 is within the grey band signifying a calibration bias of less than 7 per cent in the STEP1 figure. The closer to zero a method is, the greater its ability to recover the input shear. Figures originally published in Heymans et al. (2006a) and Massey et al. (2007a); for details on the different methods the reader is referred there.

underestimated, something most entries in STEP suffer from. A systematic offset c may be caused by e.g. insufficient PSF correction but is in general small for implementations in use today. The first STEP installment strived to provide as realistic simulations as possible, while the successor introduced some simplifications to ensure biases were not due to e.g. shape noise. Already in STEP, however, the most successful methods achieved percent-level accuracy (see Figure 1.18) which is sufficient for current weak lensing surveys but needs to reach sub-percentage accuracy in preparation for near future surveys.

The majority of shape measurement methods taking part in the STEP challenges were based on KSB, but by the time the next generation of challenges emerged this picture had changed. These new sets of blind simulations, Gravitational Lensing Accuracy Testing (GREAT08 and GREAT10; Bridle et al., 2009, 2010; Kitching et al., 2010, 2012) had a somewhat different philosophy to STEP. They were aimed not only at the weak lensing community but endeavoured to entice other communities as well, such as computer scientists. Therefore the simulations were stripped down to the core problem of estimating shear and PSF from images, rather than them being as realistic as possible. Furthermore, there were several branches which, although still kept blind for the participants, allowed for a clear picture of which galaxy properties most affect the accuracy of the measurements. The performance of each method was quantified via a quality factor Q which is essentially a combination of the m and c parameters of STEP. The higher the quality factor, the better the method performs. For future surveys, a Q of about 1000 would be ideal, and current methods achieve in general $Q \sim 20$–100. The results from the GREAT08 challenge are shown in Figure 1.19; for the GREAT10 results the reader is referred to Kitching et al. (2012) as the analysis is too extensive to display succinctly here.

There are a vast number of lensing simulations available more or less publicly. STEP and GREAT have the benefit of being able to compare several methods under the same conditions and thus providing a good measure of how well a method can recover lensing distortions in general. They are however

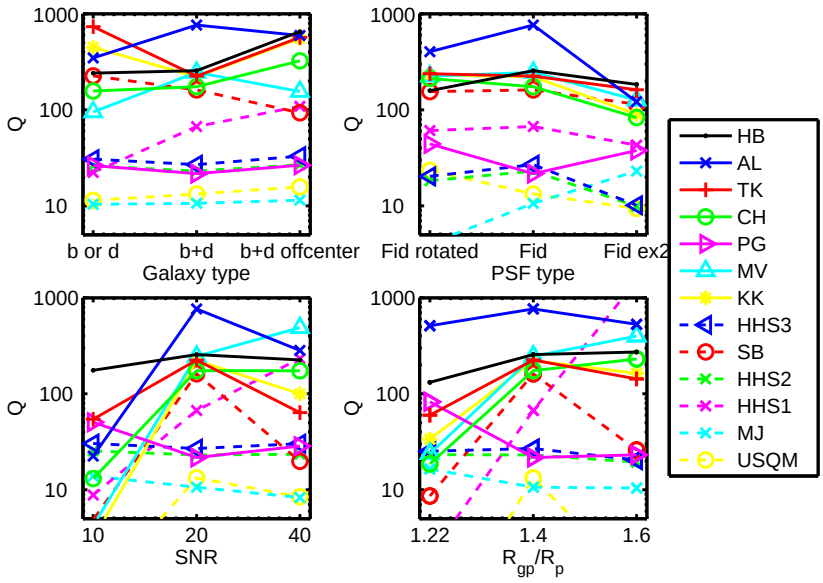

Figure 1.19 Results from GREAT08 showing the Q-values for each branch and each participating method. The higher the Q-value, the better the method performs. Figure originally published in Bridle et al. (2010); for details on the different methods the reader is referred there.

fairly idealised and not attempting to mirror a particular survey. To acquire an accurate impression of how well a method works for a specific survey, simulations imitating the exact observing conditions are necessary. Therefore there are often detailed lensing simulations created for each weak lensing survey. We will, however, always be limited by how well we understand all the effects that influence our distortion measurements, and how closely our simulations mimic reality.

1.4 This Thesis

This Thesis is concerned with studying dark matter haloes using weak lensing through a variety of different applications, observational as well as theoretical. The overall aim is to ascertain how galaxies populate their dark matter haloes, and how the haloes affect the formation and evolution of their host galaxies. To this end we create a new shape measurement pipeline based on the Shapelets formalism with the ability to determine both shear and flexion simultaneously. We also develop software to accurately model the lensing signal on large scales, taking into account contributions from neighbouring and satellite galaxies and galaxy haloes. This extensive software package is then applied to real data, both ground-based and from the Hubble Space Telescope.

In Chapter 2 we describe in detail the shape measurement software known as *the MV pipeline* and show that it is robust using both GREAT08 simulations, and simulations created specifically for the purpose of testing flexion recovery. We then apply it to galaxies which are not monochromatic as is standard in

simulations, but which have a colour gradient. This is something that could potentially be an issue for broad-band imaging, though our findings indicate that the effect is small. Chapter 3 provides the first detection of galaxy-galaxy flexion using data from the Hubble Space Telescope. We use this detection in combination with shear measurements to constrain the density profiles of galaxy-sized haloes, and show that the inclusion of flexion is advantageous to accurately determining the halo mass. In Chapter 4 we describe our halo modelling software and apply it to galaxies in the full CFHTLS survey. We study the halo mass as a function of host galaxy properties such as luminosity and stellar mass. Our constraints on the relations between light and dark matter are tighter than earlier analyses thanks to the large area and depth of the CFHTLS survey. Finally in Chapter 5 we investigate the mass distribution in clusters of galaxies and how it translates into shear and flexion profiles when averaged over several clusters. In clusters we are in general unable to accurately determine the true gravitational center, but are compelled to use visible tracers such as the brightest cluster galaxy to estimate it. As a result the observed density profile is offset from the true profile. We provide predictions for what we expect to observe when several randomly offset profiles are averaged, in shear and flexion space. Furthermore, we show that the use of flexions is particularly valuable in this application.

2 A new shape measurement method and its application to galaxies with colour gradients in weak lensing surveys

Sections to be published in Semboloni E., Velander M., Hoekstra H., Kuijken K., et al, in preparation

As one of the most powerful probes of cosmology, weak gravitational lensing is now the main motivation behind some of the largest near-future optical surveys ever undertaken. The statistical nature of the method requires analysis of a large number of sources, and the minute distortions involved demand high-quality data and precise shape measurements. Weak lensing software therefore has to be both fast and accurate, and such a software suite is introduced and tested in this Chapter. This MV pipeline is shown to be very competitive, with the added benefit of being able to measure higher-order lensing distortions, or flexion. The tests described in this Chapter involve both monochromatic and non-monochromatic simulations, where the latter have been included to assess the amount of bias induced by a wavelength-dependent PSF. Since most galaxies display colour gradients, with a core that has a different colour from the outskirts, a wavelength-dependent PSF will affect different parts of the galaxy image differently. Thus some additional shape bias may be introduced if the PSF is not precisely corrected for. Creating simulations based on real galaxies observed in two different filters, we find that the additional bias induced by this effect is not greater than the bias inherent in the shape measurement software itself. We conclude from our tests that given enough training data we will most likely be able to characterise the colour gradient bias sufficiently accurately to correct for it in future Euclid-like surveys.

2.1 Introduction

With weak gravitational lensing rapidly gaining traction as a powerful probe of cosmology, new surveys are being designed with lensing as a main science goal. Since weak lensing relies on the statistical properties of a galaxy population, large surveys are necessary to minimise systematics such as the intrinsic shape noise. The great number of precise measurements required for future weak lensing analyses increases the necessity for shape measurement software to be both fast and accurate. Currently there is a fair amount of software available, most of which is centred either around the determination of shapes from combinations of weighted second-order brightness moments, such as the method introduced in Kaiser, Squires, & Broadhurst (1995) (KSB hereafter), or around model fitting techniques such as LENSFIT (Miller et al., 2007; Kitching et al., 2008) or Shapelets (Refregier, 2003; Refregier & Bacon, 2003).

The design of a survey also has to take systematics other than those due to biases in shape measurements into account, and primary amongst them is the shape distortion induced by the telescope and, in the case of ground-based surveys, by the atmosphere. This shape distortion is known as the point-spread function (PSF) and can cause coherent distortion across a survey field, biasing the lensing signal. KSB methods have the inherent limitation of too simplistic a description of the PSF and not all realistic PSFs can be accurately accounted for using this description (see e.g. Hoekstra et al., 1998). LENSFIT has a more flexible PSF model and has been proven to be accurate when applied to simulations such as the Gravitational Lensing Accuracy Testing 2008 set (GREAT08; Bridle et al., 2009, 2010), but due to the Bayesian approach it is unfeasibly slow for large near-future surveys. We have therefore chosen to base the new shape measurement software introduced and tested in this Chapter, the MV pipeline, on Shapelets which are both flexible and fast thanks to their analytical nature. Because of their definition as a set of Gauss-Hermite polynomials, any distortion or convolution may be done analytically. This makes it straight-forward to extend the shape analysis to higher-order lensing distortions, known as flexions, without loss of time or accuracy. Flexion, which quantifies variations in shear across a source image, was first discussed in Goldberg & Natarajan (2002) and the notation was then further developed in Goldberg & Bacon (2005) and Bacon et al. (2006). Adding flexion to shear results in a weak arc-like shape which is a better description of the true lensing-induced distortion than the shear stretch alone. Flexion is sensitive to small-scale fluctuations so added detail to mass reconstructions is gained by including it. This makes flexion a powerful complement to shear, particularly for detecting substructure within dark matter haloes (Okura et al., 2008; Bacon et al., 2010; Er et al., 2010; Leonard et al., 2011), or for determining their profiles and shapes (Hawken & Bridle, 2009; Er & Schneider, 2011; Er et al., 2011).

In this Chapter we convey the details of the MV pipeline and the tests performed on it using the GREAT08 simulations and simulations created specifically for the purpose of testing the MV pipeline in preparation for the analysis of space-based data. Both sets of simulations are monochromatic in nature, but recently the question of the impact of a wavelength-dependent PSF on shape measurement accuracy was raised (Voigt et al., 2011). Since the PSF is a function of wavelength, and since galaxies in general are expected to display

different colours in their cores and disks, the PSF will look different at different points on a galaxy image. Thus two galaxies with dissimilar intrinsic shapes and colour gradients may become indistinguishable after being convolved with a wavelength-dependent PSF. Perfectly correcting for the PSF in such a case is impossible without further information on the colour gradient of the galaxy. This could present a challenge for surveys where observations are done using a broad-band filter such as the planned space-based Euclid[1] survey, scheduled for launch in 2019. The ultimate impact of this effect on weak lensing analyses will depend on the true intrinsic colours of the galaxy distribution and on the total shape measurement bias induced by the wavelength-dependent PSF. For the first part several studies into colour gradients of galaxies have been carried out in the context of galaxy evolution, most of them at low redshifts (e.g. Gonzalez-Perez et al., 2011). To assess the impact of the second part, the bias induced by a wavelength-dependent PSF, representative simulations have to be created. In this Chapter we use real galaxies from the All-Wavelength Extended Groth Strip International Survey (AEGIS; Davis et al., 2007) together with photometric redshifts from the third Canada-France-Hawaii Telescope Legacy Survey Deep field (CFHTLS-Deep3) to create realistic broad-band simulations. AEGIS is here assumed to provide a representative galaxy sample which has been observed through two filters with the Advanced Camera for Surveys (ACS) onboard the *Hubble Space Telescope* (HST). These two filters can be combined to approximate the broad-band filter proposed for Euclid and therefore these data form the ideal starting point for Euclid-like simulations. The MV pipeline is then tested on these simulations to determine the level of bias induced by colour gradients in galaxies, and to identify the galaxy properties that have the greatest impact on this bias.

This Chapter is organised as follows: in Section 2.2 we introduce the theoretical background of shear and flexion, and of Shapelets, with the MV pipeline being described in detail in Section 2.2.3. Monochromatic tests of the MV pipeline are carried out in Section 2.3 and the software is applied to non-monochromatic simulations in Section 2.4. We conclude in Section 2.5.

2.2 Theoretical background

2.2.1 Shear and flexion

If the lensing convergence and shear are not constant across a given source image, then we need to quantify how they vary. This can be done by measuring higher-order lensing distortions known as flexion. The formalism was first explored by Goldberg & Bacon (2005) and then further investigated by Bacon et al. (2006) (hereafter B06). In the weak lensing regime where convergence is small the lensed surface brightness of a source galaxy, $f(\mathbf{x})$, and the unlensed surface brightness, $f_0(\mathbf{x})$, are related through

$$f(\mathbf{x}) \simeq \left\{1 + \left[(A-I)_{ij}x_j + \frac{1}{2}D_{ijk}x_jx_k\right]\frac{\partial}{\partial x_i}\right\} f_0(\mathbf{x}). \tag{2.1}$$

where I is the identity matrix, x_i denotes lensed coordinates, and A is a distortion matrix which may be expressed in terms of convergence κ and shear

[1] http://www.euclid-ec.org

γ:

$$\mathrm{A} = \begin{pmatrix} 1-\kappa-\gamma_1 & -\gamma_2 \\ -\gamma_2 & 1-\kappa+\gamma_1 \end{pmatrix}. \tag{2.2}$$

$D_{ijk} \equiv \partial A_{ij}/\partial x_k$ describes how the lensing field varies across a source image. Assuming that there are no such fluctuations, an assumption which may be valid if e.g. the source image is very small, is equivalent to setting $D_{ijk} = 0$. We can now re-express this matrix as a sum of two quantities: $D_{ijk} = \mathcal{F}_{ijk} + \mathcal{G}_{ijk}$. These two quantities are referred to as first flexion, or *F flexion*, and second flexion, or *G flexion*, respectively and similarly to shear have two components each. To make the relation between convergence, shear and flexion clear we can express all quantities in terms of derivatives of the lensing potential ψ (see e.g. Hawken & Bridle, 2009):

$$\kappa = \frac{1}{2}(\psi_{xx} + \psi_{yy}) \tag{2.3}$$

$$\gamma_1 = \frac{1}{2}(\psi_{xx} - \psi_{yy}) \tag{2.4}$$

$$\gamma_2 = \psi_{xy} \tag{2.5}$$

$$\mathcal{F}_1 = \frac{1}{2}(\psi_{xxx} + \psi_{yyx}) \tag{2.6}$$

$$\mathcal{F}_2 = \frac{1}{2}(\psi_{xxy} + \psi_{yyy}) \tag{2.7}$$

$$\mathcal{G}_1 = \frac{1}{2}(\psi_{xxx} - 3\psi_{xyy}) \tag{2.8}$$

$$\mathcal{G}_2 = \frac{1}{2}(3\psi_{xxy} - \psi_{yyy}) \tag{2.9}$$

The full matrices $\mathcal{F}_{ijk}$ and $\mathcal{G}_{ijk}$ in terms of the four flexion components are written explicitly in B06. Visually, if the shear is a stretch in one direction then F flexion is a subtle skewness of the brightness profile reminiscent of a centroid shift and the G flexion has three-fold rotational symmetry. When all the above distortions are applied to a circular object, a weak arc is created.

2.2.2 Shapelets

The shape measurement pipeline presented in this Chapter is based on the Shapelet formalism which makes possible the linear decomposition of a galaxy image with surface brightness $f(\mathbf{x})$ into a set of complete and orthogonal basis functions B_{ab} called Shapelets:

$$f(\mathbf{x}) = \sum_{a=0}^{\infty}\sum_{b=0}^{\infty} s_{ab} B_{ab}(\mathbf{x};\beta) \tag{2.10}$$

where s_{ab} are the Shapelets coefficients. The formalism was first introduced by Refregier (2003) and its application to weak lensing shape estimates was further studied in Refregier & Bacon (2003). The basis functions employed consist of Gauss-Hermite polynomials:

$$B_{ab}(\mathbf{x};\beta) = k_{ab}\beta^{-1} e^{-\frac{|\mathbf{x}|^2}{2\beta^2}} H_a(x/\beta) H_b(y/\beta). \tag{2.11}$$

The Hermite polynomial of order n, H_n, depends on the coordinate on the image plane and on the Shapelets scale radius β, and the basis functions are normalised by a constant k_{ab}. What makes Shapelets powerful is not only their completeness but also their invariance under Fourier transforms which enables us to do convolutions analytically. This makes Shapelets a very fast method for determining distortions which is essential to weak lensing, particularly for dedicated surveys where a large number of objects have to be analysed. They are also analogous to the eigenstates of the two-dimensional quantum harmonic oscillator, and thus any linear transformation such as translation, rotation, dilation and shear and flexion can be expressed as a combination of ladder operators:

$$\hat{a}_i \equiv \frac{1}{\sqrt{2}}(\hat{x}_i + i\hat{p}_i) \tag{2.12}$$

$$\hat{a}_i^\dagger \equiv \frac{1}{\sqrt{2}}(\hat{x}_i - i\hat{p}_i) \tag{2.13}$$

where $i = 1, 2$ (for the x- and y-directions), $\hat{x} \equiv x$ and $\hat{p} \equiv \partial/\partial x$. The property raised or lowered by these operators is known as *spin*; a quantity which is invariant under rotation by an angle $\phi = 2\pi/s$ is said to be a spin-s quantity. Thus shear (or ellipticity) is a spin-2 quantity, while F flexion is spin-1 and G flexion is spin-3. The shear operators may be written in terms of raising and lowering operators as

$$\hat{S}_1 = \frac{1}{2}\left(\hat{a}_1^{\dagger 2} - \hat{a}_2^{\dagger 2} - \hat{a}_1^2 + \hat{a}_2^2\right) \tag{2.14}$$

$$\hat{S}_2 = \hat{a}_1^\dagger \hat{a}_2^\dagger - \hat{a}_1 \hat{a}_2 \tag{2.15}$$

or, in terms of the $\hat{x}$ and $\hat{p}$ operators

$$\hat{S}_1 = -\frac{1}{2}\left(\hat{x}_1\hat{p}_1 - \hat{x}_2\hat{p}_2\right) \tag{2.16}$$

$$\hat{S}_2 = -\frac{1}{2}\left(\hat{x}_1\hat{p}_2 + \hat{x}_2\hat{p}_1\right) \tag{2.17}$$

Using the same notation we can write simple analytical expressions for the flexion operators:

$$\hat{\mathcal{F}}_1 = -\frac{1}{8}\left(3\hat{x}_1^2\hat{p}_1 + 2\hat{x}_1\hat{x}_2\hat{p}_2 + \hat{x}_2^2\hat{p}_1\right) \tag{2.18}$$

$$\hat{\mathcal{F}}_2 = -\frac{1}{8}\left(\hat{x}_1^2\hat{p}_2 + 2\hat{x}_1\hat{x}_2\hat{p}_1 + 3\hat{x}_2^2\hat{p}_2\right) \tag{2.19}$$

$$\hat{\mathcal{G}}_1 = -\frac{1}{8}\left(\hat{x}_1^2\hat{p}_1 - 2\hat{x}_1\hat{x}_2\hat{p}_2 - \hat{x}_2^2\hat{p}_1\right) \tag{2.20}$$

$$\hat{\mathcal{G}}_2 = -\frac{1}{8}\left(\hat{x}_1^2\hat{p}_2 + 2\hat{x}_1\hat{x}_2\hat{p}_1 - \hat{x}_2^2\hat{p}_2\right) \tag{2.21}$$

Applying these operators to circular Shapelets we thus get an image which is 'flexed'.

Using Shapelets, the point-spread function (PSF) can be convolved with a galaxy image in a similarly analytical fashion. The PSF is described by a distortion matrix $\mathbf{P}$:

$$\mathbf{P}_{a_1a_2b_1b_2}(\beta_{\rm obj}, \beta_{\rm con}) = \sum_{a_3,b_3} C_{a_1a_2a_3}^{\beta_{\rm con}\beta_{\rm obj}\beta_{\rm psf}} C_{b_1b_2b_3}^{\beta_{\rm con}\beta_{\rm obj}\beta_{\rm psf}} p_{a_3b_3} \tag{2.22}$$

Here p_{ab} are the Shapelets coefficients of the PSF and $\beta_{\rm psf}$, $\beta_{\rm obj}$ and $\beta_{\rm con}$ are the scale radii of the PSF, the object and the resulting PSF convolved object respectively. $C_{nml}^{\beta_1\beta_2\beta_3}$ is a convolution tensor which depends on the different scale radii. The full expression is given in Refregier (2003). The PSF convolution is then done by multiplying the above matrix and the Shapelets expansion of the object being convolved.

2.2.3 The MV pipeline

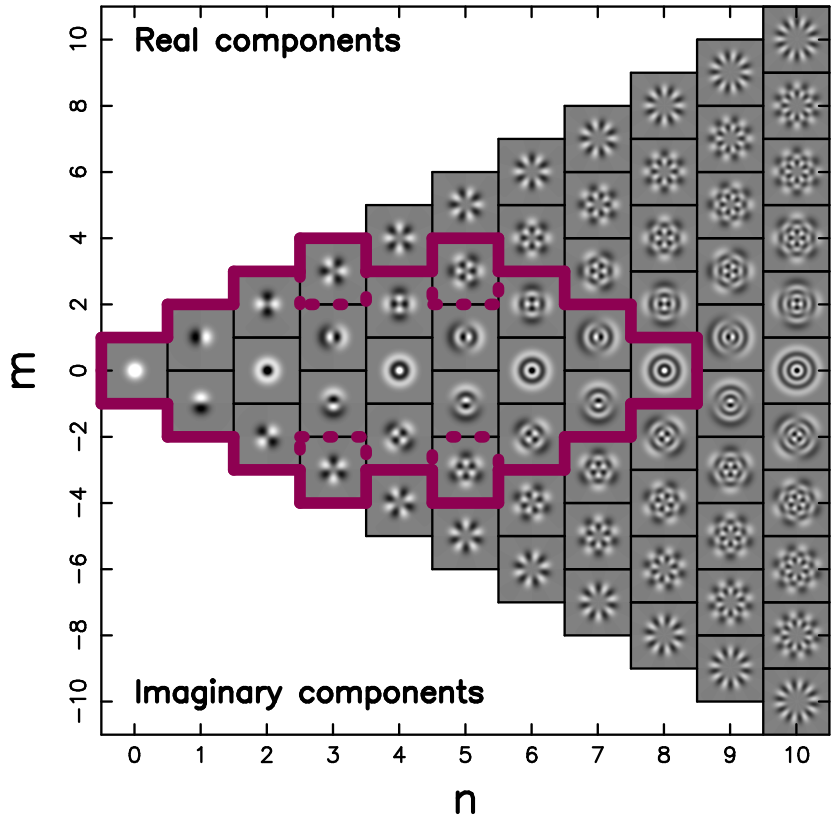

Figure 2.1 Polar Shapelets basis functions up to a maximum Shapelets order of $n_{\rm max} = 10$. For $m \geq 0$, the real components of the basis functions are shown while for $m < 0$ the imaginary components are shown. The solid purple (thick) lines mark the coefficients used by the MV pipeline to estimate the shear and flexions for an analysis with $n_{\rm max} = 10$. The dashed purple (thick) lines mark the coefficients not used by the KK06 implementation for the same $n_{\rm max}$.

The software we introduce and test in this Chapter, the *MV pipeline*, is based on an earlier Shapelets implementation described in Kuijken (2006) (hereafter KK06), which we will refer to as the *KK pipeline*. The KK pipeline is a robust piece of shear estimation software which has been thoroughly tested on simulation suits such as the two Shear TEsting Programmes (STEP1 and STEP2) (Heymans et al., 2006a; Massey et al., 2007a). The MV pipeline keeps the core

Shapelet decompositions of KK, but extends the analysis package to enable flexion measurement. The basic procedure for doing this is to

i) create a circular galaxy model
ii) apply shear and flexion to the model, and convolve with the measured PSF
iii) decompose the true PSF convolved source image into Shapelets
iv) fit the model to the observed image.

In theory a galaxy image could be perfectly described by an infinite series of Shapelets, but in practice we have to truncate this expansion. We choose to truncate at order $n_{\max} = a + b$ (see Equation 2.10). In general we also keep the choice of $n_{\max}$ constant for all galaxies in an analysis, rather than allowing for it to vary according to some criteria such as size or brightness. This ensures that we do not introduce artificial S/N-dependent biases. The trade-off is some noise at higher-order coefficients for smaller or fainter sources but these coefficients will remain unbiased.

Steps i) and ii) above can be summarised as follows to first order in ellipticity s and flexions f and g:

$$\mathbf{P} \cdot \left[1 + \sum_{i=1,2} \left(t_i \hat{T}^i + s_i \hat{S}^i + f_i \hat{F}^i + g_i \hat{G}^i \right) \right] \sum_{\text{even}}^{N_c} c_n C^n \tag{2.23}$$

where $\mathbf{P}$ is the PSF matrix and $\hat{T}^i$, $\hat{S}^i$, $\hat{F}^i$ and $\hat{G}^i$ are the translation, shear, F flexion and G flexion operators respectively, as specified in Equations 2.16–2.21. t_i, s_i, f_i and g_i are the corresponding coefficients which are determined through step iv) above. The translation operators are included in the fit to allow for some shifting to ensure that the fit is not spoilt by an inaccurate centroid. The last term is the circular model in step i) which in this case is expressed as a sum of circular Shapelets C^n with coefficients c_n. n is even (see the $m = 0$ Shapelets in Figure 2.1) and the expansion is truncated at $N_c = n_{\max} - 2$ to safeguard against PSF structure at higher orders affecting the highest order Shapelets used.

Once steps i), ii) and iii) have been carried out, the model galaxy and the cartesian Shapelets representation of the true source image are both converted into polar coordinates in preparation for the fit, as described in Refregier (2003). For cartesian Shapelets of order $n = a + b$, the corresponding polar Shapelets will have order n with angular order $m \leq n$ and $n + m$ even. This conversion is done in order to avoid truncation effects due to the mixing of orders. F flexion, shear and G flexion operators acting on a polar Shapelet of order (n, m) generate terms at order $(n \pm 1, m \pm 1)$, $(n \pm 2, m \pm 2)$ and $(n \pm 3, m \pm 3)$ respectively (see e.g. Massey et al., 2007b, Figure 2, for an illustration of the mixing of Shapelet coefficients). We therefore truncate the polar Shapelets expansion in the diamond shape shown in Figure 2.1, i.e. we only include terms up to order $(N_c, 0)$, $(N_c - 1, \pm 1)$, $(N_c - 2, \pm 2)$ and $(N_c - 3, \pm 3)$ in the fit. This minimises the impact of order mixing. As illustrated in Figure 2.1, the choice of which Shapelets to include in the fit differs slightly between the MV and the KK pipelines. The extra Shapelets included in the MV pipeline are necessitated by the fact that the spin-3 information (i.e. G flexion) is encoded in the $m \pm 3$ components.

Finally in step iv), the model object is fit to the observed source using least-squares. This gives us an estimate for all the relevant quantities simultaneously: the ellipticity (s_1, s_2), the F flexion (f_1, f_2), and the G flexion (g_1, g_2). This technique is fast and adding the four flexion parameters does not significantly increase the computation time compared to fitting for ellipticity alone. The errors on the estimates originate from the errors on the Shapelet coefficients derived from the photon noise. The χ^2 is differentiated at the best-fit in order to obtain covariances between the fit parameters. For further discussion on errors see KK06.

2.3 Monochromatic tests

As part of the development of the KK pipeline, several aspects relevant to the MV pipeline were thoroughly tested. We will therefore not delve further into tests for details which are common between the two, such as the optimal choice of scale radius β and the effect of noise. The distortion measurement routines differ, however, and so we will in this Section thoroughly assess the shear and flexion recovery performance of the MV pipeline. To this end we will use a series of simulations which will be limited to one colour in this Section with the added complication of colour gradients across galaxies and PSFs in the next.

2.3.1 GREAT08

The Gravitational Lensing Accuracy Testing 2008 (GREAT08) challenge (Bridle et al., 2009, 2010) was a competition continuing a tradition of challenges designed to test the accuracy of current state-of-the-art shear measurement software available to the weak lensing community (e.g. STEP1 and STEP2; Heymans et al., 2006a; Massey et al., 2007a). Both the MV pipeline and the KK pipeline were entered in the GREAT08 competition, allowing us to not only test the performance of the MV pipeline under different observing conditions, but also to compare and contrast its shear estimation capabilities to those of its predecessor.

Simulations

The GREAT08 challenge provided simulations designed for testing the fundamentals of shape measurement. Since part of the philosophy of the project was to entice the participation of other communities, such as computer programmers, the simulations were kept fairly simplistic and focused on the core problem of taking a noisy distorted galaxy image and measuring how much it has been sheared by. To avoid any deblending issues, the galaxies were created in individual postage stamps which were then placed on a grid to create an image of 4000×4000 pixels and 10 000 galaxies. Each galaxy postage stamp was created by i) simulating an elliptical and sheared galaxy; ii) convolving it with a PSF; iii) binning the light to create a pixellised image; iv) applying a noise model. During the course of the challenge there were four sets of simulations released to participants; two sets with known shears (low and real noise) and two blind sets (low and real noise). The main challenge consisted of the blind real noise set which consisted of 2 700 composite images as described above.

Table 2.1 Different branches of the GREAT08 RealNoise_Blind simulations. Four parameters were varied between branches according to this table, with further explanations in the text.

	Fiducial	Variation 1	Variation 2
S/N	20	10	40
R_g/R_p	1.40	1.22	1.60
PSF type	Fid	Fid rotated	Fid $e \times 2$
Galaxy type	b+d	b or d	b+d offcentre

Observing conditions were varied between images, one at a time, with the 9 different branches shown in Table 2.1. The fiducial branch had galaxies with S/N = 20 and a ratio between the radius of the PSF convolved galaxy and that of the PSF of $R_g/R_p = 1.40$. These numbers were varied to create four additional branches. The PSF used for all images was a truncated Moffat profile which was mildly elliptical in the horizontal direction for the fiducial branch. The PSF was rotated 45° or its ellipticity was doubled to create two additional branches. The final variable to be altered was the galaxy type. In the fiducial case galaxies were represented by the sum of two Sérsic profiles (Sérsic, 1968) corresponding to the bulge and disk components. For one branch, the galaxies consisted of only one Sérsic profile corresponding to either a bulge or a disk, and in another the centroids of the bulge and disk did not coincide. For more details on the different branches see the GREAT08 results paper (Bridle et al., 2010).

Both the applied shear and the PSF was kept constant across each image, although they were varied between images. The true shear values were concealed from the participants, and so was the information pertaining to which image was part of which of the 9 branches, but the PSF was provided as a star image. Participants were thus told which of the three PSFs had been applied to which image. The true applied shear values were perturbations around 5 root values, both positive and negative, with $|\gamma_{1,2}^{\rm root}| \leq 0.037$. The GREAT08 team utilised the paired rotation technique introduced in STEP2 whereby each simulated galaxy has a twin galaxy which has been rotated by 90° before shearing. This method minimises shape noise since the ellipticity estimates of each pair should cancel in the absence of applied shear and PSF. The large number of simulated galaxy images in combination with this shape noise minimisation technique allowed for high precision assessment of current shape measurement methods in preparation for future surveys.

Results

For the submitted results, we used the MV pipeline and a maximum Shapelets order of $n_{\rm max} = 8$. To average over all the galaxies in an image we used a technique known as convex hull peeling (CHP). CHP works essentially like a 2D median and is a way of eliminating outliers from a sample in a 2D parameter space (e.g. in the (γ_1, γ_2) plane). This is done by removing a so-called convex hull, i.e. the minimal convex set of data points containing all other points. By peeling away a number of convex hulls and averaging over the remaining points, a mean unaffected by extreme results may be produced (see Figure 2.2).

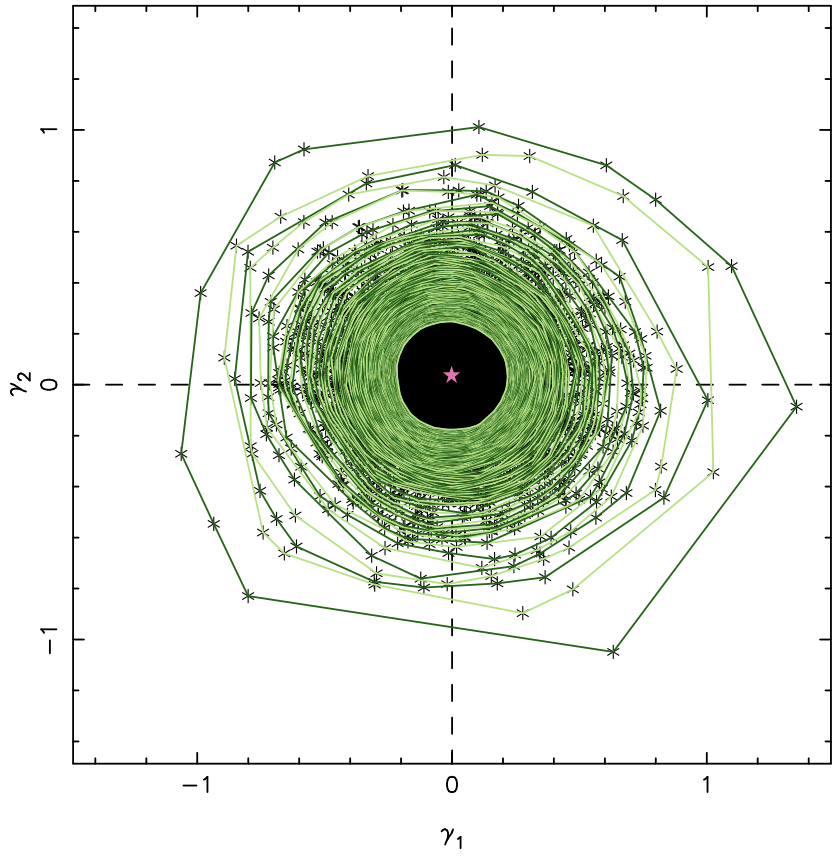

Figure 2.2 Illustration of the convex hull peeling procedure applied to the shears measured on all galaxies in a single GREAT08 image. Each asterisk represents a shear measurement, and the lines connecting data points show the points in the convex hulls being removed before averaging. The final average, after removing 50% of the data points this way, is marked by a red star.

The choice of how many points are removed before averaging may be varied according to their distribution. For GREAT08 we chose to remove 50% of the measurements before averaging.

The GREAT08 team compare the different submissions using a quality factor, or Q-value, in an attempt to consolidate the m (multiplicative bias) and c (additive bias) parameters of STEP into a single quantity. In this case, the Q-value is defined as

$$Q = \frac{k_Q \sigma^2}{\langle (\langle \gamma_{ij}^m - \gamma_{ij}^t \rangle_{j \in k})^2 \rangle_{ikl}} \tag{2.24}$$

where $\sigma^2 = \sigma^2_{\rm stat} + \sigma^2_{\rm syst}$ is a combination of the statistical spread in the simulations and the expected systematic errors. The superscripts m and t denote measured and true values respectively and γ_{ij} is the shear component i for simulation image j. The differences between the measured and true shears are averaged over root shear sets k and simulation branches l. The whole expression is normalised by k_Q such that a method with a purely statistical spread in

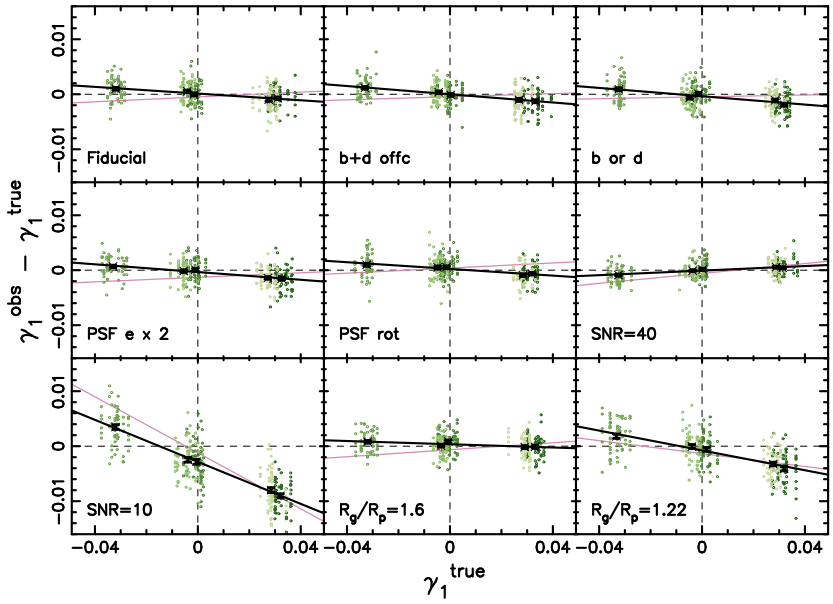

Figure 2.3 Submitted MV γ_1 results for GREAT08. Each circle represents the average γ_1 in a single image containing 10 000 galaxies, and the crosses with error bars show the resulting average for each root shear value. The fitted black line would coincide with the zero-line if there were no biases in the measurements. Also shown as a thinner pink line are the results submitted using the KK pipeline. Each panel represents a different simulation branch as specified in the bottom left corner of each panel (see also Table 2.1). The MV method does well in all cases apart from low signal-to-noise (bottom left panel) and small galaxies (bottom right panel).

the measured shears will have a Q-value of k_Q which is the level desirable for future surveys. In the case of GREAT08, $k_Q = 1000$ and $\sigma^2 = 10^{-7}$, giving a Q-value nominator of 10^{-4}. Established shape measurements at the time of the challenge, such as those based on the KSB method (Kaiser, Squires, & Broadhurst, 1995), generally achieve $10 \lesssim Q \lesssim 100$. For future surveys with greater requirements on accuracy, we would ideally use methods with $Q \to 1000$.

Both the MV and KK pipelines performed well for current surveys, reaching an overall $Q \sim 25$ in the RealNoise_Blind simulations. Due to the definition of Q however, a method is severely penalised if it presents issues in even one of the nine branches. This ensures that a method with a stable high Q across all branches wins the challenge. It is never the less instructive to look at the different branches separately to assess the impact of different observing conditions on the performance of a particular method. In Figures 2.3 and 2.4 we show the residual shear versus true shear for each branch for the submitted MV γ_1 and γ_2 results respectively. From this it is clear that the MV pipeline does very well in 7 of the 9 branches ($100 \lesssim Q_{\rm MV} \lesssim 500$). For a perfect measurement, the black solid line which has been fitted to the data would coincide with the zero-line and any deviation is parameterised via the STEP m and c parameters, defined as follows:

$$\langle \gamma_i^m \rangle - \gamma_i^t = m_i \gamma_i^t + c_i \tag{2.25}$$

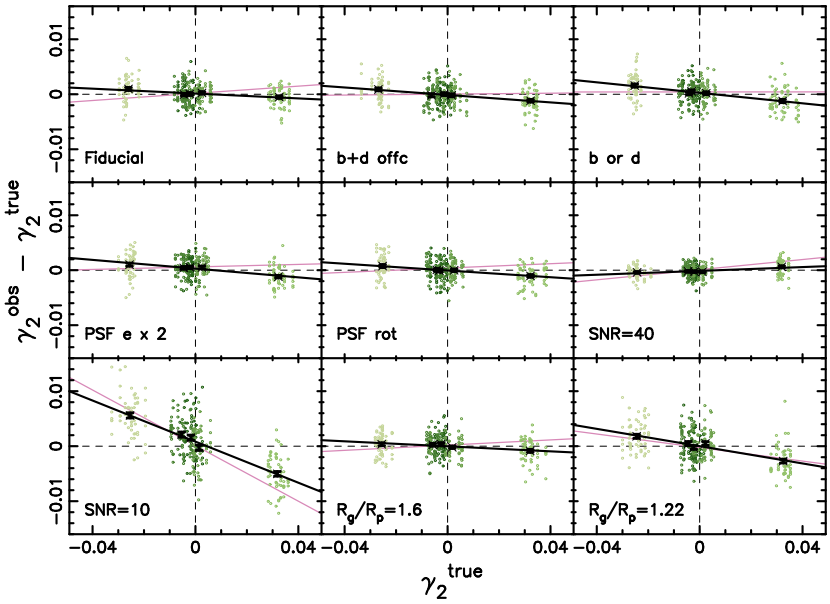

Figure 2.4 Submitted MV γ_2 results for GREAT08. Each circle represents the average γ_2 in a single image containing 10 000 galaxies, and the crosses with error bars show the resulting average for each root shear value. The fitted line would coincide with the zero-line if there were no biases in the measurements. Also shown as a thinner pink line are the results submitted using the KK pipeline. Each panel represents a different simulation branch as specified in the bottom left corner of each panel (see also Table 2.1). The MV method does well in all cases apart from low signal-to-noise (bottom left panel) and small galaxies (bottom right panel).

where $i = 1, 2$ represents the shear component. A negative multiplicative bias m_i thus indicates that the distortion is generally underestimated. A systematic offset c_i may be caused by e.g. insufficient PSF correction, and the Q-values and m and c biases for each of the 9 branches for the MV pipeline may be found in Table 2.2. Also shown for comparison in each panel of Figures 2.3 and 2.4 are the results of the KK pipeline, and the differences in accuracy between the two is small in most cases. A minor distinction is that while the MV pipeline seems to underestimate the shear in nearly all panels, the KK pipeline predominantly overestimates it. For the faint and barely resolved sources, however, both pipelines show similar trends.

Although the MV pipeline performs very well in most cases, the results for faint galaxies (bottom left panels in Figures 2.3 and 2.4) and, to a lesser extent, barely resolved galaxies (bottom right panels) cause the overall Q-value to not reach values adequate for future surveys. The KK pipeline also severely underestimates the shear, and even more so than the MV pipeline in the case of faint galaxies. The strong bias at S/N = 10 is however not consistent with the results found in the STEP challenges (for the KK pipeline; see Heymans et al., 2006a; Massey et al., 2007a) or in our own simulations (for the MV pipeline; see Section 2.3.2). One of the reasons for this discrepancy may be due to the definition of S/N. In GREAT08, the flux of a simulated object is set such that

Table 2.2 MV results for the different branches of the RealNoise_Blind simulations. The Q, m and c parameters are defined in the text (Equations 2.24 and 2.25); the larger the Q-value and the smaller the m and c, the better the recovery of the input shear.

	Q	m_1 ($\times 10^{-2}$)	m_2 ($\times 10^{-2}$)	c_1 ($\times 10^{-4}$)	c_2 ($\times 10^{-4}$)
Fiducial	241	-3.05 ± 0.43	-2.18 ± 0.56	0.24 ± 1.02	1.29 ± 0.99
b+d offset	152	-3.64 ± 0.44	-3.76 ± 0.56	0.83 ± 1.05	-0.37 ± 1.13
b or d	88.9	-4.42 ± 0.48	-4.90 ± 0.67	-2.96 ± 1.15	2.69 ± 1.21
PSF $e \times 2$	140	-3.37 ± 0.44	-3.59 ± 0.56	-3.36 ± 1.03	2.08 ± 1.03
PSF rot	173	-3.09 ± 0.45	-3.88 ± 0.60	2.05 ± 1.10	-1.28 ± 1.08
S/N = 40	471	2.06 ± 0.32	2.20 ± 0.39	-1.14 ± 0.76	-0.65 ± 0.70
S/N = 10	4.81	-18.72 ± 0.70	-20.79 ± 1.03	-17.42 ± 1.74	5.75 ± 1.81
$R_g/R_p = 1.6$	395	-1.60 ± 0.46	-2.39 ± 0.59	3.09 ± 1.11	-0.68 ± 1.03
$R_g/R_p = 1.22$	23.9	-8.76 ± 0.62	-8.41 ± 0.82	-8.05 ± 1.46	0.41 ± 1.57

the number quoted as the signal-to-noise ratio is equal to the total flux divided by the uncertainty in the flux obtained if the true shape, but not normalization, of the object is known. We find that this does not correspond to the S/N we detect as observers, defined as the total observed flux divided by the uncertainty in the flux measurement (as determined by e.g. SExtractor). With this definition we find that GREAT08 simulations with $\mathrm{S/N}_{\mathrm{GREAT08}} = 10, 20, 40$ actually correspond to an observed $\mathrm{S/N}_{\mathrm{obs}} = 6, 12, 23$ respectively, and our results are then more in agreement with previous tests. In real applications we do generally exclude galaxies with $\mathrm{S/N}_{\mathrm{obs}} < 10$ precisely because we know that the bias increases steeply below this level. It should be noted, however, that most galaxies in a weak lensing survey are small and faint, so a shape measurement which is unbiased down to low S/N is vital for future surveys, and it is clear that more work is required in this area. In general though the MV pipeline did exceptionally well under "good" observing conditions, e.g. for the high S/N branch or for well resolved galaxies. Our own simulations described in the next section will further test the dependence of the MV performance on different observing conditions.

2.3.2 FLASHES

In GREAT08, no flexion field has been applied so we are not able to test that aspect of the MV pipeline using those simulations. Because the addition of flexion measurements is the main development since the KK pipeline and all the tests performed on it, it is essential that flexion recovery is tested as well. With no public flexion simulations available, we create our own Flexion and Shear Simulations (FLASHES) using software closely related to the Monte-Carlo selection software used to create the GREAT08 simulations. FLASHES are created with the intent of testing the MV pipeline in preparation for an analysis of the space-based Cosmic Evolution Survey (COSMOS; Scoville et al., 2007), and so several observing conditions are optimised for that survey.

Table 2.3 The different branches of FLASHES. Four parameters are varied between the branches according to this table.

	Intrinsic shape	Galaxy profile	S/N	PSF
Fiducial	Round	Gaussian	100	Round
Shape branch	Elliptical	Gaussian	100	Round
Profile branch 1	Round	Exponential	100	Round
Profile branch 2	Round	de Vaucouleur	100	Round
S/N branch 1	Round	Gaussian	8	Round
S/N branch 2	Round	Gaussian	20	Round
S/N branch 3	Round	Gaussian	40	Round
PSF branch	Round	Gaussian	100	Elliptical

Simulations

The simulation creation technique is not the only similarity between GREAT08 and FLASHES. We create images containing 10 000 galaxies on a grid, with a pair-wise match of intrinsic ellipticities in the case of elliptical galaxies. And just as in GREAT08, each galaxy is created by i) simulating a lensing distorted (elliptical) galaxy; ii) convolving it with a PSF; iii) binning the light to create a pixellised image; iv) applying a noise model. However, since this is not a challenge but an investigation into the behaviour of our pipeline, we choose different observational conditions to GREAT08 and generally the S/N is kept high. An overview of the 8 branches of FLASHES is shown in Table 2.3. All galaxies are approximated as single-component Sérsic intensity profiles (rather than the bulge-plus-disk description of GREAT08), with the fiducial profile being a circular Gaussian, i.e. an intensity profile with Sérsic index $n = 0.5$. For one branch this index is set to $n = 1$ instead, corresponding to an exponential profile, and in another the index is $n = 4$, creating a de Vaucouleur profile. For the branch with intrinsic ellipticities we pick random ellipticities from the distribution in COSMOS and to minimise shape noise we use the paired rotation technique as described in the previous section. We do not, however, include any intrinsic flexion in these simulations. While we allow the lensing distortion to vary between images, it is kept constant for all galaxies across a single image. The strength of the shear and flexion fields are picked randomly but we ensure that the value never exceeds $|\gamma_{1,2}| \leq 0.05$, $|\mathcal{F}_{1,2}| \leq 0.008$ pixel^{-1} and $|\mathcal{G}_{1,2}| \leq 0.02$ pixel^{-1}.

Once a lensing distorted galaxy model has been created we convolve it with a PSF which is described by a Moffat profile with an index $m = 9$, making it nearly Gaussian. This PSF is circular in general, except for one branch where it is elliptical in the horizontal direction with $e_{1,\mathrm{PSF}} = 0.02$. As these simulations are intended to mimic COSMOS data, the size of the PSF is fairly small with a full width at half maximum (FWHM) of 2.1 pixels, resulting in a PSF convolved galaxy size of 5.8 pixels. Finally we use the definition of $\mathrm{S/N}_{\mathrm{obs}}$ from the previous section to define the four S/N branches. Most of the tests are carried out under near-perfect noise conditions to highlight any noise-independent biases, but the lower S/N branches have the function of showing the impact of noise on shape measurement accuracy. The lowest S/N = 8 branch shows the bias below the S/N = 10 cut we generally apply when using real data.

Results

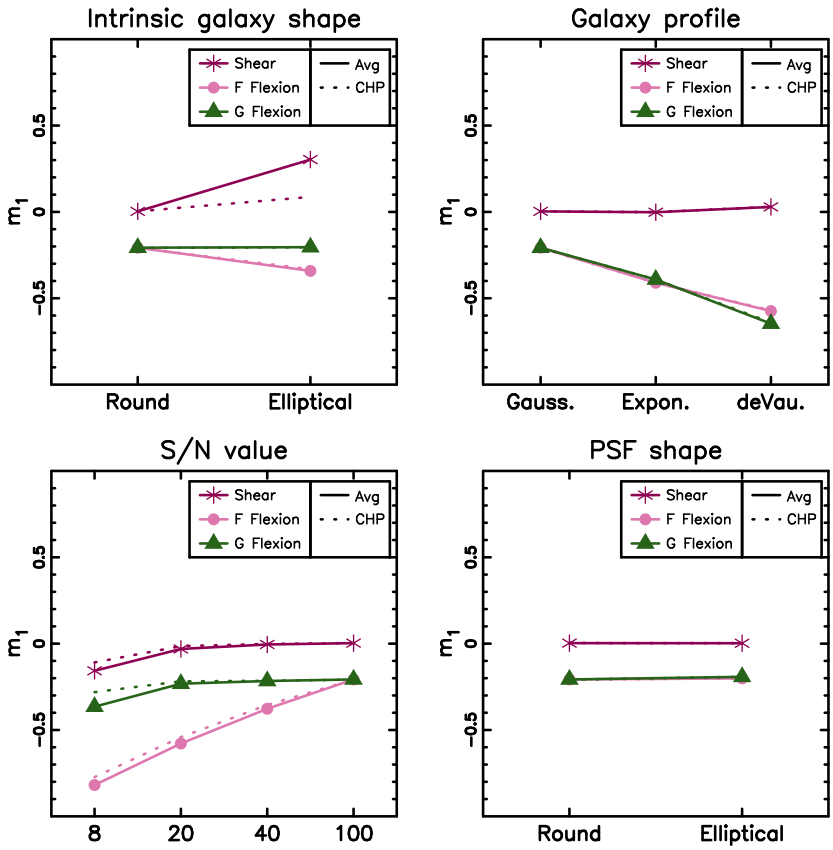

Figure 2.5 The multiplicative bias m on the first component for each of shear, F flexion and G flexion. The purple stars, pink circles and green triangles represent shear, F flexion and G flexion respectively. The symbols and solid lines show the weighted averages while the dashed lines show the CHP average. This is from running the MV pipeline on FLASHES with $n_{\max} = 10$.

The version of the MV pipeline tested on FLASHES is the same as that tested in GREAT08, with one minor difference; since the galaxies are in general better resolved we use a maximum Shapelets order of $n_{\max} = 10$. The galaxy shapes in each image are averaged using two separate methods: CHP as in GREAT08, and a weighted average with weights inversely proportional to the measurement errors. To quantify the performance we use the m and c parameters from STEP only rather than calculating a Q-value, or equivalent for flexion. The results for m_1 and c_1 are shown in Figures 2.5 and 2.6 respectively, and the fitted biases are detailed in Table 2.4. The biases and their trends are all very similar for the second component and so we choose not to show them here. It is clear from this that though the shear can be recovered with an accuracy of a few per cent in general, the flexions are likely to be underestimated. This is particularly true for higher Sérsic indices and noisier data. The dependence on galaxy brightness profile is most likely an effect of the fact that Shapelets consists of Gauss-

Table 2.4 First component multiplicative and additive biases in the MV pipeline based on FLASHES. The top, middle and bottom tables show the shear, F flexion and G flexion results respectively. Both results using a weighted average (superscript avg) and convex hull peeling (superscript CHP) are displayed. For details on the branches, see Table 2.3.

	Shear			
	$m_{1,\gamma}^{\mathrm{avg}}$ $(\times 10^{-2})$	$c_{1,\gamma}^{\mathrm{avg}}$ $(\times 10^{-4})$	$m_{1,\gamma}^{\mathrm{CHP}}$ $(\times 10^{-2})$	$c_{1,\gamma}^{\mathrm{CHP}}$ $(\times 10^{-4})$
Fiducial	0.29 ± 0.10	1.75 ± 0.11	0.33 ± 0.10	1.80 ± 0.11
Shape branch	30.31 ± 0.10	-2.52 ± 5.11	8.68 ± 0.13	-0.96 ± 5.11
Profile branch 1	-0.16 ± 0.06	-6.85 ± 0.12	-0.10 ± 0.06	-6.75 ± 0.12
Profile branch 2	2.92 ± 0.30	-3.39 ± 1.70	2.95 ± 0.32	-2.68 ± 1.70
S/N branch 1	-15.73 ± 0.15	1.02 ± 1.86	-10.86 ± 0.10	6.09 ± 1.86
S/N branch 2	-3.05 ± 0.09	2.15 ± 0.59	-1.44 ± 0.10	2.81 ± 0.59
S/N branch 3	-0.51 ± 0.09	4.87 ± 0.32	-0.15 ± 0.09	5.01 ± 0.32
PSF branch	0.25 ± 0.07	3.36 ± 0.11	0.31 ± 0.07	3.38 ± 0.11

	F flexion			
	$m_{1,\mathcal{F}}^{\mathrm{avg}}$ $(\times 10^{-2})$	$c_{1,\mathcal{F}}^{\mathrm{avg}}$ $(\times 10^{-4})$	$m_{1,\mathcal{F}}^{\mathrm{CHP}}$ $(\times 10^{-2})$	$c_{1,\mathcal{F}}^{\mathrm{CHP}}$ $(\times 10^{-4})$
Fiducial	-20.70 ± 0.05	4.83 ± 0.00	-20.84 ± 0.05	4.85 ± 0.00
Shape branch	-34.15 ± 0.03	1.12 ± 0.00	-33.16 ± 0.03	1.18 ± 0.00
Profile branch 1	-41.00 ± 0.01	-2.24 ± 0.00	-41.06 ± 0.01	-2.24 ± 0.00
Profile branch 2	-57.41 ± 0.03	-2.99 ± 0.00	-57.00 ± 0.04	-2.95 ± 0.00
S/N branch 1	-81.87 ± 0.02	1.41 ± 0.03	-77.27 ± 0.03	2.14 ± 0.03
S/N branch 2	-57.83 ± 0.02	2.84 ± 0.01	-54.16 ± 0.02	3.22 ± 0.01
S/N branch 3	-37.69 ± 0.04	3.16 ± 0.00	-35.51 ± 0.04	3.29 ± 0.00
PSF branch	-20.13 ± 0.03	4.52 ± 0.00	-20.03 ± 0.03	4.51 ± 0.00

	G flexion			
	$m_{1,\mathcal{G}}^{\mathrm{avg}}$ $(\times 10^{-2})$	$c_{1,\mathcal{G}}^{\mathrm{avg}}$ $(\times 10^{-4})$	$m_{1,\mathcal{G}}^{\mathrm{CHP}}$ $(\times 10^{-2})$	$c_{1,\mathcal{G}}^{\mathrm{CHP}}$ $(\times 10^{-4})$
Fiducial	-20.73 ± 0.04	-7.48 ± 0.00	-20.81 ± 0.04	-7.41 ± 0.00
Shape branch	-20.40 ± 0.04	-2.18 ± 0.00	-20.47 ± 0.04	-2.20 ± 0.00
Profile branch 1	-39.17 ± 0.03	0.09 ± 0.00	-39.16 ± 0.03	0.06 ± 0.00
Profile branch 2	-64.68 ± 0.15	3.78 ± 0.01	-64.03 ± 0.17	4.29 ± 0.01
S/N branch 1	-36.52 ± 0.08	-7.77 ± 0.24	-28.07 ± 0.11	-8.71 ± 0.24
S/N branch 2	-23.22 ± 0.03	-6.90 ± 0.03	-21.80 ± 0.03	-7.43 ± 0.03
S/N branch 3	-21.62 ± 0.04	-7.88 ± 0.01	-21.51 ± 0.04	-7.88 ± 0.01
PSF branch	-19.21 ± 0.03	-8.37 ± 0.00	-19.22 ± 0.04	-8.47 ± 0.00

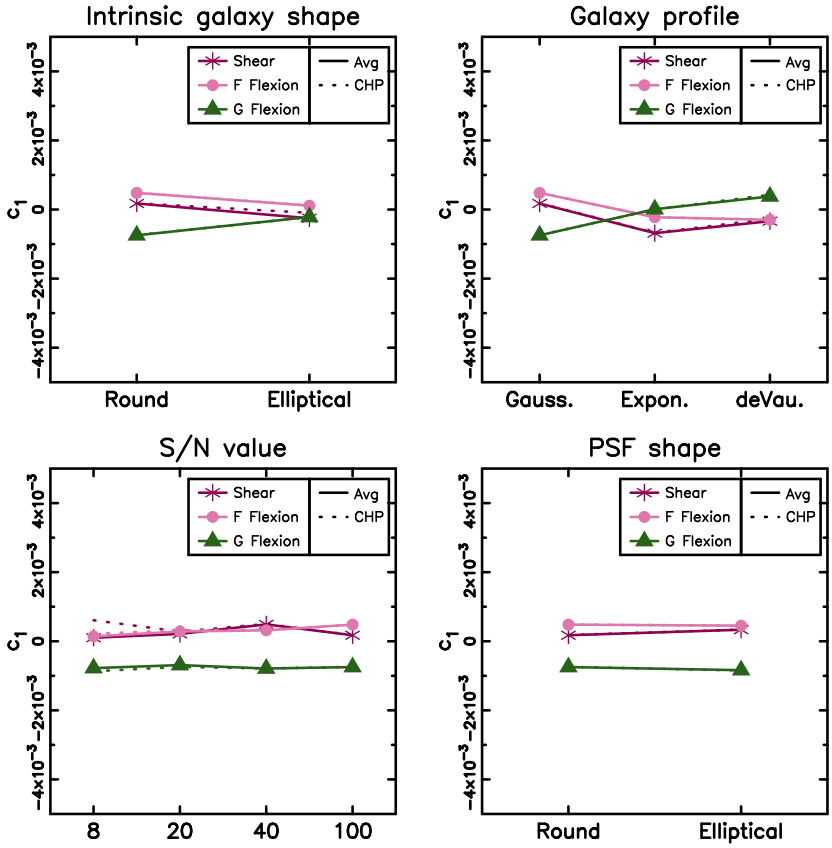

Figure 2.6 The additive bias c on the first component for each of shear, F flexion and G flexion. The purple stars, pink circles and green triangles represent shear, F flexion and G flexion respectively. The symbols and solid lines show the weighted averages while the dashed lines show the CHP average. This is from running the MV pipeline on FLASHES with $n_{\max} = 10$.

Hermite basis functions so it will be optimised for profiles similar to Gaussian profiles. As the Sérsic index increases, the central peak becomes sharper and any skewness (e.g. F flexion) may get more affected by the diluting effect of the PSF, effectively drowning out the F flexion signal. Additionally the wings of the profile reach further which means that very high order Shapelets are required to model them. However, a maximum Shapelets order of $n_{\max} = 10$ necessitates the fitting of 66 free parameters during the galaxy image decomposition stage, and a typical galaxy in these simulations only covers an area of ~ 80 pixels. Including much higher orders than already done will therefore entail fitting noise, and so we keep our maximum Shapelets order at 10. The consequence is that some information in the outer wings is not modelled, and this in turn leads to an underestimation of the flexions for higher Sérsic indices. The G flexion also displays a non-negligible systematic offset c for galaxies with fiducial Gaussian profiles, which may be a sign that this particular combination of galaxy brightness and PSF profiles causes a spurious G flexion signal.

The F flexion is more sensitive to noise than shear or G flexion, as is evident from the lower left panel of Figure 2.5. While shear and G flexion show more bias for the lowest S/N value of 8, a dataset which would be deemed too noisy in an analysis of real data, than for other values, the F flexion shows a trend of greater underestimation even for reasonably high S/N galaxies. A S/N cut is therefore essential, but for F flexion a more sophisticated treatment is necessary to calibrate the measurements. FLASHES have been designed to test the performance of the MV pipeline under COSMOS-like observing conditions. We use our findings to correct for any effects due to noise biases in our analysis of the COSMOS survey (see Chapter 3). It should be noted, however, that as of yet too little is known about potential biases under different observing conditions, so calibrating shape measurements in any other survey based on FLASHES alone is not recommended.

2.4 Non-monochromatic tests

As made clear, the PSF of a telescope will, if left uncorrected for, bias galaxy shape measurements. For a broad-band filter, such as the one included in the design of the future space-based mission Euclid, additional complications arise from the fact that the PSF usually depends on wavelength. Hence, since the colour generally varies across a galaxy, which is likely to have a redder central bulge and a bluer disk, the PSF will as well. We therefore have to determine how galaxy colour gradients affect our ability to recover the true lensing distortions, represented by shear in this Section.

2.4.1 Analytical prediction

To assess the possibility to correct for the effect of a colour-dependent PSF, we describe the observed intensity, $I^{\rm obs}(\boldsymbol{\theta})$, of a galaxy image observed in a filter of finite bandwidth as an integral over wavelength:

$$I^{\rm obs}(\boldsymbol{\theta}) = \int d\lambda\, I^{\rm obs}(\boldsymbol{\theta},\lambda) \tag{2.26}$$

$$= \int d\lambda\, I^{0}(\boldsymbol{\theta},\lambda) \otimes T(\boldsymbol{\theta},\lambda) \tag{2.27}$$

where we have made explicit that the observed intensity is the pre-seeing intensity $I^0(\boldsymbol{\theta},\lambda)$ viewed through an imaging system with a PSF $T(\boldsymbol{\theta},\lambda)$. For a broad filter, the observed centroid is

$$\bar{\theta}_i \equiv \frac{1}{F_{\rm tot}} \int d\lambda \int d\boldsymbol{\theta}\; \theta_i I^{\rm obs}(\boldsymbol{\theta},\lambda) \tag{2.28}$$

$$= \frac{1}{F_{\rm tot}} \int d\lambda \int d\boldsymbol{\theta} \int d\boldsymbol{\varphi}\; \theta_i I^{0}(\boldsymbol{\varphi},\lambda) T(\boldsymbol{\theta}-\boldsymbol{\varphi},\lambda) \tag{2.29}$$

where $F_{\rm tot}$ is the total flux. By employing a change in variable, $\mathbf{x} = \boldsymbol{\theta} - \boldsymbol{\varphi}$, we can derive the following expression:

$$\bar{\theta}_i = \frac{1}{F_{\rm tot}} \int d\lambda \int d\boldsymbol{\theta} \int d\mathbf{x}\; \left[I^{0}(\boldsymbol{\theta},\lambda)\varphi_i T(\mathbf{x},\lambda) + I^{0}(\boldsymbol{\theta},\lambda) x_i T(\mathbf{x},\lambda)\right] \tag{2.30}$$

$$= \frac{1}{F_{\rm tot}} \int d\lambda\; \left[\theta_i(\lambda) F(\lambda) + F(\lambda) p_i(\lambda) T(\lambda)\right] \tag{2.31}$$

where, for a given wavelength λ, $F(\lambda)$ is the total flux, $\theta_i(\lambda)$ is the centroid, $p_i(\lambda)$ are the first-order moments of the PSF and $T(\lambda) = \int d\boldsymbol{\theta}\ T(\boldsymbol{\theta}, \lambda)$. For a symmetric PSF the term $\int d\mathbf{x}\ I^0(\boldsymbol{\theta}, \lambda) x_i T(\mathbf{x}, \lambda)$ will vanish; for more complicated PSFs (such as imaging affected by coma) the term may be evaluated if the PSF moments are known.

Assuming that the centroids for all wavelengths coincide for each galaxy, we can estimate the pre-seeing centroid using Equation 2.31. We therefore continue our analysis using centred moments. The second-order unweighted moments of the pre-seeing and post-seeing intensities, Q^0_{ij} and $Q^{\rm obs}_{ij}$, and of the PSF, P_{ij}, are defined as

$$
\begin{aligned}
Q^0_{ij} &= \frac{1}{F_{\rm tot}} \int d\lambda \int d\boldsymbol{\theta}\ \theta_i \theta_j I^0(\boldsymbol{\theta}, \lambda) && (2.32)\\
Q^{\rm obs}_{ij} &= \frac{1}{F_{\rm tot}} \int d\lambda \int d\boldsymbol{\theta}\ \theta_i \theta_j I^{\rm obs}(\boldsymbol{\theta}, \lambda) && (2.33)\\
&= \frac{1}{F_{\rm tot}} \int d\lambda \int d\boldsymbol{\theta}\ \theta_i \theta_j \int d\boldsymbol{\varphi}\ I^0(\boldsymbol{\varphi}, \lambda) T(\boldsymbol{\theta} - \boldsymbol{\varphi}, \lambda) && (2.34)\\
P_{ij}(\lambda) &= \frac{1}{T(\lambda)} \int d\boldsymbol{\theta}\ \theta_i \theta_j T(\boldsymbol{\theta}, \lambda) && (2.35)
\end{aligned}
$$

Using the same substitution as above we can rewrite Equation 2.34 as

$$
Q^{\rm obs}_{ij} = \frac{1}{F_{\rm tot}} \int d\lambda \int d\boldsymbol{\varphi}\ I^0(\boldsymbol{\varphi}, \lambda) \int d\mathbf{x}\ T(\mathbf{x}, \lambda)(x_i x_j + \varphi_i \varphi_j + x_i \varphi_j + \varphi_i x_j) \tag{2.36}
$$

The two latter terms can be eliminated since the centroid of the pre-seeing galaxy is assumed to be independent of wavelength. We then have

$$
\begin{aligned}
Q^{\rm obs}_{ij} &= \frac{1}{F_{\rm tot}} \int d\lambda \left[\int d\boldsymbol{\varphi}\ I^0(\boldsymbol{\varphi}, \lambda) \int d\mathbf{x}\ T(\mathbf{x}, \lambda) x_i x_j \right.\\
&\qquad \left. + \int d\boldsymbol{\varphi}\ I^0(\boldsymbol{\varphi}, \lambda) \varphi_i \varphi_j \int d\mathbf{x}\ T(\mathbf{x}, \lambda) \right] && (2.37)
\end{aligned}
$$

which may be rewritten as before:

$$
Q^{\rm obs}_{ij} = \frac{1}{F_{\rm tot}} \int d\lambda\ \left[F(\lambda) P_{ij}(\lambda) T(\lambda) + Q^0_{ij}(\lambda) F(\lambda) T(\lambda) \right] \tag{2.38}
$$

i.e.

$$
Q^0_{ij} = Q^{\rm obs}_{ij} - \frac{1}{F_{\rm tot}} \int d\lambda\ T(\lambda) F(\lambda) P_{ij}(\lambda) \tag{2.39}
$$

Equation 2.39 shows that to measure second-order unweighted moments, and thus shear, we only need to know $F(\lambda)$ and $P_{ij}(\lambda)$. Assuming accurate knowledge of $F(\lambda)$, we conclude that for a perfect shape measurement method colour gradient will not cause systematic errors to dominate the error budget. However, using unweighted moments to estimate shear is not possible due to noise. Methods in use today use either weighted moments or a fitting procedure such as Shapelets, and both techniques are equivalent to a weighting scheme.

Now, assuming that we know the effective PSF, a valid assumption according to Cypriano et al. (2010), we may use the wavelength-integrated image $I^{\rm obs}(\boldsymbol{\theta})$ to derive an estimate of the pre-seeing image $I^{\rm est}(\boldsymbol{\theta})$:

$$
I^{\rm obs}(\boldsymbol{\theta}) = I^{\rm est}(\boldsymbol{\theta}) \otimes \int d\lambda\ F(\lambda) T(\boldsymbol{\theta}, \lambda) \tag{2.40}
$$

where as above, $F(\lambda)$ is the flux of the galaxy at a given wavelength and $I^{\rm est}(\boldsymbol{\theta})$ is not necessarily equal to $I^0(\boldsymbol{\theta}, \lambda)$. In the general case there will therefore be a bias since we will not have enough information to reconstruct $I^0(\boldsymbol{\theta}, \lambda)$, even with perfect knowledge of $T(\boldsymbol{\theta}, \lambda)$ and $I^{\rm obs}(\boldsymbol{\theta})$. To quantify this discrepancy we create simulations to mimic galaxies with colour gradients as observed through a broad-band filter.

2.4.2 Simulations

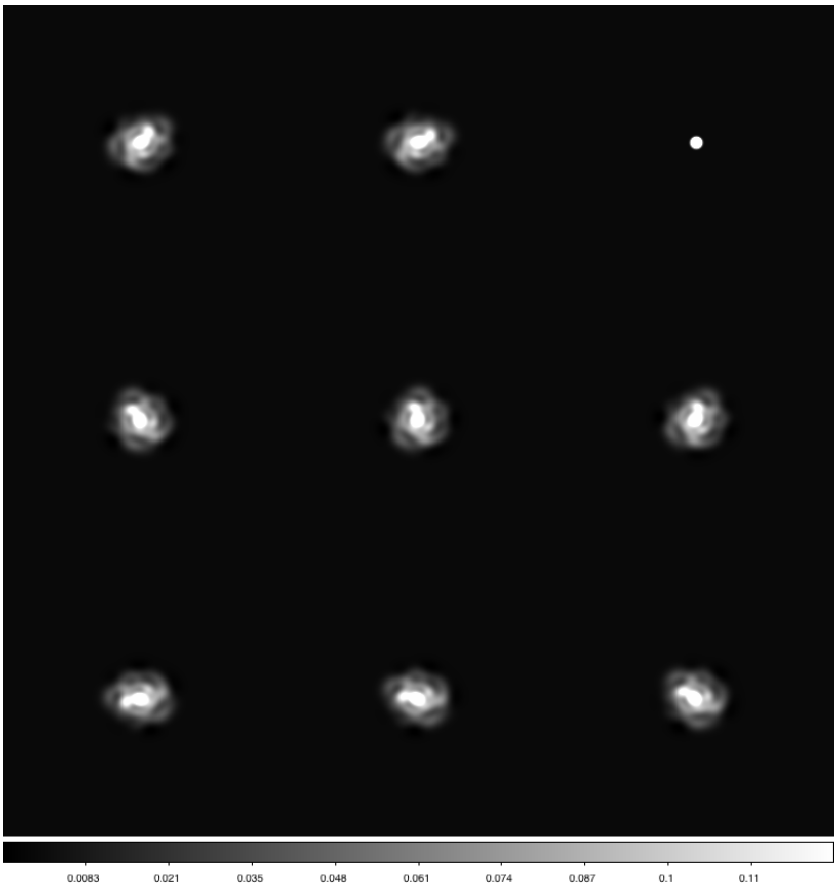

Figure 2.7 Simulated image representative of the simulations created for each galaxy in our sample. There are 8 identical galaxy images rotated in equal steps of 22.5° before a shear has been applied. In the top right corner is a star image representing the PSF.

The simulations we create to assess the impact of colour gradients on shape measurement consist of nearly 20 000 real galaxies taken from the All-Wavelength Extended Groth Strip International Survey (AEGIS; Davis et al., 2007) imaged with the Advanced Camera for Surveys (ACS) onboard the Hubble Space Telescope (HST). Our specific aim here is to evaluate the significance of this bias for Euclid, and the planned diffraction limit of this future telescope is twice the size

of the HST limit. We therefore use only AEGIS galaxies that are well resolved and can thus disregard the small effect of the HST PSF on the images.

Each galaxy has been observed in both the F606W (V-band) and the F814W (I-band) filters, and in general both the size and the flux of a galaxy will be greater in the redder band due in part to morphology and in part to telescope optics. We also have access to photometric redshifts for 11260 objects via the overlap with CFHTLS-Deep3 which gives us the ability to evaluate the bias as a function of redshift. This is in fact an important aspect of our tests because as they evolve, galaxies change morphologies and therefore their colour gradients. Our simulations then consist of a series of images with each one corresponding to a single AEGIS galaxy, as exemplified in Figure 2.7. In order to minimise noise in our simulations we choose not to use the galaxy image directly, but we decompose the observed AEGIS galaxy in each band into Shapelets. This Shapelets representation is then duplicated and rotated to create eight identical galaxy models with different orientations. The differing orientations of the galaxy images allows us to perform a 'ring test' which reduces the noise generated by the intrinsic galaxy morphology. After rotating, the same shear is applied to each galaxy realisation before we convolve them with a PSF and add them to the simulated image using a pixel-scale of 0.05 arcsec. To ensure that their brightness distributions do not overlap we place the galaxies at set positions on the image. A representation of the PSF acting on a point source (a 'star') with the same flux as the galaxy is also inserted in each image of eight galaxy realisations. This allows for the shape measurement software to be run as it normally would be on real survey images.

The shear we apply to our simulated galaxies is relatively large compared to the other simulation sets described in this Chapter, but still well within the weak lensing regime at $\gamma_1 = 0.05$, $\gamma_2 = 0.00$. A subtlety of our approach is that since we use real objects as a basis for our simulations, the original galaxies have already been sheared by foreground structure which results in a slightly different response compared to the true intrinsic galaxy. This effect is small however and will not significantly impact our ability to quantify the bias induced by colour gradients.

To simulate a broad-band Euclid-like PSF, we approximate a diffraction-limited Airy disk using a Gaussian profile with a frequency dependent FWHM. The FWHM is chosen to be $\mathrm{FWHM}_{\mathrm{PSF}}^{F606W} = 0.17$ arcsec for the bluer filter and $\mathrm{FWHM}_{\mathrm{PSF}}^{F814W} = 0.21$ arcsec for the redder one, though we note that the Eculid PSF has extended wings and may therefore effectively be slightly larger. We convolve the galaxy image in the red filter with the red PSF, and similarly for blue. Combining the two as described below results in a total PSF which is the weighted mean of the blue and red PSFs, and which thus has a different response depending on wavelength.

We now have eight sheared and PSF-convolved realisations for each galaxy combined into a single image for each of two narrow filters. To simulate a broad filter similar to the one proposed for Euclid, we stack the two narrow-band images by adding them:

$$I^{\mathrm{obs}}(\boldsymbol{\theta}) = I^{\mathrm{obs},F606W}(\boldsymbol{\theta}) + I^{\mathrm{obs},F814W}(\boldsymbol{\theta}) \quad (2.41)$$

$$= I^{0,F606W}(\boldsymbol{\theta}) \otimes T^{F606W}(\boldsymbol{\theta}) + I^{0,F814W}(\boldsymbol{\theta}) \otimes T^{F814W}(\boldsymbol{\theta}) \quad (2.42)$$

The wavelength-dependent PSF is thus approximated as the sum of two Gaus-

sian profiles of different width:

$$T(\boldsymbol{\theta}, \lambda) \simeq \frac{1}{F_{\rm tot}} \left[F^{F606W} T^{F606W}(\boldsymbol{\theta}) + F^{F814W} T^{F814W}(\boldsymbol{\theta}) \right] \tag{2.43}$$

Since we do not have access to a perfect shape measurement method and thus expect a bias even without colour gradients, we have to quantify the bias associated with the method itself. To this end we create two control images for each set of galaxy realisations. The control images consist of galaxies that have no colour gradient, but that are subjected to the same PSF as the Euclid-like simulations above. Comparing our results on the broad-band simulations to these control images will convey the *additional* bias induced through the assumption of monochromaticity. We thus first convolve the F606W galaxy image with a Gaussian PSF of the same width as the F814W simulation, and vice versa:

$$I^{\rm obs,1}(\boldsymbol{\theta}) = I^{0,F606W}(\boldsymbol{\theta}) \otimes T^{F814W}(\boldsymbol{\theta}) \tag{2.44}$$

$$I^{\rm obs,2}(\boldsymbol{\theta}) = I^{0,F814W}(\boldsymbol{\theta}) \otimes T^{F606W}(\boldsymbol{\theta}) \tag{2.45}$$

To account for the normalisations of the PSFs, we ensure that the control images are created using the appropriate proportions:

$$I^{{\rm ctrl},F606W}(\boldsymbol{\theta}) = I^{{\rm obs},F606W}(\boldsymbol{\theta}) + \frac{F^{F814W}}{F^{F606W}} I^{\rm obs,1}(\boldsymbol{\theta}) \tag{2.46}$$

$$I^{{\rm ctrl},F814W}(\boldsymbol{\theta}) = I^{{\rm obs},F814W}(\boldsymbol{\theta}) + \frac{F^{F606W}}{F^{F814W}} I^{\rm obs,2}(\boldsymbol{\theta}) \tag{2.47}$$

$I^{{\rm ctrl},F606W}$ is thus a galaxy with no colour gradient, but with the intensity distribution observed in F606W and convolved with our approximate Euclid PSF, and similarly for $I^{{\rm ctrl},F814W}$. As mentioned above, the important feature of these two control images is that they both have the same PSF as our broad-band simulation. This is crucial because we have to compare images with identical PSFs in order to avoid introducing another source of bias discrepancy between filters.

We note here that our approach does entail a simplification of the problem since we base our simulations on galaxies observed in two filters which are themselves fairly broad. One of our assumptions is therefore that the colour of a galaxy in one filter is that of the central wavelength, and that the spectral energy distribution (SED) can be approximated through an interpolation between the two filters. Ideally we would use data from several narrower filters, but we do find via analytical tests that this assumption does not impact our knowledge of the bias significantly.

2.4.3 Results

We use the MV pipeline to estimate the shear in both the control images and in the stacked simulated broad-band image. Since we do not have access to a perfect shape measurement method, we want to minimise the bias inherent in the method itself. Our simulations are created with Shapelets, and therefore a Shapelets shear measurement pipeline should be the optimal technique for analysing these images. However, because the PSF consists of two stacked

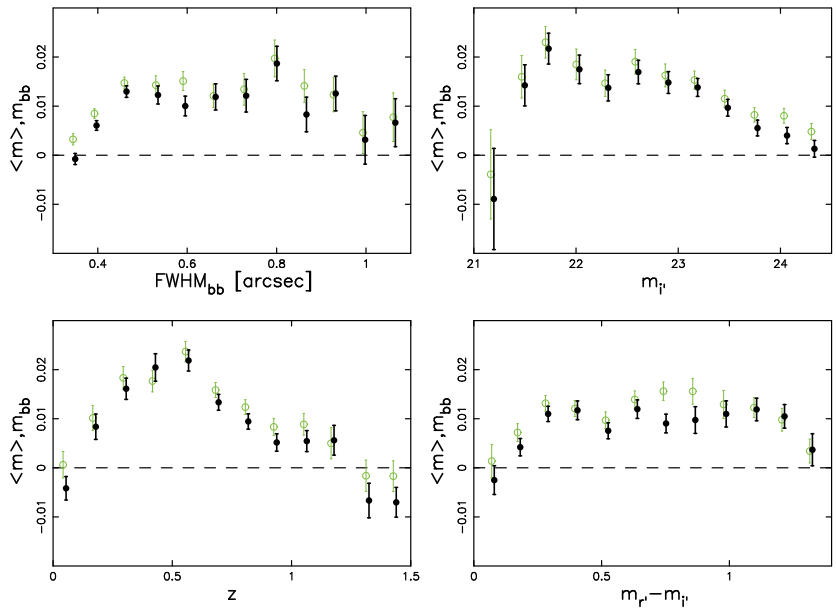

Figure 2.8 Bias measured in the non-monochromatic simulations as a function of different galaxy parameters. Filled black points represent the average multiplicative bias $\langle m \rangle = 0.5(m_{606} + m_{814})$ determined in the narrow-band filters, while open green points represent the bias measured in the Euclid-like stack, m_{bb}. $\mathrm{FWHM_{bb}}$ is the size measured in the stack, and the magnitude and redshift data are obtained via CFHTLS-Deep3.

Gaussian profiles of different widths the resulting simulation is no longer as ideal and thus there will still be a bias present. The control images are therefore vital in determining which bias is due to limitations of the shape measurement method, and which is due to galaxy colour gradients and PSF wavelength dependence.

We determine the multiplicative bias by obtaining the mean shear in each bin, dividing it by the input shear and subtracting 1 such that a perfectly recovered shear would result in $m_{\mathrm{aeg}} = 0$:

$$m_{\mathrm{aeg,bin}} = \frac{\langle \gamma_{1,\mathrm{bin}} \rangle}{\gamma_{1,\mathrm{in}}} - 1 \tag{2.48}$$

where we are only considering the first shear component as the second component has been set to zero at input. The bias we measure in these simulations, as shown in Figure 2.8, is in general positive since the galaxies are very high S/N and the MV pipeline is optimised for images with lower S/N. In the top two panels of Figure 2.8 we display the average bias determined in each filter F606W and F814W, and that measured in the broad-band simulations, as a function of galaxy size and CFHTLS i'-band magnitude. We see that the bias measured initially increases as galaxies become bigger and brighter, and the trend then plateaus. In the lower panel the bias is shown as a function of photometric redshift and colour.

The biases measured in each band only carries information about the partic-

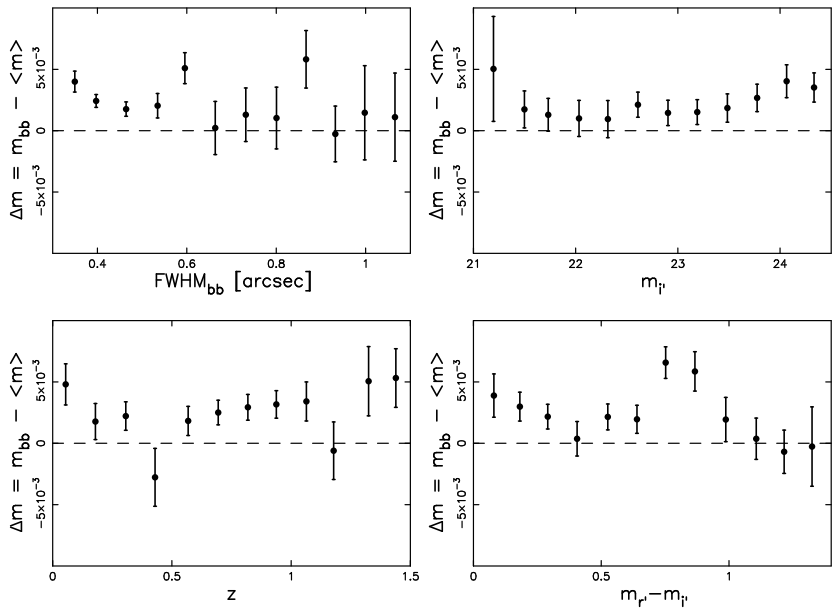

Figure 2.9 Difference between the multiplicative bias measured in the simulated stack, $m_{\rm bb}$, and that measured in the narrow-band filters on average, $\langle m \rangle = 0.5(m_{606} + m_{814})$, as a function of different galaxy parameters. $\mathrm{FWHM_{bb}}$ is the size measured in the stack, and the magnitude and redshift data are obtained via CFHTLS-Deep3.

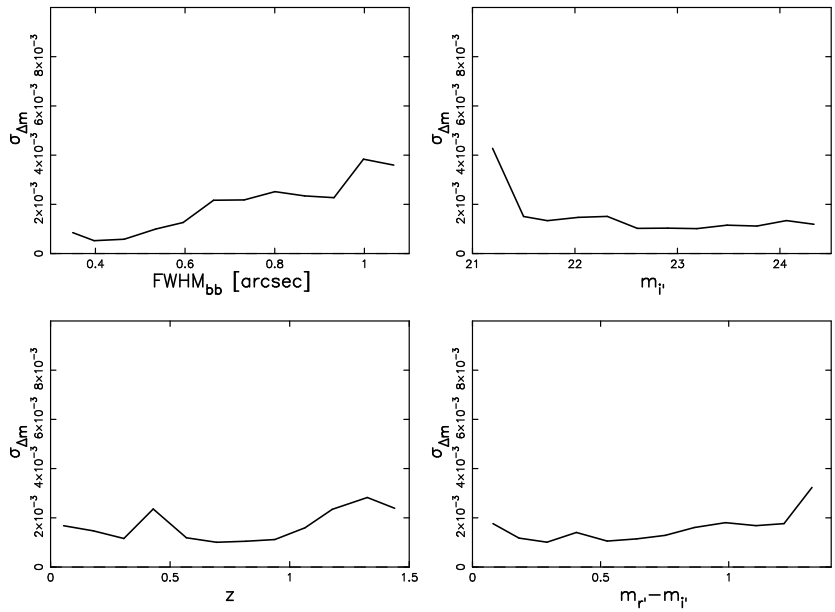

Figure 2.10 Error on the multiplicative bias difference between the simulated stack and the narrow-band images, as a function of galaxy properties.

ular shape measurement method used (the MV pipeline in this case). It is encouraging that the accuracy of the shear measurements is at percent level, but to assess the impact of a wavelength-dependent PSF we have to contrast the accuracy in the broad-band filter with that in each individual narrow-band filter. In Figure 2.9 we therefore show the difference in bias $\Delta m = m_{\rm bb} - 0.5(m_{606} + m_{814})$ as a function of the same parameters as before. Though there is a positive signal, indicating a higher bias in the broad-band filter than in the narrower ones, it is consistently sub-percentage in size so it is much smaller than the bias induced by the shape measurement software. There are some trends in the colour gradient bias, particularly as a function of redshift and average colour. These trends will need to be carefully modelled in order to account for this bias in future surveys. It is still complicated to interpret the results, however, since some of the difference in bias could still be explained by the results in individual bands. If for instance the galaxy is smaller when observed in F606W than when observed in the broad-band filter then the bias in the broad-band filter will be greater simply due to the size-dependence of the bias (see Figure 2.8).

The results we have presented here are an indication of what may be expected in terms of the bias induced by a wavelength-dependent PSF. However, the simulations have been created using two filters only and though these filters are narrower than the one proposed for Euclid, the wavelength resolution may still be too low to properly represent the colour gradient in the observed galaxy. We have also used real galaxies which have been sheared before being observed in AEGIS and this causes a small uncertainty in our bias. With more data observed in several narrow bands we will be able to constrain the bias further, but the results displayed here show that the shape measurement bias induced by assuming monochromaticity despite the use of a broad-band and the loss of colour information that entails, is lower than the bias inherent in the shape measurement method. It is also important to note that due to the noisiness of the shape measurements and due to the limited galaxy sample available, the errors on the additional bias (as shown in Figure 2.10) are a good indication of the true errors. Thus we are able to determine the level of bias, given the constraints described above, accurately. By studying the bias in more detail we will therefore most likely be able to correct for this small effect in surveys such as Euclid.

2.5 Conclusion

We have in this Chapter described and tested a new weak lensing shape measurement software suite with the capability of measuring higher order distortions known as flexion, as well as shear: the MV pipeline. Based on the Shapelets formalism, it is a new incarnation and an extension of the software described in Kuijken (2006) with which it was contrasted in the context of the GREAT08 challenge. The GREAT08 simulations provided an ideal testbed for testing the shear recovery accuracy under different observing conditions. The MV pipeline did very well in this challenge in nearly all regimes with very competitive quality factor values of $Q \sim 100$ and above. The exception was very faint and barely resolved galaxies where the S/N was just too low and this resulted in an overall Q-value of $Q \sim 25$.

To test the MV pipeline for the accuracy of the flexion measurements we

created our own simulations which we named FLASHES. These simulations were generated using software very similar to the one used to produce the GREAT08 simulations, but with the important difference of flexion distortions being added to the lensing potential. FLASHES mimic the survey conditions of the space-based COSMOS survey, and were kept generally low-noise to assess any biases induced by other factors. We confirmed that the input shear could be recovered with high accuracy, with a multiplicative bias of a few percent in most cases. The flexions displayed a greater bias in general, and a greater sensitivity to the intrinsic brightness profile of the sources. Additionally, the F flexion in particular showed a trend with S/N which may need to be calibrated in lower-quality data.

While the GREAT08 and FLASHES simulation sets were monochromatic, care is needed in future surveys where the PSF may be wavelength-dependent. If a galaxy with an intrinsic colour gradient, such as a redder core and a bluer disk, is observed through a broad filter with an imaging system which results in such a PSF, then there may be additional shear measurement bias induced. With perfect knowledge of the PSF and the intrinsic colour gradient, this may be corrected for but such perfect knowledge is not feasible for surveys such as Euclid. We therefore created simulations based on real galaxies observed in two bands as part of the HST AEGIS survey. Comparing the bias measured in each narrow-band with that measured in a simulated broad-band, we found that the additional bias induced by the galaxy colour gradient was at most at the percentage level, with some variation with redshift, magnitude, size and overall colour. This additional bias may be partly explained by inherent biases in the MV pipeline but the results indicate that it will be possible to accurately determine the magnitude of this effect and thus correct for it. To get a more precise bias estimate we will in the near future create simulations with more realistic intrinsic colour gradients and observe them through several yet narrower bands.

The MV pipeline has been shown here to be both accurate and versatile. We will in the next Chapter apply it to the real COSMOS survey and measure a flexion signal around galaxies for the first time.

Acknowledgements

This study makes use of data from AEGIS, a multiwavelength sky survey conducted with the Chandra, GALEX, Hubble, Keck, CFHT, MMT, Subaru, Palomar, Spitzer, VLA, and other telescopes and supported in part by the NSF, NASA, and the STFC.

The authors would like to thank Gary Bernstein for valuable input and discussions. MV acknowledges support from the European DUEL Research-Training Network (MRTN-CT-2006-036133) and from the Netherlands Organization for Scientific Research (NWO).

Probing galaxy dark matter haloes in COSMOS with weak lensing flexion

3

Velander M., Kuijken K., Schrabback T., 2011, MNRAS, 412, 2665

Current theories of structure formation predict specific density profiles of galaxy dark matter haloes, and with weak gravitational lensing we can probe these profiles on several scales. On small scales, higher-order shape distortions known as flexion add significant detail to the weak lensing measurements. We present here the first detection of a galaxy-galaxy flexion signal in space-based data, obtained using a new Shapelets pipeline introduced here. We combine this higher-order lensing signal with shear to constrain the average density profile of the galaxy lenses in the Hubble Space Telescope COSMOS survey. We also show that light from nearby bright objects can significantly affect flexion measurements. After correcting for the influence of lens light, we show that the inclusion of flexion provides tighter constraints on density profiles than does shear alone. Finally we find an average density profile consistent with an isothermal sphere.

3.1 Introduction

Weak gravitational lensing is a powerful technique for studying the distribution of matter in the universe due to its ability to model the matter distribution in foreground structures, independent of the nature of the matter present. As the light from background sources is bent around foreground lenses, the galaxy images get distorted by the tidal gravitational field. The first-order distortion is known as shear and is essentially an elongation of the image causing the source galaxy to appear stretched in one direction. This type of distortion measurement has been used in a wide variety of cosmological studies ranging from modeling the large-scale structure using cosmic shear (see e.g. Van Waerbeke & Mellier, 2003; Hoekstra & Jain, 2008; Munshi et al., 2008, for reviews) to determining galaxy halo shapes using galaxy-galaxy lensing (Hoekstra et al., 2004; Mandelbaum et al., 2006a; Parker et al., 2007).

First described by Goldberg & Natarajan (2002), the second-order distortion is a relatively new addition which has since been named flexion (Goldberg & Bacon, 2005; Bacon et al., 2006). There are two types of flexion relevant to weak lensing studies: the first flexion induces a skewness of the brightness profile whilst the second flexion is a three-pronged distortion. In combination with shear, these distortions cause the well-known banana shape of lensed source images. As flexion is effectively the gradient of shear, it is sensitive on small scales. This makes it an important complement to shear which is sensitive on relatively large scales only. By virtue of this, and of the orthogonality of the three measurements, flexion is highly beneficial to investigations of the inner profiles of dark matter haloes, where baryons become important, and to the detection of substructure in cluster haloes. Indeed, it was recently shown (Er et al., 2010) that mass reconstructions profit from the use of flexions in combination with shear, and flexion has already been used to constrain the halo mass distribution and to detect substructure in clusters of galaxies (Leonard et al., 2011; Okura et al., 2008). To provide more information on substructure and mass profiles, there are currently new statistical flexion tools being developed (eg. Leonard et al., 2009; Leonard & King, 2010; Bacon et al., 2010). Another application, as discussed in Hawken & Bridle (2009), is to use both flexions in combination with shear to significantly tighten the constraints on galaxy halo ellipticities compared to using shear alone.

The shape measurement technique known as Shapelets (Refregier, 2003; Refregier & Bacon, 2003) works by decomposing a galaxy image into a series of 2D Hermite polynomials. These provide a simple framework for describing the main galaxy image distortion operators, such as shear and flexion, and the convolution with the point-spread function (PSF). Due to the flexible treatment of the PSF, the Shapelets formalism has an advantage over the currently most widely used shape measurement method, KSB (from Kaiser, Squires, & Broadhurst, 1995), since KSB uses an idealised model for the PSF whilst Shapelets is more versatile. The KSB equivalent for flexion is known as HOLICs (Okura et al., 2007).

Since the field of weak lensing is relatively new, lensing measurements are continuously being improved in accuracy and applicability. Being a statistical technique, however, the accuracy of the weak lensing results depends heavily on the amount of data available. Galaxy-galaxy flexion has been tentatively

observed (Goldberg & Bacon, 2005) using the ground-based Deep Lens Survey (DLS), but to further investigate galaxy-size haloes more and better data is needed. With large surveys such as the Canada-France-Hawaii Telescope Legacy Survey (CFHTLS) and the Red Sequence Cluster Surveys (RCS, RCS2) available, and new surveys like the 1500 square degree Kilo-Degree Survey (KiDS) imminent, the future looks bright. However, a space-based data set provides better resolution and such a data set is already accessible to us: the HST COSMOS survey. Using this data we will in this Chapter improve on the galaxy-galaxy flexion measurements of Goldberg & Bacon (2005).

This Chapter is organised as follows: in Section 3.2 we review the formalism for shear and flexion, whilst we review the Shapelets method in Section 3.3 with a description of our implementation (dubbed the MV pipeline) in Section 3.3.1. In Section 3.4 we test the MV pipeline on simulations and in Section 3.5 the pipeline is applied to data from the COSMOS survey. We conclude in Section 3.6.

Throughout this Chapter we assume the following cosmology (WMAP7; Komatsu et al., 2010):
$(\Omega_M, \Omega_\Lambda, h, \sigma_8, w) = (0.27, 0.73, 0.70, 0.81, -1)$

3.2 Shear and flexion

We begin by briefly reviewing the weak lensing formalism. Flexion is a second-order lensing effect first introduced by Goldberg & Bacon (2005) and further developed by Bacon et al. (2006) (hereafter B06). It arises from the fact that convergence and shear are not constant across a source image, and can be used to describe how these fields fluctuate. In the weak lensing regime, the lensed surface brightness of a source galaxy, $f(\mathbf{x})$, is related to the unlensed surface brightness, $f_0(\mathbf{x})$, via

$$f(\mathbf{x}) \simeq \left\{ 1 + \left[(A - I)_{ij} x_j + \frac{1}{2} D_{ijk} x_j x_k \right] \frac{\partial}{\partial x_i} \right\} f_0(\mathbf{x}). \tag{3.1}$$

Here I is the identity matrix, x_i denotes lensed coordinates, and

$$\mathrm{A} = \begin{pmatrix} 1 - \kappa - \gamma_1 & -\gamma_2 \\ -\gamma_2 & 1 - \kappa + \gamma_1 \end{pmatrix} \tag{3.2}$$

with $\kappa = \frac{1}{2}(\psi_{xx} + \psi_{yy})$ a second derivative of the lensing potential ψ, where subscripts denote partial differentiation. $\gamma_1 = \frac{1}{2}(\psi_{xx} - \psi_{yy})$ and $\gamma_2 = \psi_{xy}$ are the two components of the complex shear $\gamma = \gamma_1 + i\gamma_2$. The matrix

$$D_{ijk} = \frac{\partial A_{ij}}{\partial x_k} \tag{3.3}$$

describes how convergence and shear vary across a source image. We can re-express D_{ijk} as the sum of two flexions: $D_{ijk} = \mathcal{F}_{ijk} + \mathcal{G}_{ijk}$. The two flexions, the first flexion $\mathcal{F}$ (known as F flexion or one-flexion) and the second flexion $\mathcal{G}$ (known as G flexion or three-flexion), are the derivatives of the convergence and shear fields. There are four flexion components, each of which may be written in

terms of the third derivatives of the lensing potential (Hawken & Bridle, 2009):

$$\mathcal{F}_1 = \frac{1}{2}(\psi_{xxx} + \psi_{yyx}) \tag{3.4}$$

$$\mathcal{F}_2 = \frac{1}{2}(\psi_{xxy} + \psi_{yyy}) \tag{3.5}$$

$$\mathcal{G}_1 = \frac{1}{2}(\psi_{xxx} - 3\psi_{xyy}) \tag{3.6}$$

$$\mathcal{G}_2 = \frac{1}{2}(3\psi_{xxy} - \psi_{yyy}) \tag{3.7}$$

where $\mathcal{F} = \mathcal{F}_1 + i\mathcal{F}_2$ and $\mathcal{G} = \mathcal{G}_1 + i\mathcal{G}_2$ are the complex F and G flexions respectively. The full matrices $\mathcal{F}_{ijk}$ and $\mathcal{G}_{ijk}$ in terms of the four flexion components are written explicitly in B06.

3.3 Shapelets

The Shapelets basis function set was introduced by Refregier (2003) and is more fully described there. In summary, the surface brightness of an object $f(\mathbf{x})$ can be expressed as a sum of orthogonal 2D functions

$$f(\mathbf{x}) = \sum_{a=0}^{\infty}\sum_{b=0}^{\infty} s_{ab} B_{ab}(\mathbf{x};\beta) \tag{3.8}$$

where s_{ab} are the Shapelets coefficients and the Shapelets basis functions $B_{ab}(\mathbf{x};\beta)$ are defined as

$$B_{ab}(\mathbf{x};\beta) = k_{ab}\beta^{-1} e^{-\frac{|\mathbf{x}|^2}{2\beta^2}} H_a(x/\beta) H_b(y/\beta). \tag{3.9}$$

Here k_{ab} is a normalization constant, β is the Shapelets scale radius, (x, y) are coordinates on the image plane and $H_n(x)$ is a Hermite polynomial of order n. The Shapelets basis functions are easily recognised as the energy eigenstates of the 2D Quantum Harmonic Oscillator (QHO). The formalism developed for the QHO can also be applied to Shapelets, providing analytical expressions for transformations such as shear and flexion. In theory, an object can be perfectly described through a decomposition into Shapelets up to order $n \to \infty$ but in practice the expansion has to be truncated. We truncate at combined order $n_{\max} = a + b$ to avoid introducing a preferred direction.

Convolution with the point-spread function (PSF) can also be done analytically in the Shapelets formalism by simply multiplying the Shapelets expansion by a PSF matrix $\mathbf{P}$:

$$\mathbf{P}_{a_1 a_2 b_1 b_2}(\beta_{\rm obj}, \beta_{\rm con}) = \sum_{a_3, b_3} C^{\beta_{\rm con}\beta_{\rm obj}\beta_{\rm psf}}_{a_1 a_2 a_3} C^{\beta_{\rm con}\beta_{\rm obj}\beta_{\rm psf}}_{b_1 b_2 b_3} p_{a_3 b_3} \tag{3.10}$$

where p_{ab} are the Shapelets coefficients of the PSF and $\beta_{\rm psf}$, $\beta_{\rm obj}$ and $\beta_{\rm con}$ are the scale radii of the PSF, the object and the resulting PSF convolved object respectively. $C^{\beta_1\beta_2\beta_3}_{nml}$ is a convolution tensor which depends on the different scale radii and the full expression is given in Refregier (2003).

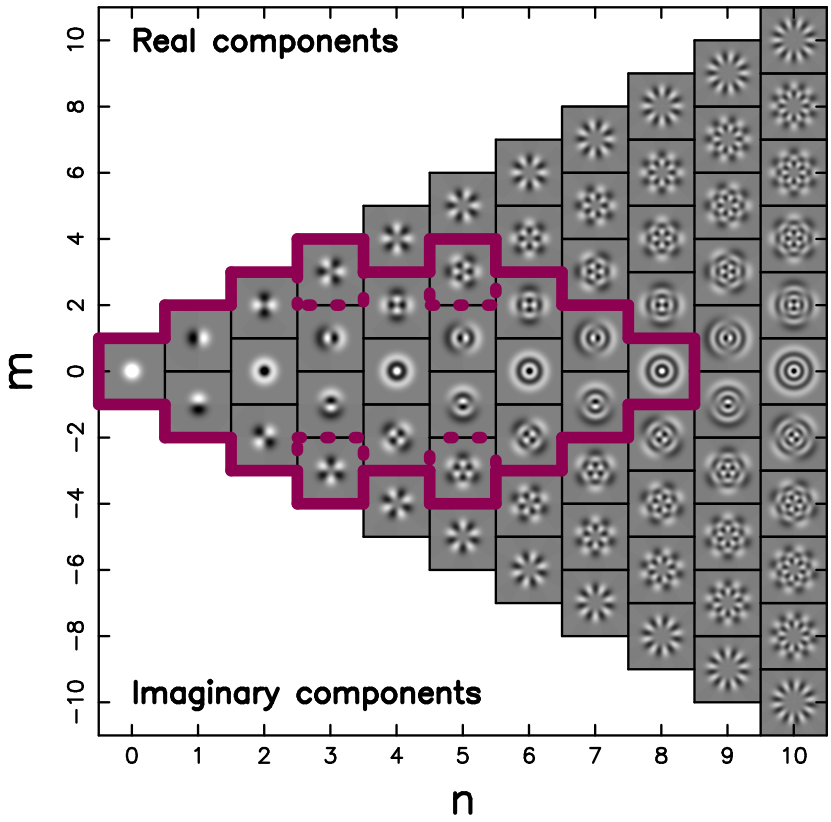

Figure 3.1 Polar Shapelets basis functions up to a maximum Shapelets order of $n_{\max} = 10$. For $m \geq 0$, the real components of the basis functions are shown whilst for $m < 0$ the imaginary components are shown. The solid purple (thick) lines mark the coefficients used by the MV pipeline to estimate the shear and flexions for an analysis with $n_{\max} = 10$. The dashed purple (thick) lines mark the coefficients not used by the KK06 implementation for the same $n_{\max}$.

3.3.1 The MV pipeline

We introduce here an implementation of the Shapelets method which builds on a previous implementation described in Kuijken (2006) (hereafter KK06). This approach creates a Shapelets representation of the brightness profile of a PSF-convolved galaxy image. It also creates a model circular source and applies shear and flexion to it before convolving it with the point-spread function (PSF). Finally it fits the galaxy image to this modeled source in order to find the amount by which it has been sheared and flexed.

To first order in ellipticity s and flexions f and g, the model object can be written as

$$\mathbf{P} \cdot \left[1 + \sum_{i=1,2} \left(t_i \hat{T}^i + s_i \hat{S}^i + f_i \hat{F}^i + g_i \hat{G}^i \right) \right] \sum_{\text{even}}^{N_c} c_n C^n \tag{3.11}$$

where $\mathbf{P}$ is the PSF matrix, $\hat{T}^i$, $\hat{S}^i$, $\hat{F}^i$ and $\hat{G}^i$ are the translation, shear, F

flexion and G flexion operators respectively and t_i, s_i, f_i and g_i are the corresponding coefficients. The translation terms here ensure that fits spoiled by undue centroid shifts are caught. The operators are acting on a circular source which can be expressed as a series of circular Shapelets C^n with coefficients c_n where n is even and the series is truncated at $N_c = n_{\max} - 2$. The reason for truncating at N_c rather than $n_{\max}$ is to safeguard against PSF structure at higher orders affecting the highest order Shapelets used. To avoid introducing signal-to-noise (S/N) dependent biases, the $n_{\max}$ is kept constant for all galaxies rather than being allowed to vary according to size or brightness. For faint sources, this means the higher-order coefficients will be noisy but unbiased.

Once we have a cartesian Shapelets representation of both the sheared, flexed and PSF convolved circular model and of the PSF convolved object we want to fit, we convert them both into polar Shapelets as described in KK06. Polar Shapelets are simply cartesian Shapelets of order $n = a + b$ expressed in polar coordinates, resulting in polar Shapelets of order n with angular order $m \leq n$ and $n + m$ even. The construction of these is discussed in Refregier (2003) and further investigated in Massey & Refregier (2005) and Massey et al. (2007b). In our implementation, the purpose of converting the model and object Shapelets expansions into polar Shapelets is to avoid truncation effects. F flexion, shear and G flexion operators acting on a polar Shapelet of order (n, m) generate terms at order $(n \pm 1, m \pm 1)$, $(n \pm 2, m \pm 2)$ and $(n \pm 3, m \pm 3)$ respectively. By truncating the polar Shapelets expansion in the diamond shape shown in Figure 3.1, i.e. only including terms up to order $(N_c, 0)$, $(N_c-1, \pm 1)$, $(N_c-2, \pm 2)$ and $(N_c - 3, \pm 3)$ in the fit, we minimise truncation effects from the mixing of orders.

The model is fit to each source using least-squares, resulting in a simultaneous estimate for the ellipticity (s_1, s_2), the F flexion (f_1, f_2), and the G flexion (g_1, g_2). As explained in KK06, the errors on the Shapelet coefficients are derived from the photon noise and propagated through the χ^2 function for this fit. By differentiating the χ^2 at the best-fit, we obtain the covariances between the fit parameters, resulting in proper error estimates.

In essence, the main development since KK06 is the addition of flexion to the model and the inclusion of higher order polar Shapelets ($m = \pm 3$) in the fit.

3.4 Testing the pipeline

Several aspects of the pipeline, such as the choice of scale radius β, the method of PSF correction and the effect of noise on ellipticity estimates, have been thoroughly tested in KK06 as part of the development of the KK06 pipeline. In this section we will therefore focus on testing the recovery of shear and flexion.

3.4.1 GREAT08

As participants in the GRavitational lEnsing Accuracy Testing 2008 (GREAT08) challenge (Bridle et al., 2009, 2010), we were able to contrast the shear measurement capability of the KK06 pipeline with that of the MV pipeline under different observing conditions. The challenge provided a large number of simulated sheared and pixelated galaxy images with added noise. The performance of the different shape measurement pipelines taking part was quoted in terms

Table 3.1 The different branches of FLASHES. Four parameters are varied between the branches according to this table.

	Intrinsic shape	Galaxy profile	S/N	PSF
Fiducial	Round	Gaussian	100	Round
Shape branch	Elliptical	Gaussian	100	Round
Profile branch 1	Round	Exponential	100	Round
Profile branch 2	Round	de Vaucouleur	100	Round
S/N branch 1	Round	Gaussian	8	Round
S/N branch 2	Round	Gaussian	20	Round
S/N branch 3	Round	Gaussian	40	Round
PSF branch	Round	Gaussian	100	Elliptical

of a quality factor, or Q-value, defined as

$$Q = \frac{k_Q \sigma^2}{\langle \langle (\langle \gamma_{ij}^m - \gamma_{ij}^t \rangle_{j \in k})^2 \rangle_{ikl}} \tag{3.12}$$

where $\sigma^2 = \sigma^2_{\rm stat} + \sigma^2_{\rm syst}$ is a combination of the statistical spread in the simulations and the expected systematic errors. The superscripts m and t denote measured and true (input) values respectively and γ_{ij} is the shear component i for simulation image j. The differences between the measured and true shears are averaged over different input shear sets k and simulation branches l. The whole expression is normalised by k_Q so that a method with a purely statistical spread in the measured shears will have a Q-value of k_Q which is the level desirable for future surveys. In the case of GREAT08, $k_Q = 1000$ and $\sigma^2 = 10^{-7}$, giving a Q-value nominator of 10^{-4}. With this definition current methods, like those that took part in the earlier Shear TEsting Programme (STEP) (Heymans et al., 2006a; Massey et al., 2007a), generally achieve $10 \lesssim Q \lesssim 100$. This is sufficient for current weak lensing surveys. For a more in-depth discussion on the Q-value and its relation to the STEP parameters m (multiplicative bias) and c (additive bias), we refer to Kitching et al. (2008).

The overall Q-value was similar for the KK06 and the MV pipelines, both in the LowNoise_Blind competition ($Q \sim 20$) and in the RealNoise_Blind ($Q \sim 25$). When broken down into the separate observing condition branches some differences became apparent. In general the MV pipeline did exceptionally well under "good" observing conditions, e.g. for the high S/N branch or for well resolved galaxies. Our own simulations described in the next section will further test the dependence of the MV performance on different observing conditions.

3.4.2 FLASHES

As there is no flexion simulation set publicly available to date, we create our own FLexion And SHEar Simulations (FLASHES). FLASHES are very similar to the GREAT08 simulations in several respects. First, each galaxy is generated on a grid, ensuring that there is no overlap of objects, thus avoiding deblending issues. Second, each simulation image consists of 10000 such objects. Third, each galaxy is generated through the following sequence: (i) simulate a sheared and/or flexed (elliptical) galaxy model (depending on simulation branch); (ii)

convolve with the PSF; (iii) apply the noise model. Four parameters are varied between the different FLASHES branches; the intrinsic galaxy shape, the light profile of the galaxies, the S/N of the galaxies and the shape of the PSF. These parameters are detailed below and summarised in Table 3.1.

Simulation details

All parameters except for the intrinsic ellipticities are kept constant in each simulation image, and all images are created using Monte-Carlo selection. This is very similar to the process described in KK06 and in Bridle et al. (2010), but with the photon trajectories being influenced by flexion as well as by shear if required.

The galaxies are modeled with Sérsic intensity profiles $I_{\rm gal} \propto e^{-kr^{1/n}}$ (Sérsic, 1968) with varying indices n. A Sérsic index of $n = 0.5$ is a Gaussian profile whilst $n = 1$ and $n = 4$ are exponential and de Vaucouleur profiles respectively. Half of the FLASHES branches have intrinsically round galaxies whilst the other half consists of galaxies with intrinsic ellipticities picked randomly from the ellipticity distribution of objects in the COSMOS survey. There is no intrinsic flexion included. The PSFs applied to the simulations are nearly Gaussian with a Moffat profile $I_{\rm PSF} = (1 + r^2/a^2)^{-m}$ of index $m = 9$. In half of the branches, the PSF is round whilst in the other half it is elliptical in the horizontal direction with $e_{1,\rm PSF} = 0.02$. To mimic the properties of the COSMOS survey, we use a PSF FWHM of 2.1 pixels and a PSF convolved galaxy size of 5.8 pixels which is the typical size of the galaxies we use in our COSMOS analysis. Finally there are four S/N branches, with S/N being defined as Flux/(Flux error). It is expected that shape measurements will be less accurate at low S/N. For this reason the MV pipeline applies a S/N cut at 10 in general. The low S/N branch of 8 is designed to test how biased measurements are below this cut. The high S/N branch of 100 tests biases under near-perfect noise conditions.

The strength of the different distortions is picked randomly but with the following maximum values: $|\gamma_{1,2}| \leq 0.05$, $|\mathcal{F}_{1,2}| \leq 0.008$ pixel^{-1} and $|\mathcal{G}_{1,2}| \leq 0.02$ pixel^{-1}. The value of each distortion component is kept constant across each image, but differs between the 30 images in each set, and between different sets.

Simulation results

To estimate the average distortion on each image we use two different techniques: a weighted average with weights inversely proportional to the measurement errors, and Convex Hull Peeling (CHP). CHP is an efficient way of eliminating outliers and is essentially a 2D median. A convex hull, in the context of a point cloud in e.g. the γ_1, γ_2 plane, is the minimal convex set of points containing that point cloud. Thus if all the points in this convex set were connected, a polygon containing the entire point cloud would be produced. By peeling away convex hulls, outliers are removed from the point cloud and the remaining points may be averaged over to produce a mean unaffected by extreme results. This is the averaging technique we used in GREAT08 where we peeled away 50% of the measurements before averaging.

We employ the parameters m and c as used in STEP (Heymans et al., 2006a;

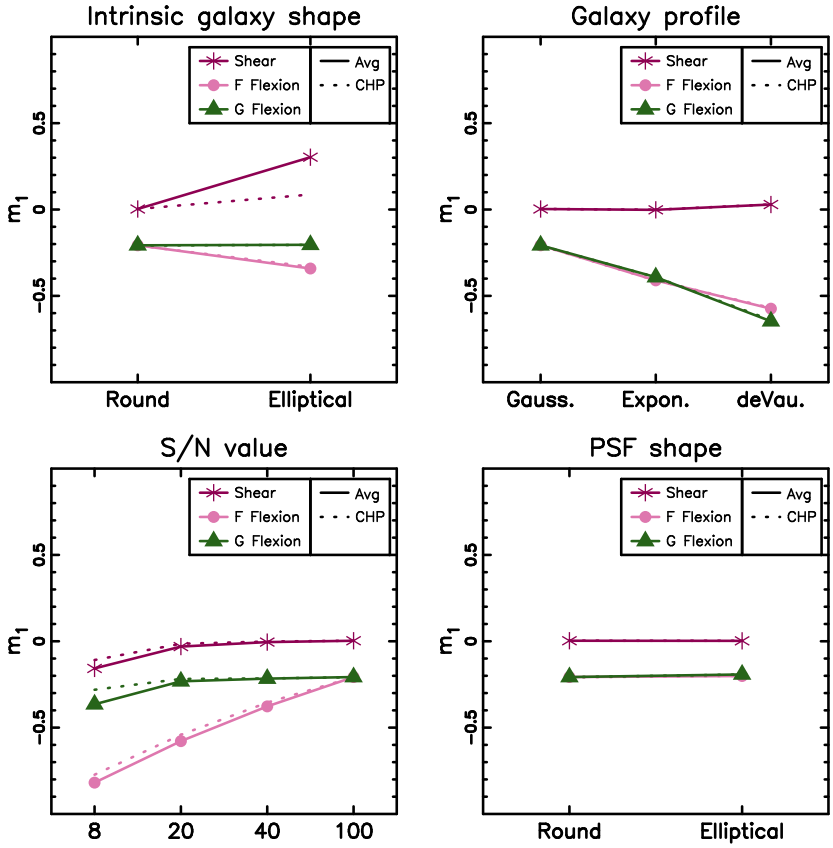

Figure 3.2 The multiplicative bias on the first component for each of shear, F flexion and G flexion. The purple stars represent shear, pink circles represent F flexion and green triangles represent G flexion. The symbols and solid lines show the weighted averages whilst the dashed lines show the CHP average. This is from running the MV pipeline on FLASHES, with $n_{\max} = 10$. For the results for m_2, c_1 and c_2 please refer to Appendix 3.A.

Massey et al., 2007a) to quantify the performance of the software:

$$\langle \gamma_i^{\text{measured}} \rangle - \gamma_i^{\text{input}} = m_i \gamma_i^{\text{input}} + c_i \tag{3.13}$$

and similarly for the flexions, where $i = 1, 2$ represents the shear component. A negative multiplicative bias m_i thus indicates that the distortion is generally underestimated. A systematic offset c_i may be caused by e.g. insufficient PSF correction.

In Figure 3.2 we show the multiplicative bias of the first component for each of shear, F flexion and G flexion as a function of the different simulation branches (please refer to Appendix 3.A for the remaining bias components). For these results we use a Shapelets order of $n_{\max} = 10$. We use `SExtractor` (Bertin & Arnouts, 1996) to detect the objects in each simulation, which we then split into clean star and galaxy catalogues by matching to the input catalogue. We keep all properties apart from the one under investigation fixed at a fiducial

value to allow for a fair comparison. The fiducial simulations in Figure 3.2 have intrinsically round, high S/N galaxies with Gaussian light profiles and a circular PSF.

From the above figure it is clear that both flexions are likely to be underestimated, especially for higher Sérsic indices. The bias is also strongly S/N dependent, particularly for the F flexion. Thus a S/N cut is essential to improve the performance of the MV pipeline, but a bias correction should also be implemented. Investigating the dependence of m on S/N further, we are able to fit the following power-law to our FLASHES results:

$$m_{1,2} = -a(\mathrm{S/N})^{-b} \tag{3.14}$$

where a and b are constants as follows: for shear $(a_\gamma, b_\gamma) = (6.48, 1.78)$; for F flexion $(a_\mathcal{F}, b_\mathcal{F}) = (2.30, 0.48)$; for G flexion $(a_\mathcal{G}, b_\mathcal{G}) = (0.36, 0.13)$. We will apply this bias correction to our shape measurements in COSMOS, but since FLASHES have been tailored for this particular data the biases should be explored further before being applied to other surveys.

3.4.3 Galaxy-galaxy simulations and bright object removal

At the core of weak galaxy-galaxy lensing is the averaging of the signal in rings centered on lenses consisting of single galaxies rather than a galaxy cluster. This type of analysis is robust as numerous systematics, induced by e.g. the PSF, cancel out. Different systematics may however be introduced, such as the light from the central, often bright, lens causing biases in the shape measurements as discussed in Rowe (2008). To study this possible effect, we created simple simulations with sources placed in evenly spaced rings around a central lens. Apart from source numbers and positions, the simulations were created in the same way as FLASHES. The S/N of the images was set to 200 to ensure minimum bias, and for the same reason the source galaxies had Gaussian light profiles. The size and profile parameters of the lens were varied between images.

The results for a lens with an exponential profile are shown in Figure 3.3 (black stars), where we have used $n_{\max} = 10$. We recover a near-perfect average signal in each source circle far from the lens. However, close to the lens the shear and G flexion are slightly affected, but, more strikingly, the F flexion is severely overestimated. The conclusion we draw from this is that *bright objects can add significantly to the F flexion signal*, due to light 'leaking' into the Shapelets fitting radius. This causes the pipeline to detect a source light profile that is skewed towards the lens, and interpreting it as extra F flexion.

Our solution is to remove any bright objects sufficiently close to the source being fit using a technique we introduce here as Bright Object Removal (BOR). Before decomposing a galaxy image into Shapelets, we identify any bright objects that could conceivably intrude using selection criteria based on distance between the two objects, Shapelets fitting radius of the source, and size and brightness of the intruding object. We then create Sérsic models of the intruding objects using `GALFIT` (Peng et al., 2002) and subtract these models from the Shapelets stamp before doing the fitting. It works well in these simulations, provided one is careful with the parameters given to `GALFIT` as input. The sky background value given to `GALFIT` is particularly important as a small error in this estimate results in postage stamp artifacts when the stamps are subtracted from the original image. In Figure 3.3 we also show the results if BOR

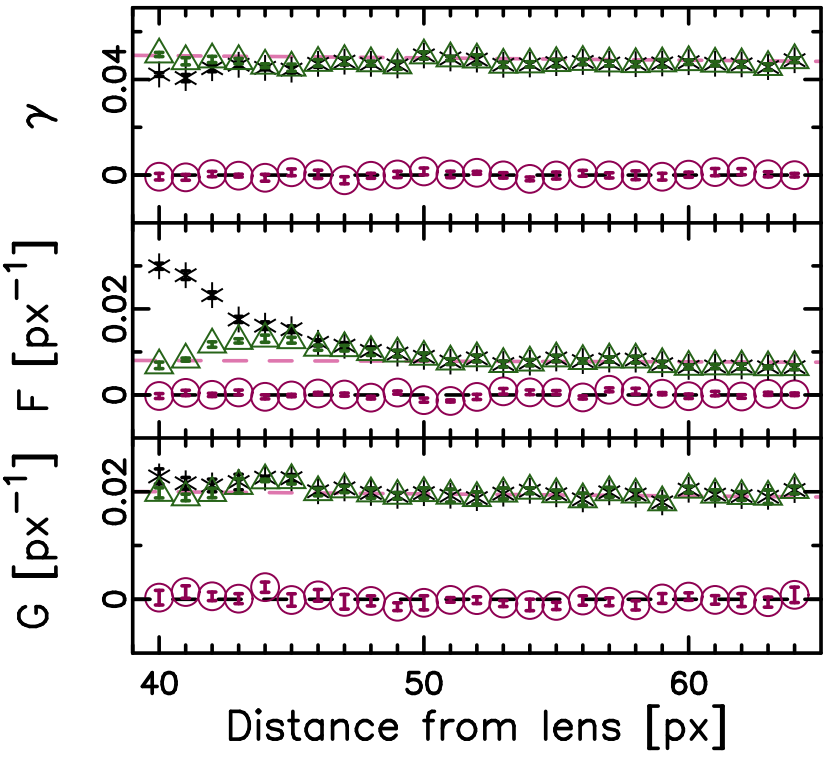

Figure 3.3 The shear (top panel), F flexion (middle panel) and G flexion (bottom panel) results from galaxy-galaxy lensing simulations, with and without Bright Object Removal (BOR). The black stars represent the tangential signal without BOR and the green triangles represent the same measurement corrected using BOR. The dashed pink line is the input signal and the purple circles are the cross-signal, which is expected to vanish, for the uncorrected measurements. Here, the FWHM of the lens is 14 pixels. Note the slight underestimation of the shear, the slight overestimation of the G flexion and the massive overestimation of the F flexion in the innermost bins when BOR is not applied.

is switched on whilst the rest of the analysis is kept identical to the previous run (green triangles). There is still some excess F flexion signal around 44 pixels, indicating that there may be some residual light remaining, but this excess is smaller than for the uncorrected measurements. This provides a confirmation that the measured signal reproduces the input signal well if BOR is applied, and no new artifacts are introduced. We note, however, that the leaking light does not affect the cross component of the measurements, with the consequence that this effect cannot be detected through the usual systematic checks.

3.5 COSMOS analysis

Goldberg & Bacon (2005) made a first detection of galaxy-galaxy flexion using the ground-based DLS, proving that flexion can indeed be detected, but ultimately they were hampered by the small size of their sample, the lack of

redshifts and the extra blurring caused by the atmosphere. Therefore we choose the space-based Cosmic Evolution Survey (COSMOS, Scoville et al. (2007)) as the first real dataset for the MV pipeline. Thanks to the depth of this survey we will have access to more than a thousand times as many lens-source pairs as Goldberg & Bacon (2005) did. More than half of these have photometric redshifts meaning that the division of the sample into lenses and sources will be more accurate. The intention is to provide independent confirmation that galaxy-galaxy flexion has high enough S/N to be detected, and that the software presented in this Chapter is able to do it. We will also look closer to the lens than previous analyses and attempt to combine shear and flexion to give constraints on galaxy dark matter halo profiles.

3.5.1 The COSMOS data set

COSMOS is to date the largest contiguous field imaged by the Hubble Space Telescope (HST) with a total area of 1.64 deg^2. The 579 tiles were observed in F814W (I-band) by the Advanced Camera for Surveys (ACS) between October 2003 and November 2005. Each tile consisted of 4 dithered exposures of 507 seconds each (2028 seconds in total) with about 95% of the survey area benefiting from the full 4 exposures.

We use the images reduced by Schrabback et al. (2010) (hereafter S10) and also their catalogues for stars and galaxies, detected using `SExtractor`. There are a total of 446 934 galaxies with $i_{814} < 26.7$ in the mosaic catalogue, almost half of which have COSMOS-30 photometric redshifts from Ilbert et al. (2009). These redshifts are magnitude limited and cover the entire COSMOS field to a depth of $i^+ < 25$.

3.5.2 Data analysis

Galaxy-galaxy lensing is less affected by the problems plaguing cosmic shear analyses, since most systematic shape distortions induced by instruments cancel out when azimuthally averaged. Still, we have to be careful not to introduce new systematic effects or biases, so correcting for the PSF and the charge-transfer inefficiency (CTI) (e.g. Rhodes et al., 2007; Massey et al., 2010) is important.

We use all galaxies with redshifts of $z < 0.6$ as lenses. At higher redshifts the light from the lensing galaxies becomes difficult to account for due to the small angular separation on the sky, as explained further in Appendix 3.C. Furthermore, imposing a lens redshift cut will ensure that the vast majority of sources are truly background objects.

Our source catalogue is comprised of all objects with a shape measurement. We clean this catalogue using a series of conditions on size and measured shape, detailed in Appendix 3.B1, the most important of which is to remove objects with S/N < 10. Roughly two-thirds of the remaining sources have individual COSMOS-30 photometric redshifts assigned to them. For the remaining third (redshift bin 6 in S10) we use the estimated redshift distribution employed by S10 to assign mean angular diameter distance ratios (D_s/D_{ls}) to each lens-source pair. We are finally left with 216 873 sources, corresponding to a source density of ~ 37 arcmin^{-2}. For the pairs we use, the median lens redshift is $z_{lens} = 0.27$ and the median source redshift is $z_{source} = 0.98$.

Despite the excellent space-based resolution, we need to correct the galaxy shapes for the instrumental PSF. The ACS PSF is known to fluctuate both spatially and temporally (e.g. Rhodes et al., 2007; Schrabback et al., 2007), a variation mostly driven by changes in telescope focus caused for example by the breathing of the telescope. We can map the PSF using stars, but, in high-galactic latitude ACS fields typically only $\sim 10-20$ stars are present. This number is too low for the standard approach of a polynomial interpolation. Instead, we closely follow the analysis of S10, who conducted a principal component analysis (PCA) of the ACS PSF variation as measured in dense stellar fields. Details for the Shapelets implementation of PCA may be found in Appendix 3.B2.

A challenge with using CCD detectors in space is that they are not protected by the atmosphere. Exposed, they continuously get bombarded by radiation, causing deterioration of the chip surface. The imperfections created in this way act as charge traps which causes inefficiency in the moving of electrons to read-out. This effect is known as CTI (e.g. Rhodes et al., 2007; Massey et al., 2010). As the electrons get trapped and then released at a later point, charge trails following objects are created in the read-out direction, effectively causing a spurious shear signal in that direction. Our correction for CTI again closely follows S10, who derive parametric corrections for the change in polarization for both galaxies and stars. For more details on this correction, please refer to Appendix 3.B3.

Once corrected, the galaxy-galaxy shear and flexion signals are weighted according to the geometric lensing efficiency of each lens-source pair. In the case of flexion there is an extra scale dependence of the signal. For the Navarro-Frenk-White (NFW) profile (Navarro, Frenk, & White, 1996), the strength of the shear signal scales as

$$\gamma_{\rm NFW} \propto \frac{D_l D_{ls}}{D_s} \tag{3.15}$$

where D_l, D_s and D_{ls} are the angular diameter distances to the lens, to the source, and between lens and source respectively (Wright & Brainerd, 2000). The flexion signals scale as

$$\mathcal{F}_{\rm NFW}, \mathcal{G}_{\rm NFW} \propto \frac{D_l^2 D_{ls}}{D_s} \tag{3.16}$$

(B06). We therefore weight the signals accordingly, scale them to a reference lens and source redshift and compute the weighted average in 25 logarithmic distance bins (see Appendix 3.B4 for details). We use a reference lens redshift of $z_{l,\rm ref} = 0.27$ since that is close to the effective median redshift of our lenses, and a reference source redshift $z_{s,\rm ref} = 0.98$. To estimate the errors on each bin and the covariances between them, we use 5000 bootstrap resamples of our source catalogue.

3.5.3 Results

The results from our galaxy-galaxy lensing analysis of the full COSMOS lens and source sample is shown in Figure 3.4. In the left panel we plot the shear results as a function of physical distance from the lens. These results agree very well with those from S10 (see Appendix 3.D), providing an independent

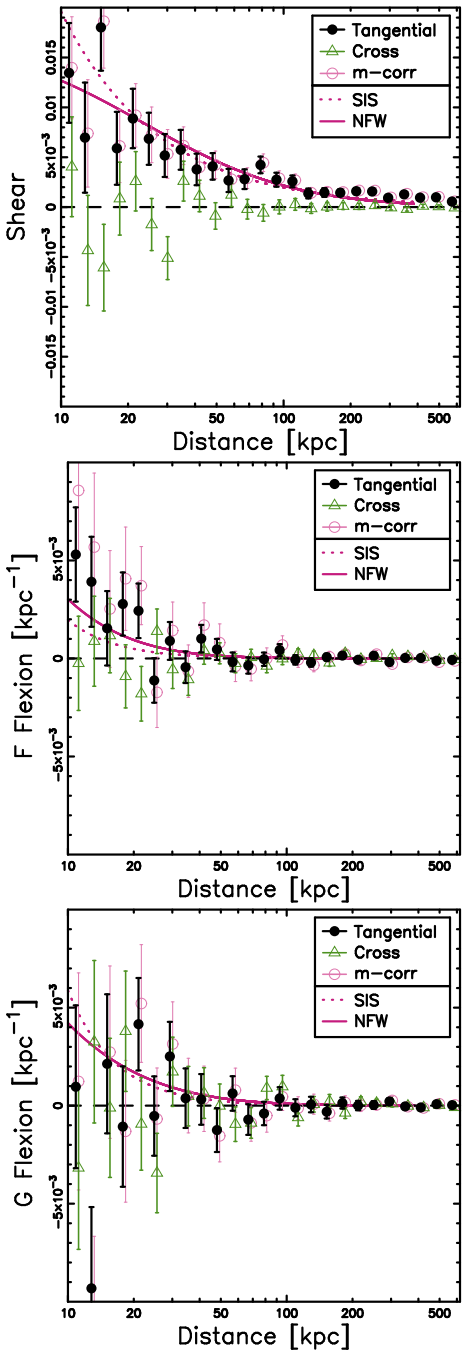

Figure 3.4 The galaxy-galaxy lensing results for the COSMOS data, using a maximum Shapelets order of $n_{\max} = 10$. Black solid points represent the tangential signal and green triangles represent the cross term. The pink circles represent the tangential signal if we apply the multiplicative bias correction implied by FLASHES. Note that the SIS and NFW profiles have been fitted to the shear data and then *translated* into predictions for $\mathcal{F}$ and $\mathcal{G}$ curves.

consistency check. To this we fit a Singular Isothermal Sphere (SIS) profile and a tentative NFW profile. Due to the dependence on mass and redshift of the mean concentration parameter (e.g. Duffy et al., 2008), the NFW profile is only an indication when the spread in lens masses and redshifts is as great as it is in the above sample. Splitting the sample up into redshift and/or mass bins would increase the confidence in the fit, but decrease the S/N of the signals significantly.

The middle and right panels show the F and G flexion results respectively, for the same lenses and sources. The profiles plotted here are identical to those plotted in the shear panel but *translated* into predictions for $\mathcal{F}$ and $\mathcal{G}$, as opposed to fitted to the flexion data directly. The F flexion has a tendency to be overestimated compared to the predicted profile from the shear, and we investigate this discrepancy further in the following sections. We also note that we measure a G flexion that is very noisy and consistent with zero. This is most likely caused by lack of information in higher m-order Shapelets for fainter sources, and we choose to use only shear and F flexion in the continued analysis.

Also shown in pink circles in Figure 3.4 is the signal if we apply the multiplicative S/N-dependent bias correction implied by FLASHES. With this correction, the F flexion signal becomes slightly higher. This bias correction is only based on one specific set of simulations and is thus rather preliminary; this is also indicated in the increased size of the error bars. Correcting for the morphology-dependent bias requires accurate source morphology determination. Using the photometric galaxy type estimates from Ilbert et al. (2009) as an indicator of morphology we find that $< 5\%$ of our source sample consists of likely de Vaucouleur objects. This type estimate is not accurate enough to implement a morphology bias correction, but simply removing the de Vaucouleur candidates we identified makes little difference to our results. It is clear, however, that an accurate bias calibration of the flexion amplitude, taking into account both source S/N and brightness profiles, requires further investigation.

3.5.4 Removing bright objects

We now explore the tendency of the F flexion points to lie above the predicted profiles. As shown in Section 3.4.3, the shape measured may be affected by bright objects nearby. We implement BOR in our COSMOS analysis to see the effect on real data. For very well resolved objects, prominent spiral arms and other complications cause `GALFIT` to reject the single Sérsic profile fit. Removing these objects, and the residual light from the wings of the profile (Figure 3.3), requires a more sophisticated model. For now we are only interested in a rough indication of the impact this light leakage has on a galaxy-galaxy signal so we will not correct for the few large objects in this Chapter. However, as shown in Figure 3.5, the correction to the innermost F flexion bin is non-zero even without accounting for the very large objects. The shear is largely unaffected, but for flexion analyses in future deeper and larger surveys it will be important to correct for this effect.

3.5.5 The effect of substructure

Since flexion is more sensitive to the underlying mass distribution on small scales than shear is, we expect it to respond differently to the presence of substructure

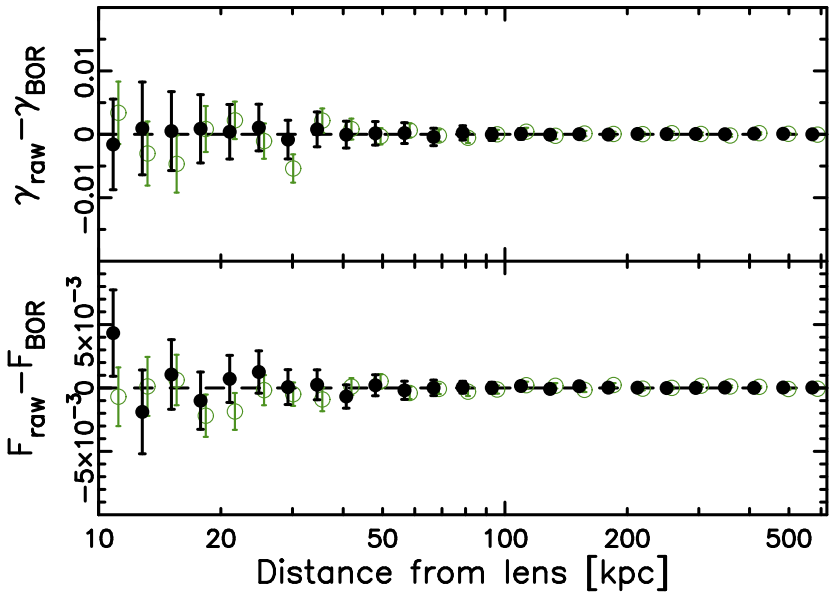

Figure 3.5 Comparison between the galaxy-galaxy shear and flexion signals with and without Bright Object Removal, showing the non-zero correction to the innermost F flexion bin (corresponding to roughly 40 px in Figure 3.3). Black solid points represent the difference between the signals before and after correction, with the F flexion in units of kpc^{-1}, whilst green circles represent the cross term.

in galaxy haloes. To test whether this has any impact on our analysis we take a galaxy-size SIS halo (see B06, for shear and flexion expressions) and populate it with subhaloes, allowing 20% of the mass to be in substructure. The total mass of the halo is $10^{12}\ h^{-1}M_{\odot}$ and the galaxy is placed at $z = 0.35$ with $D_l/D_{ls} = 0.5$. We spread the substructure mass over 100 subhaloes, randomly distributed according to an SIS density profile. Finally we average the azimuthally averaged signal over 100 such galaxies. Now, subhaloes are generally stripped. To approximate this we use a Truncated SIS (TSIS) profile for the subhaloes (see Hoekstra et al., 2004, for constraints on parameters). The TSIS convergence is given by

$$\kappa(\theta) = \frac{\theta_E}{2\theta}\left(1 - \frac{\theta}{\sqrt{\theta^2+\theta_S^2}}\right) \tag{3.17}$$

where θ_E is the Einstein radius and θ_S is a truncation scale where the profile steepens. On small scales ($\theta \ll \theta_S$) the TSIS behaves like an SIS but at large scales ($\theta \gg \theta_S$) the profile decreases as θ^4. The TSIS shear is given in Schneider & Rix (1997) and the flexions are

$$\mathcal{F}(\theta) = \frac{\theta_E}{2\theta^2}\left(\frac{\theta^3}{(\theta^2+\theta_S^2)^{3/2}} - 1\right)e^{i\phi} \tag{3.18}$$

and

$$\mathcal{G}(\theta) = \frac{\theta_E}{2\theta^3}\left(3\theta + 8\theta_S - \frac{3\theta^4 + 12\theta^2\theta_S^2 + 8\theta_S^4}{(\theta^2+\theta_S^2)^{3/2}}\right)e^{i3\phi} \tag{3.19}$$

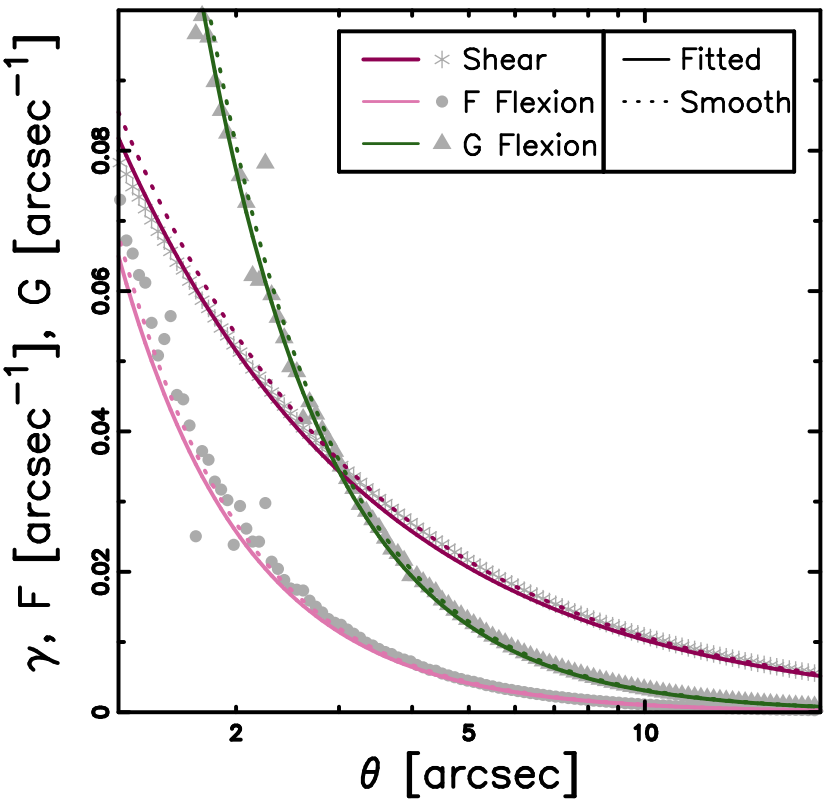

Figure 3.6 Simulated shear and flexion signals azimuthally averaged in galaxy haloes with and without TSIS subhaloes. Grey stars, circles and triangles represent the binned shear, F flexion and G flexion respectively. Purple, pink and green lines represent the shear, F flexion and G flexion signal if the halo is a smooth SIS (dashed). The solid lines are an SIS profile as fitted to the shear data points in a simulated galaxy containing TSIS subhaloes and translated into predictions for the flexions.

where ϕ is the position angle of the background source. Using the parameters above and a truncation scale $\theta_S = 2$ arcsec for the subhaloes we get the results shown in Figure 3.6. The shear profile fit is pulled down slightly compared to a smooth halo but the flexions are not similarly affected. Due to the substructure the flexions are more scattered, but the overall trend is for the points to follow the smooth profile, or even slightly above in the F flexion case. Thus the flexions seem overestimated compared to the shear fit. We stress however that the fraction of substructure used in this test (20%) is high to exaggerate the effect. The test does show that substructure may affect the flexions differently to the shear, but its influence is likely less than the excess currently observed in COSMOS.

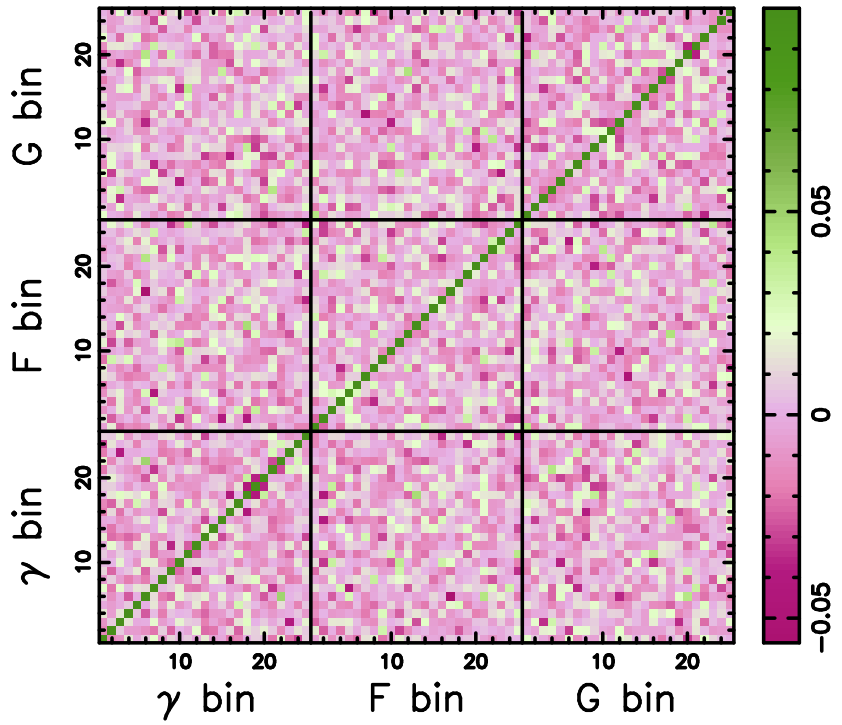

Figure 3.7 The correlation matrix between the shear and flexion bins, using 5000 bootstrap resamples. Please note the scale; to display the minute variations between off-diagonal elements we have artificially set *the diagonal elements (dark green) only* to 0.1, whilst all other elements are unscaled and normalised to diagonal elements of 1.0 as is customary.

3.5.6 Profile determination

One of the most interesting potential uses of flexion is as an aid to shear in determining the inner density profiles of dark matter haloes. The two signals are sensitive to the underlying density profile on different scales, so combining the two will give us tighter constraints than either on their own. To combine the shear and flexion signals we have to take any correlation between them into account. B06 assumed that the shear and flexion measurements would be uncorrelated. Here we confirm this assumption through the correlation matrix between the shear and flexion bins, using 5000 bootstraps, shown in Figure 3.7. This implies that it is trivial to combine the shear and flexion information to find the profile of an average lens. We use the F flexion in conjunction with the shear to fit density profiles to the measured signal. For this purpose we try two different families of profiles: the power-law and the NFW. Our general power-law is defined as

$$\gamma = -Ad^{-n} \tag{3.20}$$

with d the distance from the lens, and the amplitude A and the index n free parameters. An index of $n = 1$ would be equivalent to an SIS. The above

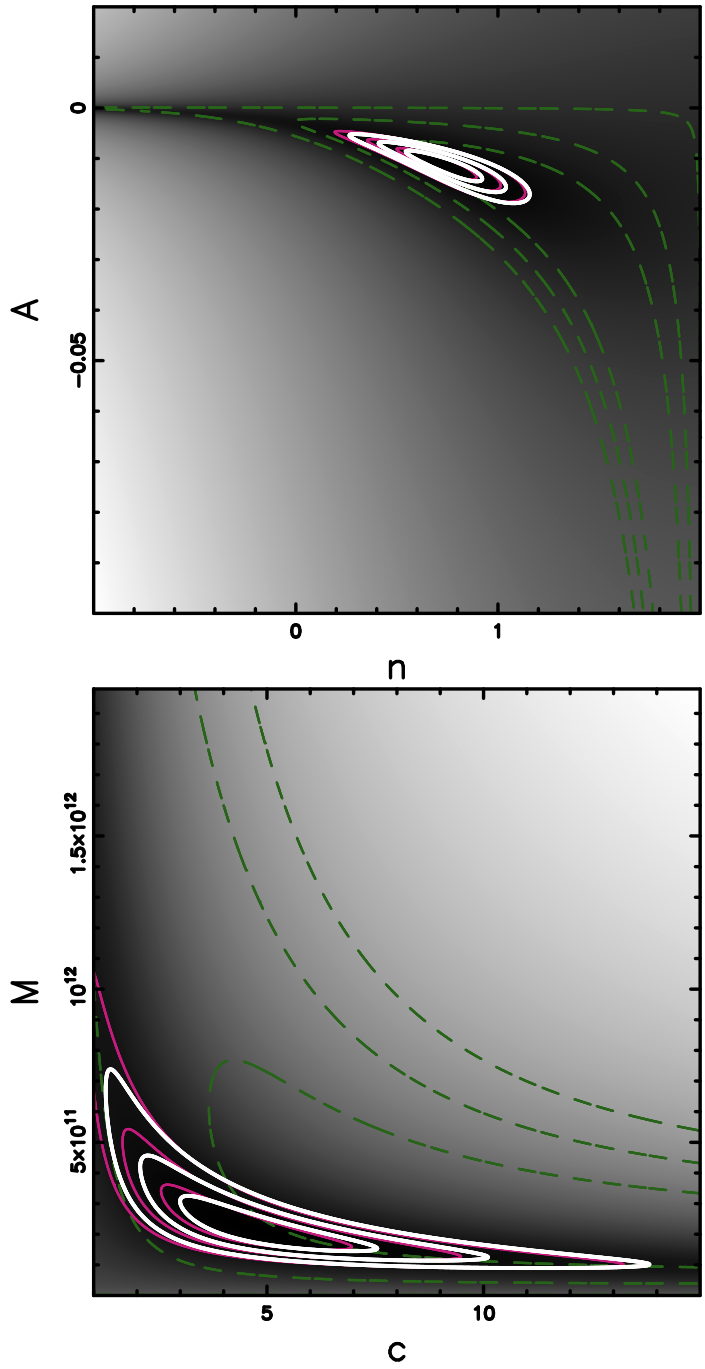

Figure 3.8 Joint profile constraints using shear and F flexion. The top (bottom) panel shows the results for the power-law (NFW) fit. Purple (thin solid) lines represent shear and green (dashed) represent F flexion. The contours show the 67.8%, 95.4% and 99.7% confidence limits respectively in terms of constant $\Delta\chi^2$ (2.30, 6.17 and 11.8 respectively). The white (thick) contour marks the joint confidence limits. The grey-scale is logarithmic in χ^2.

expression is easily differentiated to give the F flexion

$$\mathcal{F} = (n-2)Ad^{-n-1}. \tag{3.21}$$

The expressions for the NFW profiles are somewhat more complicated but they are given in full in Wright & Brainerd (2000) and B06 for shear and flexion respectively. Here we leave the virial radius M_{200} and the concentration c as free and independent parameters. We fit the power-law and NFW profiles to the inner 100 kpc only as this is the region where F flexion becomes important and the shear profile is not affected by halo-halo contamination.

The top panel in Figure 3.8 shows that both the shear and the F flexion are consistent with an SIS ($n = 1$), although together they prefer a slightly lower power-law index of $n = 0.73^{+0.40}_{-0.43}$. The bottom panel shows that it is difficult to constrain the NFW concentration if it is left completely unrestricted. This analysis with two free and independent parameters is not completely representative, however, since simulations indicate a fixed mean mass-concentration relationship (Duffy et al., 2008). It is also important to note that the average profile we constrain here is a composite of lenses in a large redshift range. Detection at the high end of the redshift distribution tend to be biased towards intrinsically brighter objects than at the low end. We also combine measurements from lenses of different sizes and morphologies. Nonetheless, combining shear and F flexion does provide tighter constraints than shear alone on the density profiles, and this is an important proof of concept. The resulting mass estimate for the average lens in COSMOS from the combined NFW fit is $M_{200} = 2.12^{+3.60}_{-1.09} \times 10^{11}\ h^{-1}M_{\odot}$ with a concentration of $c = 4.82^{+7.04}_{-3.16}$.

3.6 Discussion and conclusions

We have shown a significant detection of galaxy-galaxy F flexion for the first time with Shapelets using the space-based COSMOS data set. We used this flexion signal in conjunction with the shear to constrain the average density profile of the galaxy haloes in our lens sample. We found a power-law profile consistent with an SIS. Furthermore, we showed that the inclusion of F flexion provides tighter constraints on both power-law and NFW profiles, an important proof of concept.

The galaxy-galaxy F flexion signal measured in COSMOS is slightly higher than expected from the shear signal, especially if we apply the multiplicative bias correction. There is however no indication from the cross term that there are systematics present. The discrepancy could be partly due to insufficient nearby object light removal, but this is unlikely to explain the full offset. Substructure in galaxy haloes may cause excess F flexion compared to what the shear measures. However, a large fraction of the galaxy halo mass has to be in substructure in order for the effect to become significant. We note that Goldberg & Bacon (2005) also find shear and F flexion signals that are inconsistent with each other; the velocity resulting from an SIS profile fit to their F flexion signal is nearly twice that found using shear. This is qualitatively consistent with our findings, which leads us to believe that there is something more fundamental affecting the signal. In the near future we would like to further investigate the dependence of these discrepancies on lens properties.

We measure a galaxy-galaxy G flexion signal that is consistent with the predicted profile, but due to the large measurement errors it is also consistent with zero. This measurement is a lot noisier than the other two, an effect most likely caused by the fact that there is less information available in the higher m-order Shapelets for fainter sources. To measure a G flexion signal we thus require many well-resolved sources, an extravagance not yet awarded us. Future large space-based surveys such as EUCLID will enable us to investigate G flexion further, but for now F flexion is a promising tool in its own right.

The software introduced in this Chapter, the MV pipeline, is able to detect these higher order lensing distortions. We have shown that in practice, the Shapelets F flexion measure is affected by light from nearby bright objects and detailed a way to correct for this effect. This BOR does require further sophistication to account for large, well resolved galaxies, galaxies which are not well described by the single Sérsic light profile employed here. From the FLASHES simulations it is clear that there is more work required in order to improve the accuracy of the F flexion measurements for future surveys. Noise related biases are particularly significant for this type of shape measure, and we have modeled these biases in COSMOS.

In the future we hope to measure flexion on a larger survey, enabling us to reduce the noise so that we can investigate the trend with e.g. redshift and lens mass. A larger number of sources would also enable us to further tighten the profile constraints in the inner regions of dark matter haloes where baryons become important. It is not yet clear how well we can measure flexion on ground-based data, but surveys like KiDS, CFHTLS and RCS2 should provide an excellent test-bed.

Acknowledgements

We would like to thank our colleagues Henk Hoekstra, Edo van Uitert and Elisabetta Semboloni at Leiden Observatory, and Peter Schneider at Bonn University, for useful discussions. Gary Bernstein drew our attention to the possibility of using Convex Hull Peeling for our averages, and for this we would like to thank him. MV is supported by the European DUEL Research-Training Network (MRTN-CT-2006-036133). TS acknowledges support from the Netherlands Organization for Scientific Research (NWO).

APPENDIX 3.A: FLASHES results

The figures shown in this Appendix complement Figure 3.2 in the main Chapter 3 and provide additional detail on the results from running the MV pipeline on FLASHES, with $n_{\max} = 10$. The parameters m and c are defined through

$$\langle \gamma_i^{\text{measured}} \rangle - \gamma_i^{\text{input}} = m_i \gamma_i^{\text{input}} + c_i \tag{3.22}$$

and similarly for the flexions, where $i = 1, 2$ is the component. We use two different techniques to estimate the average distortion on each image: a weighted average and Convex Hull Peeling (CHP).

In Figure 3.9 we show the multiplicative bias of the second component for each of shear, F flexion and G flexion as a function of the different simulation branches. For these results we use a Shapelets order of $n_{\max} = 10$. This bias behaves as the multiplicative bias of the first component (Figure 3.2), as

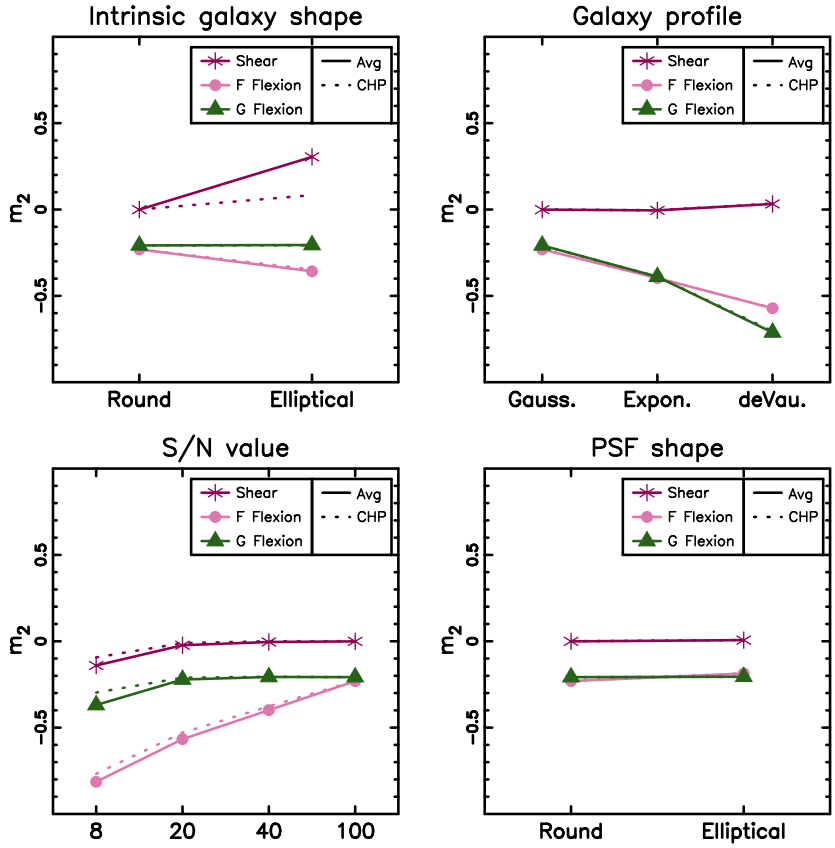

Figure 3.9 The multiplicative bias on the second component for each of shear, F flexion and G flexion. The purple stars represent shear, pink circles represent F flexion and green triangles represent G flexion. The symbols and solid lines show the weighted averages whilst the dashed lines show the CHP average.

expected. The biases of all distortion measurements, and in particular F flexion, are severely dependent on S/N and brightness profile.

The additive bias c is minimal for shear and F flexion (see Figures 3.10 and 3.11) indicating that the PSF is either well corrected for or not significantly affecting these two measurements. For the G Flexion the offset is larger.

APPENDIX 3.B: COSMOS data analysis

3.B1 Catalogue creation

To maximise the number of lens-source pairs we use all objects with assigned photometric redshifts as sources, but imposing a redshift cut of $z < 0.6$ for lenses. Additionally we use sources without individual redshifts (S10 redshift bin 6), assigning mean angular diameter distance ratios (D_s/D_{ls}) to these lens-source pairs according to the estimated redshift distribution employed by S10. We then weight all pairs with their individual lensing efficiency, similar to the

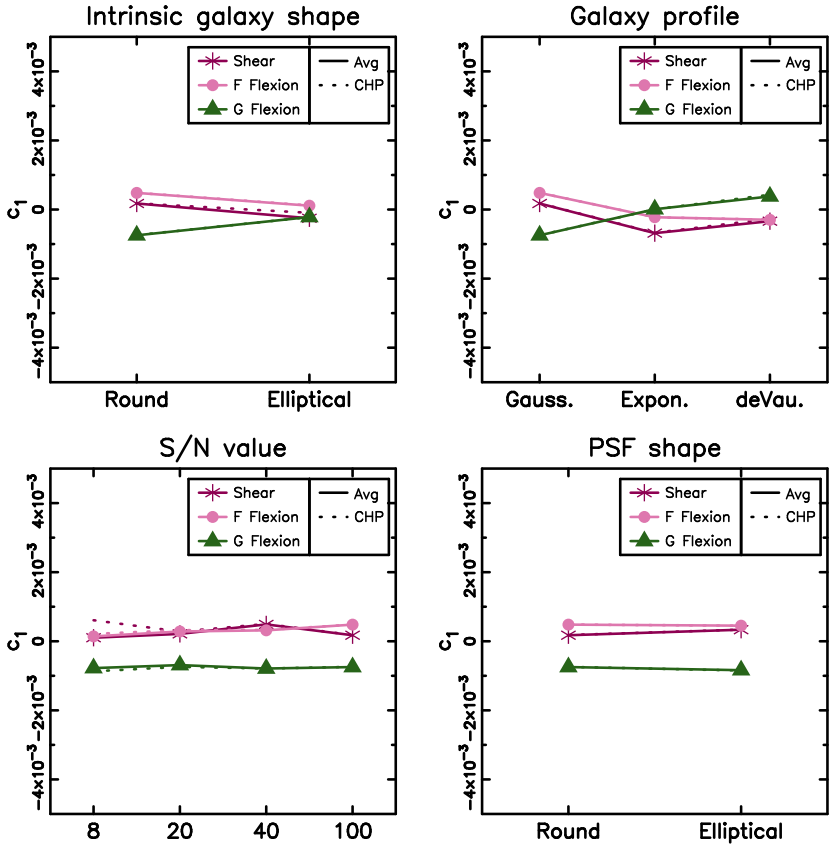

Figure 3.10 The additive bias on the first component for each of shear, F flexion and G flexion. As before, the purple stars represent shear, pink circles represent F flexion and green triangles represent G flexion. The symbols and solid lines show the weighted averages whilst the dashed lines show the CHP average.

weighting scheme in e.g. Mandelbaum et al. (2006b) (see Appendix 3.B4). This downweights pairs that are close in redshift and naturally removes pairs where the "source" is in front of the "lens". To the source catalogues we apply the following cuts:

- $S/N > 10$. This cut is important as the F flexion measurement in particular gets heavily biased towards low S/N (see Section 3.4.2).

- If the centroid cannot be determined accurately the Shapelets decomposition will be inferior. Therefore objects where the code is forced to move the centroid compared to the one estimated by `SExtractor` by more than half a pixel are excluded.

- The summed power in constant m of the polar Shapelets provides an indicator of the Shapelet fit being affected by a neighbouring object. If the fractional power is particularly high at high orders the object is excluded (see KK06, for more details).

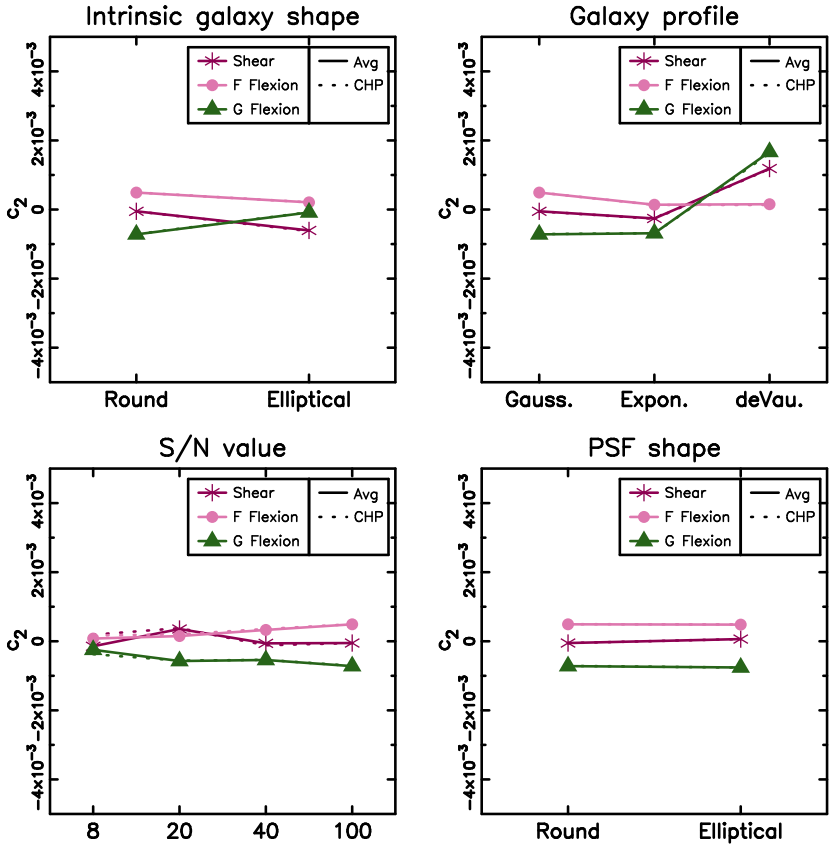

Figure 3.11 The additive bias on the second component for each of shear, F flexion and G flexion. As before, the purple stars represent shear, pink circles represent F flexion and green triangles represent G flexion. The symbols and solid lines show the weighted averages whilst the dashed lines show the CHP average.

- If the FWHM or scale radius of the object is too small compared to the scale radius of the PSF the object is excluded.
- If $\gamma^2 > 1.4$, $\mathcal{F}^2 > 3.0$ arcsec^{-1} or $\mathcal{G}^2 > 6.6$ arcsec^{-1} then the object is excluded. These numbers are based on the measured distributions and the cuts are applied to remove outliers with very noisy shape measurements.
- Finally, we remove faint objects with an assigned photometric redshift of $z < 0.6$ that have a prominent secondary peak at $z_{\rm 2nd} > 0.6$, as discussed in S10.

3.B2 PSF interpolation

The ACS PSF fluctuates both spatially and temporally (e.g. Rhodes et al., 2007; Schrabback et al., 2007), a variation mostly driven by changes in telescope focus caused for example by the breathing of the telescope. We can map the PSF using stars, but in high-galactic latitude ACS fields typically only $\sim 10-$

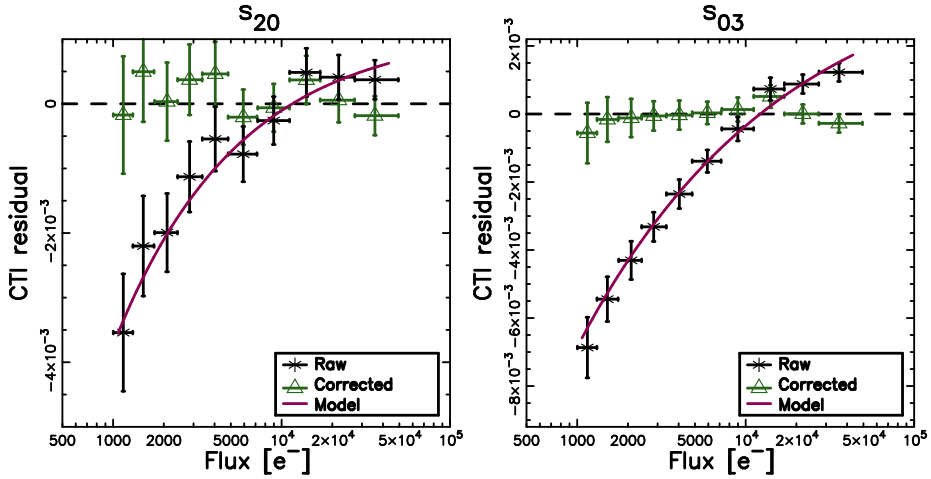

Figure 3.12 CTI-induced residuals on the stellar Shapelet coefficients s_{20} (left) and s_{03} (right) in an example star field. The black stars show the mean of the coefficients as a function of stellar flux after subtraction of a spatial third-order polynomial model derived from bright stars to separate PSF and CTI effects. Each coefficient has been scaled to a reference number of $y_{\rm trans} = 2048$ parallel readout transfers. The purple curves show the parametric CTI model, jointly determined from 700 stellar field exposures. The horizontal dashed line indicates an offset corresponding to the mean CTI model for the bright stars used for the polynomial interpolation. The green triangles indicate the corrected coefficients after subtraction of the CTI model.

20 stars are present. This number is too low for the standard approach of a polynomial interpolation. Instead, we closely follow the analysis of S10, who conducted a principal component analysis (PCA) of the ACS PSF variation as measured in dense stellar fields. They found that $\sim 97\%$ of the PSF variation can be described with a single parameter (the first principal component). This parameter is related to the HST focus position, and we therefore dub it 'focus'[1]

Here we make use of the S10 measurement of the HST focus in all COSMOS exposures and the investigated stellar field exposures. We also obtain Shapelets versions of the focus-dependent S10 PSF models, by decomposing the dense stellar field stars into Shapelets and interpolating between them with polynomials which are varied both spatially and with different powers of the focus principal component coefficient. From these models and from the COSMOS focus estimates we then compute a Shapelets PSF model for each COSMOS exposure, which we then combine to obtain a model for the stacked PSF at all galaxy positions.

3.B3 CTI correction

Our correction for CTI again closely follows S10, who derive parametric corrections for the change in polarization for both galaxies and stars. The correction for stars is important in order to measure the actual PSF, independent of the

[1]The capturing of small additional variations beyond focus was relevant for the cosmic shear analysis of S10. Here we can safely ignore these minor additional effects. Galaxy-galaxy lensing is much less sensitive to PSF anisotropy residuals as they cancel out to first order.

non-linear CTI effects. In the stellar field analysis we therefore correct the PSF cartesian Shapelet coefficients for CTI before generating the PCA PSF model. In order to estimate the influence of CTI on the different Shapelet coefficients, we follow S10 and spatially fit each coefficient within one exposure with polynomials. Due to the limited depth of the charge traps, CTI is non-linear, and has a larger relative impact on faint sources than on bright ones. The CTI effect can thus be estimated from the flux-dependent residuals, after the polynomial model has been used to subtract both the flux-independent PSF and the flux-averaged CTI signal.

Figure 3.12 shows these residuals as a function of stellar flux for the stellar Shapelets coefficients s_{20} and s_{03} in one example stellar field. Here the residuals were scaled to the same number of readout transfers (2048). The CTI effect on the coefficients is clearly visible (black stars), but with our power law model (curve) it can be well corrected for (green triangles). The model is fit simultaneously from all 700 stellar fields as a function of stellar flux, sky background, time and number of readout transfers (see S10). CTI affects object shapes in the readout direction, which also after drizzling roughly matches the y-direction. Thus CTI residuals are expected to be roughly symmetric about the y-axis and hence vanish for coefficients s_{ab} with odd a. In the drizzled images the readout direction is up for the upper and down for the lower chip and the CTI trails occur in the opposite directions. This leads to a sign switch for coefficients with basis functions that are not symmetric about the x-axis (odd b), and we have taken this into account for s_{03} in Figure 3.12. We have detected (and modeled) a significant signature of CTI on the following stellar Shapelets coefficients: s_{00}, s_{02}, s_{03}, s_{04}, s_{05}, s_{20}, s_{21}, s_{22}, s_{40}, and s_{60}.

The correction of galaxy shapes for CTI again closely follows S10. Here we fit power-law corrections to the shear and (now in addition) flexion estimates as a function of galaxy flux, flux radius, sky background, time, and number of readout-transfers. Note that Massey et al. (2010) introduced a more advanced CTI correction scheme operating directly on the pixel level. This is expected to yield higher precision, enabling for example the correction of the s_{01} component, which cannot be estimated with our method due to its degeneracy with a simple shift in object position. However, we are confident that our correction scheme is sufficiently accurate for the analysis presented here, in particular as potential residuals cancel to first order for the azimuthally averaged galaxy-galaxy lensing signal.

3.B4 Signal computation

For the Navarro-Frenk-White (NFW) profile (Navarro, Frenk, & White, 1996), the strength of the shear signal scales as

$$\gamma_{\rm NFW} \propto \frac{D_l D_{ls}}{D_s} \tag{3.23}$$

where D_l, D_s and D_{ls} are the angular diameter distances to the lens, to the source, and between lens and source respectively (Wright & Brainerd, 2000). The flexion signals scale as

$$\mathcal{F}_{\rm NFW}, \mathcal{G}_{\rm NFW} \propto \frac{D_l^2 D_{ls}}{D_s} \tag{3.24}$$

(B06). We therefore weight the signals accordingly, scale them to a reference lens and source redshift and compute the weighted average in 25 logarithmic distance bins as follows:

$$\langle \gamma_t \rangle = \frac{\sum E_{\gamma_{t,i}} w_{\gamma_{t,i}}}{\sum w_{\gamma_{t,i}}} \tag{3.25}$$

and similar for the flexions, with the shear estimator and weight

$$E_{\gamma_{t,i}} = \gamma_{t,i} \left(\frac{\eta_i}{\eta_{\rm ref}} \right)^{-1} \qquad w_{\gamma_{t,i}} = \frac{1}{\sigma^2_{\gamma,i}} \left(\frac{\eta_i}{\eta_{\rm ref}} \right)^2 \tag{3.26}$$

where

$$\eta = \frac{D_l D_{ls}}{D_s} \tag{3.27}$$

is the geometric lensing efficiency and $\sigma^2_{\gamma,i} = \sigma^2_{\gamma,{\rm intr},i} + \sigma^2_{\gamma_1,i} + \sigma^2_{\gamma_2,i}$ is the error on the shape measurement with $\sigma_{\gamma,{\rm intr}}$ the intrinsic shear noise. By contrast we use the following F flexion estimator and weight:

$$E_{\mathcal{F}_{t,i}} = \mathcal{F}_{t,i} \left(\frac{D_{l,i}}{D_{l,{\rm ref}}} \frac{\eta_i}{\eta_{\rm ref}} \right)^{-1} \qquad w_{\mathcal{F}_{t,i}} = \frac{1}{\sigma^2_{\mathcal{F},i}} \left(\frac{D_{l,i}}{D_{l,{\rm ref}}} \frac{\eta_i}{\eta_{\rm ref}} \right)^2 \tag{3.28}$$

and similarly for the G flexion.

APPENDIX 3.C: High redshift results

As specified in the main Chapter 3, the lens catalogue we use has a redshift cut of $z < 0.6$. This is to avoid having to go too close to the lens on the sky in order to see a flexion signal. Within an angular radius of 2 arcsec we have low confidence in the results; we are simply too close to the lensing galaxies and it becomes difficult to account for effects induced by the lens light. BOR corrects for light leakage at larger radii, but the correction is most likely incomplete very close to the lens due to deviations from a smooth Sérsic profile. For objects beyond our lens sample, the median redshift is close to 1.0. At this redshift the angular distance limit of 2 arcsec on the sky corresponds to a physical distance of about 17 kpc. The F flexion falls off to low values already at about 20 kpc for a typical galaxy, so we are left with a very low signal within a narrow ring around the lens. Imposing the redshift cut of $z < 0.6$ on lenses gives us a median lens redshift of $z = 0.27$ at which the inner limit corresponds to 9 kpc, leaving a wider distance interval in which we can investigate the F flexion signal.

In Figure 3.13 we show the galaxy-galaxy signal for the high redshift sample, i.e. for lenses with $z > 0.6$. The bins that are within 2 arcsec of the average lens in this sample, and which are most likely contaminated by lens light, are marked with dotted lines. The F flexion signal outside of this limit does agree well with the profile predicted by the shear, but falls off quickly.

APPENDIX 3.D: Comparison with KSB

We compare our galaxy-galaxy shear signal to the one we get using the shears from S10, using all the cuts normally applied in each analysis so that only

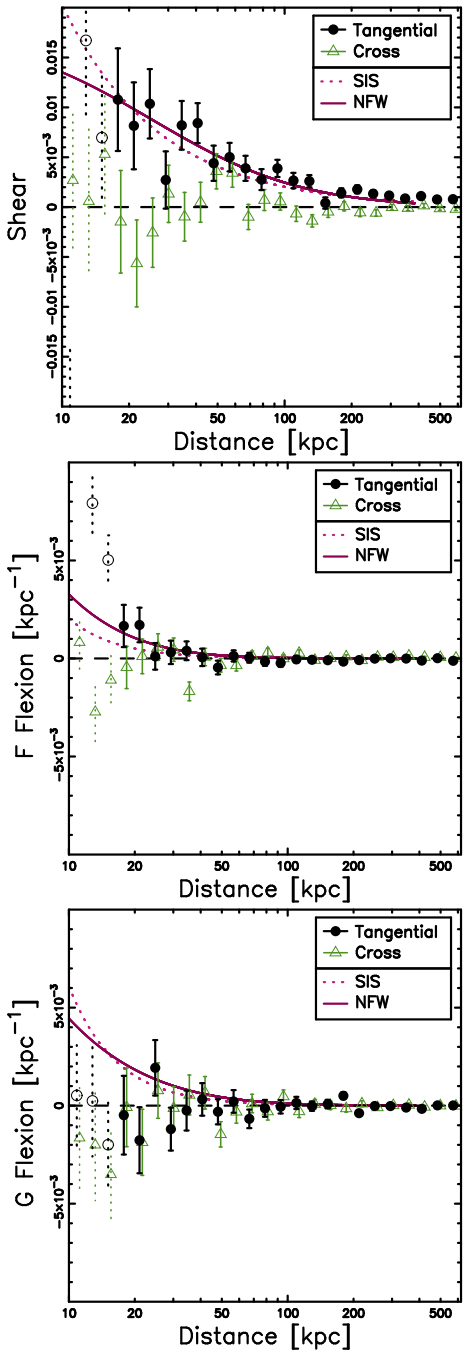

Figure 3.13 The galaxy-galaxy lensing results from running the MV pipeline on the COSMOS data, with $n_{\max} = 10$. Black solid points represent the tangential signal and green triangles represent the cross term. Open circles with dotted error bars are bins that are too close to the lens on the sky. Please note that the SIS and NFW profiles have been fitted to the shear data and then *translated* into predictions for $\mathcal{F}$ and $\mathcal{G}$ curves.

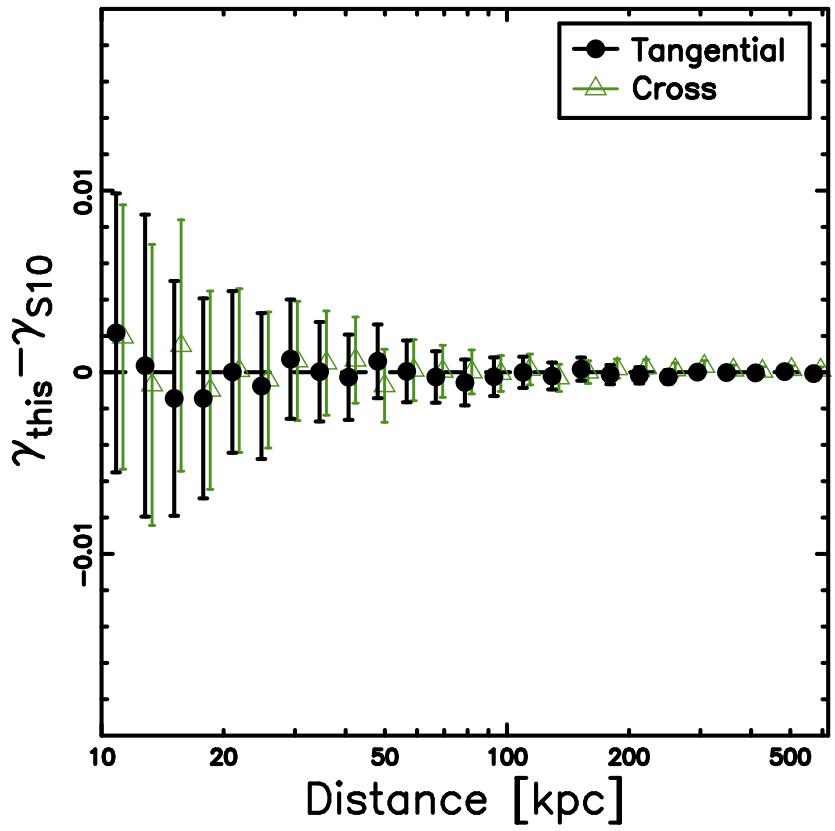

Figure 3.14 A comparison between the shears used in this Chapter and the ones used in S10. Black points (green triangles) show the difference between the tangential (cross) shear values in this Chapter and those produced by a KSB pipeline for S10.

common objects are used. The bias correction described in their paper is incorporated in their shears whilst our measurements have no correction applied. However, due to our S/N cut (see Appendix 3.B1) their correction is always less than 4.2%.

As shown in Figure 3.14 the difference between the results from the two pipelines, KSB and Shapelets, is negligible. This provides an independent confirmation that the MV pipeline produces shears of as high a quality as the state-of-the-art weak lensing analysis presented in S10.

4 The relation between galaxy dark matter haloes and baryons in the CFHTLS from weak lensing

Velander M., van Uitert E., Hoekstra H. and the CFHTLenS Collaboration, in prep.

Current theories of structure formation predict that galaxies are immersed in extensive dark matter haloes. To learn more about the baryon-dark matter connection it is therefore imperative to probe large scales as well as small. Weak galaxy-galaxy lensing has the power to do this since it not only is sensitive on a large range of scales, but also is independent of the type of matter studied. We present a study of large-scale galaxy dark matter halo properties as a function of the characteristics of the baryonic host galaxies using data from one of the largest completed weak lensing surveys to date, the CFHTLS. Dividing our lens sample into red and blue subsamples, we find that for red galaxies, the halo mass scales with luminosity as $M_{200} \propto L_r^{1.28^{+0.10}_{-0.08}}$ and with stellar mass as $M_{200} \propto M_*^{1.36^{+0.10}_{-0.06}}$, while for blue galaxies $M_{200} \propto L_r^{0.50^{+0.18}_{-0.12}}$ and $M_{200} \propto M_*^{0.54^{+0.06}_{-0.08}}$. We also find indications that blue galaxies reside in less clustered environments than red galaxies do.

4.1 Introduction

In order to fully understand the mechanisms behind galaxy formation, the connection between galaxies and the extensive dark matter haloes in which they are enveloped must be studied in exhaustive detail. In pursuit of this precision, reliable mass estimates of both the baryonic and the dark matter content of galaxies are required. The visible component may be evaluated using e.g. the galaxy luminosity or the stellar mass, which can be derived using stellar synthesis models (Kauffmann et al., 2003; Gallazzi et al., 2005; Bell & de Jong, 2001; Salim et al., 2007). The dark matter, on the other hand, cannot be observed directly but must be examined through the influence it has on its surroundings. At the largest scales reached by haloes, optical tracers such as satellite galaxies are scarce. Furthermore, estimates of halo mass from e.g. satellite galaxy kinematics not only require spectroscopic measurements of a large number of objects, which is unfeasible both in terms of time and from a financial perspective, but they also require the application of the virial theorem and all the associated assumptions. To study any and all galaxies it is therefore desirable to use probes independent of these tracers, and independent of the physical state of the halo, but with the power to explore a large range of scales. These requirements are all satisfied by weak gravitational lensing.

Weak gravitational lensing is fundamentally a consequence of general relativity. As light from distant objects travels through the Universe it is deflected by intervening matter. This deflection causes the distant objects, or *sources*, to appear distorted. In the weak regime the distortion is minute, and only by correlating the shapes of a large number of sources can information about the foreground gravitational field be extracted. There are a handful of different ways of correlating these shapes, each resulting in data about a separate category of matter accumulation. By correlating the shape of sources with those of other sources, finely detailed large-scale structure can be discerned in the foreground. The precise properties of this pattern are intimately connected with the composition of our Universe and thus allows for constraints on cosmological parameters via *cosmic shear* (see e.g. Van Waerbeke & Mellier (2003); Hoekstra & Jain (2008); Munshi et al. (2008), for reviews, and e.g. Schrabback et al. (2010) for recent results). Alternatively, source shapes may be correlated with the positions of foreground objects, or *lenses*, through a technique known as *galaxy-galaxy lensing*. The strength of the lensing signal as a function of the distance from the lens holds information on the depth and shape of the potential well causing the distortion. Thus density profiles of the dark matter haloes surrounding galaxies and, equivalently, galaxy clusters may be directly investigated. Simulations predict that dark matter haloes are well approximated by Navarro-Frenk-White profiles (Navarro, Frenk, & White, 1996) and confirming this would provide evidence for the concordance model of cosmology.

Generally, however, galaxies and their haloes are not isolated but reside in clustered environments. The ramification is that the interpretation of the observed galaxy-galaxy lensing signal becomes more complicated since the signal from nearby haloes influence the result. Over the past decade a new approach has gained traction: the weak lensing halo model (e.g. Cooray & Sheth, 2002; Guzik & Seljak, 2002; Mandelbaum et al., 2005; van Uitert et al., 2011; Leauthaud et al., 2011). Within the halo model framework, all haloes are represented

as distinct entities, each with a galaxy at the center. Enclosed in each main halo are satellite galaxies surrounded by subhaloes. In this work we seek to employ the halo model to gain a more accurate picture of galaxy-size dark matter haloes, allowing for a more precise analysis of the link between galaxies and the dark matter haloes they reside in. For this purpose we use data from the Canada-France-Hawaii Telescope Legacy Survey (CFHTLS). The CFHTLS consists of just over 170 deg^2 of images in five filters ($u^*g'r'i'z'$) to the impressive depth of $i' = 24.5$. The CFHTLS weak lensing collaboration (CFHTLenS) has extracted 8.7×10^6 galaxy shears, and provided all objects with reliable photometric redshifts, making this survey one of the most powerful completed weak lensing surveys to date. This work thus improves on the preliminary galaxy-galaxy lensing analysis carried out using a small subset of the CFHTLS data and a single-halo model fit to the inner regions only (Parker et al., 2007).

This Chapter is organised as follows: we introduce the data in Section 4.2. In Section 4.3 we review our halo model and the formalism behind it, and in Section 4.4 we test our shear catalogue for systematic effects. We investigate the lensing signal as a function of luminosity in Section 4.5 and as a function of stellar mass in Section 4.6, and we conclude in Section 4.7. The following cosmology is assumed throughout (WMAP7; Komatsu et al., 2010): $(\Omega_M, \Omega_\Lambda, h, \sigma_8, w) = (0.27, 0.73, 0.70, 0.81, -1)$

4.2 Data

In this Chapter we present a weak lensing analysis of the entire Wide Synoptic Survey of the Canada-France-Hawaii Telescope Legacy Survey (CFHTLS-Wide). The impressive expanse and depth of this survey makes it ideal for weak lensing analyses, as we will show. The CFHTLS is a joint 5-year project between Canada and France which commenced in 2003 and which is now completed. The data are imaged using the Megaprime wide field imager mounted at the prime focus of the Canada-France-Hawaii Telescope (CFHT) and equipped with the MegaCam camera. MegaCam comprises an array of 9×4 CCDs and has a field of view of 1 deg^2. The wide synoptic survey covers an effective area of about 155 deg^2 in five bands: u^*, g', r', i' and z'. This area is composed of four independent fields, W1–4, each with an area of 25-72 deg^2 and with a full multi-colour depth of $i' = 24.7$ (7σ detected source in the CFHTLenS[1] catalogue). The images have been independently reduced within the CFHTLenS Collaboration, and for details on this data reduction process, please refer to Erben et al (in prep.).

4.2.1 Lens sample

The depth of the CFHTLS enables us to investigate lenses with a large range of lens properties and redshifts, which in turn grants us the opportunity to thoroughly study the evolution of galaxy-sized dark matter haloes. An initial study was performed by van Uitert et al. (2011) (hereafter VU11) using the same halo model as the one used here, described in Section 4.3.2. That study exploited a 300 deg^2 overlap between two major lensing surveys. The foreground sample consisted of galaxies from the seventh data release of the Sloan Digital Sky

[1] `http://cfhtlens.org`

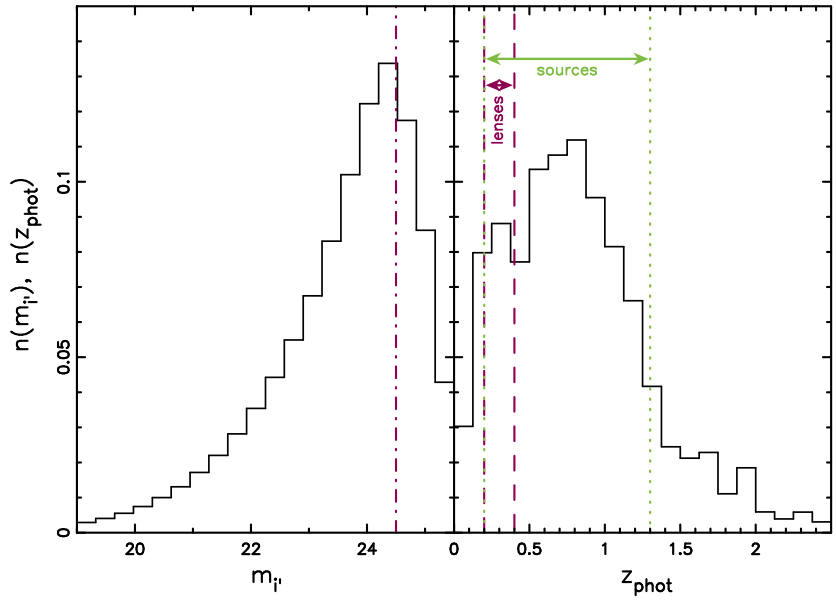

Figure 4.1 Magnitude (left panel) and photometric redshift (right panel) distributions of all objects in the CFHTLenS catalogue, with our lens (source) redshift selection marked with purple dashed (green dotted) lines. Also shown is the cutoff-point in magnitude for all objects used in our analysis (purple dash-dotted).

Survey (SDSS DR7; Abazajian et al., 2009), and objects from the intermediate-depth Second Red Sequence Cluster Survey (RCS2; Gilbank et al., 2011) were used as background sources, improving greatly on previous analyses based on the shallow SDSS alone. However, while their lenses had accurate spectroscopic redshift estimates, their sources did not have enough photometric data available at the time to provide redshift estimates for the sources. Thus the CFHTLS has, aside from the increased depth, a further advantage over the VU11 analysis owing to the high-precision photometric redshifts available for all objects used in our analysis.

Throughout this Chapter, we place an upper cut in apparent magnitude of $i' \leq 24.5$ and select our lenses in redshift such that $0.2 \leq z_{\rm lens} \leq 0.4$, unless explicitly stated otherwise. These selections are illustrated in Figure 4.1. For the full CFHTLS-Wide we achieve a lens count of $N_{\rm lens} = 1.53 \times 10^6$, nearly a hundred times the size of the lens sample used in VU11. We then further split our lens sample in luminosity or stellar mass bins as described in Sections 4.5 and 4.6 to investigate the halo mass trends as a function of lens properties.

4.2.2 Source catalogue

The shear estimates for the sources used in this Chapter have been obtained using LENSFIT as detailed in Miller et al (in prep.), and thoroughly tested by the CFHTLenS Collaboration. During the testing process, the LENSFIT shears were compared to those extracted using other shape measurement methods (such as those introduced in Hoekstra et al., 1998; Kuijken, 2006; Schrabback et al.,

2007; Velander et al., 2011) to successfully eliminate software-specific issues. All sources also have multi-band photometric redshift estimates as described in Hildebrandt et al. (2012).

To ensure photometric accuracy, we use only sources with redshifts of $z_{\rm lens} \leq z_{\rm source} \leq 1.3$, and we impose the same cut in magnitude as we do for the lenses: $i' \leq 24.5$. Furthermore, we ensure that our sources have been detected in at least six exposures. Our source count for the full CFHTLS-Wide (excluding masked areas) is then $N_{\rm source} = 3.9 \times 10^6$, corresponding to a source density of 9.3 arcmin^{-2} which is a factor of 1.5 greater than that of the RCS2.

4.3 Method

To analyse the dark matter haloes in the CFHTLS we use a method known as weak galaxy-galaxy lensing, and compare the measured signal with a halo model. In this section we will introduce the basic formalism and give an overview of our halo model.

4.3.1 Weak galaxy-galaxy lensing

Weak gravitational lensing is the measure of weak distortions induced by foreground structure on background source galaxies. By correlating the shapes of background galaxies, statistical properties of the matter in the foreground can be inferred.

The first-order lensing distortion, shear, is a stretch in one direction which is applied to the intrinsic shape of a source galaxy. By averaging over enough randomly oriented sources we can assume the mean intrinsic galaxy to be circular, and thus any distortion measured is due to lensing. In this analysis we use galaxy-galaxy lensing where source galaxy distortions are averaged in concentric rings centered on lens galaxies. We measure the tangential shear as a function of radial distance from the lens this way, and also the cross shear which is a 45deg rotated signal. The cross shear can never be induced by a lens which means that it may be used as a systematics check. The amplitude of the tangential shear is directly related to the differential surface density $\Delta\Sigma(r)$ via

$$\Delta\Sigma(r) = \Sigma_{\rm crit}\langle\gamma_t(r)\rangle \tag{4.1}$$

where $\Sigma_{\rm crit}$ is the critical surface density

$$\Sigma_{\rm crit} = \frac{c^2}{4\pi G}\frac{D_s}{D_l D_{ls}} \tag{4.2}$$

with D_s, D_l and D_{ls} the angular diameter distance to the source, to the lens and between the lens and source respectively. By using differential surface densities rather than tangential shears, the geometric factor is neutralised and the amplitude of the signals can be directly compared between different samples. The only caveat is that the properties of lenses depend on the lens redshift so this difference still has to be taken into account.

The circular average makes this type of analysis robust against small-scale systematics introduced by e.g. the telescope. None the less, there will be large-scale systematics present, mainly due to areas being masked. By masking areas,

or by considering lenses close to the edge of the area covered, the circular average is in fact not perfectly circular. This effect, most noticeable on large scales, is important to correct for, particularly in the case of precision galaxy-galaxy lensing such as the analysis in this Chapter. Our correction is done by measuring the signal around random lens positions. Were there no systematics present the measured signal would be zero. If it is not, it can easily be corrected for by subtracting it from the observed lensing signal.

As for any concerns regarding the fidelity of the photometric redshifts, the weights we employ use the geometric lensing efficiency $D_s/(D_l D_{ls})$ to down-weight close pairs as described in e.g. Velander et al. (2011) (Chapter 3 of this Thesis), effectively minimising any influence of redshift inaccuracies on the measured signal. Additionally we calculate a correction factor based on the redshift error distribution for each mass estimate to remove any remaining redshift systematics. This calculation is described further in Section 4.5.1.

4.3.2 The halo model

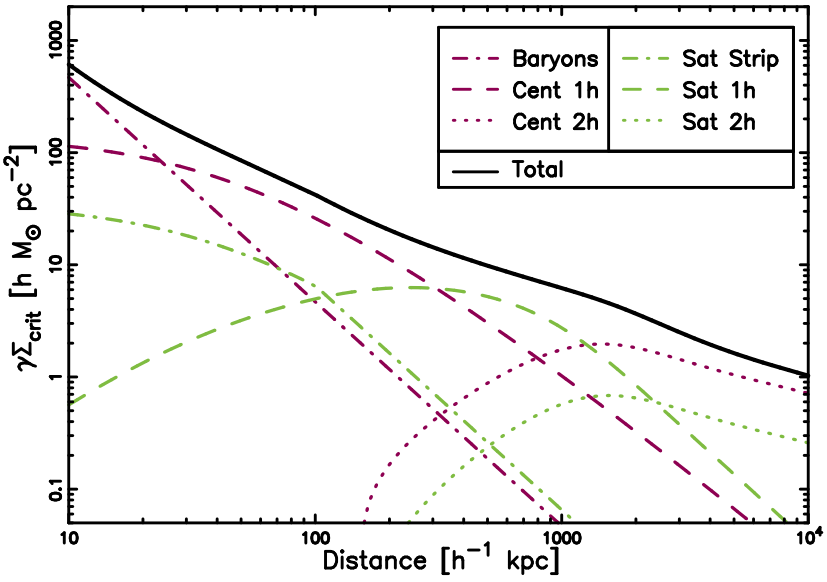

Figure 4.2 Illustration of the halo model used in this Chapter. Here we have used a halo mass of $M_{200} = 10^{12}\ h^{-1}\ M_\odot$, a stellar mass of $M_* = 3 \times 10^{11}\ M_\odot$ and a satellite fraction of $\alpha = 0.2$. The lens redshift is $z_{\rm lens} = 0.5$. Purple lines represent quantities tied to galaxies which are centrally located in their haloes while green lines correspond to satellite quantities. The purple dash-dotted line is the baryonic component, the green dash-dotted line is the stripped satellite halo, dashed lines are the 1-halo components induced by the main dark matter halo and dotted lines are the 2-halo components originating from nearby haloes.

To accurately model the weak lensing signal observed around galaxy-size haloes, we have to account for the fact that galaxies generally reside in clustered environments. In this work we do this by employing the halo model software first introduced in VU11. For full details on the exact implementation, please

see VU11; here we give a qualitative overview.

Our halo model builds on work presented in Guzik & Seljak (2002) and Mandelbaum et al. (2005), where the full lensing signal is modelled by accounting for the central galaxies and their satellites separately. Here we assume that a fraction $(1-\alpha)$ of our galaxy sample reside at the centre of a dark matter halo, and the remaining objects are satellite galaxies surrounded by subhaloes which in turn reside inside a larger halo. In this context α is the *satellite fraction* of a given sample.

The lensing signal induced by central galaxies consists of two components: the signal arising from the main halo (the *1-halo* term $\Delta\Sigma^{\rm 1h}$) and the contribution from neighbouring haloes (the *2-halo* term $\Delta\Sigma^{\rm 2h}$). The two components simply add to give the lensing signal due to central galaxies:

$$\Delta\Sigma_{\rm cent} = \Delta\Sigma^{\rm 1h}_{\rm cent} + \Delta\Sigma^{\rm 2h}_{\rm cent} \tag{4.3}$$

In our model we assume that all main dark matter haloes are well represented by a Navarro-Frenk-White density profile (NFW; Navarro, Frenk, & White, 1996) with a mass-concentration relationship as given by Duffy et al. (2008).

We assume that satellite galaxies reside in subhaloes which have been tidally stripped of dark matter in the outer regions. Adopting a truncated NFW profile which has been stripped of about 50% of its dark matter, we acquire a satellite term which supplies signal on small scales. Thus satellite galaxies add three further components to the total lensing signal: the contribution from the stripped subhalo ($\Delta\Sigma^{\rm strip}$), the satellite 1-halo term which is off-centred since the satellite galaxy is not at the centre of the main halo, and the 2-halo term from nearby haloes. Just as for the central galaxies, the three terms add to give the satellite lensing signal:

$$\Delta\Sigma_{\rm sat} = \Delta\Sigma^{\rm strip}_{\rm sat} + \Delta\Sigma^{\rm 1h}_{\rm sat} + \Delta\Sigma^{\rm 2h}_{\rm sat} \tag{4.4}$$

There is an additional contribution to the lensing signal, not yet considered in the above equations. This is the signal induced by the lens baryons ($\Delta\Sigma^{\rm bar}$). This last term is a refinement to the halo model presented in VU11, necessary since weak lensing measures the total mass of a system and not just the dark matter mass. The baryonic component is modelled as a point source with a mass equal to the mean stellar mass of the lenses in the sample (as in e.g. Leauthaud et al., 2011):

$$\Delta\Sigma^{\rm bar} = \frac{\langle M_* \rangle}{\pi r^2} \tag{4.5}$$

where r is the physical distance from the lens. This term could technically be decomposed into a central and a satellite component. In this work we do not leave the baryon term as a free variable and so we do not need to distinguish between the two. Thus we treat this term as a single entity.

Finally, to obtain the total lensing signal of a galaxy sample of which a fraction α are satellites we combine the baryon, central and satellite galaxy signals, applying the appropriate proportions:

$$\Delta\Sigma = \Delta\Sigma^{\rm bar} + (1-\alpha)\Delta\Sigma_{\rm cent} + \alpha\Delta\Sigma_{\rm sat} \tag{4.6}$$

All components of our halo model are illustrated in Figure 4.2. In this example the halo mass is $M_{200} = 1 \times 10^{12}\ h^{-1} M_\odot$, the stellar mass is $M_* =$

$3 \times 10^{11}\ M_{\odot}$, the satellite fraction is $\alpha = 0.2$, the lens redshift is $z_{\rm lens} = 0.5$ and $D_{ls}/D_s = 0.5$. On small scales the baryonic component is prominent, while on large scales the 2-halo components dominate.

4.4 Systematics tests

4.4.1 Verification of the shear catalogue

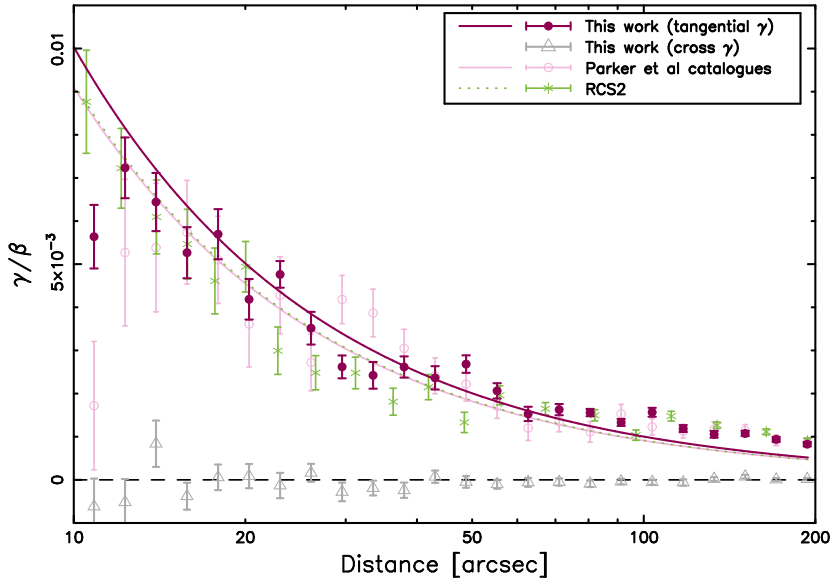

Figure 4.3 Comparison of three data sets: the KSB catalogues from ~ 22 deg^2 CFHTLS (pink circles), the results from RCS2 (green stars) and our results (purple dots). The lines show the best fit singular isothermal sphere for each dataset (with green and pink nearly identical), and the grey triangles show the cross-shear from our results which should be zero in the absence of systematic errors.

In this study we use lenses and sources from the 155 deg^2 CFHTLS, with high-quality photometric data and redshifts available for all objects. To validate the quality of our shear catalogue we compare with the results from two previous analyses of a very similar nature. The first is a preliminary weak galaxy-galaxy lensing analysis of the CFHTLS-Wide conducted by Parker et al. (2007). At that time, the survey was not yet finished, so they only had access to an area of ~ 22 deg^2 in i'-band corresponding to about 15% of our area. Since they only had data from one band their analysis also lacked redshift estimates for lenses and sources, but they separated lenses from sources using magnitude cuts. They then obtained shear estimates for their sources using a version of the technique introduced by Kaiser, Squires, & Broadhurst (1995) as outlined in Hoekstra et al. (1998). For their average lens they derived a best-fit velocity dispersion of $\sigma_v = 132 \pm 10$ km s^{-1} using a singular isothermal sphere profile (SIS) to model the lensing signal, though there is some disagreement between this number and our findings (see discussion below). The second analysis is based on the shear

Table 4.1 Details of the seeing bins.

Sample	$N_{\rm fields}$	$\langle r_* \rangle$ [arcsec]	θ_E [arcsec]	σ_{θ_E}
P1	27	0.50	0.053	0.005
P2	23	0.57	0.044	0.006
P3	33	0.62	0.050	0.005
P4	38	0.67	0.047	0.005
P5	28	0.72	0.040	0.006
P6	36	0.80	0.049	0.005

catalogue from VU11 (see Section 4.2). The data used in that study is from the RCS2 which is slightly shallower than the CFHTLS and for which no redshifts were available for the sources at the time of this analysis.

To compare and contrast our lensing signal with the one obtained by Parker et al. (2007) we apply the same i'-band magnitude cuts as they did, viz. $19.0 < i' < 22.0$ for lenses and $22.5 < i' < 24.5$ for sources. A slight difference between their analysis and ours is that Parker et al. (2007) boosts their signal by an approximate factor to correct for contamination by sources that are in front of, or physically associated with, the lens while we use our redshift information to minimise this contamination. The resulting galaxy-galaxy signal, scaled with the angular diameter distance ratio $\beta = D_{ls}/D_s = 0.67$, is shown as purple dots in Figure 4.3. The best-fit SIS profile corresponds to a velocity dispersion of $\sigma_v = 83.3 \pm 1.6$ km s^{-1}, which is somewhat lower than the one quoted in Parker et al. (2007). However, we re-analysed the actual shear catalogues used for the Parker et al. (2007) analysis and the results are shown as light circles in Figure 4.3. For that signal, which is corrected for contamination using the Parker et al. (2007) boost factor, we find a velocity dispersion of $\sigma_v = 79.4 \pm 3.3$ km s^{-1} using the redshifts stated in Parker et al. (2007). This is in good agreement with our analysis of the full CFHTLS-Wide. The discrepancy with the velocity dispersion quoted in Parker et al. (2007) remains unexplained, but we have shown that the shear estimates are consistent between the two CFHTLS catalogues.

Furthermore, also shown as green stars in Figure 4.3 is the signal obtained by VU11 using RCS2 and the same magnitude selection as Parker et al. (2007). The shears have been corrected for contamination by physically associated sources, as described in VU11, and scaled with the $\beta = 0.48$ appropriate for the RCS2. For this signal we find a velocity dispersion of $\sigma_v = 79.7 \pm 2.3$ km s^{-1} which is again in good agreement with our results. Based on this, and based on our re-analysis of the original Parker et al. (2007) shear catalogues, we conclude that our shear estimates are valid and reliable for further galaxy-galaxy lensing studies.

4.4.2 Seeing test

In general a round PSF causes circularisation of source images which in turn causes a multiplicative bias of the shapes measured. The amount of bias depends on the size of the PSF. Assuming that the shapes of very well resolved galaxies

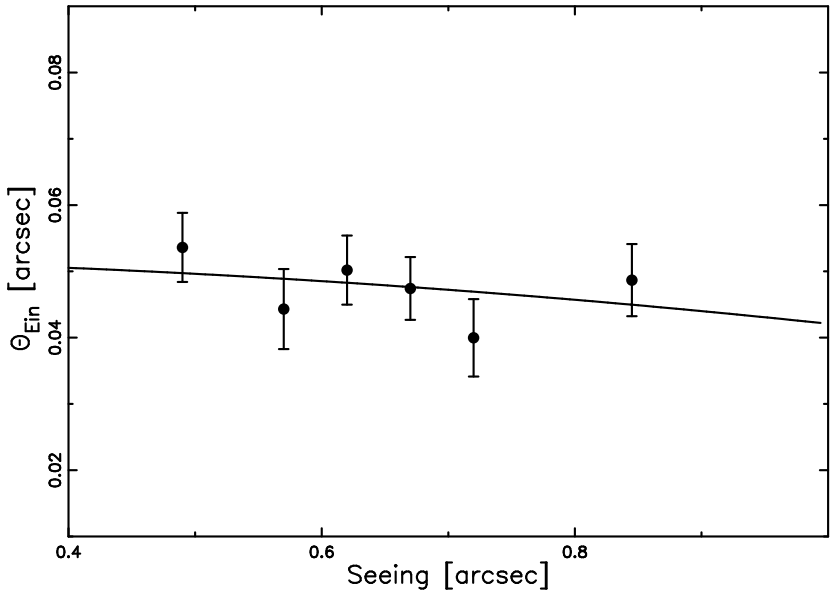

Figure 4.4 The weak galaxy-galaxy signal measured in each of 6 seeing bins, according to Table 4.1.

can be accurately recovered we can model the effect of the PSF as

$$\gamma^{\rm obs} = \gamma^{\rm true}\left[1 + \mathcal{M}\left(\frac{r_*}{r_0}\right)^2\right] \tag{4.7}$$

where $\gamma^{\rm obs}$ is the observed shear, $\gamma^{\rm true}$ is the true shear, r_* is the PSF size and r_0 is the intrinsic (Gaussian) size of the galaxy. The particular dependence on PSF size is the result of a full moments analysis. $\mathcal{M}$ is a function close to zero representing the multiplicative bias and may be separated into two components:

$$\mathcal{M} = \mathcal{M}' + \mathcal{P} \tag{4.8}$$

where $\mathcal{M}'$ is the true limitation of the shape measurement method and $\mathcal{P}$ is the bias contribution induced by the PSF. This last term depends on the statistical and systematic errors in the size estimates. Thus if the shape measurement software has no intrinsic bias and if the PSF is perfectly known, then the dominant source of shear bias is the accuracy of the size estimates of the faint, small galaxies. For the Bayesian shape measurement method used in this Chapter, LENSFIT, this term will be negligible.

This multiplicative bias may be related to the parameterisation used in the Shear Testing Programme (STEP Heymans et al., 2006a; Massey et al., 2007a), $m_{\rm STEP}$, via

$$m_{\rm STEP} = \mathcal{M}\left\langle\left(\frac{r_*}{r_0}\right)^2\right\rangle \tag{4.9}$$

The smallest bias achieved by the pipelines taking part in STEP was $m_{\rm STEP} \sim 0.01$ which, for the adopted size distribution and simulated ground-based data used in STEP, corresponds to $\mathcal{M} \sim 0.005$.

Since the bias depends on the size of the PSF, data with a spread in seeing should enable us to determine the bias $\mathcal{M}$ directly from the data, thus allowing us to deduce the true performance of the shape measurement pipeline. The CFHTLS has such a spread, with the best seeing being 0.44 arcsec and the worst being 0.94 arcsec.

Galaxy-galaxy lensing provides us with a neat way of determining the bias. Assuming that the systematic offset due to PSF anisotropy is negligible (a fair assumption given our correction for spurious signal around random lenses; see Section 4.3.1) the observed shear is related to the true shear via

$$\gamma^{\rm obs} = (1 + m_{\rm STEP})\gamma^{\rm true} \tag{4.10}$$

For a singular isothermal sphere (SIS), the amplitude of the shear signal as a function of distance θ from the lens is

$$\gamma(\theta) = \frac{\theta_E}{2\theta} \tag{4.11}$$

where θ_E is the Einstein radius. Thus there is a simple relationship between the observed Einstein radius and the true one:

$$\theta_E^{\rm obs} = \left(1 + \mathcal{M}\left\langle\left(\frac{r_*}{r_0}\right)^2\right\rangle\right)\theta_E^{\rm true} \tag{4.12}$$

By measuring the Einstein radius of the average lens as a function of seeing we can therefore determine both the true Einstein radius and the performance of the shape measurement pipeline.

We split the data according to Table 4.1, measure the galaxy-galaxy lensing signal in each seeing bin and fit an SIS to the innermost 140 h^{-1} kpc. By fitting only small scales we avoid the influence of neighbouring haloes. The results are shown in Figure 4.4 and quoted in Table 4.1. We then fit the relation described by Equation 4.12 to the resulting Einstein radii and find a value of $\mathcal{M} = -0.048 \pm 0.071$ which implies a STEP bias of $m_{\rm STEP} = -0.094 \pm 0.14$. This is consistent with no bias given the error bars, but with a greater range in seeing we would be able to constrain this bias even further. According to this analysis, the true Einstein radius of the average lens galaxy in our sample is $\theta_E^{\rm true} = 0.052" \pm 0.007"$.

4.5 Luminosity trend

The luminosity of a galaxy is an easily obtainable indicator of its baryonic content. To investigate the relation between dark matter halo mass and galaxy mass we therefore split the lenses into 8 bins according to MegaCam r'-band magnitudes as detailed in Table 4.2 and illustrated in Figure 4.5. The choice of bin limits follow the lens selection in VU11, a previous analysis carried out using the shallower RCS2 and an earlier version of the halo model we use here. This choice will allow us to compare our results to the results obtained by VU11 because the RCS2 data have been obtained using the same filters and telescope. Since the behaviour of early-type galaxies is expected to differ from that of late-type galaxies, using only one luminosity estimate to characterise a lens sample results in an average relation which may be difficult to interpret.

Table 4.2 Details of the luminosity bins. (1) Absolute magnitude range; (2) Number of lenses; (3) Mean redshift; (4) Fraction of lenses that are blue; (5) Mean luminosity for red lenses [10^{10} $L_\odot$]; (6) Mean stellar mass for red lenses [10^{10} $M_\odot$]; (7) Redshift-corrected best-fit halo mass for red lenses [10^{11} h^{-1} $M_\odot$]; (8) Best-fit satellite fraction for red lenses; (9) Mean luminosity for blue lenses [10^{10} $L_\odot$]; (10) Mean stellar mass for blue lenses [10^{10} $M_\odot$]; (11) Redshift-corrected best-fit halo mass for blue lenses [10^{11} h^{-1} $M_\odot$]; (12) Best-fit satellite fraction for blue lenses

Sample	$M_r{}^{(1)}$	$n_{\rm lens}{}^{(2)}$	$\langle z\rangle^{(3)}$	$f_{\rm blue}{}^{(4)}$	$\langle L_r^{\rm red}\rangle^{(5)}$	$\langle M_*^{\rm red}\rangle^{(6)}$	$M_h^{\rm red(7)}$	$\alpha^{\rm red(8)}$	$\langle L_r^{\rm blue}\rangle^{(9)}$	$\langle M_*^{\rm blue}\rangle^{(10)}$	$M_h^{\rm blue(11)}$	$\alpha^{\rm blue(12)}$
L1	[-21.0,-20.0]	89215	0.30	0.61	0.91	4.72	$2.36^{+0.68}_{-0.53}$	$0.30^{+0.02}_{-0.02}$	0.83	2.48	$0.87^{+0.57}_{-0.35}$	$0.00^{+0.01}_{-0.00}$
L2	[-21.5,-21.0]	31889	0.30	0.40	1.76	8.97	$4.39^{+1.40}_{-1.06}$	$0.20^{+0.03}_{-0.02}$	1.71	5.12	$1.78^{+1.18}_{-0.71}$	$0.00^{+0.03}_{-0.00}$
L3	[-22.0,-21.5]	22492	0.30	0.29	2.77	14.1	$4.55^{+1.45}_{-1.10}$	$0.24^{+0.03}_{-0.03}$	2.71	8.16	$3.39^{+2.50}_{-1.44}$	$0.00^{+0.02}_{-0.00}$
L4	[-22.5,-22.0]	13105	0.30	0.21	4.32	22.1	$10.4^{+3.30}_{-2.50}$	$0.20^{+0.03}_{-0.03}$	4.28	12.9	$0.87^{+1.53}_{-0.82}$	$0.13^{+0.06}_{-0.06}$
L5	[-23.0,-22.5]	5840	0.30	0.15	6.75	34.6	$17.5^{+5.58}_{-4.23}$	$0.22^{+0.04}_{-0.04}$	6.71	20.2	$0.53^{+2.60}_{-0.52}$	$0.04^{+0.10}_{-0.10}$
L6	[-23.5,-23.0]	1769	0.29	0.12	10.5	53.8	$39.4^{+13.7}_{-10.2}$	$0.17^{+0.06}_{-0.06}$	10.8	32.0	$0.99^{+6.50}_{-0.98}$	$0.27^{+0.22}_{-0.22}$
L7	[-24.0,-23.5]	389	0.29	0.16	16.5	84.0	$132^{+46.1}_{-34.2}$	$0.01^{+0.11}_{-0.11}$	17.3	49.7	$0.01^{+6.04}_{-0.00}$	$0.00^{+0.18}_{-0.00}$
L8	[-24.5,-24.0]	87	0.27	0.24	25.8	132	$167^{+137}_{-75.2}$	$0.38^{+0.26}_{-0.26}$	29.6	84.2	$7.48^{+31.8}_{-7.47}$	$0.00^{+0.25}_{-0.00}$

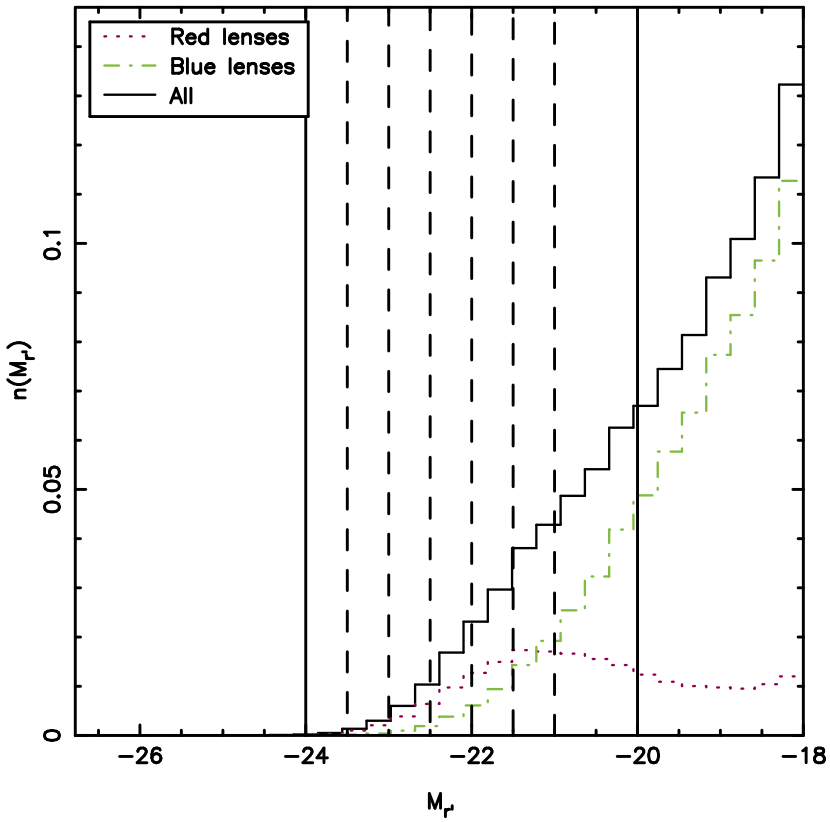

Figure 4.5 r'-band absolute magnitude distribution in the CFHTLS for lenses with redshifts $0.2 \leq z_{\rm lens} \leq 0.4$ (black solid histogram). The distribution of red (blue) lenses is shown in dotted purple (dot-dashed green). Our lens bins are marked with vertical lines.

Since we have access to multi-colour data, we are able to further divide our lenses in each bin into a red and a blue sample, approximately corresponding to early-type and late-type galaxies. In practice we do this using their photometric types $T_{\rm BPZ}$. $T_{\rm BPZ}$ is a number in the range of $[1.0, 6.0]$ representing the best-fit spectral energy distribution (SED) and we define our red and blue samples as galaxies with $T_{\rm BPZ} < 1.5$ and $T_{\rm BPZ} > 2.0$ respectively where the latter captures most spiral galaxies. A colour-colour comparison confirms that these samples are well defined. We proceed to measure the galaxy-galaxy lensing signal for each sample, and fitting it with our halo model, leaving the halo mass M_{200} and the satellite fraction α as free parameters. The results are shown in Figure 4.6 for all luminosity bins and for each red and blue lens sample, with details of the fitted halo model parameters quoted in Table 4.2. Qualitatively comparing these results to the ones presented in VU11 we see that the amplitudes of the signals agree well.

An overview of the broad trends in Figure 4.6 is given in Figure 4.7 for red galaxies and Figure 4.8 for blue. As expected, the amplitude of the signal increases with luminosity for both red and blue samples indicating an increased

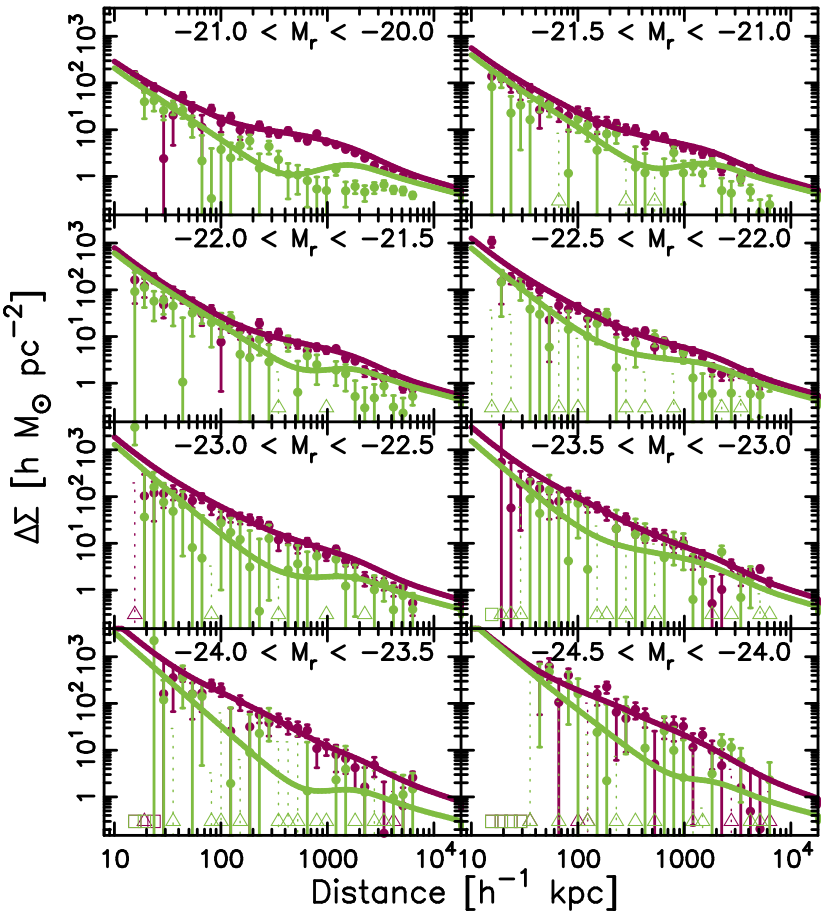

Figure 4.6 The weak galaxy-galaxy signal around lenses which have been split into luminosity bins according to Table 4.2, modelled using the halo model described in Section 4.3.2. The purple (green) dots represent the measured differential surface density of the red (blue) lenses, and the solid line is the best-fit halo model. Triangles represent negative points that are included unaltered in the model fitting procedure, but that have here been moved up to positive values as a reference. The dotted error bars are the unaltered error bars belonging to the negative points. The squares represent distance bins containing no objects. For a detailed decomposition into the halo model components, please refer to Appendix 4.A.

halo mass. In general, for identical luminosity selections blue galaxies have less massive haloes than red do. For the red sample, lower luminosity bins display a slight bump at scales of $\sim 0.5\ h^{-1}$ Mpc. This is due to the satellite 1-halo term becoming significant and indicates that a large fraction of the galaxies in those bins are in fact satellite galaxies inside a larger halo. Thus brighter galaxies are more likely to be centrally located in a halo. The blue galaxies also display a bump for the lower luminosity bins, but this feature is at larger scales than the satellite 1-halo term. The signal breakdown shown in Figure 4.20 (Appendix 4.A) reveals that this bump is due to the central two-halo term, i.e. it

is the contribution from nearby haloes.

To make a quantitative comparison with VU11, however, there are several differences between the analyses that have to be taken into account. Firstly, including the baryonic component in our halo model results in a lower halo mass estimate than not doing so (see Section 4.5.2 and Figure 4.12 for a more extensive discussion on this topic). This is intuitive since gravitational lensing measures the total mass of a system and we are allowing some of that mass to be baryonic, leaving less mass for the dark matter halo. Secondly, the red and blue selection in our analysis does not necessarily correspond to the early- and late-type classification in VU11, making a completely fair comparison difficult. Thirdly, we have a strong enough signal to be able to limit our lens sample to a small redshift range, which minimises any contamination of the relations due to redshift evolution. Finally, we do not have spectroscopic redshifts for our lenses which means that our lenses may have been assigned an inaccurate redshift. This will cause a luminosity-dependent bias in the halo mass estimate, as discussed in e.g. Hoekstra et al. (2005). We will examine this effect further in the next Section.

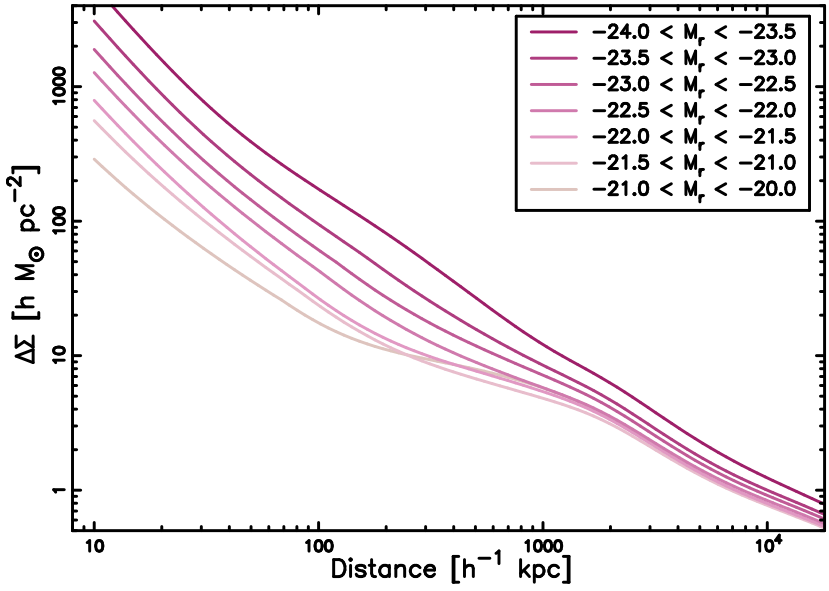

Figure 4.7 Best-fit halo models for red lenses for all luminosity bins.

4.5.1 Photometric redshift error corrections

Before interpreting the luminosity results we have to take into account the redshift bias effect previously mentioned. The accuracy of our photometric redshifts is high, but never the less the errors on the redshift estimates have to be taken into account. If the true redshift differs from the estimated one, this will affect all derived quantities. An underestimated redshift, for example, would cause the estimated absolute magnitude to be fainter than the true absolute magnitude and the lens would be placed in the wrong luminosity bin. As can be seen in Fig-

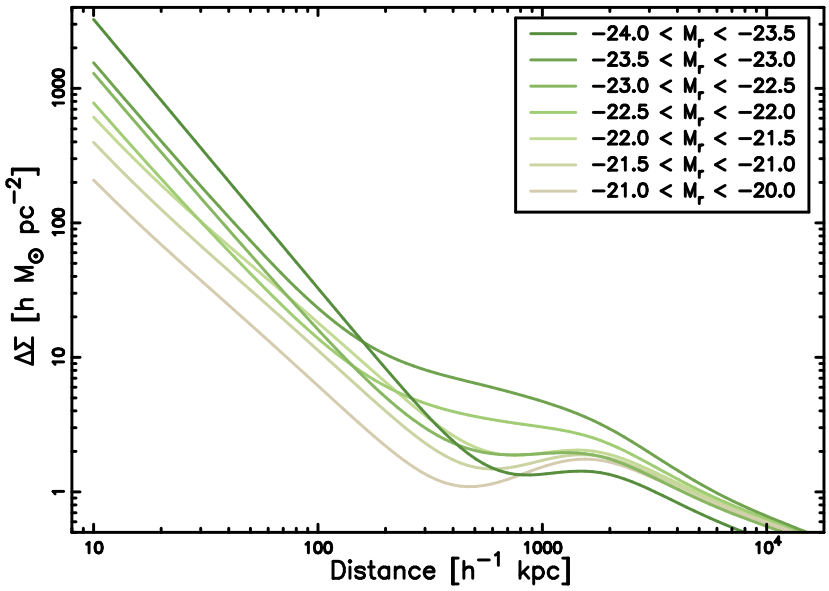

Figure 4.8 Best-fit halo models for blue lenses for all luminosity bins.

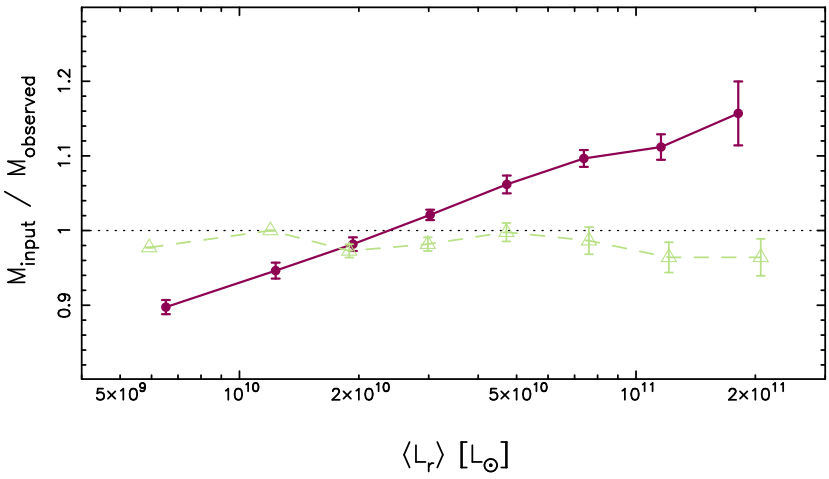

Figure 4.9 Bias as a function of luminosity induced through inaccuracies in the photometric redshift estimates. The purple solid (green dashed) line with dots (triangles) shows the bias for the red (blue) lens sample. The error bars are obtained using ten lens catalogue realisations.

ure 4.5 there are more faint objects than bright, which means that more objects will scatter from fainter bins into brighter bins than the other way around. This will lower the lensing signal in each bin and bias the observed halo mass low, and the amount of bias will be luminosity dependent. To estimate the impact of this bias we create a simulated version of the CFHTLS-Wide as follows. We fit an initial powerlaw mass-luminosity relation of the form $M_{200} = M_{0,L}(L/L_{\rm pivot})^{\beta_L}$ to the estimated halo masses as described in VU11, with $L_{\rm pivot} = 10^{11}\ L_{r',\odot}$.

This relation we then use to assign halo masses to our lenses. Constructing NFW haloes from these halo masses at the photometric redshift of the lenses, we create mock source catalogues with the observed source redshift distribution but with simulated shear estimates with strengths corresponding to those which would be induced by our lens haloes. Finally we measure the mock signal within 200 h^{-1} kpc of the lenses in each luminosity bin and take this to be the 'true' signal. We only use the small scales for our mass estimate to avoid complications due to insufficient treatment of clustering, and we force our satellite fraction to zero to obtain a pure NFW fit. Scattering the lenses, assuming a Gaussian error distribution of width $\Delta z = (0.004 m_{i'} - 0.04)(1 + z)$ (see Hildebrandt et al. (2012) for a plot of the photometric redshift errors as a function of magnitude), we then measure the signal in each of 10 realisations and compare the resulting estimated halo masses to the 'true' halo masses. The average of these realisations provides the observed halo mass given the bias, with errors equal to the standard deviation. Since the starting point is a perfect signal, the number of realisations given the area is adequate to retrieve the bias.

The results from this test are shown in Figure 4.9. The quality of our photometric redshifts is high which means that the correction factor is small overall, reaching only $\sim 15\%$ for a luminosity of $L_{r'} \sim 2.5 \times 10^{11}\ L_{\odot}$. Here the contamination is largest due to the shape of the luminosity function causing a larger fraction of low luminosity objects to scatter into the higher-luminosity bin. For our faintest red luminosity bin the correction is $\sim 10\%$, in this case caused by larger errors in the photometric redshift estimates. The correction factor is less than unity for lower-luminosity bins due to the turn-over of the distribution of red lenses at $M_{r'} \sim -21.2$ (see Figure 4.5). The small correction factor for blue lenses is due to their flatter mass-luminosity relation (see Figure 4.10). Because of the relative insensitivity of halo mass to changes in luminosity, minor errors in luminosity measurements due to photometric redshift inaccuracies will not strongly affect the halo mass estimate. The process described in this section could in principle be iterated over, starting from the fitting of a mass-luminosity relation, until convergence is reached. Since Hoekstra et al. (2005) find that different choices for that relation yield similar curves, we choose not to iterate further.

4.5.2 Luminosity scaling relations

The estimated halo masses for all luminosity bins, corrected for bias due to errors in the photometric redshifts, are shown as a function of luminosity in the top panel of Figure 4.10. Red lenses display a steeper relationship between halo mass and luminosity than blue lenses do, and the higher luminosity bins contain too few blue lenses to adequately constrain the mass. As done in VU11, we fit a powerlaw of the form $M_{200} = M_{0,L}(L/L_{\rm pivot})^{\beta_L}$ to our lensing signal, with $L_{\rm pivot} = 10^{11} L_{r',\odot}$. Rather than fitting to the final mass estimates we fit this relation directly to the lensing signals themselves. We do this because the error bars are asymmetric in the former case, making a fit more complicated. The difference in results between the two fitting techniques is small however.

For our red lenses we find $M_{0,L} = 3.53^{+0.29}_{-0.29} \times 10^{12}\ h^{-1}\ M_{\odot}$ and $\beta_L = 1.28^{+0.10}_{-0.08}$, while for our blue lenses the corresponding numbers are $M_{0,L} = 3.45^{+0.98}_{-1.47} \times 10^{11}\ h^{-1}\ M_{\odot}$ and $\beta_L = 0.50^{+0.18}_{-0.12}$. The constraints for these fits

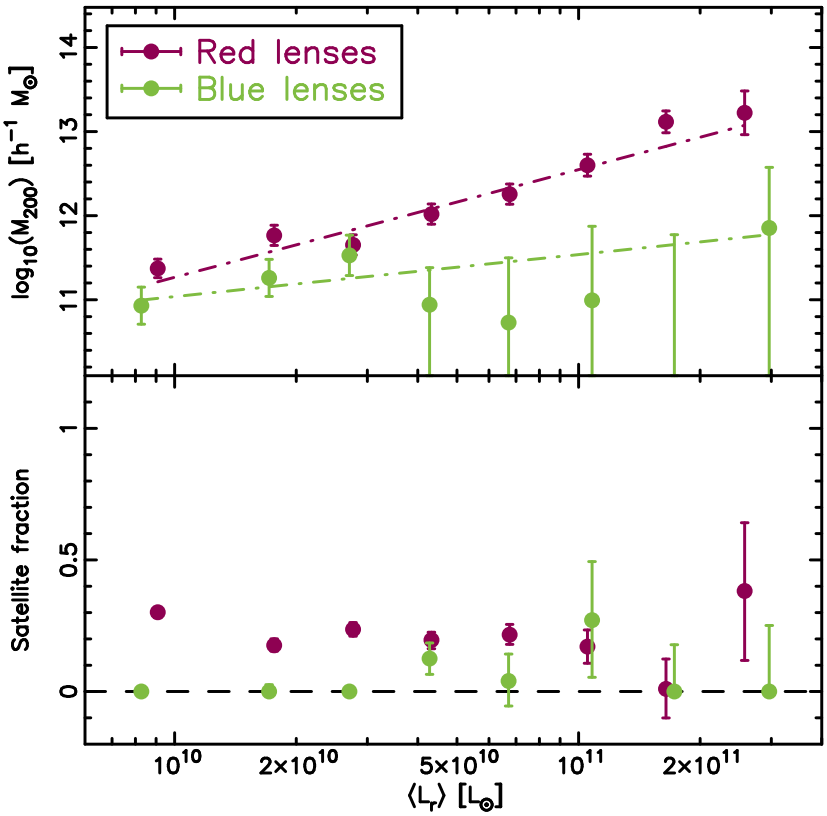

Figure 4.10 Satellite fraction α and bias-corrected halo mass M_{200} as a function of r'-band luminosity. Purple (green) dots represent the results for red (blue) lens galaxies, and the dash-dotted lines show the powerlaw scaling relations as described in the text.

are shown in Figure 4.11. Here we again see that the red lenses are better constrained than the blue. This is partly because we have more red lenses, and partly because red lenses in general are more massive making the lensing signal stronger. Our powerlaws are shallower than the ones found by VU11, but there are some differences between the analyses, making a direct comparison difficult. The way we select our red and blue samples differs significantly from the VU11 selection of early- and late-type samples (which is based on estimated Sérsic profiles rather than colours). Furthermore, in our halo model we account for the baryonic mass of each lens, something that was not done in VU11. Removing the baryonic component from our model, we find that the masses for some bins are overestimated by as much as 60%. It may appear counter-intuitive that including a baryonic component with a mass which is of order 10% of the total mass should result in such a significantly lowered halo mass estimate. The explanation lies in the halo model fitting, and specifically in the way the satellite fraction is allowed to vary. Adding a baryonic component on small scales will result in a lowered central halo mass. The central halo profile reaches further than the baryonic component however, and thus power on intermediate

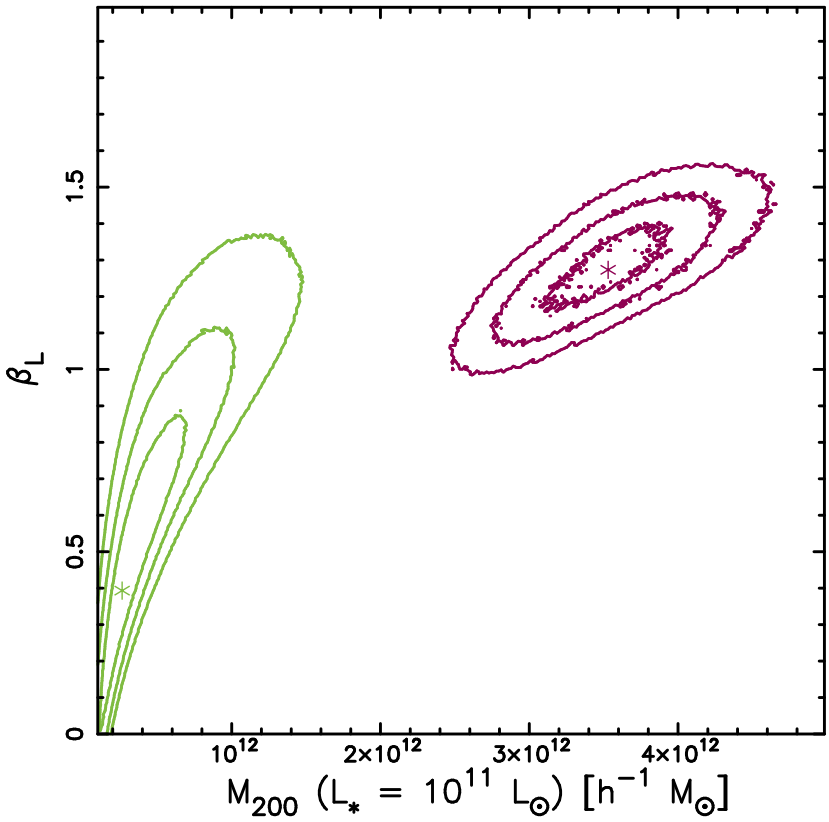

Figure 4.11 Constraints on the powerlaw fits shown in Figure 4.10. In purple (green) we show the constraints on the fit for red (blue) lenses, with lines representing the 67.8%, 95.4% and 99.7% confidence limits and stars representing the best-fit value.

scales is also diminished. To compensate for this loss of power, the halo model will increase the satellite 1-halo term by increasing the satellite fraction, which also increases the stripped satellite halo term, lowering the central 1-halo term further until an equilibrium is reached. These mechanisms are illustrated for red galaxies in luminosity bin L4 in Figure 4.12, where we have allowed halo mass, satellite fraction and stellar mass fraction to vary simultaneously for both panels. This Figure also makes clear the degeneracies introduced to the halo model if the stellar mass is left as a free parameter.

Higher-luminosity bins are more severely affected by this effect than the lower-luminosity end due to the lack of a prominent satellite 1-halo feature. The net effect is a steeper slope, which is exactly what VU11 are displaying. The general overestimation of halo mass in VU11 also means that the mass of a $L = 10^{11} L_{r',\odot}$ galaxy is overestimated, partly explaining the discrepancy between the $M_{0,L}$ estimates.

VU11 also convert their best-fit halo masses to mean halo masses, accounting for the fact that the halo mass function is a declining function, causing us to preferentially pick lower-mass haloes. The lensing best-fit halo mass therefore

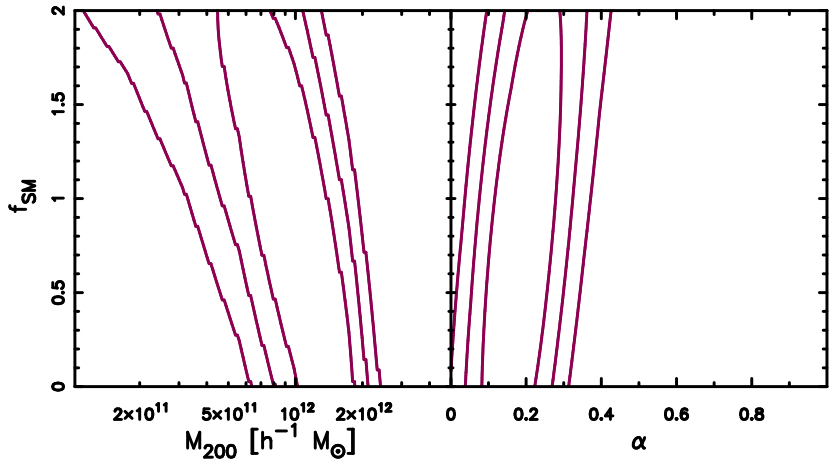

Figure 4.12 Dependence of halo model fitting parameters halo mass M_{200} and satellite fraction α on stellar mass, with $f_{\rm SM}$ the fraction of true mean stellar mass used in the halo model and contours showing the 67.8%, 95.4% and 99.7% confidence intervals. The left panel shows that including a baryonic component in the model (i.e. setting $f_{\rm SM} = 1$) will result in a significantly lower best-fit halo mass than not doing so ($f_{\rm SM} = 0$), and the right panel shows that the reason for this is an increased satellite fraction.

does not correspond to the mean halo mass in a given bin. The correction factors they apply range between a few percent for the lower-luminosity bins to $\sim 30\%$ at the highest luminosities.

Another important factor to take into account is the fact that we limit our lens samples to redshifts of $0.2 < z_{\rm lens} < 0.4$ keeping our mean lens redshift fairly stable at $\langle z_{\rm lens} \rangle \sim 0.3$. This is not done in VU11 and as a result, the median redshift of our lower-luminosity bins is higher than for the same bins in VU11, with the opposite being true for the higher-luminosity bins. Recent numerical simulations indicate that the relation between stellar mass and halo mass will evolve with redshift (e.g. Conroy & Wechsler, 2009; Moster et al., 2010). Lower-mass host galaxies ($M_* < 10^{11}\ M_\odot$) increase in stellar mass faster than their halo mass increases, i.e. for higher redshifts the halo mass is lower for the same stellar mass. The opposite trend holds for higher-mass host galaxies ($M_* > 10^{11}\ M_\odot$). As a result, the relation between halo mass and stellar mass (or an indicator thereof, such as luminosity) steepens with increasing redshift. This means that for the lower-luminosity bins, where our redshifts are higher, we may measure a steeper slope than VU11 and vice-versa for higher-luminosity bins. There are other factors which could affect the measured slope, such as the scatter between luminosity bins due to errors in the estimated luminosities. VU11 find that this bias is only relevant for the two highest luminosity bins, and that the correction factor is small compared to the error on the halo mass. We therefore choose not to model this effect in this Chapter.

4.5.3 Satellite fraction

The lower panel of Figure 4.10 shows the satellite fraction α as a function of luminosity for both the red and the blue sample. At lower luminosities the satellite fraction is $\sim 40\%$ for red lenses and as luminosity increases the satellite fraction decreases. This indicates that a large number of faint red lenses are satellites inside a larger dark matter halo, consistent with previous findings (e.g. Mandelbaum et al., 2006b; van Uitert et al., 2011). In the highest luminosity bins the satellite fraction is difficult to constrain due to the shape of the halo model satellite terms (green lines in Figure 4.2) becoming indistinguishable from the central 1-halo term (purple dashed), as discussed in Appendix 4.A. For blue lenses, the satellite fraction remains low across all luminosities indicating that almost none of our blue galaxies are satellites, again consistent with previous findings. This may be a sign that blue galaxies in our analysis are in general more isolated than red ones, a theory corroborated by the low signal on large scales for blue galaxies (see Figure 4.20 in Appendix 4.A). Here we have made no distinction between field galaxies and galaxies residing in a more clustered environment.

4.6 Stellar mass trend

A more accurate indicator of the baryonic content of a galaxy than its luminosity is its stellar mass, since luminosity is sensitive to recent star formation. We therefore study the relation between stellar mass and the dark matter content in this Section, dividing the lenses into 9 stellar mass bins as illustrated in Figure 4.13 with details in Table 4.3. As in Section 4.5 we further split each stellar mass bin into a red and a blue sample using their photometric types to approximate early- and late-type galaxies.

We measure the galaxy-galaxy lensing signal for each sample as before, and fit using our halo model with the halo mass M_{200} and the satellite fraction α as free parameters. Similarly to the previous section, the results are shown in Figure 4.14 for all stellar mass bins and for each red and blue lens sample, with details of the fitted halo model parameters quoted in Table 4.3. In the case of blue lenses, the two highest stellar mass bins are not well-constrained, due to a lack of lenses, and we therefore remove them from our analysis. The same issues with a direct comparison between this analysis and the one presented in VU11 remain: (1) their halo masses are likely overestimated due to inadequate modelling of the baryonic component, (2) our red and blue samples do not necessarily correspond to their early- and late-type galaxies, (3) we limit our analysis to a narrow redshift range of $0.2 < z_{\rm lens} < 0.4$ and (4) we have photometric redshifts for all our objects while VU11 had access to spectroscopic redshifts but for their lenses only. The latter effect we again account for in a similar fashion to the procedure described in Section 4.5.1.

An overview of the trends in Figure 4.14 is given in Figure 4.15 for red lenses and Figure 4.16 for blue. The mean mass in each bin increases with increasing stellar mass as expected, resulting in an increased signal amplitude. Similar to what we saw in the luminosity samples in the previous Section, the lower-mass bins display a bump at scales of $\sim 0.5\ h^{-1}$ Mpc. Here the lowest bins contain less massive galaxies than the lowest luminosity bins and the bump is more

Table 4.3 Details of the stellar mass bins. (1) Stellar mass range [$M_\odot$]; (2) Number of lenses; (3) Mean redshift; (4) Fraction of lenses that are blue; (5) Mean luminosity for red lenses [10^{10} $L_\odot$]; (6) Mean stellar mass for red lenses [10^{10} $M_\odot$]; (7) Best-fit mean halo mass for red lenses [10^{11} h^{-1} $M_\odot$]; (8) Best-fit satellite fraction for red lenses; (9) Mean luminosity for blue lenses [10^{10} $L_\odot$]; (10) Mean stellar mass for blue lenses [10^{10} $M_\odot$]; (11) Best-fit mean halo mass for blue lenses [10^{11} h^{-1} $M_\odot$]; (12) Best-fit satellite fraction for blue lenses

Sample	$\log_{10} M_*{}^{(1)}$	$n_{\rm lens}{}^{(2)}$	$\langle z\rangle^{(3)}$	$f_{\rm blue}{}^{(4)}$	$\langle L_r^{\rm red}\rangle^{(5)}$	$\langle M_*^{\rm red}\rangle^{(6)}$	$M_h^{\rm red(7)}$	$\alpha^{\rm red(8)}$	$\langle L_r^{\rm blue}\rangle^{(9)}$	$\langle M_*^{\rm blue}\rangle^{(10)}$	$M_h^{\rm blue(11)}$	$\alpha^{\rm blue(12)}$
S1	[9.00,9.50]	399730	0.29	0.88	0.04	0.20	$0.01^{+0.01}_{-0.00}$	$0.53^{+0.02}_{-0.03}$	0.06	0.18	$0.35^{+0.10}_{-0.14}$	$0.00^{+0.01}_{-0.00}$
S2	[9.50,10.00]	240732	0.30	0.85	0.11	0.56	$0.07^{+0.04}_{-0.03}$	$0.78^{+0.02}_{-0.02}$	0.19	0.56	$0.50^{+0.14}_{-0.20}$	$0.02^{+0.01}_{-0.01}$
S3	[10.00,10.50]	146657	0.30	0.73	0.37	1.95	$0.43^{+0.28}_{-0.17}$	$0.58^{+0.02}_{-0.02}$	0.57	1.73	$1.16^{+0.33}_{-0.26}$	$0.00^{+0.01}_{-0.00}$
S4	[10.50,11.00]	91556	0.30	0.39	1.14	6.05	$3.02^{+0.96}_{-0.73}$	$0.26^{+0.01}_{-0.02}$	1.66	5.15	$1.63^{+0.47}_{-0.65}$	$0.00^{+0.01}_{-0.00}$
S5	[11.00,11.25]	26942	0.30	0.15	2.60	13.3	$5.75^{+1.83}_{-1.39}$	$0.21^{+0.02}_{-0.02}$	4.20	12.8	$1.16^{+1.32}_{-0.83}$	$0.11^{+0.05}_{-0.05}$
S6	[11.25,11.50]	13287	0.30	0.07	4.51	23.2	$11.6^{+3.71}_{-2.81}$	$0.20^{+0.03}_{-0.03}$	7.31	22.1	$3.78^{+4.88}_{-2.53}$	$0.10^{+0.09}_{-0.09}$
S7	[11.50,11.75]	4481	0.30	0.04	7.82	40.2	$25.7^{+8.17}_{-6.19}$	$0.25^{+0.03}_{-0.04}$	13.6	40.0	$0.01^{+2.31}_{-0.00}$	$0.00^{+0.22}_{-0.00}$
S8	[11.75,12.00]	890	0.30	0.04	13.5	68.9	$121^{+42.2}_{-31.3}$	$0.26^{+0.07}_{-0.07}$	25.3	72.3	$10.2^{+30.5}_{-10.2}$	$0.15^{+0.36}_{-0.30}$
S9	[12.00,12.50]	147	0.29	0.20	24.5	127	$115^{+40.1}_{-51.8}$	$0.59^{+0.19}_{-0.19}$	51.9	144	$0.01^{+9.86}_{-0.00}$	$0.00^{+0.35}_{-0.00}$

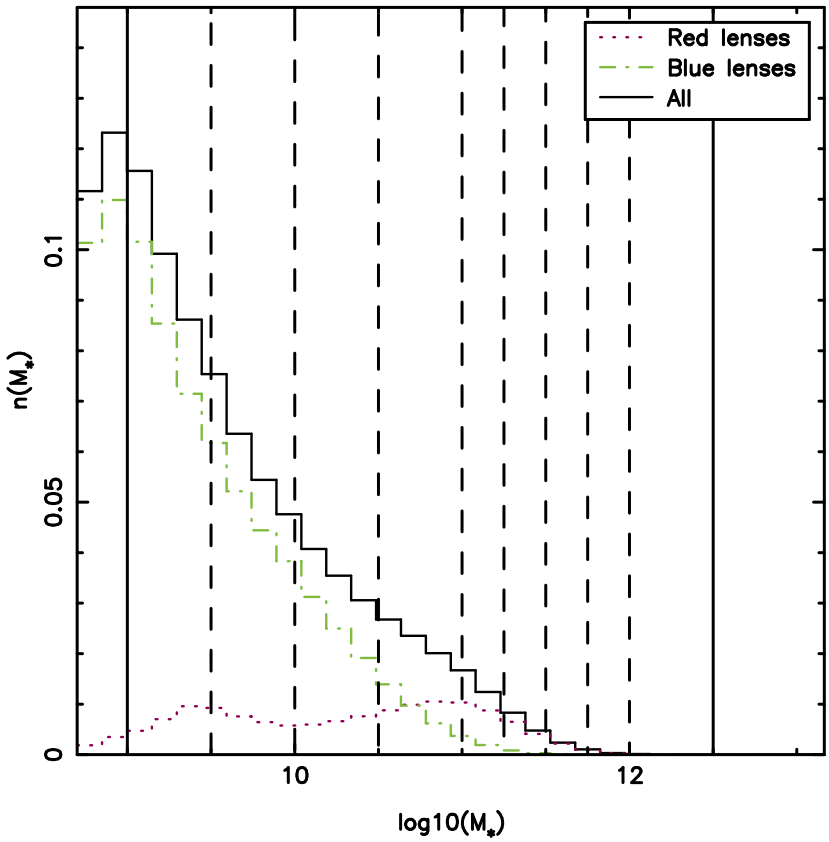

Figure 4.13 Stellar mass distribution in the CFHTLS for lenses with redshifts $0.2 \leq z_{\rm lens} \leq 0.4$ (black solid histogram). The distribution of red (blue) lenses is shown in dotted purple (dot-dashed green). Our lens bins are marked with vertical lines.

pronounced, indicating that most of the galaxies in these low-mass samples are satellite galaxies. The contribution from nearby haloes is again clearly visible in the lower-mass blue samples. The two highest-mass bins contain too few lenses to constrain the signal and have therefore been removed.

4.6.1 Stellar mass scaling relations

The best-fit halo masses and satellite fractions for each stellar mass bin are shown in Figure 4.17. We have corrected the halo masses for the bias induced by errors in our photometric redshift estimates using the mean luminosity in each bin as before. It is clear that the relation between dark matter halo and stellar mass is different for red and blue lenses as expected. To quantify the difference, we fit a powerlaw to the lensing signals in each bin simultaneously, similarly to our treatment of the luminosity bins in the previous Section. The form of the powerlaw is $M_{200} = M_{0,M}(M_*/M_{\rm pivot})^{\beta_M}$ with $M_{\rm pivot} = 2{\times}10^{11}\ M_\odot$ as in VU11. We note here that for the lowest red stellar mass bins, though the halo model fits the data very well (see Figure 4.14), the sample consists of nearly

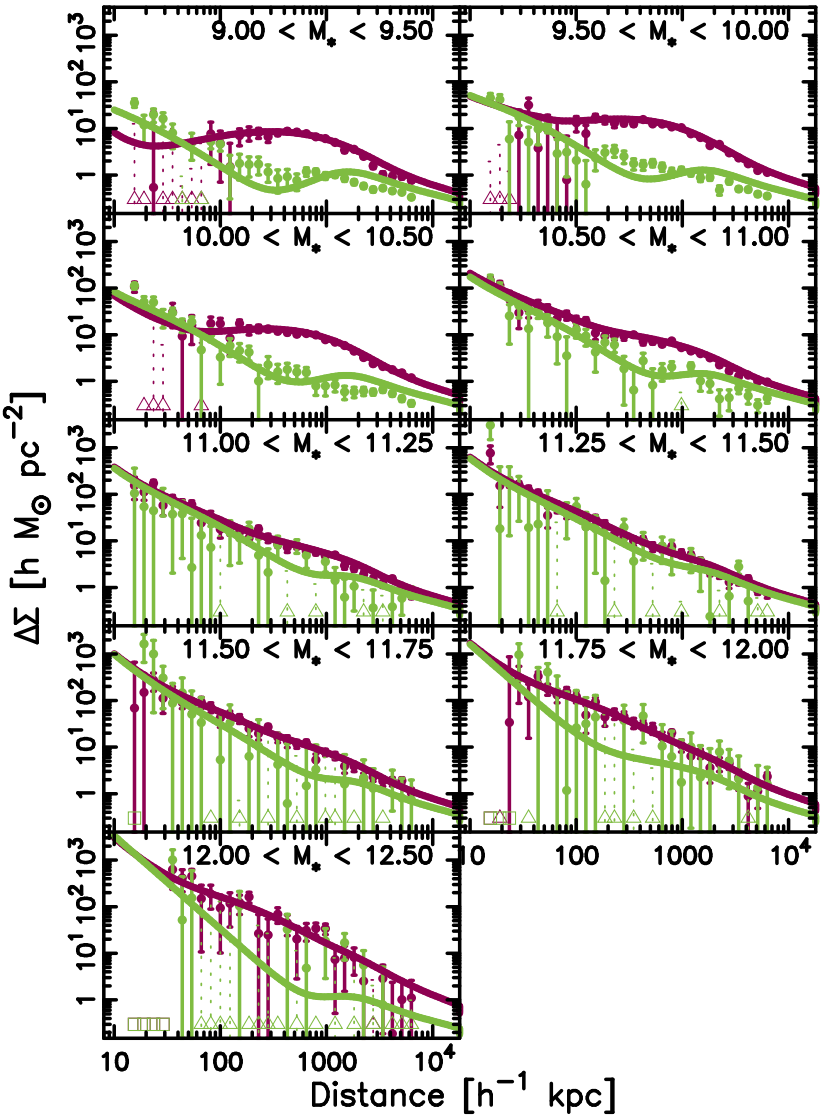

Figure 4.14 The weak galaxy-galaxy signal around lenses which have been split into stellar mass bins according to Table 4.3, modelled using the halo model described in Section 4.3.2. The purple (green) dots represent the measured differential surface density of the red (blue) lenses, and the solid line is the best-fit halo model. Triangles represent negative points that are included unaltered in the model fitting procedure, but that have here been moved up to positive values as a reference. The dotted error bars are the unaltered error bars belonging to the negative points. The squares represent distance bins containing no objects. For a detailed decomposition into the halo model components, please refer to Appendix 4.B.

100% satellite galaxies. It is therefore not a central halo mass associated with these lenses that is constrained by the halo model and so we exclude the two

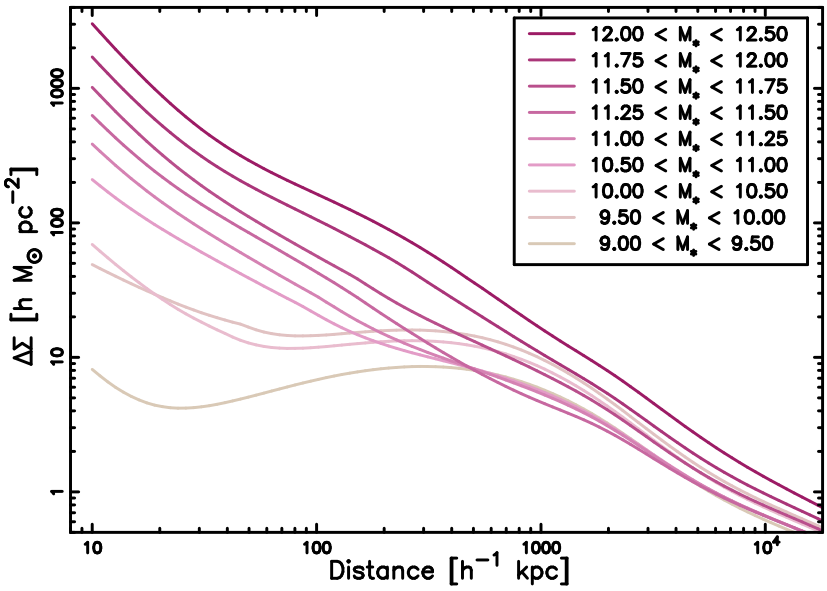

Figure 4.15 Best-fit halo models for red lenses for all stellar mass bins.

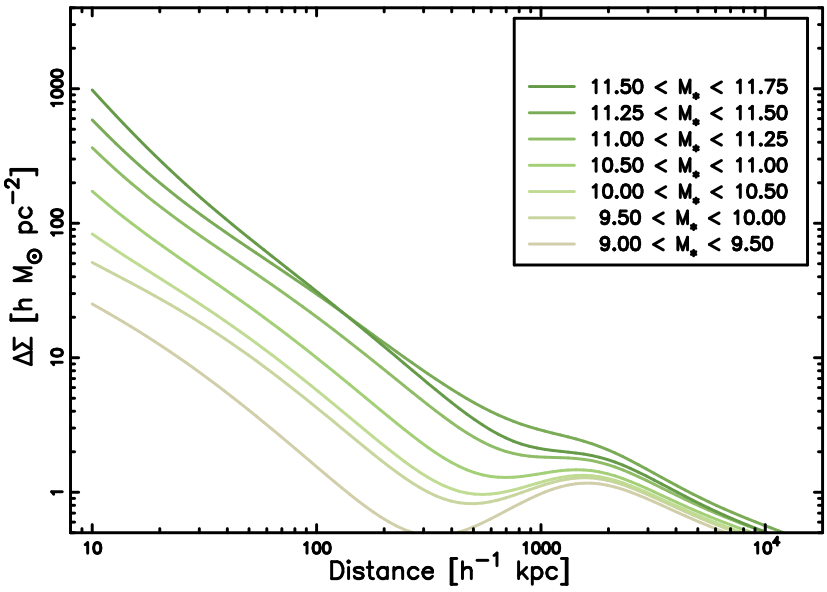

Figure 4.16 Best-fit halo models for blue lenses for all stellar mass bins.

lowest stellar mass bins from our analysis.

The resulting best-fit values for red lenses are $M_{0,M} = 1.07^{+0.10}_{-0.06} \times 10^{12}\ h^{-1}\ M_{\odot}$ and $\beta_M = 1.36^{+0.10}_{-0.06}$, and for blue lenses $M_{0,M} = 3.52^{+0.70}_{-0.70} \times 10^{11}\ h^{-1}\ M_{\odot}$ and $\beta_M = 0.54^{+0.06}_{-0.08}$. We show the constraints and best-fit values in Figure 4.18. The red lenses are clearly better constrained than the blue due to the higher-

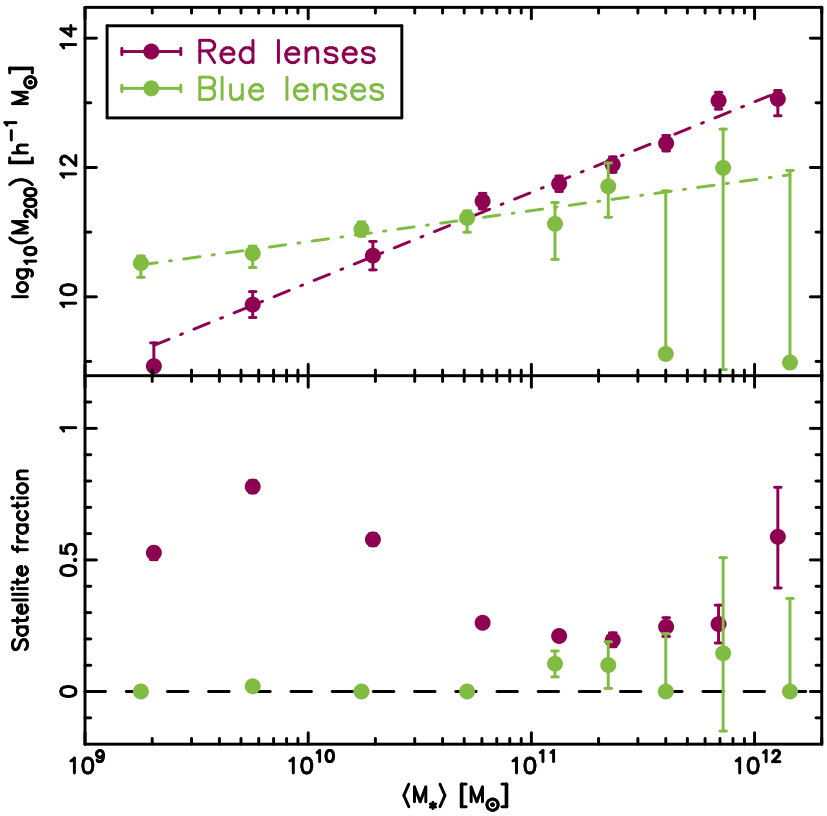

Figure 4.17 Satellite fraction α and halo mass M_{200} as a function of stellar mass. Purple (green) dots represent the results for red (blue) lens galaxies.

quality signal generated by these generally more massive and more abundant galaxies. Similarly to our luminosity relation, this powerlaw is shallower than the one found by VU11 but as discussed in the previous section the two analyses differ in ways that make a direct comparison difficult. Primarily the object selection differs, both in redshift and in defining red and blue lenses, and our halo masses are in general lower since we account for the baryonic mass in the lens while VU11 takes only dark matter into account. This also partly explains the differences in $M_{0,M}$. Furthermore, the stellar mass estimates we use here are based on the luminosity-stellar mass relations derived in Bell et al. (2003). It has since emerged that these relations tend to significantly overestimate the stellar mass (Zibetti et al., 2009). The accuracy of our stellar masses is thus somewhat limited, and new estimates will be derived in the near future using the Zibetti et al. (2009) relations instead.

An effect VU11 does account for, however, is the scatter between mass bins due to inaccuracies in the stellar mass estimate. Due to the shape of the mass distribution (see Figure 4.13), objects will preferentially scatter from lower-mass to higher-mass bins, biasing our halo masses low. The effect is greatest at the highest mass end since the distribution tapers off there and as a result fractionally more low-mass objects will scatter into the higher-mass bin. For

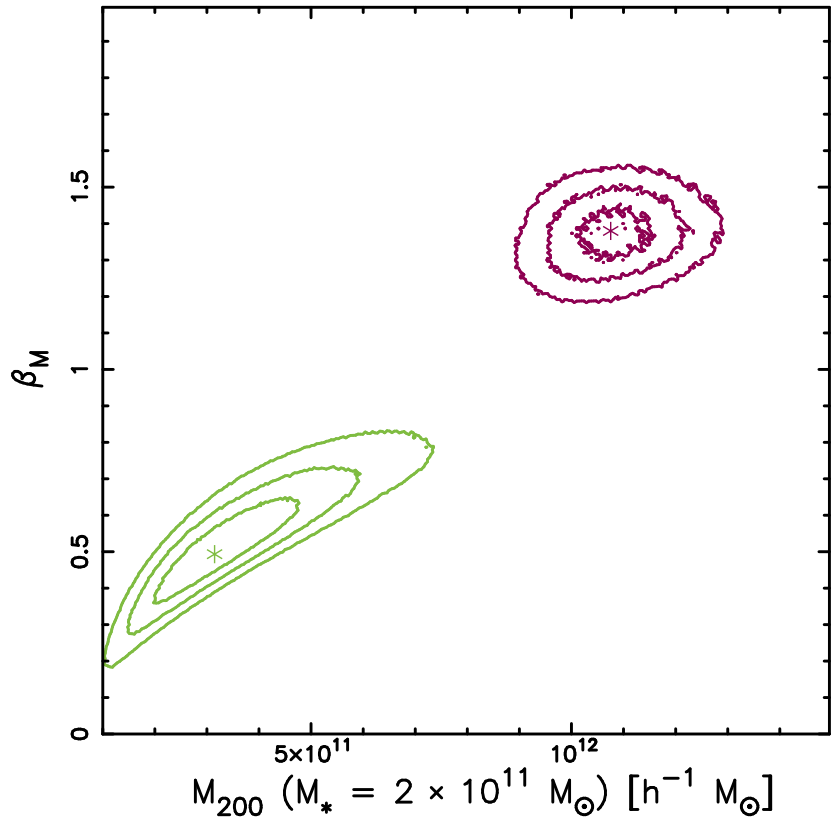

Figure 4.18 Constraints on the powerlaw fits shown in Figure 4.17. In purple (green) we show the constraints on the fit for red (blue) lenses, with lines representing the 67.8%, 95.4% and 99.7% confidence limits and stars representing the best-fit value.

their late-type galaxies, roughly corresponding to our blue sample, VU11 applies a correction of up to 20%, while for their early-type galaxies the correction is $\sim 10\%$ at the low-mass end and reaches $\sim 40\%$ for higher stellar masses. Just as for the luminosity results, they also convert their best-fit halo mass to mean halo mass with corrections of up to $\sim 30\%$ for the highest stellar masses. As a result, their halo mass relation is steepened compared to the uncorrected case, but this is not enough to explain the differences with our results.

The satellite fraction α as a function of stellar mass is shown in the lower panel of Figure 4.17 for both red and blue lenses. In the lower-mass red bins, nearly all lenses are satellites while for higher masses, nearly all are located centrally in their halo as expected. As discussed in the previous section, this fraction is difficult to constrain for high masses due to the shape of the satellite terms. The overall low satellite fraction for blue galaxies, suggesting together with low large-scale signal that most blue galaxies are isolated, is consistent with the luminosity results.

4.7 Discussion and conclusions

In this Chapter we have used high-quality weak lensing data from the CFHTLS to place constraints on the relation between dark matter halo mass and the baryonic content of the lenses, quantified through luminosity and stellar mass estimates. We verified the fidelity of our shear catalogue by comparing our lensing signal with that of two independent shear catalogues, and by using a method based on seeing variations in the data. The impressive source number density in this survey has made it possible to achieve tighter constraints than have so far been attained using previous lensing surveys such as the SDSS or the RCS2. Splitting our lens samples into red and blue subsamples, we approximated the trends for early- and late-type galaxies separately. We also extended our study to lower stellar masses than have been studied before using a halo model such as the one described in this Chapter. We note, however, that the stellar mass estimates used in this analysis are somewhat outdated, which may affect the trends found. In the near future this will be remedied.

As luminosity and stellar mass increases, the halo mass increases as well. For red lenses, the halo mass increases with greater baryonic content at a higher rate than for blue galaxies, independent of whether the measure of baryonic content is luminosity or stellar mass. The two measures thus produce consistent results. For each we fit powerlaw relations to quantify the rate of increase in halo mass. We find that for red galaxies, the halo mass scales with luminosity as $M_{200} \propto L_{r'}^{1.28^{+0.10}_{-0.08}}$ and with stellar mass as $M_{200} \propto M_*^{1.36^{+0.10}_{-0.06}}$, while for blue galaxies $M_{200} \propto L_{r'}^{0.50^{+0.18}_{-0.12}}$ and $M_{200} \propto M_*^{0.54^{+0.06}_{-0.08}}$. For a fiducial red galaxy with a luminosity of $L_0 = 10^{11}\ L_{r',\odot}$ we find a halo mass of $M_{200} = 3.53^{+0.29}_{-0.29} \times 10^{12}\ h^{-1}\ M_\odot$. This number is lower than the number found by VU11, but the two analyses differ significantly in object selection. Furthermore, in this chapter we have included a component of our halo model which was neglected by VU11: the baryonic component. Since the lensing signal is a response to the total mass of a system, it is essential to account for baryons in order to not overestimate the mass contained in the dark matter halo. However, we also showed that great care has to be taken when including a baryonic component since doing so has a greater impact on the fitted halo mass than one might naïvely expect due to the complicated interplay between stellar mass, satellite fraction and halo mass.

For our blue galaxy selection, the satellite fraction is low across all luminosities and stellar masses considered here. The signal at large scales for these samples is also generally low, indicating that these galaxies are relatively isolated and reside in less clustered environments than the red galaxies do and that we may be overestimating the bias for these samples. At low luminosity/stellar mass, a considerable fraction of red galaxies are satellites within a larger dark matter halo. This fraction decreases steadily with increasing luminosity or stellar mass.

The tight constraints on the relation between baryonic content indicators and dark matter halo mass achieved in this work will help improve our understanding of the mechanisms behind galaxy formation. If the halo mass threshold for galaxy formation is accurately known for all galaxies then cosmological simulations can be further improved and phenomena such as the missing satellite problem may be better studied. Furthermore, by studying red and blue lenses

separately we have determined that the bias description which works well for red galaxies is not optimal for blue galaxies. The environments the two samples reside in are thus radically different and the difference will have to be taken into account in the future.

With currently ongoing (e.g. KiDS) and planned (e.g. Euclid) surveys, weak lensing analyses will become yet more powerful than the one presented in this Chapter. In preparation for the future there are therefore several sources of uncertainty that should be investigated. As mentioned above, the bias description may not be optimal for blue lenses and with future data this bias can likely be constrained directly using galaxy-galaxy observations. Recent simulations have also indicated that there is a redshift evolution of the halo mass relations, and this evolution can be studied with weak lensing. Other possible improvements to the halo model used here include studies of the distribution of satellites within a galaxy dark matter halo, and investigations of the stripping of satellite haloes. The analysis presented in this Chapter is already a great improvement on recent analyses, and with future surveys we will be able to use galaxy-galaxy lensing to study the connection between baryons and dark matter in exquisite detail.

Acknowledgements

This Chapter is based on observations obtained with MegaPrime/MegaCam, a joint project of CFHT and CEA/DAPNIA, at the Canada-France-Hawaii Telescope (CFHT) which is operated by the National Research Council (NRC) of Canada, the Institut National des Science de l'Univers of the Centre National de la Recherche Scientifique (CNRS) of France, and the University of Hawaii. This work is based in part on data products produced at TERAPIX and the Canadian Astronomy Data Centre as part of the Canada-France-Hawaii Telescope Legacy Survey, a collaborative project of NRC and CNRS.

MV acknowledges support from the European DUEL Research-Training Network (MRTN-CT-2006-036133) and from the Netherlands Organization for Scientific Research (NWO).

APPENDIX 4.A: Detailed luminosity bins

In this Appendix we show the decomposition of the best-fit halo model for red (Figure 4.19) and blue (Figure 4.20) lenses, split in luminosity according to Table 4.2. Showing the full decomposition is highly informative because it highlights some of the major trends and clarifies which effects dominate in each case.

The baryonic component based on the mean stellar mass in each bin (purple dot-dashed line) becomes more dominant for higher luminosities, but the luminous size of the lenses also increases, making measurement of background source shapes in the innermost distance bins difficult. Thus it is not possible to reliably constrain the baryonic component with our data. Never the less, the effect of including the baryons in our model is an overall lowering of the dark matter halo profile (purple dashed) compared to without baryons. For the red lenses we see that a considerable fraction of the sample at lower luminosities necessarily consists of satellite galaxies, since there is a clear bump in the signal at intermediate scales which has to be accounted for. This satellite fraction continuously drops as luminosity increases, and simultaneously becomes more difficult to constrain since the combination of the stripped satellite profile (green dash-dotted) and satellite 1-halo terms (green dashed) becomes almost indistinguishable from a single NFW profile for high halo masses. This effect was discussed in more detail in VU11, Appendix C.

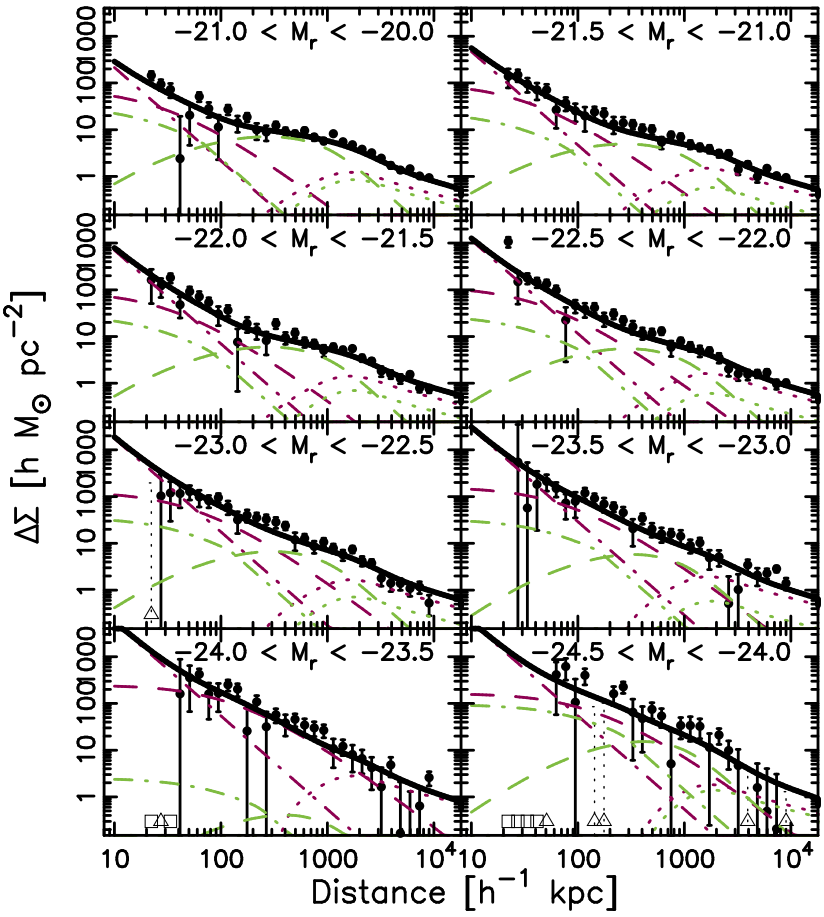

Figure 4.19 The weak galaxy-galaxy signal around *red* lenses which have been split into luminosity bins according to Table 4.2, and modelled using the halo model described in Section 4.3.2. The black dots are the measured differential surface density, and the black line is the best-fit halo model with the separate components displayed using the same convention as in Figure 4.2. Grey triangles represent negative points that are included unaltered in the model fitting procedure, but that have here been moved up to positive values as a reference. The dotted error bars are the unaltered error bars belonging to the negative points. The grey squares represent distance bins containing no objects.

For the blue lenses, the signal becomes very noisy for the two highest-luminosity bins due to a lack of lenses. These two bins are therefore discarded from the full analysis in Section 4.5. In general, blue galaxies produce a noisier signal than red galaxies for the same luminosity cuts. This is because blue lenses are in general less massive, and there are fewer of them which results in a weaker signal. We also notice that nearly all blue lenses are galaxies located at the centre of their halo, rather than being satellites. This is consistent with previous findings. It is possible that satellite galaxies in general are redder because they have been stripped of their gas and thus have had their star formation quenched. It could also mean that most blue galaxies in our analysis

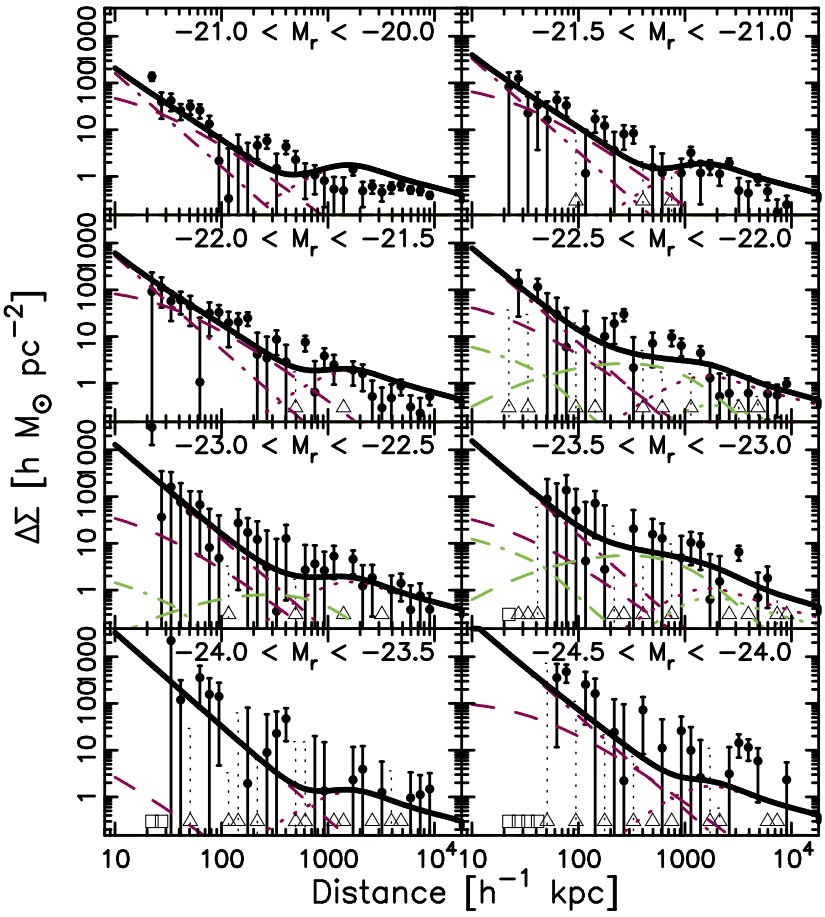

Figure 4.20 The weak galaxy-galaxy signal around *blue* lenses which have been split into luminosity bins according to Table 4.2, and modelled using the halo model described in Section 4.3.2. The black dots are the measured differential surface density, and the black line is the best-fit halo model with the separate components displayed using the same convention as in Figure 4.2. Grey triangles represent negative points that are included unaltered in the model fitting procedure, but that have here been moved up to positive values as a reference. The dotted error bars are the unaltered error bars belonging to the negative points. The grey squares represent distance bins containing no objects.

are isolated; we have made no distinction between field galaxies and galaxies in a more clustered environment. If blue galaxies are more isolated than red ones then the contribution from nearby haloes (dotted lines) would also be less. It is clear from Figure 4.20 that the large scales are not optimally fit by our model, and isolation may be one of the reasons since we assume the same mass-bias relation for blue galaxies as for red. With current data it is not possible to constrain the bias as a free parameter, but with future wider surveys this could be done.

APPENDIX 4.B: Detailed stellar mass bins

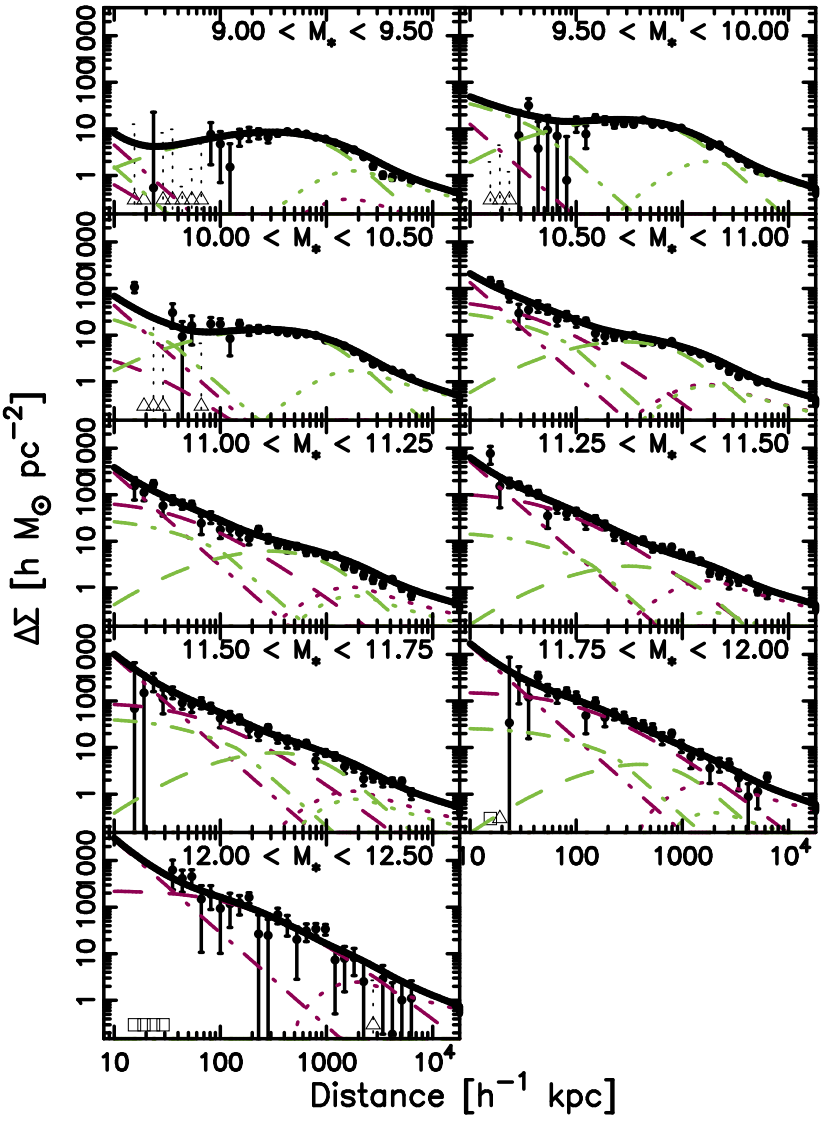

Figure 4.21 The weak galaxy-galaxy signal around *red* lenses which have been split into stellar mass bins according to Table 4.3, and modelled using the halo model described in Section 4.3.2. The black dots are the measured differential surface density, and the black line is the best-fit halo model with the separate components displayed using the same convention as in Figure 4.2. Grey triangles represent negative points that are included unaltered in the model fitting procedure, but that have here been moved up to positive values as a reference. The dotted error bars are the unaltered error bars belonging to the negative points. The grey squares represent distance bins containing no objects.

The decomposition of the best-fit halo model for red and blue lenses, divided

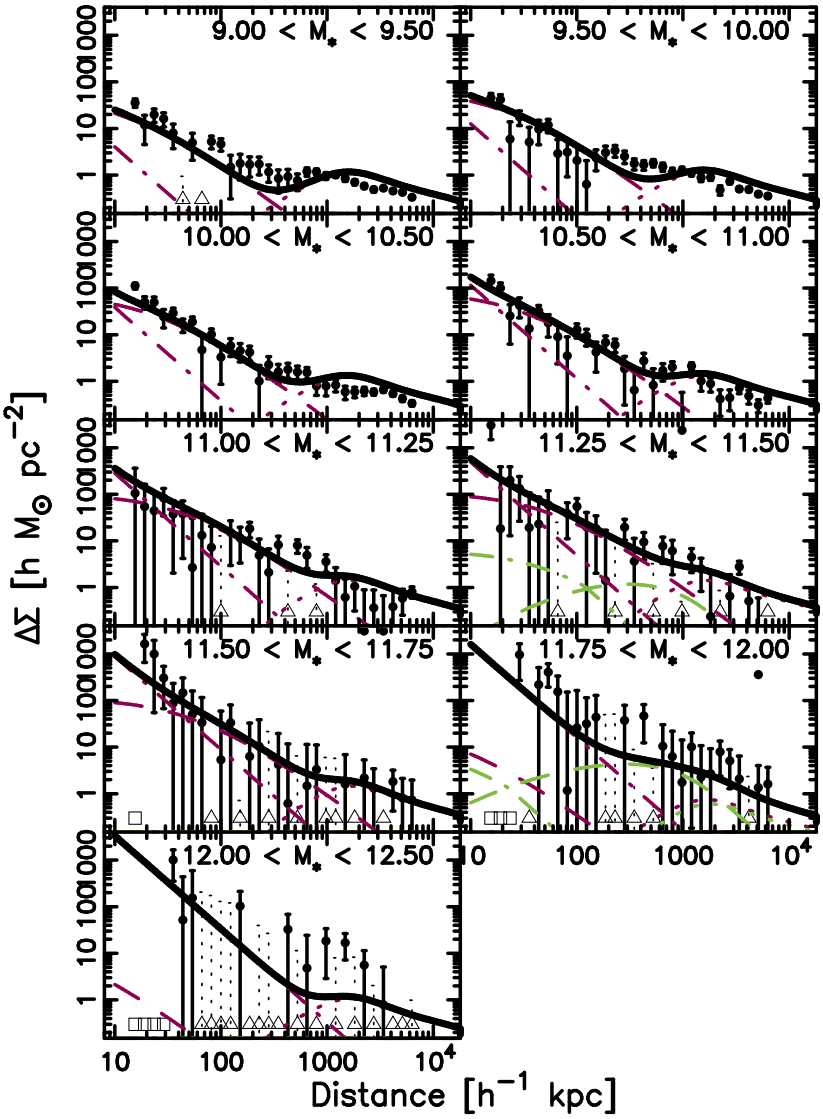

Figure 4.22 The weak galaxy-galaxy signal around *blue* lenses which have been split into stellar mass bins according to Table 4.3, and modelled using the halo model described in Section 4.3.2. The black dots are the measured differential surface density, and the black line is the best-fit halo model with the separate components displayed using the same convention as in Figure 4.2. Grey triangles represent negative points that are included unaltered in the model fitting procedure, but that have here been moved up to positive values as a reference. The dotted error bars are the unaltered error bars belonging to the negative points. The grey squares represent distance bins containing no objects.

using stellar mass as detailed in Table 4.3, is shown in Figures 4.21 and 4.22 respectively.

By construction the baryonic component amplitude (purple dash-dotted line)

increases with increasing bin number, and so does the dark matter halo mass (dashed lines). Note that with our stellar mass selections we push to smaller and fainter objects, so the objects in the three lowest-mass bins are on average less massive and less luminous than the galaxies in the faintest luminosity bin. In these bins, nearly all red galaxies are satellites, while for higher stellar mass bins the satellite fraction diminishes, a behaviour which is consistent with the trends we saw for luminosity (Appendix 4.A). For the higher stellar mass bins, as for the higher luminosity bins, the sum of the satellite stripped and 1-halo terms result in a profile which resembles a single NFW profile, making the satellite fraction more difficult to determine. For the blue lenses we run into the same issues for the highest mass bin as for the highest luminosity bins; the number of lenses is too small to constrain the halo model and so the bin has to be discarded. Furthermore, the satellite fraction is low across all blue lens bins indicating that these lenses are most likely isolated, which is consistent with the low large-scale signal and with our findings for luminosity.

Constraining cluster profiles with weak lensing shear and flexion

5

Clusters of galaxies are important probes of the background cosmology since their numbers as a function of mass and redshift are sensitive to cosmological parameters. Most of the mass in a cluster of galaxies is in the form of dark matter, and in order to learn about cosmology this mass has to be accurately estimated given visible observables only. Weak lensing has the power to constrain mass profiles of dark matter haloes, on scales ranging from a few kiloparsecs to several megaparsecs. To take full advantage, the cluster lensing profile has to be accurately modelled even if the centre of the cluster is not accurately known. In this Chapter we model the misaligned profile for both the first-order lensing distortion (shear) and for higher-order distortions known as flexions. We also show that the slope of the differential surface density can be recovered via a simple combination of flexions. These flexions are sensitive to small-scale density variations, making them important complements to the shear. Through a series of tests we find that this is particularly true when it comes to constraining the misaligned cluster profile.

5.1 Introduction

Clusters of galaxies are amongst the most massive gravitationally bound structures in the Universe. By studying how the masses and abundances of these striking galaxy communities evolve, crucial constraints on current theories of cosmology, and of structure formation, may be yielded. However, N-body simulations consistently show galaxy clusters to be immersed in expansive dark matter haloes. Thus one of the main challenges of using clusters of galaxies as a probe for cosmology becomes to accurately predict the total mass of a system given baryonic observables only.

There are currently a number of methods in use for estimating cluster masses. The gas trapped in the potential well of a cluster, the intracluster medium (ICM), may be exploited for this purpose via e.g. the Sunyaev-Zel'dovic (SZ) effect (Sunyaev & Zeldovich, 1972; Motl et al., 2005; Nagai, 2006) or X-ray studies (e.g. Reiprich & Böhringer, 2002; Nagai et al., 2007; Mantz et al., 2010). These techniques do however suffer inaccuracies due to e.g. intervening radio point sources (Vale & White, 2006) or assumptions such as hydrostatic equilibrium (e.g. Evrard, 1990; Nagai et al., 2007). To estimate the cluster mass from the dynamics of cluster members is theoretically straight-forward (Biviano & Girardi, 2003; Rines et al., 2003; Katgert et al., 2004; Rines & Diaferio, 2006) but it also requires several assumptions on e.g. the dynamical equilibrium of the cluster. Finally, there is gravitational lensing. Strong gravitational lensing is powerful when investigating the mass profiles of individual massive clusters (e.g. Shu et al., 2008; Zitrin et al., 2011), but it requires high mass densities in the inner regions. The clusters in which strong lensing is observed are therefore not necessarily representative of all clusters, or even of clusters of the same mass. Weak gravitational lensing, on the other hand, obtains cluster masses while making no assumptions on the physical state of the cluster, and is observable in all clusters with sufficient background source density (recently Holhjem et al., 2009; Abate et al., 2009; Sheldon et al., 2009; Okabe et al., 2010; Hoekstra et al., 2011; Lerchster et al., 2011; Jee et al., 2012). Weak lensing provides a direct estimate of the *total* mass of a cluster, irrespective of whether that mass is baryonic or non-baryonic. This is in essence what makes weak lensing one of the most promising cluster mass determination methods in use today.

One of the main challenges with weak lensing is that it is subject to degeneracy since it is sensitive not only to the cluster in question but also to any other intervening structure. However, for the purpose of determining mass-observable relationships, clusters may be grouped according to their observable properties and then averaged. This effectively eliminates the degeneracy since foreground structures no longer add coherent distortions to the weak lensing signal. However, the centre of a cluster is generally difficult to determine. Often it is done by identifying the brightest cluster galaxy (BCG), but a misidentification of said BCG would cause the assumed cluster centre to be offset from the true centre of the dark matter halo. As a result the lensing signal would peak at some distance from the assumed centre. Stacking several clusters where the BCG may be offset from the true centre by a random amount would therefore affect the cluster mass estimate.

Fortunately, the offset distribution can be statistically modelled and taken into account when interpreting the weak lensing signal, as described in Johnston

et al. (2007) (from here on referred to as J07). The effect of miscentred BCGs is subtle in the case of first-order weak lensing (shear), but if not taken into account it will cause an overestimation of the mass of the average halo in the cluster sample. The analysis could therefore benefit from the use of higher-order weak lensing distortions known as flexion (Goldberg & Bacon, 2005; Bacon et al., 2006). Flexion is a measure of the gradient of the lensing convergence, making it much more sensitive to small-scale density fluctuations than shear is. As it is an independent method for obtaining the lensing signal it may be used in conjunction with shear to improve the mass estimate of an ensemble of clusters. Previously, these higher-order distortions have been used to study individual clusters (e.g. Okura et al., 2008; Leonard et al., 2011; Cain et al., 2011) and galaxy-sized haloes (Velander et al. (2011), Chapter 3 of this Thesis). This Chapter, however, is concerned with modelling the flexion signal for a cluster *ensemble* where a significant fraction of BCGs are misaligned with their associated dark matter haloes, following the general recipe outlined in J07. The resulting flexion signal is then compared to that of shear, and studied as a function of cluster mass, cluster redshift and offset distribution.

In Section 5.2 we describe our cluster model by first introducing shear and flexion in Section 5.2.1 and then giving an overview of the contributions to our model in Sections 5.2.2 through 5.2.5. In Section 5.3 we investigate the dependence of our model on halo mass, halo concentration and offset distribution properties. We conclude in Section 5.4. Throughout this Chapter we assume the following cosmology (WMAP7; Komatsu et al., 2010): $(\Omega_M, \Omega_\Lambda, h, \sigma_8, w) = (0.27, 0.73, 0.70, 0.81, -1)$

5.2 Cluster lensing formalism

To deduce the mass and density profile of an ensemble of clusters from weak lensing is qualitatively similar to doing the same for a selection of galaxies (see Chapters 3 and 4). By averaging the weak lensing signal over enough sources we can assume that the average background source is circular, and any residual coherent distortion must be due to lensing. If we then average the signal in azimuthal bins centred on the lens we can acquire an accurate picture of the density profile of the total mass in the lens. Worth noting here is that the circular average makes this type of analysis robust against most systematic errors that can affect weak lensing measurements, such as insufficiently corrected residual point-spread function (PSF) anisotropy.

However, interpreting the signal we measure around clusters differs slightly from the interpretation of the signal around galaxies, mainly because the position that the measured lensing signal should be centred on is generally not as accurately determined. In clusters, the brightest cluster galaxy (BCG) is typically assumed to be located at the very centre of the cluster dark matter halo. This assumption does not hold in all cases. The cluster finding algorithm may for instance have misidentified the BCG, or the true BCG may be offset from the halo centre, causing the peak of the lensing signal to be shifted from the assumed centre.

In the model we present here we will closely follow the procedure outlined in J07, but extend it from the first-order lensing signal (shear) to the higher-order signals known as F and G flexion.

5.2.1 Shear and flexion

Before moving onto the interpretation of the lensing signal, we will give a brief overview of shear and flexion. In the weak lensing regime, the lensed surface brightness of a source galaxy, $f(\mathbf{x})$, is related to the unlensed surface brightness, $f_0(\mathbf{x})$, via

$$f(\mathbf{x}) \simeq \left\{1 + \left[(A - I)_{ij}x_j + \frac{1}{2}D_{ijk}x_j x_k\right]\frac{\partial}{\partial x_i}\right\} f_0(\mathbf{x}). \tag{5.1}$$

Here I is the identity matrix, x_i denotes lensed coordinates, and A_{ij} is a combination of the lensing convergence κ and the shear γ. The matrix

$$D_{ijk} = \frac{\partial A_{ij}}{\partial x_k} \tag{5.2}$$

describes how convergence and shear vary across a source image and is the sum of the two flexions: $D_{ijk} = \mathcal{F}_{ijk} + \mathcal{G}_{ijk}$. These two quantities are thus the derivatives of the convergence and shear fields. The full expressions for A_{ij}, $\mathcal{F}_{ijk}$ and $\mathcal{G}_{ijk}$ may be found in e.g. Bacon et al. (2006).

The shear is a stretch in one direction which is applied to the intrinsic shape of a source galaxy. This type of lensing distortion has been used in weak lensing analyses for nearly two decades. Flexion on the other hand was first studied by Goldberg & Bacon (2005) and then further developed by Bacon et al. (2006). As observations are increasing in accuracy, flexion is now gaining in popularity as a tool for cluster studies (e.g. Okura et al., 2008; Er et al., 2010; Bacon et al., 2010; Leonard et al., 2011; Cain et al., 2011). The first flexion, F flexion, is a skewness of the brightness profile which is reminiscent of a centroid shift, while the second flexion, G flexion, is a triangular distortion. The signal-to-noise (S/N) of flexion is proportional to the size of the source, and Goldberg & Bacon (2005) estimate that the S/N of the shear and flexion signals will be comparable at a distance $\theta \simeq 4r_{\rm source}$ from the lens with the flexion S/N being higher within this limit. Furthermore, for relaxed sources there is no intrinsic flexion signal expected, making the shape noise small. Thus the theoretical flexion S/N will exceed the shear S/N on small scales. However, measurement biases are still fairly large for flexion while biases for shear are at sub-percentage level.

As noted in Chapter 4, assuming circular symmetry the amplitude of the azimuthally averaged tangential shear, γ_t, is directly related to the differential surface density $\Delta\Sigma(R)$ via

$$\Delta\Sigma(R) = \overline{\Sigma}(< R) - \overline{\Sigma}(R) = \Sigma_{\rm crit}\gamma_t(R) \tag{5.3}$$

where $\Sigma_{\rm crit}$ is the critical surface density

$$\Sigma_{\rm crit} = \frac{c^2}{4\pi G}\frac{D_s}{D_l D_{ls}} \tag{5.4}$$

with D_s, D_l and D_{ls} the angular diameter distance to the source, to the lens and between the lens and the source respectively. The differential surface density is the difference between $\overline{\Sigma}(< R)$, the average surface density inside a disk of radius R, and $\overline{\Sigma}(R)$, the azimuthal average of the surface density in a thin annulus of radius R. This is a convenient measure of the amplitude of the shear signal

since it is independent of the specific configuration between lens and source. Equivalent quantities for the flexion signals are $\mathcal{F}_\Diamond(R) \equiv (\Sigma_{\rm crit}/D_l)\mathcal{F}_t(R)$ and $\mathcal{G}_\Diamond(R) \equiv (\Sigma_{\rm crit}/D_l)\mathcal{G}_t(R)$, where the dependence on lens redshift is more apparent due to the D_l factor. Σ and $\Delta\Sigma$ both have units of mass per area, while the equivalent flexion quantities gain an extra inverse length unit (here $\mathcal{F}_t$ and $\mathcal{G}_t$ have units of radians^{-1}). For the rest of this Chapter, all shear and flexion quantities will refer to the tangential signal, and so we will drop the subscript t.

The two flexion quantities are related to the surface density Σ as follows (Lasky & Fluke, 2009):

$$\mathcal{F}_\Diamond(R) = -\frac{d\Sigma(R)}{dR} \tag{5.5}$$

$$\mathcal{G}_\Diamond(R) = \frac{d\Sigma(R)}{dR} - \frac{4\Sigma(R)}{R} + \frac{4M(R)}{\pi R^3} \tag{5.6}$$

where $M(R)$ is the projected mass distribution, i.e. the area integral of the surface density $\Sigma(R)$, and the negative sign for the F flexion signal depends on the definition of tangential flexion.

The two flexion quantities may also be directly related to the differential surface density $\Delta\Sigma$:

$$\mathcal{F}_\Diamond(R) = \frac{2\Delta\Sigma(R)}{R} + \Delta\Sigma'(R) \tag{5.7}$$

$$\mathcal{G}_\Diamond(R) = \frac{2\Delta\Sigma(R)}{R} - \Delta\Sigma'(R) \tag{5.8}$$

where $\Delta\Sigma'(R)$ is the derivative of $\Delta\Sigma$ with respect to R. It is clear from this that we can recover $\Delta\Sigma$ either through shear (Equation 5.3) or through a linear combination of flexions:

$$\Delta\Sigma(R) = \frac{R}{4}(\mathcal{F}_\Diamond(R) + \mathcal{G}_\Diamond(R)) \tag{5.9}$$

Similarly, we can obtain the slope of $\Delta\Sigma$ by combining the flexions in a different way:

$$\Delta\Sigma'(R) = \frac{1}{2}(\mathcal{F}_\Diamond(R) - \mathcal{G}_\Diamond(R)) \tag{5.10}$$

These equations highlight yet again that the flexions are an independent measure of the surface density, and a direct measure of its slope, and therefore an important complement to shear.

5.2.2 Contribution from the BCG

Similarly to our treatment of the baryonic lens galaxies in our galaxy-galaxy halo model (see Section 4.3.2, page 98), we model the contribution from the BCG as a point source. The surface density for a point source is simply a delta function which is a reasonable approximation since the individual galaxy is small compared to the cluster halo:

$$\Sigma(R) = \delta_D(R) \tag{5.11}$$

The shears and flexions for the baryonic contribution are then given by (Lasky & Fluke, 2009)

$$\Delta\Sigma^b(R) = \frac{M_0}{\pi R^2} \tag{5.12}$$

$$\mathcal{F}^b_\Diamond(R) = 0 \tag{5.13}$$

$$\mathcal{G}^b_\Diamond(R) = \frac{4M_0}{\pi R^3} \tag{5.14}$$

where M_0 could be fixed to e.g. the estimated stellar mass of the BCG or left as a free parameter when fitting the model. Note that the F flexion is zero in this case since it is the gradient of the surface density, so there is no contribution from the BCG to the F flexion cluster lensing signal.

5.2.3 Contribution from centred cluster dark matter haloes

To model the cluster dark matter halo, we will assume that the halo density distribution is well described by an NFW profile (Navarro, Frenk, & White, 1996) in terms of the three-dimensional radius r:

$$\rho(r) = \frac{\delta_c \rho_c(z)}{(r/r_s)(1 + r/r_s)^2} \tag{5.15}$$

where δ_c is an amplitude determined by the NFW concentration parameter, $c_{\rm NFW}$, $\rho_c(z)$ is the critical density for closure at the cluster redshift and r_s is a scale radius. This density profile is $\propto r^{-1}$ on small scales ($r \ll r_s$) and $\propto r^{-3}$ on large scales ($r \gg r_s$). In our description of the cluster model we will define all quantities in terms of a virial radius r_{200} within which the mean density is 200 times the critical density. The enclosed mass is then

$$M_{200} = 200\rho_c(z)\frac{4}{3}\pi r^3_{200} \tag{5.16}$$

and the NFW concentration parameter at this radius is

$$c_{200} = \frac{r_{200}}{r_s} = 5.71 \left(\frac{M_{200}}{2 \times 10^{12}\ h^{-1}\ {\rm M}_\odot}\right)^{-0.084} (1+z)^{-0.47} \tag{5.17}$$

where the second relationship was determined by Duffy et al. (2008) using N-body simulations based on a WMAP5 cosmology. In this Chapter we generally use the more recent WMAP7 cosmology, but the difference is negligible. For a discussion on other choices of virial radii, please refer to J07. Analytical expressions exist for the NFW halo description, both for surface density $\Sigma(R)$ and shear $\gamma(R)$ (see e.g. Wright & Brainerd, 2000), and for the two flexions $\mathcal{F}(R)$ and $\mathcal{G}(R)$ (see Bacon et al., 2006; Lasky & Fluke, 2009). The contribution from the well-centred population in our cluster sample is then simply $\Sigma^c(R) = \Sigma_{\rm NFW}(R)$.

5.2.4 Contribution from a cluster population with miscentred BCGs

It is likely that for a fraction of clusters in a given sample the assumed centre will be offset from the true centre of the dark matter halo. In this Chapter, we will

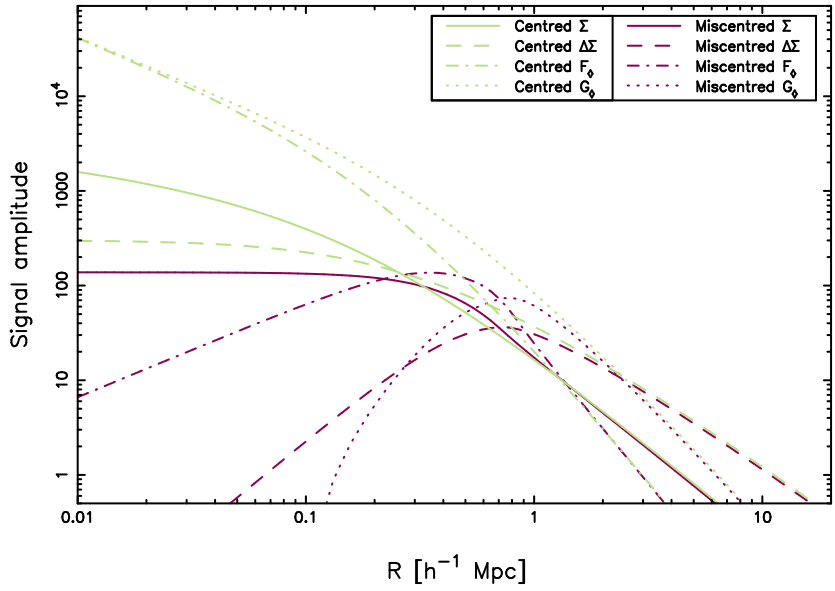

Figure 5.1 The effect of miscentred BCGs. The lighter green lines represent a centred NFW profile while the darker purple lines represent the corresponding average profiles for a miscentred population with offsets drawn from a Gaussian distribution with width $\sigma_s = 0.42\ h^{-1}$ Mpc. In order, the solid, dashed, dash-dotted and dotted lines represent Σ, $\Delta\Sigma$, $\mathcal{F}_\diamondsuit$ and $\mathcal{G}_\diamondsuit$, where the two former signals have units of $h\ \mathrm{M}_\odot\ \mathrm{pc}^{-2}$ and the two latter signals have units of $\mathrm{Mpc}^{-1}\ h\ \mathrm{M}_\odot\ \mathrm{pc}^{-2}$.

assume that the position of the centre of every cluster dark matter halo coincides with the associated BCG position so that any offset between the assumed and true halo centres stems from a misidentification of the BCG. There are other possible reasons for a misalignment, such as the BCG truly being offset from the centre of its halo. In what follows here, this assumption may affect the miscentrering distribution used but the principles remain the same.

For our model we will largely follow the procedure outlined in J07. The azimuthally averaged surface density $\Sigma(R)$ of a miscentred halo is given by

$$\Sigma(R|R_s) = \frac{1}{2\pi}\int_0^{2\pi} \Sigma\left(\sqrt{R^2 + R_s^2 + 2RR_s\cos(\theta)}\right) d\theta \tag{5.18}$$

(Yang et al., 2006), where R_s is the 2D offset in the lens plane. This expression applies to a single misaligned halo, but for an ensemble the offsets will follow some distribution. Using N-body simulations, J07 find for their maxBCG sample that the distribution of miscentred BCGs is well described by a Gaussian distribution:

$$P(R_s) = \frac{R_s}{\sigma_s^2}\exp\left[-\frac{1}{2}\left(\frac{R_s}{\sigma_s}\right)^2\right] \tag{5.19}$$

with width $\sigma_s = 0.42\ h^{-1}$ Mpc. For our model we will keep the shape of the distribution the same as above but allow σ_s to vary. The resulting mean surface

density profile for the miscentred population is then given by

$$\Sigma^s(R) = \int P(R_s)\Sigma_{\rm NFW}(R|R_s)dR_s \tag{5.20}$$

where we have explicitly noted our assumption that all dark matter haloes are NFW profiles.

From this surface density we can then numerically obtain the shear and flexion profiles using Equations 5.3, 5.5 and 5.6 (or, equivalently, Equations 5.7 and 5.8). In Figure 5.1 we show the four signals as a function of distance R from the assumed cluster centre, for a cluster mass of $10^{13}\ h^{-1}$ Mpc, cluster redshift $z_l = 0.22$ and offset distribution dispersion (Equation 5.19) $\sigma_s = 0.42\ h^{-1}$ Mpc. As noted by J07, the effect of miscentrering on the $\Sigma(R)$ essentially flattens the profile on small scales (purple solid), making it a mass-sheet which causes very little shear. This is the reason why the miscentred shear profile (purple dashed) is strongly suppressed at small scales. The shear then peaks at a radius $R \sim 2.5\sigma_s$ and, as we will show in Section 5.3.3, this approximate scale relationship holds for all σ_s. The miscentred flexion signals are also strongly suppressed at small scales. The F flexion signal (purple dash-dotted) peaks at slightly lower cluster-centric distances than shear, while the peak of the G flexion signal (purple dotted) roughly coincides with the shear peak. The G flexion is in fact the most strongly affected signal and would thus be an important aid in determining the width of the offset distribution. Note that, given the appropriate units of D_l, the amplitudes of the four signals are similar at intermediate scales. For reference we have also included the corresponding centred signals (green) where we see the by now well-known behaviour of the flexion signals; $\mathcal{F}_\Diamond$ falls off quickly with distance while $\mathcal{G}_\Diamond$ has a greater range.

5.2.5 Other contributions

There are other contributions to the lensing signal to be taken into account. Neighbouring haloes contribute significant signal on large scales ($\gtrsim 5\ h^{-1}$ Mpc) similar to the 2-halo term in our galaxy-galaxy halo model (Section 4.3.2, page 98), but since we are focusing this Chapter on the effect of BCG misalignment which is only significant on intermediate scales, we will not take this term into account here. Similarly, we will not model the non-linear term due to the basic weak lensing assumption of $\kappa \ll 1$ no longer being valid, as noted in J07 since this term is only relevant on small scales ($\lesssim 0.1\ h^{-1}$ Mpc), and in all but the most massive cases contributes significantly less to the shear signal than the baryonic component does. For flexion it could prove important though, since this is the region in which this lensing measurement is most sensitive, so in full cluster models it should be taken into account.

Finally we summarise our cluster model. Assuming that the BCG has been correctly identified in a fraction f_c of the clusters, the average profile will be given by

$$\Delta\Sigma(R) = \Delta\Sigma^b(R) + f_c\Delta\Sigma^c(R) + (1 - f_c)\Delta\Sigma^s(R) \tag{5.21}$$

and similarly for the flexions, where $\Delta\Sigma^b(R)$ is the baryonic component, $\Delta\Sigma^c(R)$ is the contribution from accurately centred haloes and $\Delta\Sigma^s(R)$ is the contribution from haloes that are not centred.

Table 5.1 Fiducial values of the cluster model parameters.

BCG stellar mass M_*	$5.00 \times 10^{11}\ h^{-1}\ M_\odot$
Halo mass M_{200}	$1.00 \times 10^{14}\ h^{-1}\ M_\odot$
Halo concentration c_{200}	As in Equation 5.17
Cluster redshift z	0.34
Offset distribution width σ_s	$0.42\ h^{-1}$ Mpc
Offset fraction f_c	0.50

5.3 Results

We now turn to studying the change in the lensing signal profiles as we vary the properties of our cluster model. In the following sections we will vary the halo mass M_{200}, the halo concentration c_{200} and the offset distribution width σ_s to assess and contrast the impact of BCG misalignment on the different types of lensing distortions, i.e. Σ, $\Delta\Sigma$, $\Delta\Sigma'$, $\mathcal{F}_\Diamond$ and $\mathcal{G}_\Diamond$. The first signal, the surface density, is not directly observable through lensing but is included in this study for reference since it is a more intuitive physical quantity than the other four. The parameters that are not explicitly varied in each section will be kept constant at the values listed in Table 5.1. The offset distribution width σ_s is set to the value found by J07 to approximately fit most of their maxBCG cluster ensembles. They also found that an offset fraction of $f_c \sim 0.60$ fit their samples well, but we will set our f_c to 0.5 to allow for a direct comparison of the centred and miscentred profiles in the following sections.

In general, as can be seen in Figure 5.1, miscentred haloes will cause a flattening of the Σ profile on small scales, and suppress the other three signals (for clarity we do not include $\Delta\Sigma'$ in that figure). On intermediate scales, however, there is a slight increase, or 'bump', in the signal amplitude for Σ, $\mathcal{F}_\Diamond$ and $\mathcal{G}_\Diamond$, something which is not noticeable or detectable in the $\Delta\Sigma$ profile. This bump, as will be seen in the following sections, causes a fairly sharp feature in the flexion profiles at the position of the offcentre profile peak, potentially allowing for an improved estimate of the distribution width σ_s through its relationship with the peak location.

5.3.1 Mass dependence

We first investigate how the different signals corresponding to our cluster model change with halo mass. Figures 5.2 to 5.4 show the five lensing signals Σ, $\Delta\Sigma$, $\Delta\Sigma'$, $\mathcal{F}_\Diamond$ and $\mathcal{G}_\Diamond$ as a function of distance R from the *assumed* cluster centre, for five different halo masses M_{200}. All other parameters are kept constant at the fiducial values given in Table 5.1. The solid line in each panel represents the total signal for a cluster ensemble where a fraction $f_c = 0.5$ of the clusters have misaligned BCGs, while the dotted, dash-dotted and dashed lines represent the components of the signal as specified in the captions.

As expected, the amplitude increases with increasing halo mass. We also clearly see that the bump in the offcentre profile at $\sim 1\ h^{-1}$ Mpc becomes more pronounced for lower masses. This trend, which is visible in the Σ signal (Figure 5.2), is not discernible in the $\Delta\Sigma$ (Figure 5.3) or $\mathcal{G}_\Diamond$ (Figure 5.4) signals. It is, however, clearly prominent in the $\mathcal{F}_\Diamond$ signal (Figure 5.4) and, particularly,

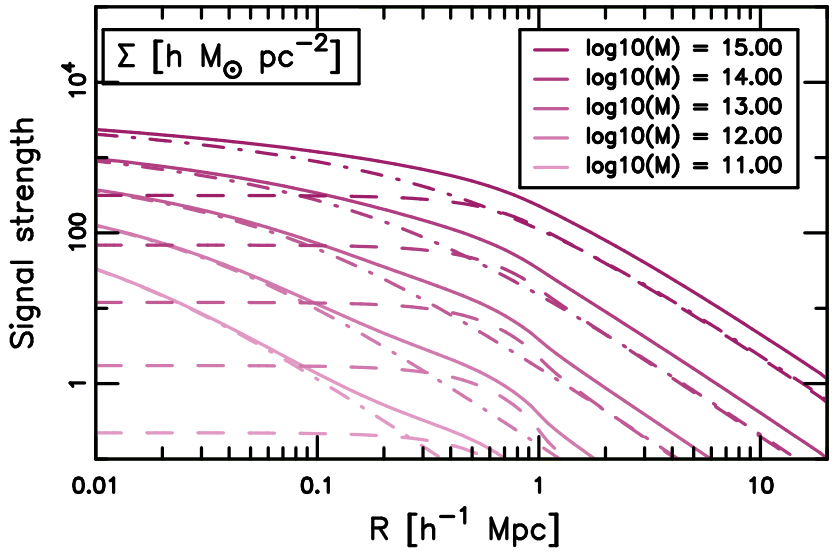

Figure 5.2 Dependence of the cluster model surface density Σ on halo mass. The dash-dotted and dashed lines represent the cluster model components (centred clusters and miscentred clusters respectively) while the solid line is the sum of the components. Here, the fraction of miscentred clusters is $f_c = 0.5$. The signal amplitude increases with mass, colour coded as per the legend. Note that in the case of Σ there is no contribution from the BCG other than at $R = 0$.

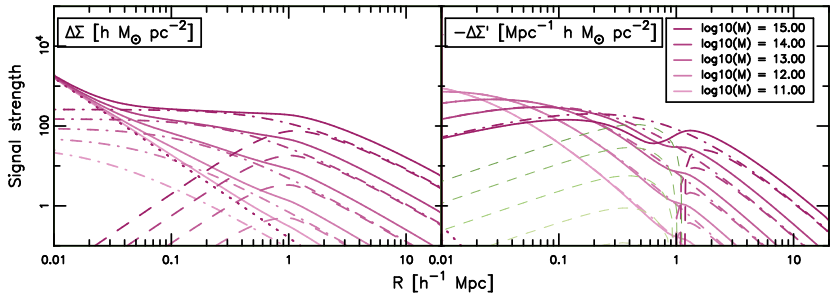

Figure 5.3 Dependence of the cluster model differential surface density $\Delta\Sigma$ (left panel) and its derivative $\Delta\Sigma'$ (right panel) on halo mass. Note the different units as specified in the legend, and that $\Delta\Sigma'$ has been negated since it is mostly negative. The dotted, dash-dotted and dashed lines represent the cluster model components (BCG, centred clusters and miscentred clusters respectively) while the solid line is the sum of the components. Here, the fraction of miscentred clusters is $f_c = 0.5$. The signal amplitude increases with mass, colour coded as per the legend, with thick purple (thin green) representing positive (negative) quantities. Only the inner dashed lines in the right panel are negative.

in the combination of the two flexion signals $\Delta\Sigma'$ (Figure 5.3) where for the latter it turns into a dip due to the switch between positive and negative slope of $\Delta\Sigma$ for the offcentred distribution, further illustrating the sensitivity of these types of distortion to the underlying density variations. The feature in the

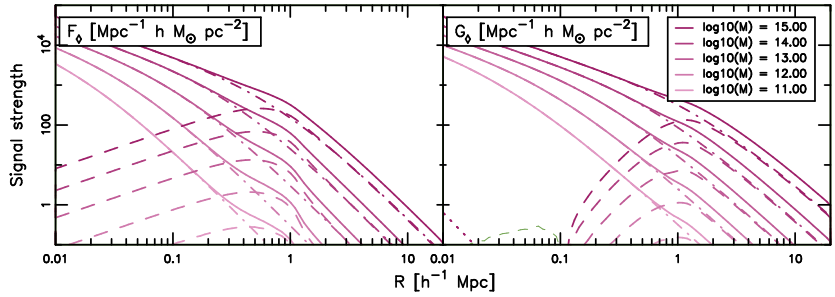

Figure 5.4 Dependence of the cluster model flexions $\mathcal{F}_\diamondsuit$ (left panel) and $\mathcal{G}_\diamondsuit$ (right panel) on halo mass. The dotted, dash-dotted and dashed lines represent the cluster model components (BCG, centred clusters and miscentred clusters respectively) while the solid line is the sum of the components. Note that there is no contribution from the BCG to $\mathcal{F}_\diamondsuit$. Here, the fraction of miscentred clusters is $f_c = 0.5$. The signal amplitude increases with mass, colour coded as per the legend, with thick purple (thin green) representing positive (negative) quantities. Only the highest mass bin has significant negative signal in the inner regions.

signal is always located at the same cluster-centric distance for all masses since it only depends on the width of the misalignment distribution. This is also the explanation for the bump becoming less prominent with increasing mass in all signals but $\Delta\Sigma'$; we force the distribution width to $\sigma_s = 0.42\ h^{-1}$ Mpc, meaning that the Σ^s profile is roughly flat out to that distance. For the highest mass profile, where $M_{200} = 10^{15}\ h^{-1}\ M_\odot$, the scale radius is $r_s = 0.49\ h^{-1}$ Mpc $\gtrsim \sigma_s$ and this allows the flat Σ^s distribution to transition into the large-scale powerlaw in a smooth fashion. For the lowest mass bin, however, $M_{200} = 10^{11}\ h^{-1}\ M_\odot$ and the scale radius is $r_s = 0.01\ h^{-1}$ Mpc $\ll \sigma_s$. This causes the apparent bump at $R \sim 2.5\sigma_s$, which in turn causes the turnover in the derived signals $\Delta\Sigma^s$, $\mathcal{F}^s_\diamondsuit$ and $\mathcal{G}^s_\diamondsuit$, and the switch from positive to negative in $\Delta\Sigma'^s$. J07 do claim that the offset width is roughly independent of cluster richness, so they give this fitting parameter a strong prior centred on our fiducial value. For their lowest richness bins the feature should thus be clearly discernible in a flexion measurement, and particularly in the combination $\mathcal{F}_\diamondsuit - \mathcal{G}_\diamondsuit \propto \Delta\Sigma'$, given high-quality data.

5.3.2 Concentration dependence

We now turn to studying the change in the cluster profiles as the NFW concentration parameter $c_{\rm NFW}$ is varied. The resulting profiles are shown in Figures 5.5 to 5.7. As concentration increases the NFW scaling radius r_s, or pivot point, is forced to decrease in order to keep the physical scale of the halo, r_{200}, the same (see Equation 5.17). Thus the amplitude of Σ increases on small scales but decreases on large scales, seen most clearly in the accurately centred halo profiles. The miscentred profiles have similar amplitudes independent of concentration within $R \sim 2.5\sigma_s$, but on larger scales they follow the same trend as the centred profiles. Thus the differences between different c_{200} become amplified on large scales, making the feature at ~ 1 Mpc more prominent for higher concentrations. This is also true for the flexions, but as before the trend is reversed for $\Delta\Sigma'$; the feature becomes less prominent as the transition between

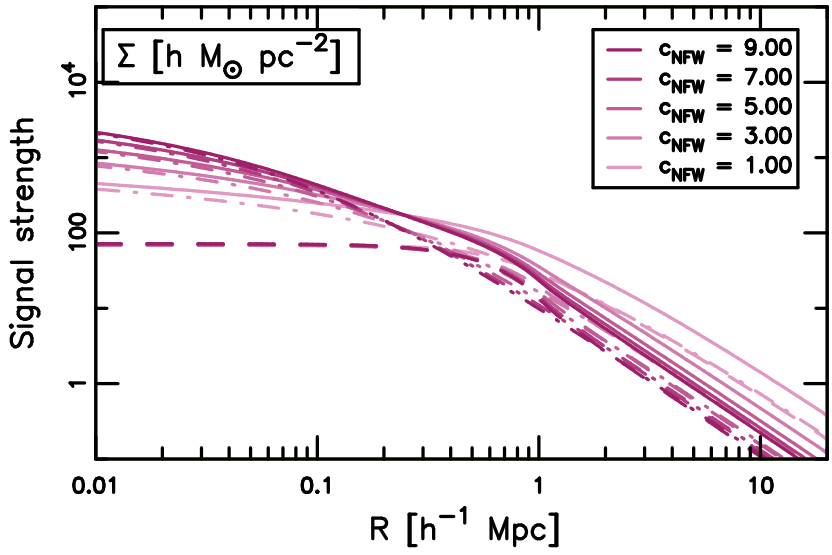

Figure 5.5 Dependence of the cluster model surface density Σ on halo concentration. The dash-dotted and dashed lines represent the cluster model components (centred clusters and miscentred clusters respectively) while the solid line is the sum of the components. Here, the fraction of miscentred clusters is $f_c = 0.5$. The signal amplitude increases with concentration in the inner regions, colour coded as per the legend. Note that in the case of Σ there is no contribution from the BCG other than at $R = 0$.

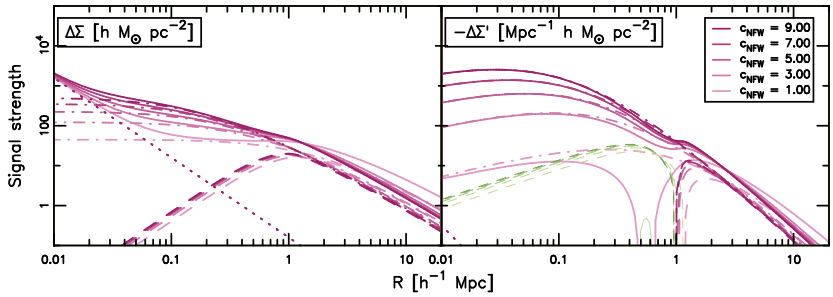

Figure 5.6 Dependence of the cluster model differential surface density $\Delta\Sigma$ (left panel) and its derivative $\Delta\Sigma'$ (right panel) on halo concentration. Note the different units as specified in the legend, and that $\Delta\Sigma'$ has been negated since it is mostly negative. The dotted, dash-dotted and dashed lines represent the cluster model components (BCG, centred clusters and miscentred clusters respectively) while the solid line is the sum of the components. Here, the fraction of miscentred clusters is $f_c = 0.5$. The signal amplitude increases with concentration, colour coded as per the legend, with thick purple (thin green) representing positive (negative) quantities. Only the inner dashed lines in the right panel are negative.

positive and negative $\Delta\Sigma$ slopes becomes sharper. Assuming the Duffy et al. (2008) relationship between concentration, mass and redshift (Equation 5.17), the c_{200} for a halo mass equal to our fiducial mass would range between ~ 4 at

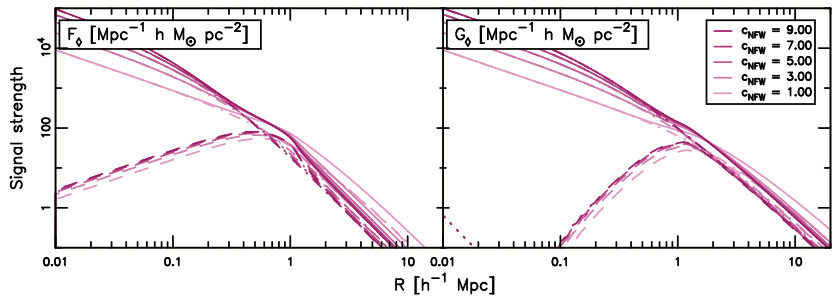

Figure 5.7 Dependence of the cluster model flexions $\mathcal{F}_\diamondsuit$ (left panel) and $\mathcal{G}_\diamondsuit$ (right panel) on halo concentration. The dotted, dash-dotted and dashed lines represent the cluster model components (BCG, centred clusters and miscentred clusters respectively) while the solid line is the sum of the components. Note that there is no contribution from the BCG to $\mathcal{F}_\diamondsuit$. Here, the fraction of miscentred clusters is $f_c = 0.5$. The signal amplitude increases with concentration, colour coded as per the legend.

low redshifts and ~ 3 at $z = 0.8$.

5.3.3 Offset width dependence

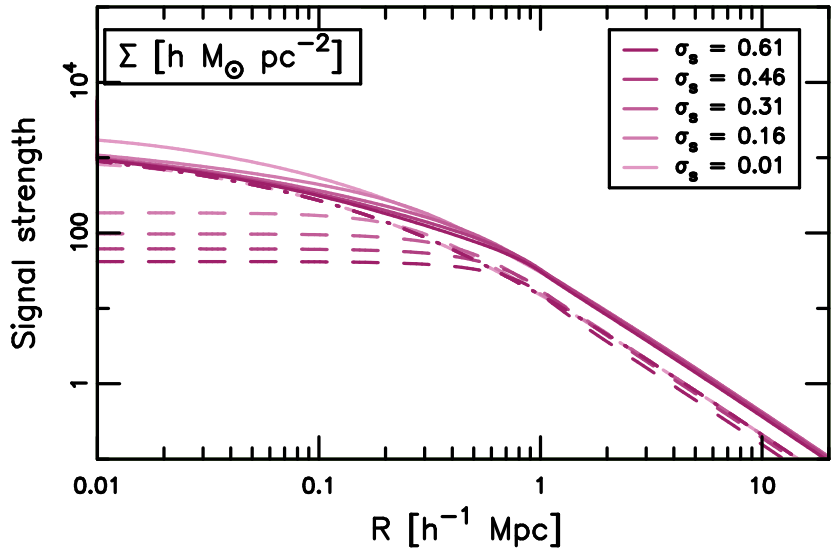

Figure 5.8 Dependence of the cluster model surface density Σ on the width of the miscentrering distribution. The dash-dotted and dashed lines represent the cluster model components (centred clusters and miscentred clusters respectively) while the solid line is the sum of the components. Here, the fraction of miscentred clusters is $f_c = 0.5$. The signal amplitude decreases with distribution width in the inner regions, colour coded as per the legend. Note that in the case of Σ there is no contribution from the BCG other than at $R = 0$.

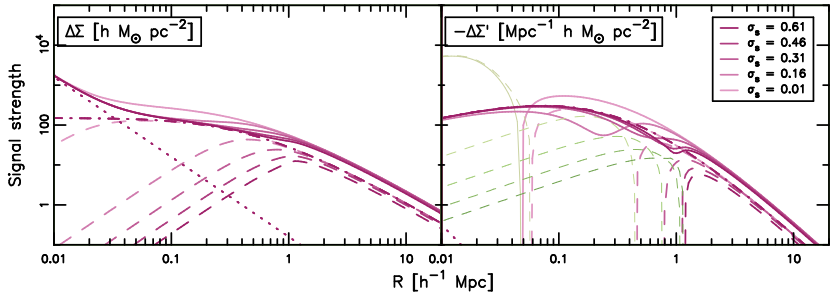

Figure 5.9 Dependence of the cluster model differential surface density $\Delta\Sigma$ (left panel) and its derivative $\Delta\Sigma'$ (right panel) on the width of the miscentrering distribution. Note the different units as specified in the legend, and that $\Delta\Sigma'$ has been negated since it is mostly negative. The dotted, dash-dotted and dashed lines represent the cluster model components (BCG, centred clusters and miscentred clusters respectively) while the solid line is the sum of the components. Here, the fraction of miscentred clusters is $f_c = 0.5$. The signal amplitude changes with distribution width, colour coded as per the legend, with purple (green) representing positive (negative) quantities. Only the inner regions in the right panel are negative.

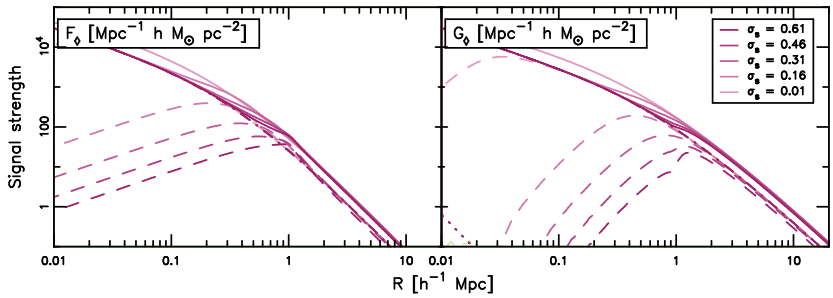

Figure 5.10 Dependence of the cluster model flexions $\mathcal{F}_\diamond$ (left panel) and $\mathcal{G}_\diamond$ (right panel) on the width of the miscentrering distribution. The dotted, dash-dotted and dashed lines represent the cluster model components (BCG, centred clusters and miscentred clusters respectively) while the solid line is the sum of the components. Note that there is no contribution from the BCG to $\mathcal{F}_\diamond$. Here, the fraction of miscentred clusters is $f_c = 0.5$. The signal amplitude decreases with distribution width in the inner regions, colour coded as per the legend.

Finally we study the lensing signals due to misaligned BCGs as the offset distribution width σ_s is varied, and assess the impact on the composite signal, as shown in Figures 5.8 to 5.10. As the offset width increases, the Σ^s profile is flattened to larger scales, causing the features in the other four signals to shift, closely following the relation $R_{\rm peak} \sim 2.5\sigma_s$ pointed out by J07. What we also notice is that for the greatest offset distribution widths, the offset signal never quite reaches the amplitude of the centred signal, even on the largest scales. Additionally, the bump in the total Σ and flexion signals becomes more pronounced for increased σ_s due to the same mechanisms described in the previous Section. Here we can clearly see the sensitivity of the flexions to the relative sizes of σ_s

and the NFW scale radius r_s. For the largest offsets, where $\sigma_s \gg r_s$, prominent features are visible in both the flexion signals and $\Delta\Sigma'$, and as mentioned in the previous section, these features could be visible in reasonable cluster samples.

5.4 Conclusions

In this Chapter we have closely followed the initial work of Johnston et al. (2007) and derived model cluster profiles for the two flexions, $\mathcal{F}$ and $\mathcal{G}$, for an ensemble of clusters where a significant fraction have a misidentified dark matter halo centre. We have compared these profiles to the corresponding surface density Σ and shear γ (or $\Delta\Sigma$) profiles and found that both flexions are promising tools for determining properties of misalignment distributions, particularly if they are combined to produce $\Delta\Sigma'$, and thus important in removing systematic errors when determining the overall halo mass. In theory, the signal-to-noise for flexion is higher than for shear on small scales, though this is currently limited by the accuracy of shape measurement software.

We studied the lensing profiles as a function of halo mass, halo concentration and offset distribution width and found that for feasible cluster samples the flexion signals in different combinations will display clear indicators of the true offset distribution widths, something shear is less sensitive to. We also verified that the peak of the offset distribution will be located at a cluster-centric distance of $R_{\rm peak} \sim 2.5\sigma_s$, as claimed by J07.

Our cluster lensing profiles are a composite of the contribution from the BCG, from the accurately centred haloes and from the misaligned haloes. In the near future we plan to include further components in our flexion signals, such as the contribution on large scales from neighbouring haloes, and the contribution on small scales due to non-linearity in the shear. This latter component may turn out to be more important for the flexions than it is for shear, since this is at scales where flexion has the most power. We will also investigate the use of combinations of the two flexion signals to produce new measures of the underlying density distribution. In conclusion, modelling the cluster density profile using all three orthogonal lensing observables in conjunction will better constrain the offset distribution and improve halo mass estimates, which in turn will yield a greater understanding of scaling relations important to cosmology.

Acknowledgements

MV acknowledges support from the European DUEL Research-Training Network (MRTN-CT-2006-036133) and from the Netherlands Organization for Scientific Research (NWO).

Bibliography

Abate A., Wittman D., Margoniner V. E., Bridle S. L., Gee P., Tyson J. A., Dell'Antonio I. P., 2009, ApJ, 702, 603

Abazajian K. N., Adelman-McCarthy J. K., Agüeros M. A., Allam S. S., Allende Prieto C., An D., Anderson K. S. J., Anderson S. F., Annis J., Bahcall N. A., et al., 2009, ApJS, 182, 543

Alcock C., Allsman R. A., Alves D. R., Axelrod T. S., Becker A. C., Bennett D. P., Cook K. H., Dalal N., Drake A. J., Freeman K. C., Geha M., Griest K., Lehner M. J., Marshall S. L., Minniti D., Nelson C. A., Peterson B. A., Popowski P., Pratt M. R., Quinn P. J., Stubbs C. W., Sutherland W., Tomaney A. B., Vandehei T., Welch D., 2000a, ApJ, 542, 281

Alcock C., Allsman R. A., Alves D. R., Axelrod T. S., Becker A. C., Bennett D. P., Cook K. H., Drake A. J., Freeman K. C., Geha M., Griest K., Lehner M. J., Marshall S. L., Minniti D., Nelson C. A., Peterson B. A., Popowski P., Pratt M. R., Quinn P. J., Stubbs C. W., Sutherland W., Tomaney A. B., Vandehei T., Welch D. L., MACHO Collaboration, 2000b, ApJ, 541, 734

Andrae R., Melchior P., Jahnke K., 2011, MNRAS, 417, 2465

Bacon D. J., Amara A., Read J. I., 2010, MNRAS, 409, 389

Bacon D. J., Goldberg D. M., Rowe B. T. P., Taylor A. N., 2006, MNRAS, 365, 414

Bacon D. J., Refregier A. R., Ellis R. S., 2000, MNRAS, 318, 625

Bartelmann M., Huss A., Colberg J. M., Jenkins A., Pearce F. R., 1998, A&A, 330, 1

Bartelmann M., Schneider P., 2001, PhR, 340, 291

Bekenstein J. D., 2004, PhRvD, 70, 083509

Bell E. F., de Jong R. S., 2001, ApJ, 550, 212

Bell E. F., McIntosh D. H., Katz N., Weinberg M. D., 2003, ApJS, 149, 289

Benjamin J., Heymans C., Semboloni E., van Waerbeke L., Hoekstra H., Erben T., Gladders M. D., Hetterscheidt M., Mellier Y., Yee H. K. C., 2007, MNRAS, 381, 702

Bennett C. L., Halpern M., Hinshaw G., Jarosik N., Kogut A., Limon M., Meyer S. S., Page L., Spergel D. N., Tucker G. S., Wollack E., Wright E. L., Barnes C., Greason M. R., Hill R. S., Komatsu E., Nolta M. R., Odegard N., Peiris H. V., Verde L., Weiland J. L., 2003, ApJS, 148, 1

Bennett D. P., Sumi T., Bond I. A., Kamiya K., Abe F., Botzler C. S., Fukui A., Furusawa K., Itow Y., Korpela A. V., Kilmartin P. M., Ling C. H., Masuda K., Matsubara Y., Miyake N., Muraki Y., Ohnishi K., Rattenbury N. J., Saito T., Sullivan D. J., Suzuki D., Sweatman W. L., Tristram P. J., Wada K., Yock P. C. M., 2012, preprint (astro-ph/1203.4560)

Bernstein G. M., Jarvis M., 2002, AJ, 123, 583

Bertin E., Arnouts S., 1996, A&AS, 117, 393

Biviano A., Girardi M., 2003, ApJ, 585, 205

Blandford R., Narayan R., 1986, ApJ, 310, 568

Bond I. A., Abe F., Dodd R. J., Hearnshaw J. B., Honda M., Jugaku J., Kilmartin P. M., Marles A., Masuda K., Matsubara Y., Muraki Y., Nakamura T., Nankivell G., Noda S., Noguchi C., Ohnishi K., Rattenbury N. J., Reid M., Saito T., Sato H., Sekiguchi M., Skuljan J., Sullivan D. J., Sumi T., Takeuti M., Watase Y., Wilkinson S., Yamada R., Yanagisawa T., Yock P. C. M., 2001, MNRAS, 327, 868

Bouwens R. J., Illingworth G. D., Labbe I., Oesch P. A., Trenti M., Carollo C. M., van Dokkum P. G., Franx M., Stiavelli M., González V., Magee D., Bradley L., 2011, Nature, 469, 504

Bowler B. P., Liu M. C., Kraus A. L., Mann A. W., Ireland M. J., 2011, ApJ, 743, 148

Bridle S., Balan S. T., Bethge M., Gentile M., Harmeling S., Heymans C., Hirsch M., Hosseini R., Jarvis M., Kirk D., Kitching T., Kuijken K., Lewis A., Paulin-Henriksson S., Schölkopf B., Velander M., Voigt L., Witherick D., Amara A., Bernstein G., Courbin F., Gill M., Heavens A., Mandelbaum R., Massey R., Moghaddam B., Rassat A., Réfrégier A., Rhodes J., Schrabback T., Shawe-Taylor J., Shmakova M., van Waerbeke L., Wittman D., 2010, MNRAS, 405, 2044

Bridle S., Shawe-Taylor J., Amara A., Applegate D., Balan Berge J. S. T., Bernstein G., Dahle H., Erben T., Gill M., Heavens A., Heymans C., High F. W., Hoekstra H., Jarvis M., Kirk D., Kitching T., Kneib J., Kuijken K., Lagatutta D., Mandelbaum R., Massey R., Mellier Y., Moghaddam B., Moudden Y., Nakajima R., Paulin-Henriksson S., Pires S., Rassat A., Refregier A., Rhodes J., Schrabback T., Semboloni E., Shmakova M., van Waerbeke L., Witherick D., Voigt L., Wittman D., 2009, Annals of Applied Statistics, 3, 6

Bridle S. L., Kneib J.-P., Bardeau S., Gull S. F., 2002, in The Shapes of Galaxies and their Dark Halos, P. Natarajan, ed., pp. 38–46

Brown M. L., Taylor A. N., Bacon D. J., Gray M. E., Dye S., Meisenheimer K., Wolf C., 2003, MNRAS, 341, 100

Cain B., Schechter P. L., Bautz M. W., 2011, ApJ, 736, 43

Cline J. M., Grojean C., Servant G., 1999, PhRvL, 83, 4245

Clowe D., Bradač M., Gonzalez A. H., Markevitch M., Randall S. W., Jones C., Zaritsky D., 2006, ApJl, 648, L109

Cole S., Percival W. J., Peacock J. A., Norberg P., Baugh C. M., Frenk C. S., Baldry I., Bland-Hawthorn J., Bridges T., Cannon R., Colless M., Collins C., Couch W., Cross N. J. G., Dalton G., Eke V. R., De Propris R., Driver S. P., Efstathiou G., Ellis R. S., Glazebrook K., Jackson C., Jenkins A., Lahav O., Lewis I., Lumsden S., Maddox S., Madgwick D., Peterson B. A., Sutherland W., Taylor K., 2005, MNRAS, 362, 505

Conroy C., Wechsler R. H., 2009, ApJ, 696, 620

Cooray A., Sheth R., 2002, Phys. Rep., 372, 1

Cypriano E. S., Amara A., Voigt L. M., Bridle S. L., Abdalla F. B., Réfrégier A., Seiffert M., Rhodes J., 2010, MNRAS, 405, 494

D'Aloisio A., Natarajan P., 2011, MNRAS, 415, 1913

Davis M., Guhathakurta P., Konidaris N. P., Newman J. A., Ashby M. L. N., Biggs A. D., Barmby P., Bundy K., Chapman S. C., Coil A. L., Conselice C. J., Cooper M. C., Croton D. J., Eisenhardt P. R. M., Ellis R. S., Faber S. M., Fang T., Fazio G. G., Georgakakis A., Gerke B. F., Goss W. M., Gwyn S., Harker J., Hopkins A. M., Huang J.-S., Ivison R. J., Kassin S. A., Kirby E. N., Koekemoer A. M., Koo D. C., Laird E. S., Le Floc'h E., Lin L., Lotz J. M., Marshall P. J., Martin D. C., Metevier A. J., Moustakas L. A., Nandra K., Noeske K. G., Papovich C., Phillips A. C., Rich R. M., Rieke G. H., Rigopoulou D., Salim S., Schiminovich D., Simard L., Smail I., Small T. A., Weiner B. J., Willmer C. N. A., Willner S. P., Wilson G., Wright E. L., Yan R., 2007, ApJL, 660, L1

Duffy A. R., Schaye J., Kay S. T., Dalla Vecchia C., 2008, MNRAS, 390, L64

Dunkley J., Komatsu E., Nolta M. R., Spergel D. N., Larson D., Hinshaw G., Page L., Bennett C. L., Gold B., Jarosik N., Weiland J. L., Halpern M., Hill R. S., Kogut A., Limon M., Meyer S. S., Tucker G. S., Wollack E., Wright E. L., 2009, ApJS, 180, 306

Dyson F. W., Eddington A. S., Davidson C., 1920, RSPTA, 220, 291

Eisenstein D. J., Zehavi I., Hogg D. W., Scoccimarro R., Blanton M. R., Nichol R. C., Scranton R., Seo H.-J., Tegmark M., Zheng Z., Anderson S. F., Annis J., Bahcall N., Brinkmann J., Burles S., Castander F. J., Connolly A., Csabai I., Doi M., Fukugita M., Frieman J. A., Glazebrook K., Gunn J. E., Hendry J. S., Hennessy G., Ivezić Z., Kent S., Knapp G. R., Lin H., Loh Y.-S., Lupton

R. H., Margon B., McKay T. A., Meiksin A., Munn J. A., Pope A., Richmond M. W., Schlegel D., Schneider D. P., Shimasaku K., Stoughton C., Strauss M. A., SubbaRao M., Szalay A. S., Szapudi I., Tucker D. L., Yanny B., York D. G., 2005, ApJ, 633, 560

Ellis R., Santos M. R., Kneib J.-P., Kuijken K., 2001, ApJL, 560, L119

Er X., Li G., Schneider P., 2010, A&A, submitted (arXiv:1008.3088)

Er X., Schneider P., 2011, A&A, 528, A52

Er X., Tereno I., Mao S., 2011, preprint (astro-ph/1112.4670)

Erben T., Van Waerbeke L., Bertin E., Mellier Y., Schneider P., 2001, A&A, 366, 717

Evrard A. E., 1990, ApJ, 363, 349

Falco E. E., Gorenstein M. V., Shapiro I. I., 1985, ApJL, 289, L1

Faltenbacher A., Gottlöber S., Kerscher M., Müller V., 2002, A&A, 395, 1

Franx M., Illingworth G. D., Kelson D. D., van Dokkum P. G., Tran K.-V., 1997, ApJL, 486, L75

Freeman K. C., 1970, ApJ, 160, 811

Fu L., Semboloni E., Hoekstra H., Kilbinger M., van Waerbeke L., Tereno I., Mellier Y., Heymans C., Coupon J., Benabed K., Benjamin J., Bertin E., Doré O., Hudson M. J., Ilbert O., Maoli R., Marmo C., McCracken H. J., Ménard B., 2008, A&A, 479, 9

Gallazzi A., Charlot S., Brinchmann J., White S. D. M., Tremonti C. A., 2005, MNRAS, 362, 41

Gilbank D. G., Gladders M. D., Yee H. K. C., Hsieh B. C., 2011, AJ, 141, 94

Goldberg D. M., Bacon D. J., 2005, ApJ, 619, 741

Goldberg D. M., Natarajan P., 2002, ApJ, 564, 65

Golse G., Kneib J.-P., Soucail G., 2002, A&A, 387, 788

Gonzalez-Perez V., Castander F. J., Kauffmann G., 2011, MNRAS, 411, 1151

Gulkis S., Lubin P. M., Meyer S. S., Silverberg R. F., 1990, Scientific American, 262, 132

Guzik J., Seljak U., 2002, MNRAS, 335, 311

Hao J. G., Akhoury R., 2009, IJMPD, 18, 1039

Hawken A. J., Bridle S. L., 2009, MNRAS, 400, 1132

Heymans C., Brown M. L., Barden M., Caldwell J. A. R., Jahnke K., Peng C. Y., Rix H.-W., Taylor A., Beckwith S. V. W., Bell E. F., Borch A., Häußler B., Jogee S., McIntosh D. H., Meisenheimer K., Sánchez S. F., Somerville R., Wisotzki L., Wolf C., 2005, MNRAS, 361, 160

Heymans C., Van Waerbeke L., Bacon D., Berge J., Bernstein G., Bertin E., Bridle S., Brown M. L., Clowe D., Dahle H., Erben T., Gray M., Hetterscheidt M., Hoekstra H., Hudelot P., Jarvis M., Kuijken K., Margoniner V., Massey R., Mellier Y., Nakajima R., Refregier A., Rhodes J., Schrabback T., Wittman D., 2006a, MNRAS, 368, 1323

Heymans C., White M., Heavens A., Vale C., van Waerbeke L., 2006b, MNRAS, 371, 750

Hildebrandt H., Erben T., Kuijken K., van Waerbeke L., Heymans C., Coupon J., Benjamin J., Bonnett C., Fu L., Hoekstra H., Kitching T. D., Mellier Y., Miller L., Velander M., Hudson M. J., Rowe B. T. P., Schrabback T., Semboloni E., Benítez N., 2012, MNRAS, 421, 2355

Hirata C. M., Seljak U., 2004, PhRvD, 70, 063526

Hoekstra H., Donahue M., Conselice C. J., McNamara B. R., Voit G. M., 2011, ApJ, 726, 48

Hoekstra H., Franx M., Kuijken K., Squires G., 1998, ApJ, 504, 636

Hoekstra H., Hsieh B. C., Yee H. K. C., Lin H., Gladders M. D., 2005, ApJ, 635, 73

Hoekstra H., Jain B., 2008, Annual Review of Nuclear and Particle Science, 58, 99

Hoekstra H., Mellier Y., van Waerbeke L., Semboloni E., Fu L., Hudson M. J., Parker L. C., Tereno I., Benabed K., 2006, ApJ, 647, 116

Hoekstra H., Yee H. K. C., Gladders M. D., 2002, ApJ, 577, 595

—, 2004, ApJ, 606, 67

Holhjem K., Schirmer M., Dahle H., 2009, A&A, 504, 1

Horesh A., Ofek E. O., Maoz D., Bartelmann M., Meneghetti M., Rix H.-W., 2005, ApJ, 633, 768

Hu E. M., Cowie L. L., McMahon R. G., Capak P., Iwamuro F., Kneib J.-P., Maihara T., Motohara K., 2002, ApJL, 568, L75

Hu W., White M., 1996, ApJ, 471, 30

Huff E. M., Eifler T., Hirata C. M., Mandelbaum R., Schlegel D., Seljak U., 2011, preprint (astro-ph/1112.3143)

Ilbert O., Capak P., Salvato M., Aussel H., McCracken H. J., Sanders D. B., Scoville N., Kartaltepe J., Arnouts S., Le Floc'h E., Mobasher B., Taniguchi Y., Lamareille F., Leauthaud A., Sasaki S., Thompson D., Zamojski M., Zamorani G., Bardelli S., Bolzonella M., Bongiorno A., Brusa M., Caputi K. I., Carollo C. M., Contini T., Cook R., Coppa G., Cucciati O., de la Torre S., de Ravel L., Franzetti P., Garilli B., Hasinger G., Iovino A., Kampczyk P., Kneib J., Knobel C., Kovac K., Le Borgne J. F., Le Brun V., Fèvre O. L., Lilly S., Looper D., Maier C., Mainieri V., Mellier Y., Mignoli M., Murayama T.,

Pellò R., Peng Y., Pérez-Montero E., Renzini A., Ricciardelli E., Schiminovich D., Scodeggio M., Shioya Y., Silverman J., Surace J., Tanaka M., Tasca L., Tresse L., Vergani D., Zucca E., 2009, ApJ, 690, 1236

Jarosik N., Bennett C. L., Dunkley J., Gold B., Greason M. R., Halpern M., Hill R. S., Hinshaw G., Kogut A., Komatsu E., Larson D., Limon M., Meyer S. S., Nolta M. R., Odegard N., Page L., Smith K. M., Spergel D. N., Tucker G. S., Weiland J. L., Wollack E., Wright E. L., 2011, ApJS, 192, 14

Jarvis M., Bernstein G. M., Fischer P., Smith D., Jain B., Tyson J. A., Wittman D., 2003, AJ, 125, 1014

Jee M. J., Mahdavi A., Hoekstra H., Babul A., Dalcanton J. J., Carroll P., Capak P., 2012, ApJ, 747, 96

Johnston D. E., Sheldon E. S., Wechsler R. H., Rozo E., Koester B. P., Frieman J. A., McKay T. A., Evrard A. E., Becker M. R., Annis J., 2007, preprint (astro-ph/0709.1159)

Jones L., Smail I., Couch W. J., 2000, ApJ, 528, 118

Jullo E., Natarajan P., Kneib J.-P., D'Aloisio A., Limousin M., Richard J., Schimd C., 2010, Science, 329, 924

Kaiser N., 1992, ApJ, 388, 272

—, 2000, ApJ, 537, 555

Kaiser N., Squires G., Broadhurst T., 1995, ApJ, 449, 460

Kaiser N., Wilson G., Luppino G. A., 2000, preprint (astro-ph/0003338)

Katgert P., Biviano A., Mazure A., 2004, ApJ, 600, 657

Kauffmann G., Heckman T. M., White S. D. M., Charlot S., Tremonti C., Brinchmann J., Bruzual G., Peng E. W., Seibert M., Bernardi M., Blanton M., Brinkmann J., Castander F., Csábai I., Fukugita M., Ivezic Z., Munn J. A., Nichol R. C., Padmanabhan N., Thakar A. R., Weinberg D. H., York D., 2003, MNRAS, 341, 33

Khoury J., Ovrut B. A., Steinhardt P. J., Turok N., 2001, PhRvD, 64, 123522

Kitching T., Balan S., Bernstein G., Bethge M., Bridle S., Courbin F., Gentile M., Heavens A., Hirsch M., Hosseini R., Kiessling A., Amara A., Kirk D., Kuijken K., Mandelbaum R., Moghaddam B., Nurbaeva G., Paulin-Henriksson S., Rassat A., Rhodes J., Schölkopf B., Shawe-Taylor J., Gill M., Shmakova M., Taylor A., Velander M., van Waerbeke L., Witherick D., Wittman D., Harmeling S., Heymans C., Massey R., Rowe B., Schrabback T., Voigt L., 2010, preprint (astro-ph/1009.0779)

Kitching T. D., Balan S. T., Bridle S., Cantale N., Courbin F., Gentile M., Gill M. S. S., Harmeling S., Heymans C., Hirsch M., Kacprzak T., Kirkby D., Margala D., Massey R. J., Melchior P., Nurbaeva G., Patton K., Rhodes J., Rowe B. T. P., Taylor A. N., Tewes M., Viola M., Witherick D., Voigt L., Young J., Zuntz J., 2012, preprint (astro-ph/1202.5254)

Kitching T. D., Miller L., Heymans C. E., van Waerbeke L., Heavens A. F., 2008, MNRAS, 390, 149

Kneib J.-P., Ellis R. S., Santos M. R., Richard J., 2004, ApJ, 607, 697

Kneib J.-P., Natarajan P., 2011, A&ARv, 19, 47

Kodama T., Bower R. G., 2001, MNRAS, 321, 18

Komatsu E., Smith K. M., Dunkley J., Bennett C. L., Gold B., Hinshaw G., Jarosik N., Larson D., Nolta M. R., Page L., Spergel D. N., Halpern M., Hill R. S., Kogut A., Limon M., Meyer S. S., Odegard N., Tucker G. S., Weiland J. L., Wollack E., Wright E. L., 2010, ApJS, accepted (arXiv:1001.4538)

Kowalski M., Rubin D., Aldering G., Agostinho R. J., Amadon A., Amanullah R., Balland C., Barbary K., Blanc G., Challis P. J., Conley A., Connolly N. V., Covarrubias R., Dawson K. S., Deustua S. E., Ellis R., Fabbro S., Fadeyev V., Fan X., Farris B., Folatelli G., Frye B. L., Garavini G., Gates E. L., Germany L., Goldhaber G., Goldman B., Goobar A., Groom D. E., Haissinski J., Hardin D., Hook I., Kent S., Kim A. G., Knop R. A., Lidman C., Linder E. V., Mendez J., Meyers J., Miller G. J., Moniez M., Mourão A. M., Newberg H., Nobili S., Nugent P. E., Pain R., Perdereau O., Perlmutter S., Phillips M. M., Prasad V., Quimby R., Regnault N., Rich J., Rubenstein E. P., Ruiz-Lapuente P., Santos F. D., Schaefer B. E., Schommer R. A., Smith R. C., Soderberg A. M., Spadafora A. L., Strolger L.-G., Strovink M., Suntzeff N. B., Suzuki N., Thomas R. C., Walton N. A., Wang L., Wood-Vasey W. M., Yun J. L., Supernova Cosmology Project, 2008, ApJ, 686, 749

Kuijken K., 1999, A&A, 352, 355

—, 2006, A&A, 456, 827

Larson D., Dunkley J., Hinshaw G., Komatsu E., Nolta M. R., Bennett C. L., Gold B., Halpern M., Hill R. S., Jarosik N., Kogut A., Limon M., Meyer S. S., Odegard N., Page L., Smith K. M., Spergel D. N., Tucker G. S., Weiland J. L., Wollack E., Wright E. L., 2011, ApJS, 192, 16

Lasky P. D., Fluke C. J., 2009, MNRAS, 396, 2257

Leauthaud A., Tinker J., Behroozi P. S., Busha M. T., Wechsler R., 2011, ArXiv Astrophysics e-prints

Lee J., Pen U.-L., 2008, ApJ, 681, 798

Leonard A., King L. J., 2010, MNRAS, 405, 1854

Leonard A., King L. J., Goldberg D. M., 2011, MNRAS, 413, 789

Leonard A., King L. J., Wilkins S. M., 2009, MNRAS, 395, 1438

Lerchster M., Seitz S., Brimioulle F., Fassbender R., Rovilos M., Böhringer H., Pierini D., Kilbinger M., Finoguenov A., Quintana H., Bender R., 2011, MNRAS, 411, 2667

Link R., Pierce M. J., 1998, ApJ, 502, 63

Luppino G. A., Kaiser N., 1997, ApJ, 475, 20

Lynds R., Petrosian V., 1986, in Bulletin of the American Astronomical Society, Vol. 18, Bulletin of the American Astronomical Society, p. 1014

Mahdavi A., Hoekstra H., Babul A., Balam D. D., Capak P. L., 2007, ApJ, 668, 806

Mandelbaum R., Hirata C. M., Broderick T., Seljak U., Brinkmann J., 2006a, MNRAS, 370, 1008

Mandelbaum R., Seljak U., Kauffmann G., Hirata C. M., Brinkmann J., 2006b, MNRAS, 368, 715

Mandelbaum R., Tasitsiomi A., Seljak U., Kravtsov A. V., Wechsler R. H., 2005, MNRAS, 362, 1451

Mantz A., Allen S. W., Ebeling H., Rapetti D., Drlica-Wagner A., 2010, MNRAS, 406, 1773

Massey R., Heymans C., Bergé J., Bernstein G., Bridle S., Clowe D., Dahle H., Ellis R., Erben T., Hetterscheidt M., High F. W., Hirata C., Hoekstra H., Hudelot P., Jarvis M., Johnston D., Kuijken K., Margoniner V., Mandelbaum R., Mellier Y., Nakajima R., Paulin-Henriksson S., Peeples M., Roat C., Refregier A., Rhodes J., Schrabback T., Schirmer M., Seljak U., Semboloni E., van Waerbeke L., 2007a, MNRAS, 376, 13

Massey R., Refregier A., 2005, MNRAS, 363, 197

Massey R., Refregier A., Bacon D. J., Ellis R., Brown M. L., 2005, MNRAS, 359, 1277

Massey R., Rowe B., Refregier A., Bacon D. J., Bergé J., 2007b, MNRAS, 380, 229

Massey R., Stoughton C., Leauthaud A., Rhodes J., Koekemoer A., Ellis R., Shaghoulian E., 2010, MNRAS, 401, 371

Mather J. C., 1982, Optical Engineering, 21, 769

Mather J. C., Cheng E. S., Eplee Jr. R. E., Isaacman R. B., Meyer S. S., Shafer R. A., Weiss R., Wright E. L., Bennett C. L., Boggess N. W., Dwek E., Gulkis S., Hauser M. G., Janssen M., Kelsall T., Lubin P. M., Moseley Jr. S. H., Murdock T. L., Silverberg R. F., Smoot G. F., Wilkinson D. T., 1990, ApJL, 354, L37

McGaugh S. S., 2004, ApJ, 611, 26

Melchior P., Viola M., Schäfer B. M., Bartelmann M., 2011, MNRAS, 412, 1552

Meneghetti M., Fedeli C., Pace F., Gottlöber S., Yepes G., 2010, A&A, 519, A90

Milgrom M., 1983, ApJ, 270, 365

Miller L., Kitching T. D., Heymans C., Heavens A. F., van Waerbeke L., 2007, MNRAS, 382, 315

Moster B. P., Somerville R. S., Maulbetsch C., van den Bosch F. C., Macciò A. V., Naab T., Oser L., 2010, ApJ, 710, 903

Motl P. M., Hallman E. J., Burns J. O., Norman M. L., 2005, ApJL, 623, L63

Munshi D., Valageas P., van Waerbeke L., Heavens A., 2008, Phys. Rep., 462, 67

Nagai D., 2006, ApJ, 650, 538

Nagai D., Vikhlinin A., Kravtsov A. V., 2007, ApJ, 655, 98

Nakajima R., Bernstein G., 2007, AJ, 133, 1763

Natarajan P., De Lucia G., Springel V., 2007, MNRAS, 376, 180

Natarajan P., Kneib J.-P., Smail I., Treu T., Ellis R., Moran S., Limousin M., Czoske O., 2009, ApJ, 693, 970

Navarro J. F., Frenk C. S., White S. D. M., 1996, ApJ, 462, 563

Ngan W., van Waerbeke L., Mahdavi A., Heymans C., Hoekstra H., 2009, MNRAS, 396, 1211

Oguri M., 2007, ApJ, 660, 1

Okabe N., Zhang Y.-Y., Finoguenov A., Takada M., Smith G. P., Umetsu K., Futamase T., 2010, ApJ, 721, 875

Okura Y., Umetsu K., Futamase T., 2007, ApJ, 660, 995

—, 2008, ApJ, 680, 1

Paraficz D., Hjorth J., 2010, ApJ, 712, 1378

Parker L. C., Hoekstra H., Hudson M. J., van Waerbeke L., Mellier Y., 2007, ApJ, 669, 21

Peacock J. A., 1999, Cosmological physics. Cambridge University Press

Peng C. Y., Ho L. C., Impey C. D., Rix H., 2002, AJ, 124, 266

Percival W. J., Reid B. A., Eisenstein D. J., Bahcall N. A., Budavari T., Frieman J. A., Fukugita M., Gunn J. E., Ivezić Ž., Knapp G. R., Kron R. G., Loveday J., Lupton R. H., McKay T. A., Meiksin A., Nichol R. C., Pope A. C., Schlegel D. J., Schneider D. P., Spergel D. N., Stoughton C., Strauss M. A., Szalay A. S., Tegmark M., Vogeley M. S., Weinberg D. H., York D. G., Zehavi I., 2010, MNRAS, 401, 2148

Perlmutter S., Aldering G., Goldhaber G., Knop R. A., Nugent P., Castro P. G., Deustua S., Fabbro S., Goobar A., Groom D. E., Hook I. M., Kim A. G., Kim M. Y., Lee J. C., Nunes N. J., Pain R., Pennypacker C. R., Quimby R., Lidman C., Ellis R. S., Irwin M., McMahon R. G., Ruiz-Lapuente P., Walton N., Schaefer B., Boyle B. J., Filippenko A. V., Matheson T., Fruchter A. S., Panagia N., Newberg H. J. M., Couch W. J., Supernova Cosmology Project, 1999, ApJ, 517, 565

Randall L., Sundrum R., 1999a, PhRvL, 83, 4690

—, 1999b, PhRvL, 83, 3370

—, 1999c, NuPhB, 557, 79

Refregier A., 2003, MNRAS, 338, 35

Refregier A., Bacon D., 2003, MNRAS, 338, 48

Reiprich T. H., Böhringer H., 2002, ApJ, 567, 716

Rhodes J., Leauthaud A., Stoughton C., Massey R., Dawson K., Kolbe W., Roe N., 2010, PASP, 122, 439

Rhodes J. D., Massey R. J., Albert J., Collins N., Ellis R. S., Heymans C., Gardner J. P., Kneib J., Koekemoer A., Leauthaud A., Mellier Y., Refregier A., Taylor J. E., Van Waerbeke L., 2007, ApJS, 172, 203

Richard J., Kneib J.-P., Ebeling H., Stark D. P., Egami E., Fiedler A. K., 2011, MNRAS, 414, L31

Riehm T., Mörtsell E., Goobar A., Amanullah R., Dahlén T., Jönsson J., Limousin M., Paech K., Richard J., 2011, A&A, 536, A94

Riess A. G., Filippenko A. V., Challis P., Clocchiatti A., Diercks A., Garnavich P. M., Gilliland R. L., Hogan C. J., Jha S., Kirshner R. P., Leibundgut B., Phillips M. M., Reiss D., Schmidt B. P., Schommer R. A., Smith R. C., Spyromilio J., Stubbs C., Suntzeff N. B., Tonry J., 1998, AJ, 116, 1009

Riess A. G., Macri L., Casertano S., Sosey M., Lampeitl H., Ferguson H. C., Filippenko A. V., Jha S. W., Li W., Chornock R., Sarkar D., 2009, ApJ, 699, 539

Rines K., Diaferio A., 2006, AJ, 132, 1275

Rines K., Geller M. J., Kurtz M. J., Diaferio A., 2003, AJ, 126, 2152

Rowe B. P. T., 2008, PhD thesis, The University of Edinburgh

Rubin V. C., Ford Jr. W. K., 1970, ApJ, 159, 379

Rubin V. C., Ford W. K. J., Thonnard N., 1980, ApJ, 238, 471

Saha P., Coles J., Macciò A. V., Williams L. L. R., 2006, ApJL, 650, L17

Salim S., Rich R. M., Charlot S., Brinchmann J., Johnson B. D., Schiminovich D., Seibert M., Mallery R., Heckman T. M., Forster K., Friedman P. G., Martin D. C., Morrissey P., Neff S. G., Small T., Wyder T. K., Bianchi L., Donas J., Lee Y.-W., Madore B. F., Milliard B., Szalay A. S., Welsh B. Y., Yi S. K., 2007, ApJS, 173, 267

Sanders R. H., 2007, MNRAS, 380, 331

Saraniti D. W., Petrosian V., Lynds R., 1996, ApJ, 458, 57

Schneider P., 2005, preprint (astro-ph/0509252)

Schneider P., Er X., 2008, A&A, 485, 363

Schneider P., Rix H., 1997, ApJ, 474, 25

Schneider P., Seitz C., 1995, A&A, 294, 411

Schrabback T., Erben T., Simon P., Miralles J., Schneider P., Heymans C., Eifler T., Fosbury R. A. E., Freudling W., Hetterscheidt M., Hildebrandt H., Pirzkal N., 2007, A&A, 468, 823

Schrabback T., Hartlap J., Joachimi B., Kilbinger M., Simon P., Benabed K., Bradač M., Eifler T., Erben T., Fassnacht C. D., High F. W., Hilbert S., Hildebrandt H., Hoekstra H., Kuijken K., Marshall P. J., Mellier Y., Morganson E., Schneider P., Semboloni E., van Waerbeke L., Velander M., 2010, A&A, 516, A63+

Scoville N., Abraham R. G., Aussel H., Barnes J. E., Benson A., Blain A. W., Calzetti D., Comastri A., Capak P., Carilli C., Carlstrom J. E., Carollo C. M., Colbert J., Daddi E., Ellis R. S., Elvis M., Ewald S. P., Fall M., Franceschini A., Giavalisco M., Green W., Griffiths R. E., Guzzo L., Hasinger G., Impey C., Kneib J., Koda J., Koekemoer A., Lefevre O., Lilly S., Liu C. T., McCracken H. J., Massey R., Mellier Y., Miyazaki S., Mobasher B., Mould J., Norman C., Refregier A., Renzini A., Rhodes J., Rich M., Sanders D. B., Schiminovich D., Schinnerer E., Scodeggio M., Sheth K., Shopbell P. L., Taniguchi Y., Tyson N. D., Urry C. M., Van Waerbeke L., Vettolani P., White S. D. M., Yan L., 2007, ApJS, 172, 38

Seitz S., Saglia R. P., Bender R., Hopp U., Belloni P., Ziegler B., 1998, MNRAS, 298, 945

Semboloni E., Mellier Y., van Waerbeke L., Hoekstra H., Tereno I., Benabed K., Gwyn S. D. J., Fu L., Hudson M. J., Maoli R., Parker L. C., 2006, A&A, 452, 51

Sérsic J. L., 1968, Atlas de galaxias australes. Observatorio Astronomico, Cordoba, Argentina

Sheldon E. S., Johnston D. E., Masjedi M., McKay T. A., Blanton M. R., Scranton R., Wechsler R. H., Koester B. P., Hansen S. M., Frieman J. A., Annis J., 2009, ApJ, 703, 2232

Shu C., Zhou B., Bartelmann M., Comerford J. M., Huang J.-S., Mellier Y., 2008, ApJ, 685, 70

Skordis C., Mota D. F., Ferreira P. G., Bœhm C., 2006, PhRvL, 96, 011301

Soucail G., Fort B., Mellier Y., Picat J. P., 1987, A&A, 172, L14

Soucail G., Kneib J.-P., Golse G., 2004, A&A, 417, L33

Spergel D. N., Verde L., Peiris H. V., Komatsu E., Nolta M. R., Bennett C. L., Halpern M., Hinshaw G., Jarosik N., Kogut A., Limon M., Meyer S. S., Page L., Tucker G. S., Weiland J. L., Wollack E., Wright E. L., 2003, ApJS, 148, 175

Splinter R. J., Melott A. L., Linn A. M., Buck C., Tinker J., 1997, ApJ, 479, 632

Springel V., White S. D. M., Jenkins A., Frenk C. S., Yoshida N., Gao L., Navarro J., Thacker R., Croton D., Helly J., Peacock J. A., Cole S., Thomas P., Couchman H., Evrard A., Colberg J., Pearce F., 2005, Nature, 435, 629

Stark D. P., Ellis R. S., Richard J., Kneib J.-P., Smith G. P., Santos M. R., 2007, ApJ, 663, 10

Sumi T., Abe F., Bond I. A., Dodd R. J., Hearnshaw J. B., Honda M., Honma M., Kan-ya Y., Kilmartin P. M., Masuda K., Matsubara Y., Muraki Y., Nakamura T., Nishi R., Noda S., Ohnishi K., Petterson O. K. L., Rattenbury N. J., Reid M., Saito T., Saito Y., Sato H., Sekiguchi M., Skuljan J., Sullivan D. J., Takeuti M., Tristram P. J., Wilkinson S., Yanagisawa T., Yock P. C. M., 2003, ApJ, 591, 204

Sumi T., Kamiya K., Bennett D. P., Bond I. A., Abe F., Botzler C. S., Fukui A., Furusawa K., Hearnshaw J. B., Itow Y., Kilmartin P. M., Korpela A., Lin W., Ling C. H., Masuda K., Matsubara Y., Miyake N., Motomura M., Muraki Y., Nagaya M., Nakamura S., Ohnishi K., Okumura T., Perrott Y. C., Rattenbury N., Saito T., Sako T., Sullivan D. J., Sweatman W. L., Tristram P. J., Udalski A., Szymański M. K., Kubiak M., Pietrzyński G., Poleski R., Soszyński I., Wyrzykowski Ł., Ulaczyk K., Microlensing Observations in Astrophysics (MOA) Collaboration, 2011, Nature, 473, 349

Sunyaev R. A., Zeldovich Y. B., 1972, Comments on Astrophysics and Space Physics, 4, 173

Takahashi R., Chiba T., 2007, ApJ, 671, 45

Tegmark M., Blanton M. R., Strauss M. A., Hoyle F., Schlegel D., Scoccimarro R., Vogeley M. S., Weinberg D. H., Zehavi I., Berlind A., Budavari T., Connolly A., Eisenstein D. J., Finkbeiner D., Frieman J. A., Gunn J. E., Hamilton A. J. S., Hui L., Jain B., Johnston D., Kent S., Lin H., Nakajima R., Nichol R. C., Ostriker J. P., Pope A., Scranton R., Seljak U., Sheth R. K., Stebbins A., Szalay A. S., Szapudi I., Verde L., Xu Y., Annis J., Bahcall N. A., Brinkmann J., Burles S., Castander F. J., Csabai I., Loveday J., Doi M., Fukugita M., Gott III J. R., Hennessy G., Hogg D. W., Ivezić Ž., Knapp G. R., Lamb D. Q., Lee B. C., Lupton R. H., McKay T. A., Kunszt P., Munn J. A., O'Connell L., Peoples J., Pier J. R., Richmond M., Rockosi C., Schneider D. P., Stoughton C., Tucker D. L., Vanden Berk D. E., Yanny B., York D. G., SDSS Collaboration, 2004, ApJ, 606, 702

Tisserand P., Le Guillou L., Afonso C., Albert J. N., Andersen J., Ansari R., Aubourg É., Bareyre P., Beaulieu J. P., Charlot X., Coutures C., Ferlet R., Fouqué P., Glicenstein J. F., Goldman B., Gould A., Graff D., Gros M., Haissinski J., Hamadache C., de Kat J., Lasserre T., Lesquoy É., Loup C., Magneville C., Marquette J. B., Maurice É., Maury A., Milsztajn A., Moniez M., Palanque-Delabrouille N., Perdereau O., Rahal Y. R., Rich J., Spiro M., Vidal-Madjar A., Vigroux L., Zylberajch S., EROS-2 Collaboration, 2007, A&A, 469, 387

Treu T., Ellis R. S., Kneib J.-P., Dressler A., Smail I., Czoske O., Oemler A., Natarajan P., 2003, ApJ, 591, 53

Tyson J. A., Wenk R. A., Valdes F., 1990, ApJL, 349, L1

Udalski A., 2003, Acta Astronomica, 53, 291

Udalski A., Szymanski M., Kaluzny J., Kubiak M., Mateo M., 1992, Acta Astronomica, 42, 253

Vale C., White M., 2006, New Atronomy, 11, 207

van Uitert E., Hoekstra H., Velander M., Gilbank D. G., Gladders M. D., Yee H. K. C., 2011, A&A, 534, A14+

Van Waerbeke L., Mellier Y., 2003, preprint (astro-ph/0305089)

Van Waerbeke L., Mellier Y., Erben T., Cuillandre J. C., Bernardeau F., Maoli R., Bertin E., McCracken H. J., Le Fèvre O., Fort B., Dantel-Fort M., Jain B., Schneider P., 2000, A&A, 358, 30

Van Waerbeke L., Mellier Y., Hoekstra H., 2005, A&A, 429, 75

Vegetti S., Koopmans L. V. E., Bolton A., Treu T., Gavazzi R., 2010, MNRAS, 408, 1969

Velander M., Kuijken K., Schrabback T., 2011, MNRAS, 412, 2665

Viola M., Melchior P., Bartelmann M., 2012, MNRAS, 419, 2215

Voigt L. M., Bridle S. L., 2010, MNRAS, 404, 458

Voigt L. M., Bridle S. L., Amara A., Cropper M., Kitching T. D., Massey R., Rhodes J., Schrabback T., 2011, preprint (astro-ph/1105.5595)

Walsh D., Carswell R. F., Weymann R. J., 1979, Nature, 279, 381

Wittman D. M., Tyson J. A., Kirkman D., Dell'Antonio I., Bernstein G., 2000, Nature, 405, 143

Wright C. O., Brainerd T. G., 2000, ApJ, 534, 34

Wyrzykowski L., Skowron J., Kozłowski S., Udalski A., Szymański M. K., Kubiak M., Pietrzyński G., Soszyński I., Szewczyk O., Ulaczyk K., Poleski R., Tisserand P., 2011, MNRAS, 416, 2949

Yang X., Mo H. J., van den Bosch F. C., Jing Y. P., Weinmann S. M., Meneghetti M., 2006, MNRAS, 373, 1159

Yee J. C., Shvartzvald Y., Gal-Yam A., Bond I. A., Udalski A., Kozlowski S., Han C., Gould A., Skowron J., Suzuki D., the MOA Collaboration, the OGLE Collaboration, the MicroFUN Collaboration, 2012, preprint (astro-ph/1201.1002)

Zhao H., 2007, IJMPD, 16, 2055

Zibetti S., Charlot S., Rix H.-W., 2009, MNRAS, 400, 1181

Zitrin A., Broadhurst T., Barkana R., Rephaeli Y., Benítez N., 2011, MNRAS, 410, 1939

Zwicky F., 1933, Helvetica Physica Acta, 6, 110

—, 1937, ApJ, 86, 217

Nederlandse samenvatting

Donkere materie en kosmologie

Het lijkt misschien verwonderlijk, maar de sterren en sterrenstelsels die we zien als we omhoog kijken zijn slechts een klein deel van waar ons universum werkelijk uit bestaat. Zelfs de meest geavanceerde telescopen op aarde of in de ruimte kunnen de echte massa die zich rondom alle bekende lichtbronnen bevindt niet direct waarnemen. Deze onzichtbare materie beïnvloedt echter door zijn zwaartekracht alles wat we zien, van onze eigen melkweg tot de rand van het universum, en dat is hoe we van het bestaan ervan af weten. Omdat het geen licht uitzendt of absorbeert kunnen we het niet 'zien' in de traditionele zin, en het heeft dan ook de naam *donkere materie* gekregen.

Kosmologie is de studie van de oorsprong en de ontwikkeling van het heelal. Aangezien donkere materie veel invloed heeft op dit proces vanaf het begin 13,7 miljard jaar geleden, zijn wij als kosmologen vooral geïnteresseerd in hoe het zich gedraagt in verschillende omgevingen. Simulaties die gebruik maken van alle ingewikkelde natuurkundige wetten die we tot nu toe hebben verzameld laten ons zien dat de donkere materie zich verdeelt in een netwerk van filamenten dat bekend staat als het *Kosmische Web* (zie Figuur 7.1). Wanneer de draden elkaar kruisen ontstaan grote concentraties, of *halo's*, van donkere materie waarin de sterren en sterrenstelsels zich verzamelen. Door observaties kunnen we kaarten met de verdeling van donkere materie maken, en door het vergelijken van deze kaarten met de voorspellingen van simulaties kunnen we bepalen of onze natuurkundige wetten juist zijn of niet.

Er zijn veel manieren om donkere materie te bestuderen, en verschillende technologieën worden gebruikt voor verschillende ruimte-omgevingen, maar een techniek die in de meeste gevallen kan worden toegepast is *zwakke zwaartekrachtlenswerking*. Zwaartekrachtlenzen gebruiken, zoals de naam al aangeeft, de zwaartekracht om het licht van sterrenstelsels in de verre achtergrond te buigen in een proces dat vergelijkbaar is met een gewone lens in, bijvoorbeeld, brillen. Een zwaartekrachtlens kan elke verzameling van massa zijn, zoals een cluster van sterrenstelsels, een enkel sterrenstelsel of zelfs maar een dun donker filament in het Kosmische Web. Wanneer de materie zeer geconcentreerd is, veroorzaakt die een ernstige verstoring van het beeld van de erachter gelegen sterrenstelsels. Dit resulteert in de prachtige bogen die men kan zien in het

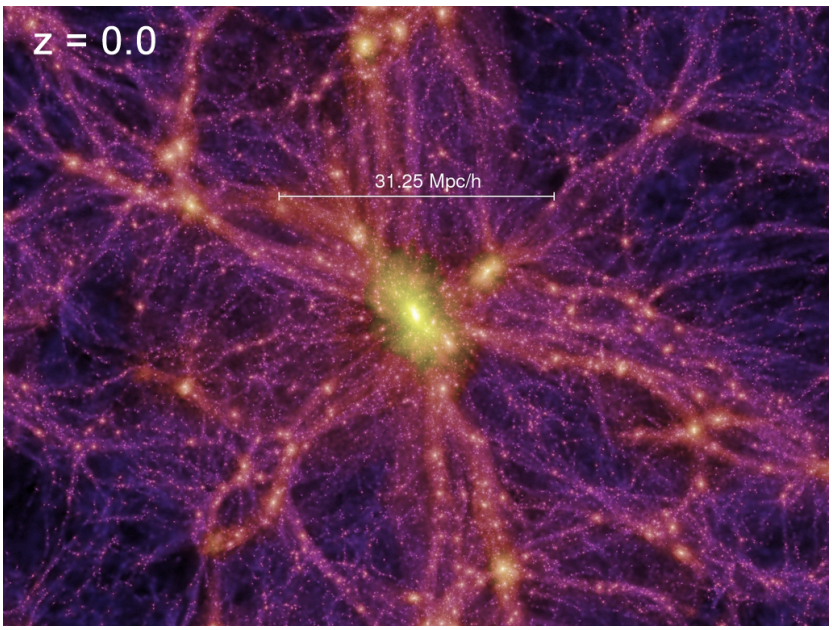

Figuur 7.1 De voorspelling van de Millenniumsimulatie voor het heelal zoals het er vandaag uitziet, gemaakt door Volker Springel en zijn medewerkers. Wat we zien zijn de verbonden filamenten van het Kosmische Web, met een ophoping van donkere materie in het midden. De centrale concentratie komt overeen met een zeer rijk cluster van sterrenstelsels.

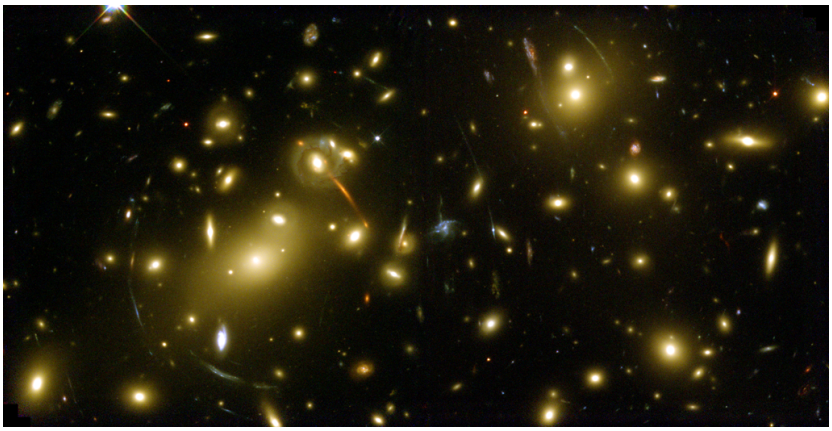

Figuur 7.2 Voorbeeld van een zwaartekrachtlens: de rijke cluster van sterrenstelsels Abell 2218 afgebeeld door de ruimtetelescoop *Hubble Space Telescope* in 1999. Afbeelding: NASA/ESA, A. Fruchter en het ERO Team (STScI, ST-ECF).

cluster Abell 2218 (Figuur 7.2). Omdat een grotere massaconcentratie meer vervorming veroorzaakt, kunnen we door gebruik te maken van deze bogen afleiden waar de donkere materie zich bevindt. Wanneer de massaconcentratie laag is, hetgeen bijna overal het geval is, kunnen we zwakke vervormingen door

zwaartekrachtlenswerking, genoemd *shear*, gebruiken om statistisch te bepalen waar de donkere materie is. Dit is het regime waar de zwakke lenswerking-techniek zich mee bezig houdt.

Met dit Proefschrift heb ik ernaar gestreefd om onze kennis over de verdeling van materie in sterrenstelsels en clusters van sterrenstelsels te vergroten, door zowel het ontwikkelen van de theoretische kant van de zwakke zwaartekracht-lenswerking, als door het gebruik van grote optische waarneemprogramma's om de zwakke zwaartekrachtlenswerkingeffect in de werkelijkheid te observeren. Ik zet mijn werk uiteen in de vier afzonderlijke maar verwante Hoofdstukken die hieronder worden samengevat.

Dit Proefschrift

Ik begin dit Proefschrift met een kort overzicht van de huidige status van kosmologie in Hoofdstuk 1, en beschrijf de verschillende manieren om meer te leren over het heelal als geheel. Dit Hoofdstuk bevat ook een gedetailleerdere kennismaking met de zwakke zwaartekrachtlenswerking en de software die beschikbaar is om de zwakke vervormingen van de achtergrond sterrenstelsels te meten. Daarna volgen de Hoofdstukken waarin ik mijn onderzoek van de afgelopen vier jaar in detail beschrijf, waarvan sommige al zijn gepubliceerd in het tijdschrift Monthly Notices of the Royal Astronomical Society (MNRAS). Ik vat hier deze Hoofdstukken samen.

Hoofdstuk 2: Een nieuwe vormmeting-techniek, en de toepassing ervan op sterrenstelsels met kleurgradiënten in de context van zwakke zwaartekrachtlenswerking waarneemprogramma's

Zwakke zwaartekrachtlenswerking, als een van de meest krachtige methoden van kosmologie, is de belangrijkste drijvende kracht achter de grootste optische waarneemprogramma's die gepland zijn in de nabije toekomst. De statistische aard van de methode vereist de analyse van een groot aantal achtergrond sterrenstelsels, en de minimale vervormingen vereisen waarnemingen van hoge kwaliteit en uiterst precieze vervormingsmetingen. Software voor de zwakke zwaartekrachtlenswerking techniek moet dus zowel snel als accuraat zijn, en zo'n software pakket wordt geïntroduceerd en getest in dit Hoofdstuk. Deze *MV pipeline* heeft bewezen zeer competitief te zijn, met extra voordeel de mogelijkheid om lensvervormingen van hogere orde dan shear, oftewel flexion, te meten. De tests beschreven in dit Hoofdstuk beslaan zowel monochromatische als niet-monochromatische simulaties, waarbij de laatste zijn opgenomen om het effect van een golflengte-afhankelijke puntspreidingsfunctie (PSF) veroorzaakt door de telescoop te bepalen. Aangezien de meeste sterrenstelsels kleurgradiënten hebben, met in de kern een andere kleur dan aan de buitenkant, heeft een golflengte-afhankelijke PSF en variërende invloed op verschillende delen van het waargenomen beeld van het sterrenstelsel. Hierdoor kan een bias worden geïntroduceerd wanneer niet precies voor de PSF kan worden gecorrigeerd. Door het creëren van simulaties op basis van werkelijke sterrenstelsels, waargenomen in twee verschillende filters, zien we dat de extra bias die wordt veroorzaakt door dit effect niet erger is dan de bias in de meetsoftware. Wij stellen uit onze tests vast dat als er voldoende trainingsgegevens beschikbaar zijn, we waarschijnlijk

het kleurgradiënteffect voldoende nauwkeurig kunnen karakteriseren om hiermee toekomstige onderzoeken, zoals de Euclid ruimtemissie, wiens lancering gepland staat voor 2019, te corrigeren.

Hoofdstuk 3: Studie van de galactische donkere materie halo's in het COSMOS onderzoek door middel van zwakke zwaartekrachtlenswerking flexion

De huidige theorieën van structuurvorming voorspellen dat sterrenstelsels ingebed zijn in uitgestrekte donkere materie halo's. Van deze halo's wordt verwacht dat zij een specifiek dichtheid profiel hebben, en met zwakke zwaartekrachtlenswerking kunnen we deze profielen meten op verschillende schalen. Op kleine schaal voegen de hogere-orde vervormingen, bekend als flexion, belangrijke informatie toe aan de zwakke zwaartekrachtlenswerking metingen. We presenteren in dit Hoofdstuk de eerste detectie van het flexionsignaal rond sterrenstelsels in data die in de ruimte is waargenomen. Het signaal is gemeten met de *MV pipeline*, geïntroduceerd en getest in Hoofdstuk 2. Wij combineren dit flexionsignaal met shear om het gemiddelde dichtheid profiel van sterrenstelsels in het Hubble Space Telescope COSMOS onderzoek nauwkeurig te bepalen. We tonen ook aan dat het licht uitgezonden door nabijgelegen lichtbronnen een aanzienlijk storend effect op flexion metingen kan hebben. Na correctie voor de invloed van het licht van de lens sterrenstelsels, tonen we aan dat het opnemen van flexion sterkere beperkingen geeft op de dichtheid profielen dan het gebruik van louter shear.

Hoofdstuk 4: De relatie tussen baryonen en de donkere materie halo's van sterrenstelsels in de CFHTLS bepaald met zwakke zwaartekrachtlenswerking

Omdat donkere materie halo's zo uitgebreid zijn is het belangrijk om ze zowel op grote als kleine schaal te onderzoeken om zo meer te leren over de invloed die donkere materie heeft op normale 'baryonische' materie, en vice versa. Zwakke zwaartekrachtlenswerking biedt de mogelijkheid om dit te doen omdat de technologie niet alleen bruikbaar is op verschillende schalen, maar ook omdat ze onafhankelijk is van de aard van de materie die onderzocht wordt. In dit Hoofdstuk presenteren we een studie van de algemene eigenschappen van donkere halo's van sterrenstelsels als functie van de eigenschappen van het sterrenstelsel dat ermee geassocieerd wordt, op basis van gegevens uit een van de grootste voltooide zwakke zwaartekrachtlenswerking waarneemprogramma's tot nu toe: CFHTLS. We verdelen de lens sterrenstelsels in een rode en een blauwe set en bevestigen dat er een duidelijk verband bestaat tussen de donkere halo-massa en de helderheid, en tussen halo-massa en stellaire massa. Deze relaties zijn verschillend voor blauwe en rode sterrenstelsels, en we vinden ook aanwijzingen dat blauwe sterrenstelsels zich in minder geclusterde omgevingen dan rode sterrenstelsels bevinden.

Hoofdstuk 5: Het beperken van cluster profielen door middel van zwakke zwaartekrachtlenswerking shear en flexion

Clusters van sterrenstelsels zijn belangrijk voor ons begrip van de kosmologie, omdat hun aantal als functie van massa en afstand van ons afhankelijk is van de

kosmologische parameters. De meerderheid van de massa van een cluster van sterrenstelsels is in de vorm van donkere materie. Om meer te leren over kosmologie willen we deze massa zorgvuldig bepalen, maar alleen zichtbare eigenschappen zijn beschikbaar. Zwakke zwaartekrachtlenswerking heeft, zoals reeds vermeld, de mogelijkheid om de dichtheid profielen van donkere halo's in kaart te brengen op zowel grote als kleine schalen. Om hiervan ten volle te profiteren, moeten de profielen van de donkere halo's zorgvuldig zijn gemodelleerd, zelfs als het centrum van het cluster niet nauwkeurig bekend is. In dit Hoofdstuk modelleren we de profielen die niet correct gecentreerd zijn voor zowel shear als flexion. We tonen ook dat de helling van de curve van de differentiële oppervlaktedichtheid kan worden verkregen door een eenvoudige combinatie van flexions. Deze flexions zijn gevoelig voor kleine locale variaties in de dichtheid, waardoor ze een belangrijke aanvulling op shear zijn. Door middel van een reeks tests zien wij dat dit met name relevant is als het gaat om het bepalen van cluster profielen die niet correct gecentreerd zijn.

Svensk sammanfattning

Mörk materia och kosmologi

Det kan verka förbluffande, men de stjärnor och galaxer vi ser när vi blickar uppåt är bara en liten del av det som verkligen finns ute i vårt universum. Inte ens de mest avancerade teleskopen på jorden eller i rymden kan urskilja den materia som omsluter alla kända ljuskällor eftersom den inte avger eller absorberar något ljus. Därför kan vi inte 'se' den i ordets traditionella mening, och den har därav fått namnet *mörk materia*. Denna osynliga materia påverkar däremot genom sin tyngdkraft allt vi ser, från vår egen galax till universums yttersta kant, och det är så vi känner till dess existens.

Kosmologi är läran om universums ursprung och utveckling. Eftersom mörk materia har haft så stor inverkan på denna process från dess allra första början för 13,7 miljarder år sedan, så är vi som kosmologer särskilt intresserade av hur den beter sig i olika omgivningar. Simuleringar som utnyttjar alla de intrikata fysikaliska lagar som vi hittills upptäckt visar oss att den mörka materien är fördelad i ett nätverk av filament som på engelska kallas för *the Cosmic Web* (se Figur 8.1). Där filamenten korsas skapas stora moln, eller *haloer*, av mörk materia där stjärnor och galaxer ackumuleras. Genom observationer kan vi skapa kartor över fördelningen av mörk materia och genom att jämföra sådana kartor med förutsägelserna från simuleringarna så kan vi avgöra om våra fysikaliska lagar är korrekta.

Det finns många sätt att undersöka mörk materia på och olika tekniker används för olika rymdmiljöer, men en teknik som kan tillämpas i de flesta fall är *svag gravitationslinsning*. Gravitationslinser använder, som namnet antyder, gravitation till att böja ljus från avlägsna bakgrundsgalaxer i en process som kan liknas vid en vanlig lins i till exempel ett par glasögon. En gravitationslins kan bestå av vilken ansamling av massa som helst, såsom en galaxhop, en enstaka galax eller bara ett tunt mörkt filament. När materien är mycket koncentrerad orsakar den en kraftig förvrängning av bilden av bakgrundsgalaxen, vilket resulterar i de vackra bågar som syns i galaxhopar som Abell 2218 (Figur 8.2). Eftersom en större masskoncentration innebär mer förvrängning så kan vi använda dessa bågar till att härleda var den mörka materien finns. När masskoncentrationen är låg, vilket förekommer i huvudsak överallt annars i universum, så kan vi använda svagare linsningsdistorsioner, kallade *shear*, till att statistiskt

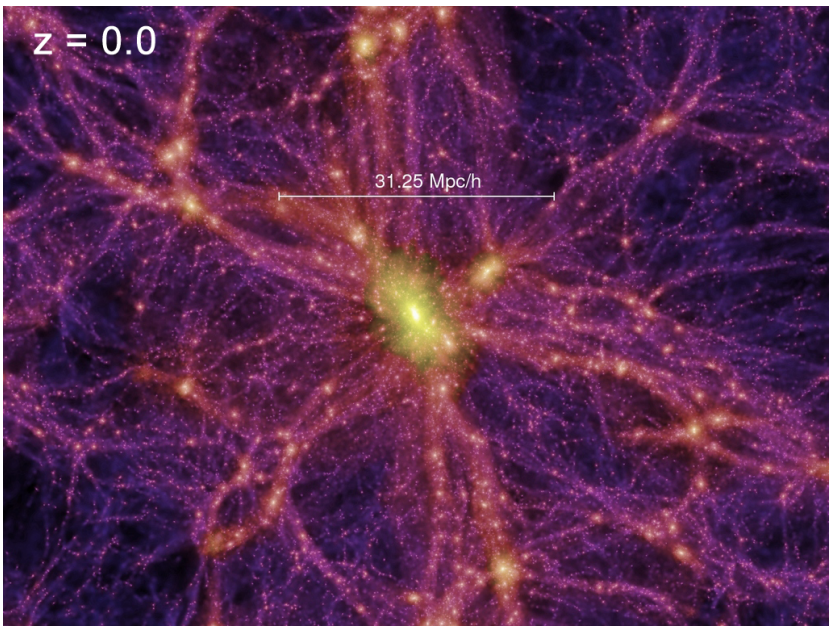

Figur 8.1 Millenniumsimuleringens vision av vårt universum som det ser ut idag, skapad av Volker Springel och hans medarbetare. Det vi ser är filamenten tillhörande det kosmiska nätverk som på engelska benämns *the Cosmic Web*, med en ansamling av mörk materia i mitten. Ansamlingen motsvarar en mycket rik galaxhop.

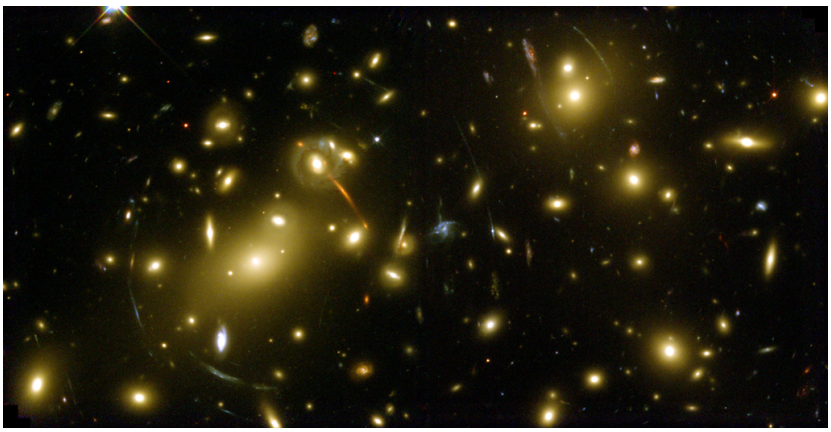

Figur 8.2 Exempel på gravitationslinsning: den rika galaxhopen Abell 2218 avbildad med hjälp av rymdteleskopet *Hubble Space Telescope* 1999. Bildkälla: NASA/ESA, A. Fruchter och ERO-teamet (STScI, ST-ECF).

fastställa var den mörka materien finns; det är detta som den svaga linsningstekniken uträttar.

Med den här Avhandlingen har jag som målsättning att öka vår kunskap om fördelningen av materia i galaxer och galaxhopar, både genom att utveckla

den teoretiska sidan av svag gravitationslinsning och genom att använda stora optiska datainsamlingar till att observera den svaga linseffekten i verkligheten. Jag skildrar mitt arbete i de fyra separata men sammanlänkade Kapitlen som finns sammanfattade härnedan.

Denna Avhandling

Jag börjar Avhandlingen med att i Kapitel 1 ge en kort översikt av kosmologins aktuella status och av de olika sätt som finns tillgängliga för att studera vårt universum i sin helhet. Där ger jag även en mer ingående introduktion till svag gravitationslinsning och till de programvaror som finns till hands för att mäta de svaga linsningsdistorsionerna av bakgrundsgalaxer. Därefter följer Kapitel där jag mer detaljerat beskriver min forskning under de senaste fyra åren, varav en del redan har publicerats i Monthly Notices of the Royal Astronomical Society (MNRAS). Jag sammanfattar här dessa Kapitel.

Kapitel 2: En ny distorsionsmätningsmetod och dess tillämpning på galaxer med färggradienter i gravitationslinsningsundersökningar

Som en av kosmologins mest kraftfulla metoder så är svag gravitationslinsning nu den främsta drivkraften bakom några av de mest omfattande aktuella optiska datainsamlingarna som någonsin gjorts. Teknikens statistiska karaktär kräver analys av ett stort antal bakgrundsgalaxer, och de minimala distorsionerna det handlar om fordrar data av hög kvalitet och ytterst exakta distorsionsmätningar. Mjukvara för svag linsningsteknik måste därför vara både snabb och korrekt, och en sådan programsvit introduceras och testas i detta Kapitel. Denna *MV pipeline* har visat sig vara mycket konkurrenskraftig, med den extra egenskapen att kunna mäta linsförvrängningar av högre ordning än shear, även kallade flexion. De tester som beskrivs i detta Kapitel inbegriper både monokromatiska och polykromatiska simuleringar, där de senare har inkluderats för att bedöma effekten av en våglängdsberoende punktspridningsfunktion (PSF) förorsakad av teleskopet. Eftersom de flesta galaxer uppvisar färggradienter, med en kärna som har en annan färg än utkanten, kommer en våglängdsberoende PSF att påverka skilda delar av galaxavbildningen olika. Således kan viss felaktighet introduceras om PSF:en inte korrigeras för exakt resultat. Genom att skapa simuleringar baserade på verkliga galaxer som observerats i två olika filter, finner vi att extra felaktigheter orsakade av denna effekt inte är värre än de felaktigheter som finns i själva mätningsprogramvaran. Vi drar slutsatsen från våra tester att om tillräcklig mängd träningsdata ges så kommer vi sannolikt att kunna karaktärisera färggradienteffekten tillräckligt noggrant för att kunna korrigera för den i framtida undersökningar såsom det rymdbaserade Euclid-uppdraget med planerad uppskjutning år 2019.

Kapitel 3: Studie av galaktiska mörkmateriehaloer i COSMOS-undersökningen med svag gravitationslinsningsflexion

Nuvarande teorier om strukturbildning förutspår att galaxer är inneslutna i omfattande haloer bestående av mörk materia. Haloerna förväntas ha specifika densitetsprofiler och med svag gravitationslinsning kan vi undersöka dessa profiler på flera skalor. På små skalor kompletterar distorsioner av högre ordning,

som kallas flexion, distorsionsmätningarna med högre detaljnoggrannhet. Vi presenterar i detta Kapitel den första detekteringen av en flexionsignal kring galaxer i rymdbaserade data. Signalen har erhållits med hjälp av *the MV pipeline* som introducerats och testats i Kapitel 2. Vi kombinerar denna flexionsignal med shear för att definiera den genomsnittliga densitetsprofilen hos galaxerna i Hubble Space Telescopes COSMOS-undersökning. Vi visar också att ljuset från närliggande ljuskällor kan ha en betydande effekt på flexionsmätningar. Efter korrigering för påverkan av galaxlinsernas ljus visar vi att inkluderingen av flexion ger strängare restriktioner på densitetsprofiler än vad enbart shear gör.

Kapitel 4: Relationen mellan galaxers mörkmateriehaloer och baryoner i CFHTLS via svag gravitationslinsning

Eftersom mörkmateriehaloer är så omfattande är det viktigt att undersöka både stora och små skalor för att förstå mer om det inflytande mörk materia har på normala atomer, och vice versa. Svag linsning har förmågan att göra detta eftersom tekniken inte bara är känslig på flera avståndsskalor, utan också oberoende av vilken typ av materia som studeras. I detta Kapitel presenterar vi en studie av de generella egenskaperna hos galaxers mörka haloer som en funktion av egenskaperna hos deras värdgalaxer med hjälp av data från en av de största färdigställda svaga linsningsundersökningarna hittills: CFHTLS. Vi delar in linsgalaxerna i en röd och en blå kategori och bekräftar att det finns ett klart samband mellan den mörka halomassan och luminositet, och mellan halomassan och stjärnmassan. Dessa relationer är olika för blå och röda galaxer, och vi finner också indikationer på att blå galaxer vistas i mindre klustrade omgivningar än vad röda galaxer gör.

Kapitel 5: Undersökning av galaxhopsprofiler via svag linsningsshear och -flexion

Galaxhopar är viktiga för vår förståelse av bakgrundskosmologin eftersom deras antal som en funktion av massa och avstånd från oss beror på kosmologiska parametrar. Majoriteten av massan i en galaxhop är i form av mörk materia, och för att vi ska lära oss mer om kosmologi måste denna massa noggrant beräknas trots att bara synliga storheter finns att tillgå. Svag linsning har, som redan nämnts, förmågan att kartlägga mörka haloers densitetsprofiler på både små och stora skalor. För att kunna dra full nytta av detta måste galaxhopens profil omsorgsfullt modelleras även om dess centrum inte är exakt fastställt. I detta Kapitel har vi tagit fram ocentrerade profiler för både shear och flexion. Vi visar också att lutningen på kurvan för den differentiella ytdensiteten kan erhållas via en enkel kombination av flexioner. Dessa flexioner är känsliga för små variationer i densitet, vilket gör dem till viktiga komplement till shear. Genom en serie tester finner vi att detta är särskilt relevant när det gäller att kartlägga den ocentrerade galaxhopsprofilen.

Publications

1. *CFHTLenS: improving the quality of photometric redshifts with precision photometry*
   Hildebrandt, Erben, Kuijken, van Waerbeke, Heymans, Coupon, Benjamin, Bonnett, Fu, Hoekstra, Kitching, Mellier, Miller, Velander, Hudson, Rowe, Schrabback, Semboloni, & Benítez 2012
   MNRAS, 421, 2355-2367
   This publication is publicly available at `http://arxiv.org/abs/1111.4434`

2. *Galaxy-galaxy lensing constraints on the relation between baryons and dark matter in galaxies in the Red Sequence Cluster Survey 2*
   van Uitert, Hoekstra, Velander, Gilbank, Gladders, & Yee 2011
   A&A, 534, A14+
   This publication is publicly available at `http://arxiv.org/abs/1107.4093`

3. *Probing galaxy dark matter haloes in COSMOS with weak lensing flexion*
   Velander, Kuijken, & Schrabback 2011
   MNRAS, 412, 2665-2677 (Chapter 3, page 64)
   This publication is publicly available at `http://arxiv.org/abs/1011.3041`

4. *Gravitational Lensing Accuracy Testing 2010 (GREAT10) Challenge Handbook*
   Kitching, Balan, Bernstein, Bethge, Bridle, Courbin, Gentile, Heavens, Hirsch, Hosseini, Kiessling, Amara, Kirk, Kuijken, Mandelbaum, Moghaddam, Nurbaeva, Paulin-Henriksson, Rassat, Rhodes, Schölkopf, Shawe-Taylor, Gill, Shmakova, Taylor, Velander, van Waerbeke, Witherick, Wittman, Harmeling, Heymans, Massey, Rowe, Schrabback, & Voigt 2010
   preprint (astro-ph/1009.0779)
   This publication is publicly available at `http://arxiv.org/abs/1009.0779`

5. *Results of the GREAT08 Challenge: an image analysis competition for cosmological lensing*
   Bridle, Balan, Bethge, Gentile, Harmeling, Heymans, Hirsch, Hosseini, Jarvis, Kirk, Kitching, Kuijken, Lewis, Paulin-Henriksson, Schölkopf, Velander, Voigt, Witherick, Amara, Bernstein, Courbin, Gill, Heavens, Mandelbaum, Massey, Moghaddam, Rassat, Réfrégier, Rhodes, Schrabback, Shawe-Taylor, Shmakova, van Waerbeke, & Wittman 2010
   MNRAS, 405, 2044-2061
   This publication is publicly available at `http://arxiv.org/abs/0908.0945`

6. *Evidence of the accelerated expansion of the Universe from weak lensing tomography with COSMOS*
   Schrabback, Hartlap, Joachimi, Kilbinger, Simon, Benabed, Bradač, Eifler, Erben, Fassnacht, High, Hilbert, Hildebrandt, Hoekstra, Kuijken, Marshall, Mellier, Morganson, Schneider, Semboloni, van Waerbeke, & Velander 2010
   A&A, 516, A63+
   This publication is publicly available at `http://arxiv.org/abs/0911.0053`

Curriculum Vitæ

Born in 1983 in Lund of southern Sweden, I grew up in a small village about a Swedish mile (10 km) from the city, surrounded by sweeping fields of green, yellow and blue. It was when I started seventh grade, in 1996 at the age of thirteen, that I first came in contact with science. I had always been curious and always asked the big questions about how the world worked, and now suddenly I was being taught the answers. My teacher at that time was a warm and inspiring person who encouraged me to use my own approach to internalise the material, such as creating a website about our Solar System. I thoroughly enjoyed making the computer show what I wanted it to display using the secret language of HTML, and the subject of my work — astronomy — caught my attention as well.

Once I had finished ninth grade in 1999 I got accepted to the International Baccalaureate (IB) in Malmö, the Big City. From then on my life changed dramatically as I was now amongst others who asked as many questions as I did. All subjects were taught in English, which is why I do not have an established science vocabulary in Swedish. After the introductory year I was allowed to deepen my knowledge in a few subjects of my choice, and apart from languages and maths I also chose physics and economics. Both subjects held the sublime promise of explaining the workings of the world, but in the end physics appealed to me more. Therefore I chose *What mass does the Hydra 1 cluster of galaxies (Abell 1060) contain?* as the subject of my Extended Essay for which I carried out the research with the help of Lund University. This project constituted my first encounter with the mysterious dark matter, a taunting enigma which has fascinated me ever since.

I had decided early on during the IB that I wanted to attend university in the UK, partly because of the language barrier I would otherwise face in my own country, and partly because of the adventure it entailed. As I scrolled down the UCAS list of subjects aiming for physics, a subject at the top of the list once again caught my attention: astronomy & astrophysics. Going through the directory of institutions offering such a specialised programme, I knew straight away that Edinburgh University had to be my highest priority choice, though since I had never been my main reason for this decision was having seen *Braveheart*. To my great joy I was accepted and in 2002 my parents and I took the ferry across the North Sea to the wonderful city of Edinburgh which still holds a special place in my heart. As an interesting aside, the second person I spoke to in this city was my beloved future husband though I did not

yet know it.

In my fifth year at Edinburgh University, it was time to chose my master's research project. My fascination with dark matter had only grown during my time there, and amongst the choice of about thirty project titles only one seemed appropriate to me: *Probing dark matter and baryonic sub-structure with gravitational lensing* with Andy Taylor. I did not rest until I had secured that project, and I thoroughly enjoyed the research the rest of that year and received my Master of Physics degree in 2007. The project gave me a taste of what weak lensing could do, and as a result I limited my PhD applications to institutes where I knew I would be able to research further using this technique. The only non-UK institute I applied to was Leiden, at the recommendation of Andy, as there was an opportunity to become an Early Stage Researcher within the European Marie Curie network *the Dark Universe with Extragalactic Lensing* (DUEL) with Konrad Kuijken. When I went for a visit I instantly liked the atmosphere at the department and the fact that I would be able to design large parts of my PhD research myself. Once again I therefore took the ferry across the North Sea, this time together with my then fiancé and our cat Trouble, and with the Netherlands as destination.

Five years on I know I made the right decision as the Sterrewacht at Leiden University has been a truly fantastic place to conduct my research. I have been in charge of the direction to take and have at the same time received great support from my supervisors and brilliant colleagues. The department also gave me the chance to act as a teaching assistant on the master's course *Astrophysical Accretion* where I created solutions to problem sheets and corrected the students' work. The plethora of international conferences and meetings I have been able, and encouraged, to attend have also given me a broad knowledge of topical cosmology and a large number of friends both within the weak lensing clique and in the greater astrophysical community. My travels have also given me the opportunity to present my work in settings as awe-inspiring as OZ Lens 2008 or the winter AAS meeting in 2012. On a more personal level, I have through these conferences also had the honour to meet and talk to many of my heroes. Most notable of these is Vera Rubin who fifty years ago helped change the world of cosmology forever even though she, as a woman, had to face and overcome obstacles every step of the way. Although I do not face the same obstacles, as women in science now enjoy much the same opportunities as men, I find her story highly inspirational.

My husband and I have now taken the ferry back across the North Sea and I am currently a post-doctoral Beecroft Fellow at Oxford University, working with Lance Miller. Already I have tutored *Optics* at Oriel College as I am a fellow there. Though I did act as a teaching assistant in Leiden, here my responsibilities towards the students are greater and include being in charge of tutorials and revision sessions, and setting and correcting collections papers. I have also quickly gotten involved in the one thing I was unable to do in Leiden due to my own lack of Dutch skills: outreach activities. Connecting with the public, and interacting with school children who are as inquisitive as I was, truly inspires me and provides me with the motivational sustenance that makes doing research so fulfilling. I do hope I will have the opportunity to do both for many years to come.

Afterword

The Sterrewacht at Leiden University has been a truly outstanding environment in which to conduct the research for this Thesis. The international focus of the Sterrewacht is, I believe, one of the main reasons why this department attracts so many great scientists and why it is so successful. And not only is the academic staff both encouraging and highly skilled, but so is the IT support. Were there any computer related issues, something which did not happen often, they were soon sorted thanks to the considerable efforts of Eric, David, Aart and Tycho. For this I am eternally grateful. Other support staff also helped make things run smoothly, and amongst them I would particularly like to thank Jan, Jeanne and Evelijn.

The lensing group consisted of an incredible collection of people. Soon after I arrived, several inspiring individuals were recruited to the group, creating a very stimulating environment for a green PhD-student like myself. Amongst them was Tim who became both a friend and a mentor to me. Tim, I am not sure if you are aware of how much you actually taught me. You sped up my learning significantly and equipped me with all the tools I needed to finish this research. You also made certain that I was not completely absorbed with work through games' nights and the occasional all-night Lord of the Rings (though not as often as you would have liked). I cannot even begin to tell you how much I appreciate your support and friendship. In fact, I consider everyone in the lensing group a friend above all else. Edo, your path to a PhD degree ran parallel to mine for more than four years, with you just pipping me to the post. Though I am not entirely happy about this, I do know that you fully deserve it. Working with you was a true pleasure; your intelligence always shone through and you were never afraid to argue your (often correct) point. You also became a close friend of mine, and I thoroughly enjoy the gossip sessions we both still indulge in. Once Stefania and Elisabetta joined us the group felt complete, although the noise level in my corridor certainly increased. Stefania, you are great fun and I wish I had gotten the chance to know you better. And Elisabetta, oh Elisabetta. With your arrival the Sterrewacht improved a hundredfold, thanks to your special take on life. You always make me see things in a different (and often better) light, both in science and otherwise. You are a fun and loud person and completely my opposite, which is probably why I find your company so refreshing. Finally, I would like to thank the lensing group as a whole and any sporadic add-ons as well, including Freeke, Berenice, Merijn, Remco and Hendrik, for being such a sociable bunch and for making coffee breaks and evenings that much more

enjoyable.

Actually Hendrik, you were part of another side to my life in Leiden as well: AA-Awesome. This band truly lived up to its name, arguably not in talent but definitely in terms of band members. You were all awesome Rik, Hendrik, Rob and Craig and I had an awesome time while it lasted. But Craig, you were probably the awesomest of them all. Your harsh sarcasm coupled with your strange politeness made me feel right back in Britain, and I often indulged in taking the mickey out of you. I think you did intensify my own sarcasm though, which means that I now frequently accidentally offend my own family. This is to your credit.

I would also like to take this opportunity to thank the two extended groups I have been a part of: the DUEL network, and the CFHTLenS collaboration. Through frequent DUEL meetings I was continuously spurred on to do my research, and I made many social connections with other young researchers in the field. CFHTLenS has also been very good to me and provided me with a great network that now spans the globe. Catherine, you in particular have been very encouraging. Thank you for believing in me; it has without doubt helped build my confidence as a scientist. You have also always been there to lend advice on a more personal level, something I greatly appreciate.

Of course, my family has also always been there for me and have always managed to muster the proper amount of awe at each one of my achievements. Thank you, Mum and Dad, for never pressuring me unnecessarily but nudging me in the right direction when appropriate. Mum, you always read through all my essays for school and university to make sure that the language was correct and fluent. As a thank you for that, I will *not* make you read my Thesis. Dad, thank you for coaxing me into doing things I would never have dared do otherwise, from joining that class at högstadiet which allowed me to be taught by Arne who got me interested in science in the first place, to contacting Lund University for guidance on my Extended Essay. These and many other choices have had a long-lasting positive effect on my life and career. Kattis, and lately also Ivar, thank you for always treating me without respect whenever I come home to Sweden and that way making me feel like I never left. Jonas, you and Ann have also supported me through this simply by making home still seem like home. I do sometimes wonder who the real big sister is though, since you and Kattis have turned into such sensible adults in my absence. Richelle, though you are not officially my sister, I do consider you one and I am grateful that you have remained my close friend even though I have been somewhat unavailable over the past year.

My wonderful family-in-law has also helped see me through. In particular, thank you Ellen for your kind-heartedness, thank you Gabrian for adding a sense of art to my Thesis, and thank you Josha for keeping my motivation high by being so fascinated by what I do that you decided to try it out for yourself. Special thanks also to all of my cousins who have always been great friends, and in particular to Tove with whom I have always been close. Furthermore, I am grateful to Johanna for taking the time to read and correct my Swedish summary. For this reason I also thank Fredrik who has been a friend ever since I recognised him as a fellow Swede in Edinburgh because of his Loka bottle.

Last, but most certainly not least, I would like to thank my own budding family. Marcus, without your tireless efforts to keep our home tidy and me fed, without your continuous and unfailing support, and without your endless love I would never have been able to do this. And little one, still dwelling within me, without your encouraging kicks to keep me motivated and focused towards the end, this would be work in progress even now.